UNEXPECTED UNIVERSALITY IN DISORDERED SYSTEMS AND MODELING PERPENDICULAR RECORDING MEDIA

BY

YANG LIU

B.S., Nanjing University, 2000
M.S., Nanjing University, 2003

DISSERTATION

Submitted in partial fulfillment of the requirements
for the degree of Doctor of Philosophy in Physics
in the Graduate College of the
University of Illinois at Urbana-Champaign, 2009

Urbana, Illinois

Abstract

In this thesis, I study the random-field Ising model (RFIM) in both theoretical and applied perspectives. For theoretical interests, I compare the avalanche behavior in equilibrium and non-equilibrium and find an unexpected universality. The application part focuses on the reliability test of the $\Delta H(M, \Delta M)$ methodology, which has been used to measure microscopic properties of magnetic recording media. Based on RFIM, an interacting random hysteron model has been developed and used to systematically test the reliability of the $\Delta H(M, \Delta M)$ methodology.

Avalanche behavior in response to slowly changing external conditions is ubiquitous in a remarkably wide variety of dynamical systems. When driven far from equilibrium, those systems display impulsive cascade of dynamic avalanches spanning a broad range of sizes. Independent of their microscopic details, many non-equilibrium systems have been shown to have exactly the same dynamic avalanche behavior on many scales. This fact is called universality. So far, non-equilibrium systems were believed to be completely different from equilibrium ones. However, here we show that the zero-temperature RFIM exhibits surprisingly similar avalanche behavior in equilibrium and out of equilibrium. This finding solves a highly controversial question, i.e. whether the equilibrium and non-equilibrium disorder-induced phase transitions of RFIM belong to the same universality class. Our finding also indicates that generally equilibrium systems and their non-equilibrium counterparts may have deep connections.

In state-of-the-art storage applications such as hard disk drives, the intrinsic switching field distribution of the media grains is one of the most crucial properties defining the recording quality. However, this piece of microscopic information is very hard to measure macroscopically, especially for the perpendicular recording media. Using the interacting random hysteron model, we have studied the reliability of the recently developed $\Delta H(M, \Delta M)$ method. We demonstrated that this method does have several advantages over comparable methods. First, it has a well-defined reliability range and it allows for self-consistency checks. Second, the presence of dipolar interactions in the range of typical recording media substantially enhances the reliability of this method. Third, it is robust even in the presence of randomness in exchange or magnetostatic coupling within the range of a typical recording media.

To my parents.

Acknowledgments

This work would not have been possible without the support of many people.

Many thanks to my adviser, Karin A. Dahmen, who read my numerous revisions and helped make some sense of the confusion. Also thanks to my committee members, Yoshitsugu Oono, Alfred Hubler and Michael Weissman, who offered guidance and support.

I thank James P. Sethna, A. Alan Middleton, Gil Refael, Robert A. White, Andrew R. Missel, Matthew Delgado and Georgios Tsekenis for valuable discussions. I thank my collaborators, Andreas Berger, Ondrej Hovorka, Pierre Le Doussal and Kay Jörg Wiese for extensive discussions.

Many thanks to the Harry G. Drickamer fund, providing me with the financial means to complete part of this work. I also acknowledge the support of NSF Grant No. DMR 03-14279 and NSF Grant No. DMR 03-25939 ITR (Materials Computation Center).

All the numerical calculations presented here were conducted on the Beowolf cluster of the Materials Computation Center and the Turing cluster maintained and operated by the Computational Science and Engineering Program at the University of Illinois.

Finally, many thanks to my parents, and my fiancee who endured this long process with me, always offering support and love.

Table of Contents

List of Tables

List of Figures

List of Abbreviations

RFIM	random-field Ising model
zt-RFIM	zero-temperature random-field Ising model
ztne-RFIM	zero-temperature non-equilibrium random-field Ising model
RG	renormalization group
MFT	mean field theory
DIPT	disorder-induced phase transition
GS	ground state
MS	metastable state
DS	demagnetized state
FSS	finite size scaling
DLD	discrete logarithmic derivative
HDD	hard disk drive
SFD	switching field distribution
PRM	perpendicular recording media
LRM	longitudinal recording media
IRHM	interacting random hysteron model
FIFO	first in first out
EOS	end of shell
DRFIM	dipolar random-field Ising model

Part I

Theoretical Perspective: Unexpected Universality in Disordered Systems

Chapter 1

Introduction

1.1 Random field Ising model

As a prototypical model for magnets with quenched disorder, the random-field Ising Model (RFIM) has been intensively studied during the last thirty years [8]. The RFIM is defined by the Hamiltonian

$$\mathcal{H} = -\sum_{<i,j>} J\, s_i s_j - \sum_i (H + h_i)\, s_i \tag{1.1}$$

where the spins $s_i = \pm 1$ sit on a D-dimensional hypercubic lattice with periodic boundary conditions. The spins interact ferromagnetically with their nearest neighbors with strength J and experience a uniform external field H and a local field h_i. To model quenched disorders, the local fields h_i are often randomly chosen from a Gaussian distribution with mean zero and variance R^2:

$$\rho(h) = \frac{1}{\sqrt{2\pi} R}\, e^{-h^2/2R^2} \tag{1.2}$$

R is often called the disorder parameter or just disorder.

1.1.1 Equilibrium

In equilibrium, the existence of an ordered phase in 3D has been proved by rigorous work [45, 10, 11]. It is generally believed that in 3D the transition between the ordered and disordered phases is continuous and controlled by a stable zero-temperature fixed point [99,24]. Critical exponents of this transition have been numerically studied, for example, using Monte Carlo simulations [106, 77,74,105], real space renormalization group calculations [75], and ground-state calculations [76, 40, 71]. Note that at $T = 0$ the phase transition undergone by the ground state (GS) as the disorder parameter, often denoted as R, is tuned to its critical value R_c is called the disorder-induced phase transition (DIPT). On the other hand, for a given disorder R ($R < R_c$), near the critical temperature T_c there seems to appear a "glassy" regime where relaxation to equilibrium becomes very slow, as shown in experimental work [4, 35], simulations [33] and analytical calculations [67, 66]. This is due to the quenched disorder, which changes the free energy landscape of the system and introduces large energy

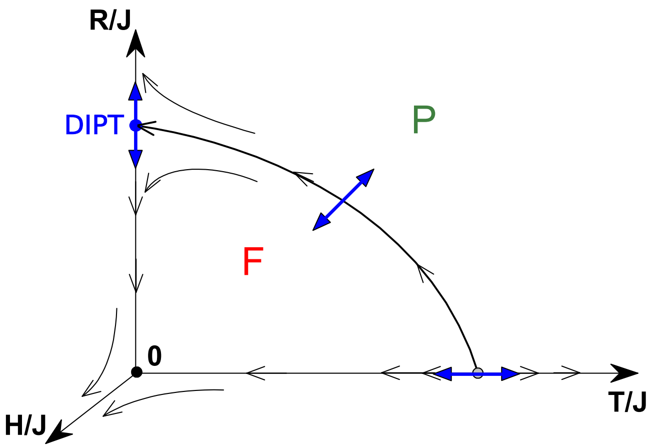

Figure 1.1: RG flow of RFIM in equilibrium at dimension higher than the lower critical dimension $d_l = 2$. R, H, and T represent disorder, external field, and temperature, respectively. F: ferromagnetic phase. P: paramagnetic phase.

barriers with respect to thermal fluctuations. At low temperature, some of the barriers are so large that the system gets stuck in some metastable states, which leads to extremely slow relaxation towards the equilibrium state.

1.1.2 Non-equilibrium

The zero-temperature non-equilibrium RFIM, introduced by Sethna *et al.*, has proven to be a very successful model in studying disordered systems that show hysteretic and jerky behavior when driven by an external force (for reviews, see e.g. [90, 91]). On long length scales and practical time scales, the system driven by an external field will move from one local valley in the free-energy landscape to the next. Due to its sluggish response, the state of the system will typically depend on its history, a phenomenon called *hysteresis*. The motion from one local valley to the next is a collective process that can involve many magnetic domains whose magnetic moments are flipped in *an avalanche*. In magnetic materials, as the external magnetic field H is changed continuously, these avalanches of spin flips can be measured as voltage pulses induced in a pick up coil wound around the sample in a Barkhausen noise experiment [65,48]. With a single-spin-flip dynamics, the non-equilibrium DIPT was first numerically observed in the hysteretic behavior at $T = 0$ and $D \geq 3$ [89]. It is found that there is a critical point (R_c, H_c) which separates macroscopically smooth saturation hysteresis loops in the magnetization $M(H)$ (for $R > R_c$) from saturation loops with a macroscopic jump or burst (for $R < R_c$). Here, H_c is the non-universal magnetic field value at which the magnetization curve has infinite slope. A rich variety of universal quantities, associated with characteristic universal scaling functions and critical exponents of this non-equilibrium DIPT, have been studied analytically [17], numerically [80] and experimentally [3].

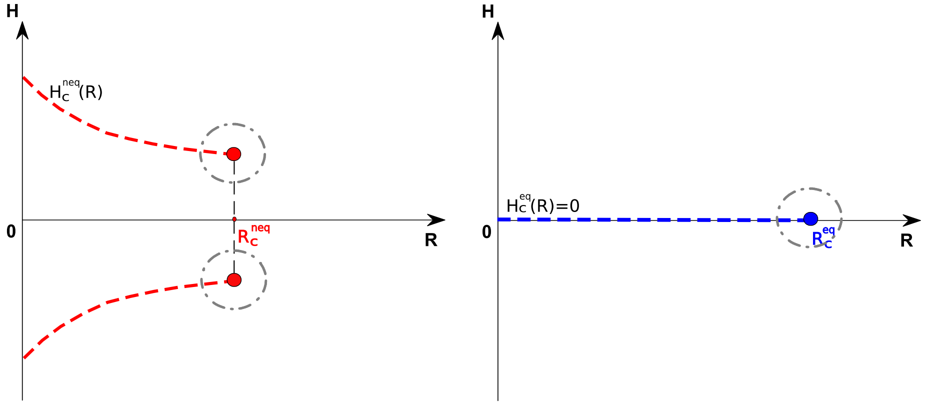

Figure 1.2: Schematic phase diagram of zero-temperature RFIM. (left) non-equilibrium RFIM with single-spin-flip dynamics; (right) equilibrium RFIM with ground state evolution. The critical points $(R_\mathrm{c}, \pm H_\mathrm{c}(R_\mathrm{c}))$ are surrounded by grey circles. The dashed lines $H_\mathrm{c}(R)$ indicate the first-order phase transition. Note that in non-equilibrium, $H_\mathrm{c}(R)$ could have nonmonotonic behavior in finite dimensions. In equilibrium, $H_\mathrm{c} = 0$ simply due to symmetry.

1.2 Universality?

Despite these intensive studies, some theoretically and experimentally important questions are still not well answered. For example, it is still controversial whether the equilibrium and non-equilibrium DIPT of the zero-temperature RFIM belong to the same universality class. Actually, comparing the equilibrium and non-equilibrium DIPT is very interesting. In mean field theory (MFT), they have the same thermodynamic critical exponents and the same exponent relations [86, 89]. Renormalization group (RG) calculations show that the $6-\epsilon$ expansion for the non-equilibrium critical exponents maps to all orders in ϵ onto the controversial equilibrium ones: The temperature dependence is irrelevant in the equilibrium RFIM and the time dependence is irrelevant in the zero-temperature non-equilibrium RFIM, leaving us with the same starting point for the calculation in both cases [17]. In 3D and even 4D, numerical values of the critical exponents of the two DIPTs seem to match within the error bars [61, 80, 37, 68], see Table 1.1.

Recently, Vives *et al.* suggested that the two DIPTs belong to the same universality class by conjecturing the extrapolation result of a RG type argument [78]. Meanwhile, Colaiori *et al.* numerically compared the equilibrium DIPT, i.e. the DIPT of the GS, to that of the demagnetized state (DS), considering the DS as a non-equilibrium hysteretic counterpart of the GS often used in experiments and applications [16]. Here, the DS is obtained by applying an external oscillating field with slowly decreasing amplitude to the non-equilibrium system. The system will then be taken through a series of subloops and the line connecting the tips of those subloops is known as the demagnetization curve.

Table 1.1: Critical points and critical exponents for equilibrium and non-equilibrium Gaussian RFIM in 3D, 4D and Mean field theory. The critical point in equilibrium does not coincide with that corresponding to the non-equilibrium. Nevertheless, the values of the critical exponents of the two models remain within each other's error bars. Note that some critical exponents can not be extracted directly from scaling collapses, but instead are derived from exponent combinations using scaling laws. Here, (...) denotes values calculated from the critical exponents or their combinations given in the literatures using scaling laws. ν is the correlation length exponent. β is the magnetization exponent. δ is the critical isotherm exponent. γ is the susceptibility exponent. η is the two-point correlation function exponent.

			ν	β	$\beta\delta$	γ	η	R_c	$H_c(R_c)$
3D	NEQ	Perkovic [80]	1.41 ± 0.18	0.035 ± 0.028	1.81 ± 0.32	(1.78 ± 0.32)	(0.74 ± 0.28)	2.16 ± 0.03	1.435 ± 0.004
		Vives [78]	1.2 ± 0.1	0.024 ± 0.012	(1.80 ± 0.19)	(1.78 ± 0.19)	(0.52 ± 0.20)	2.21 ± 0.02	1.425 ± 0.010
	EQ	Ogielski [76]	1.3 ± 0.3	~ 0.05	(2.05 ± 0.5)	2.0 ± 0.5	0.5 ± 0.1	2.35	0
		Newman [74]	1.02 ± 0.06	0.06 ± 0.07	(1.95 ± 0.18)	1.89 ± 0.17	(0.15 ± 0.20)	2.3 ± 0.2	
		Hartmann [40]	1.32 ± 0.07				0.50 ± 0.03	2.28 ± 0.01	
		Middleton [71]	1.37 ± 0.09	0.017 ± 0.005	(1.99 ± 0.09)	(1.98 ± 0.09)	(0.56 ± 0.12)	2.27 ± 0.004	
4D	NEQ	Perkovic [80]	0.89 ± 0.09	0.17 ± 0.05		(1.56 ± 0.29)	0.25 ± 0.38	4.10 ± 0.02	1.265 ± 0.007
	EQ	Hartmann [37]	0.78 ± 0.10	0.13 ± 0.05		1.42 ± 0.20	0.18 ± 0.01	4.18 ± 0.01	0
		Middleton [68]	0.82 ± 0.06	0.16 ± 0.03				4.179 ± 0.002	
MFT			$1/2$	$1/2$	$3/2$	1	0	$\sqrt{2/\pi}J$	0

Colaiori *et al.* compare the scaling behavior of the magnetization M for the DS and the GS near their respective R_c and at H_c. ($H_c = 0$ for both cases.) Doing finite-size scaling with the known thermodynamic critical exponents, they present evidence that the DIPT of the DS and that of the GS are in the same universality class, in both 3D and the Bethe lattice. On the other hand, Carpenter *et al.* found a related DIPT for the demagnetization curve, which displays similar critical behavior as that of the saturation loop [12].

1.3 Avalanches

Even there are so many evidences in favor of universality, the original question is still not fully answered. We notice that some important critical exponents and universal quantities of the equilibrium and non-equilibrium DIPTs have never been compared. Also, we notice that by comparing universal scaling functions rather than just critical exponents, we are comparing an infinite amount of more information than was done previously.

Moreover, we think the whole idea of looking at avalanches is quite neat: Not only are we directly testing more sensitive features of the problem, but we are giving insight into why the two DIPTs could be similar: the equilibrium and non-equilibrium systems could have similar avalanches during the magnetization process.

Actually, avalanche behavior in diverse dynamical systems has been extensively studied in the past decade [90, 42, 20, 100, 56, 23, 34]. In those systems, there are often large number of metastable states, which cannot lower their energy by small rearrangement of configurations. When pushed by an external driving field, those systems shift from one metastable state to another, showing collective behavior in the form of avalanches. A dynamic avalanche is the rearrangement of the system configuration, which connects two different metastable states. In experiments, avalanches are often associated with crackling noise as measured in acoustic emission and Barkhausen noise experiments [100, 20]. A power law distribution of avalanche sizes over several decades up to certain cutoffs has been observed in many experiments ranging from magnets to earthquakes [20, 56, 23, 43]. The critical exponents associated with avalanche size distribution are universal, i.e they will be shared among a large family of materials and systems. The universality class typically just depends on the dimensionality, interaction range and symmetry, rather than the microscopic details of the diverse materials [90]. This has been well explained by the RG method, which is a tool to describe the way the space of all physical systems maps into itself under coarse-graining.

A common feature in many of the above systems is the competition between interaction and disorder. With slowly changing driving fields, the interaction tends to promote avalanches while the disorder tends to stop them. When interaction dominates, avalanches become so big that they span the whole system.

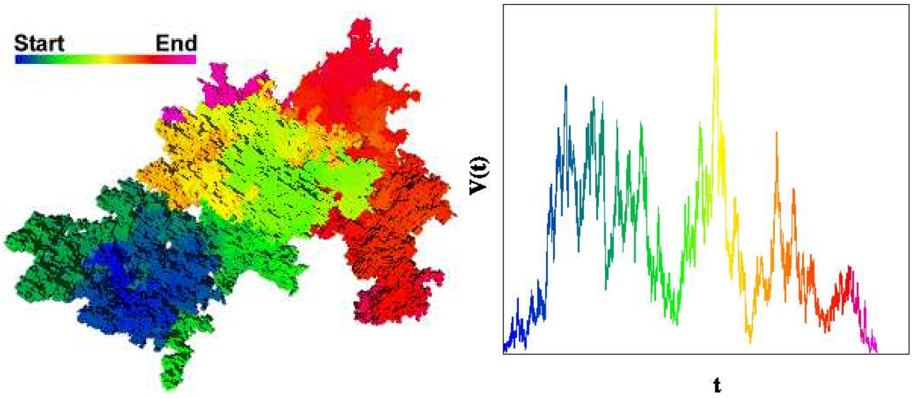

Figure 1.3: (left) A three-dimensional view from one side of a single avalanche in non-equilibrium RFIM with 200^3 spins at $R = 2.3$ (within 6% of the critical disorder R_c). The avalanche contains 282,785 spins. The time when each spin flipped is shown by its color. The avalanche generally grew from left to right. Notice that it has many branches and holes. Also notice that on the right hand side, there are several dark red spots poking through in the middle of the light green area. The green area stopped growing, but other parts of the avalanche later filled in the holes. (right) Typical avalanche time series. Voltage pulse during a single large avalanche (arbitrary units). Notice how the avalanche almost stops several times.

When disorder dominates, avalanches are tiny. In between, i.e when the interaction and disorder are comparable, a very broad distribution of avalanche sizes is observed. Based on this simple scenario, a non-equilibrium disorder-induced phase transition has been extensively studied both theoretically [89, 17, 80] and experimentally [3]. The key result is that there is a plain old critical point near which a power law distribution of avalanche sizes is expected, see Fig. 1.4.

So far, avalanche behavior in equilibrium systems ("static" avalanches) have rarely be studied. With a "static" avalanche we refer to a configuration rearrangement connecting two neighboring different ground states at two different external fields. Note that at zero temperature, a ground state is the globally stable state with the lowest energy possible for the system at a certain external field. It is distinguished from the metastable state, which is just a local minimum in the energy landscape. The static avalanche is very difficult to study for a very simple reason: the disordered system cannot approach the equilibrium or its ground state very easily. Due to the presence of disorder and the consequent diverging free energy barriers, disordered systems will usually occupy some history dependent metastable states. Jumps over large free energy barrier to reach more favorable state are very unlikely often even at room temperature [99, 24, 92]. This makes the general study of the equilibrium properties of any disordered systems very hard, especially in experiments.

Up to now, equilibrium systems were believed to be completely different from non-equilibrium ones simply because the underlying physics is so different:

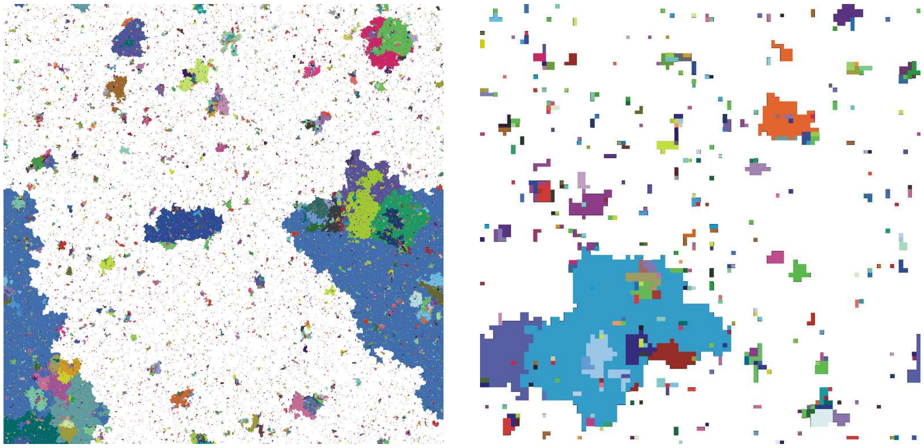

Figure 1.4: Avalanches: scale invariance. (left) Cross section of all avalanches in a 10^9-spin simulation at $R = R_c$. The white background is the infinite, spanning avalanches, which only exists for $R \leq R_c$. (right) Cross section of all avalanches in a 10^6-spin simulation at $R = R_c$. Comparing (right) with (left), one sees that the system is (statistically) invariant under the change in length scale.

equilibrium systems occupy stable states and have no history dependence while non-equilibrium systems occupy metastable states and are history dependent. How can they behave similarly? Here, a natural question arises: Do static and dynamic avalanches have the same critical behavior? Answering this basic question would be very important for two obvious reasons: (1) Theoretically, it is crucial to understand whether there are any possible deep connections between equilibrium systems and their non-equilibrium counterparts. More specially, we want to know whether the dynamics is crucial in determining the universality class of disorder-induced phase transitions [61, 88, 16]. (2) Experimentally, if static and dynamic avalanches do have the same critical behavior, then systems out of equilibrium may be used to predict equilibrium critical behavior. This would save us a lot of time waiting for the system relaxing to equilibrium.

Chapter 2

Method

We focus on the random-field Ising model (RFIM) at zero-temperature, which is a caricature of disordered magnets and has been very successful in explaining dynamic avalanches and crackling noise observed in magnets [89, 17, 80, 3].

The zero-temperature approximation makes sense in the RFIM because thermal fluctuations become less and less important on longer and longer length scales when scaling predictions are valid. This will simplify our studies. We further assume that the external field is adiabatically slowly changing, i.e. it doesn't change during the propagation of an avalanche. This will avoid the temporal overlap of multiple avalanches and simplify our analysis further [102]. With these assumptions, a static (dynamic) avalanche connects two *nearest* ground (metastable) states in the free energy landscape. Both kinds of avalanches can be clearly identified in numerical calculations, as discussed below.

An avalanche in the RFIM refers to the flip of neighboring spins during the magnetization process, corresponding to a jump in the magnetization curve $M(H)$. To study the static and dynamic avalanches in the RFIM, we calculate the zero-temperature magnetization process in equilibrium and non-equilibrium, respectively.

Equilibrium case: The equilibrium magnetization curves are obtained by using the efficient algorithm reported in Ref. [36,26]. Essentially, this algorithm finds steps by narrowing down range where jumps in magnetization occur rather than naively increasing the external field H adiabatically slowly from $-\infty$ to ∞. A linear interpolation scheme used by those authors is based on the fact that the ground state energy has a convexity property which allows for estimates of the fields H where the magnetization jumps [26]. To get the exact ground state (GS) for a given disorder R at external field H, the RFIM GS problem is mapped onto the min-cut/max-flow problem in combinatorial optimization, which can be solved via the so-called push-relabel algorithm [13,1]. Once we get the series of exact ground states along the M-H curve, the "avalanches" are just associated with the magnetization jumps during the ground state evolution.

Non-equilibrium case: The non-equilibrium magnetization curves (the hysteresis loops) are calculated using the adiabatic local metastable dynamics, i.e. each spin flips deterministically when it can gain energy by doing so [89]. That is, it flips when its effective local field

$$h_i^{\mathrm{eff}} = J \sum_j s_j + h_i + H \tag{2.1}$$

changes sign. This change can occur in two ways: a spin can be triggered when one of its neighbors flips (by participating in an avalanche), or a spin can be triggered because of an increase in the external field $H(t)$ (starting a new avalanche). Thus the domain nucleation is allowed in our model. [1] Initially, the external field is set to a very negative value, such that all the spins start pointing down ($s_i = -1$ for all i). As the field is adiabatically slowly increased, a spin will flip. Due to the nearest neighbor interaction, a flipped spin will push a neighbor to flip, which in turn might push another neighbor, and so on, thereby generating an avalanche of spin flips. Thanks to the ferromagnetic nature of the couplings, the final state does not depend on the sequential order of spin flips. This is the so-called Abelian property of this dynamics. During each avalanche, the external field is kept constant. In this sense, the field is adiabatically slowly changing: $\Omega = \mathrm{d}H/\mathrm{d}t = 0$. Three different algorithms to simulate this dynamics are described in Ref. [51].

Shown in Fig. 2.1 are the $M(H)$ curves at different disorders and corresponding avalanches occurring during the magnetization processes. For $R > R_\mathrm{c}$ (see subfigure/curve (c) and (f)), spins tend to flip individually and result in many tiny avalanches and a macroscopically smooth magnetization curve. For $R \sim R_\mathrm{c}$ (see subfigure/curve (b) and (e)), avalanches of a large range of sizes are observed and jumps of all sizes show up in the magnetization curve. For $R < R_\mathrm{c}$ (see subfigure/curve (a) and (d)), most spins tend to flip in a system spanning avalanche seen as a macroscopic jump in the magnetization curve.

We have studied system sizes ranging from $L^3 = 32^3$ to 192^3. All the measured properties are averaged over a large number of realizations of the random-field configuration. Typical averages are performed over a number of realizations that ranges between 10^4 for $L = 32$ and 45 for $L = 192$.

---

[1] Note that in the literature there is also a different dynamics discussed — the front propagation dynamics, which has been used to model fluids invading porous materials [47]. In the invasion problem, the fluid can push into the rock only along an invading front. So domain nucleation is not allowed in this front propagation dynamics.

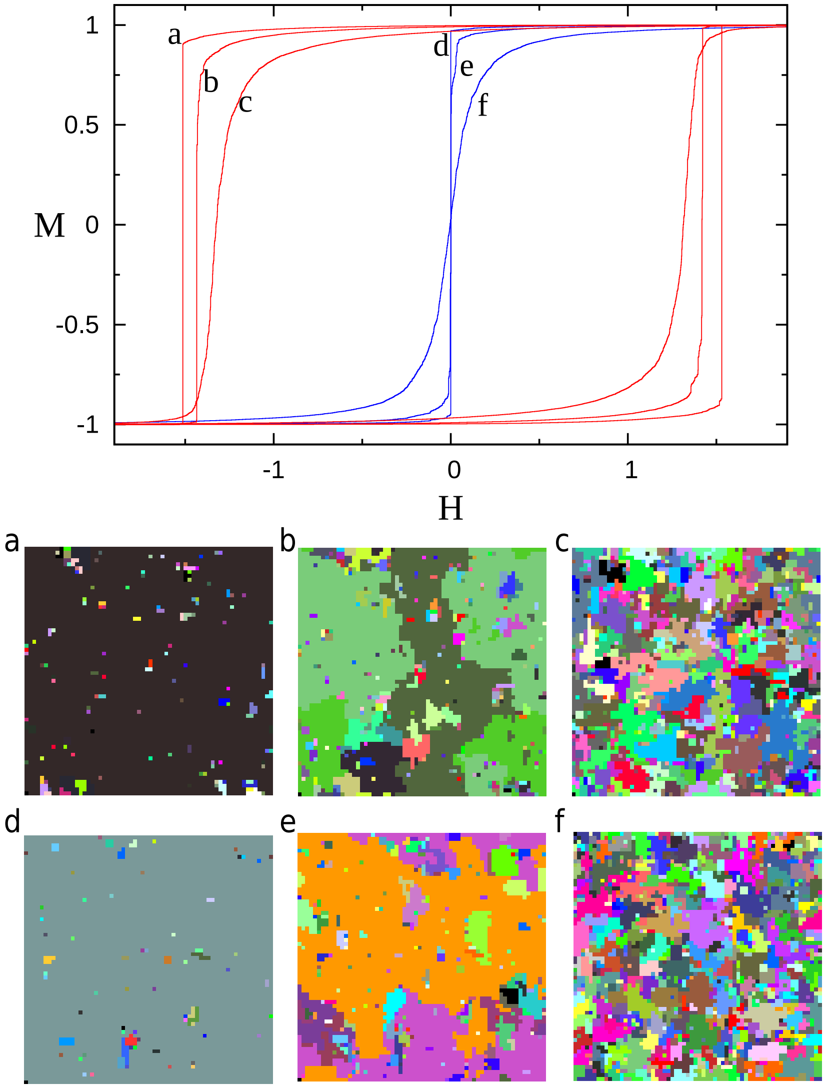

Figure 2.1: **Disorder dependent avalanche behavior in RFIM.** (Top) Magnetization curves in equilibrium (blue) and non-equilibrium (red) at different disorders (below, near and above the critical disorder R_{c}). (Bottom) The corresponding static and dynamic avalanches occurring during those magnetization processes. The calculation is done on 3D Gaussian RFIM at zero-temperature with system size 64^3. Non-equilibrium: (a) $R = 2.0$, (b) $R = 2.224$, (c) $R = 2.6$. Equilibrium: (d) $R = 2.25$, (e) $R = 2.45$, (f) $R = 2.9$. Note that $R_{\mathrm{c}}^{\mathrm{neq}} = 2.16 \pm 0.03$ and $R_{\mathrm{c}}^{\mathrm{eq}} = 2.28 \pm 0.01$ for 3D Gaussian RFIM [80, 40].

Chapter 3

Analytical results

Here, we show two additional similarities between the equilibrium and non-equilibrium RFIM beyond any finite-dimensional simulations.

3.1 MFT avalanche critical exponents

The avalanche critical exponents in MFT must be the same for the two DIPTs. We start the proof by noticing that in non-equilibrium the hard spin MFT magnetization curve has no hysteresis for $R \geq R_\mathrm{c}$ [17].

The mean-field Hamiltonian can be written as

$$\mathcal{H} = -\sum_i (JM + H + h_i)\, s_i \tag{3.1}$$

Initially, $H = -\infty$, all spins are pointing down. Then the field is adiabatically slowly increasing. Each spin flips if its local effective field $h_i^{\mathrm{eff}} = JM + H + h_i$ changes sign. In other words, at a given field H, spins with $h_i < -JM - H$ will be pointing down and spins with $h_i > -JM - H$ will be pointing up. Therefore, we have

$$\begin{aligned} M(H) &= (-1) \cdot \int_{-\infty}^{-JM-H} \rho(h)\mathrm{d}h + (+1) \cdot \int_{-JM-H}^{+\infty} \rho(h)\mathrm{d}h \\ &= 1 - 2\int_{-\infty}^{-JM-H} \rho(h)\mathrm{d}h \\ &= 1 - 2\int_{-\infty}^{x} \rho(h)\mathrm{d}h \end{aligned} \tag{3.2}$$

with $x \equiv -JM - H$. For Gaussian $\rho(h)$, we have

$$M(H) = \mathrm{erf}\left(\frac{JM + H}{\sqrt{2}R}\right) \tag{3.3}$$

This is best solved graphically. The result is shown in Fig. 3.1. Since there is only one $M(H)$ solution for $R \geq R_\mathrm{c}$ in MFT, it must be the non-equilibrium and the equilibrium solution at the same time. In MFT, every spin couples to $M(H)$. Since $M(H)$ is unique, this implies that as H is increased there is a unique series of local-field configurations and therefore a unique series of states.

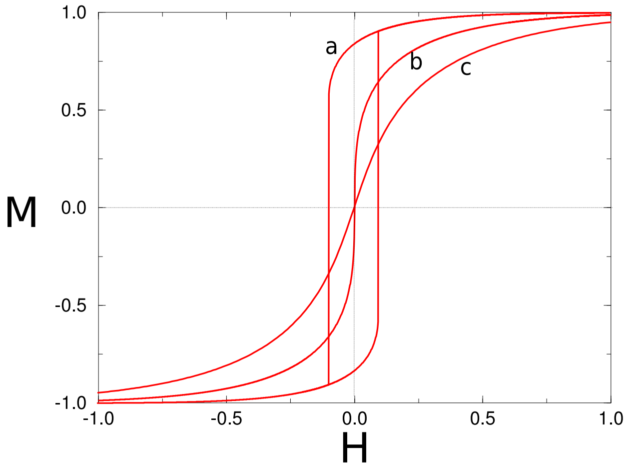

Figure 3.1: Mean-field magnetization curve for the non-equilibrium zero temperature Gaussian RFIM at different disorders. (a) $R = 0.6J < R_c$. (b) $R = R_c = \sqrt{2/\pi}J$. (c) $R = J > R_c$.

This means that in MFT for $R \geq R_c$ the avalanches in equilibrium must be the same as the avalanches in non-equilibrium. So the MFT avalanche exponents must be the same in both DIPTs.

Here, I briefly discuss the calculation of MFT critical exponents. From Eq. 3.2, one has

$$\chi = \frac{\mathrm{d}M}{\mathrm{d}H} = \frac{2\rho(x)}{1-2J\rho(x)}. \tag{3.4}$$

Define x_c to be the root of $1 - 2J\rho(x) = 0$ so that χ diverges (because the spanning avalanche occurs and $H = H_c(R)$). For Gaussian $\rho(h)$, it is easy to derive that

$$x_c(R) = \pm\sqrt{2R^2 \log(R_c/R)} = \pm\sqrt{2}R_c(r^{1/2} + \mathcal{O}(r)) \tag{3.5}$$

with scaling variable $r \equiv (R_c - R)/R$.

Near the critical point $(R_c, H_c(R_c))$, successive Taylor expansions with respective to $x_c(R)$ and $x_c(R_c)$ on Eq. 3.4 yield

$$\frac{\mathrm{d}M}{\mathrm{d}H} \approx \frac{2R_c^2}{J}(x^2 - x_c^2(R))^{-1} \tag{3.6}$$

After rearranging terms and solving the differential equation of $x(R)$, we have a cubic equation (in the limit of $r \to 0$)

$$x^3 - 6R_c^2 rx + 6R_c^2 h = 0 \tag{3.7}$$

with scaling variable $h \equiv H - H_c(R_c)$. [1] This gives the scaling behavior of

---

[1] It can be proven that in MFT, $H_c(R_c) = 0$. Proof. From Eq. 3.5, we see that $x_c(R_c) = -JM(H_c(R_c)) - H_c(R_c) = 0$. According to Eq. 3.2, if $x = 0$, then $M = 1 - 2\int_{-\infty}^{0} \rho(h)\mathrm{d}h = 0$. Now it is clear that $x_c(R_c) = 0 \Rightarrow H_c(R_c) = 0$. Q.E.D

$M(r,h)$:

$$M(r,h) \sim |r|^{\beta} g_{\pm}(h/|r|^{\beta\delta}) \tag{3.8}$$

for small h , r and $\pm$ refers to the sign of $r = (R_{\rm c} - R)/R$. MFT gives $\beta = 1/2$, $\delta = 3$ and $g_{\pm}(y)$ is given by the smallest real root of the cubic equation

$$g^3_{\pm}(y) \mp \frac{12}{\pi} g_{\pm}(y) - \frac{12\sqrt{2}}{\pi^{3/2} R_{\rm c}} y = 0. \tag{3.9}$$

In non-equilibrium, using a Poisson statistics argument [17], it has been found that

$$D(S,t) \sim S^{-3/2} \exp(-St^2/2) \tag{3.10}$$

with $t \equiv 2J\rho(x) - 1$. Again, near $H_{\rm c}(R_{\rm c})$, successive Taylor expansions on $x_{\rm c}(R)$ and $x_{\rm c}(R_{\rm c})$ yield

$$t = 2J\rho(x) - 1 \sim J\rho''(x_{\rm c}(R_{\rm c}))(x^2 - x_{\rm c}(R)). \tag{3.11}$$

Considering Eq. 3.5 and as $r \to 0$, $h \to 0$, $x = -JM - H \sim -JM \sim -J|r|^{\beta} g_{\pm}(h/|\beta\delta|)$, one has

$$t \approx \frac{J^3}{\sqrt{2\pi} R^3_{\rm c}} \frac{4}{\pi}\; r \; \left[1 \mp \frac{\pi}{4} g^2_{\pm}(h/|r|^{\beta\delta})\right] \tag{3.12}$$

with $\beta\delta = 3/2$ and . Insert Eq. 3.12 into Eq. 3.10, we have

$$D(S,r,h) \sim S^{-\tau} \mathcal{D}_{\pm}(S^{\sigma}|r|, h/|r|^{\beta\delta}) \tag{3.13}$$

with $\tau = 3/2$, $\sigma = 1/2$ and $\mathcal{D}_{\pm}$ is given by

$$\mathcal{D}_{\pm}(x,y) = \frac{1}{\sqrt{2\pi}} \exp[-\frac{x}{2}(1 \mp \frac{\pi}{4} g^2_{\pm}(y))^2] \tag{3.14}$$

3.2 Middleton's no-passing rule

Middleton's no-passing rule [69]: One defines the natural partial ordering of two states: a state $C = \{s_1, \cdots, s_N\} \geq \tilde{C} = \{\tilde{s}_1, \cdots, \tilde{s}_N\}$ if $s_i \geq \tilde{s}_i$ for each site i of the system. Let a system $C(t)$ be evolved under the fields $H(t)$ and similarly $\tilde{C}(t)$ evolved under $\tilde{H}(t)$. Suppose the fields $H(t) \geq \tilde{H}(t)$ and the initial states satisfy $C(0) \geq \tilde{C}(0)$, then the no-passing rule guarantees the partial ordering will be preserved, i.e. $C(t) \geq \tilde{C}(t)$ at all times later $t > 0$. For the magnetization process, this is equivalent to the absence of reverse spin flips as H is swept from $-\infty$ to ∞. In non-equilibrium, this rule has been proven and applied to explain the return-point memory [89]. In equilibrium, the main idea of the proof follows. For any state C_2 at field H_2 which evolves from the GS C_1 at field H_1 ($H_1 < H_2$) with reverse avalanches, we can always find a corresponding state $\tilde{C}$ which evolves from C_1 without any reverse avalanches and has lower energy than

C_2 at field H_2. So as H is increased, the GS evolves without any reverse spin flips. Since flipped spins need not be considered any more in the GS calculation for all higher fields, the algorithm will be accelerated dramatically [26].

3.2.1 Introduction

The no-passing rule was first introduced by Middleton in the study of sliding charge-density waves (CDW's) [69]. The CDW problem belongs to the more general class of driven elastic manifolds in random media. If one defines a simple one-dimensional order parameter within the model, then a *natural partial ordering* of the configurations can be defined. In the simple CDW model considered by Middleton, the CDW configuration $\{\varphi_i(t)\}$ describes the CDW distortions at N lattice sites indexed by i, with $\varphi_i(t)$ real phase variables and t the time. The equation of motion for an overdamped CDW is governed by the Langevin dynamics

$$\dot{\varphi}_i = \Delta\varphi_i - V_i'(\varphi_i) + f(t) \tag{3.15}$$

Here, the $\Delta\varphi_i$ term represents the simple elastic interactions. $V_i'(\varphi_i)$ is the pinning force at site i due to the 2π periodic pinning potential $V(\varphi_i)$. And $f(t)$ stands for the external driving force. Then one can define the natural partial ordering of two configurations: $C^{\mathrm{G}} = \{\varphi_i^{\mathrm{G}}\} \geq C^{\mathrm{L}} = \{\varphi_i^{\mathrm{L}}\}$ if $\varphi_i^{\mathrm{G}} \geq \varphi_i^{\mathrm{L}}$ for each site i of the system. The no-passing rule states that given a driving force f if initially $C^{\mathrm{G}}(0) \geq C^{\mathrm{L}}(0)$, then $C^{\mathrm{G}}(t) \geq C^{\mathrm{L}}(t)$ for all $t > 0$, i.e. the "greater" (C^{G}) is never passed by the "lesser" (C^{L}). As stressed by Middleton, this rule relies crucially on the elastic potential being *convex*. In other words, the elastic potential tends to decrease the separation of nearest-neighbor φ's. More recently, Krauth *et al.* found a similar no-passing rule in the study of driven elastic strings in disordered media [84, 50]. Obviously, this is the same general problem. Again, the rule is crucially dependent on the fact that the elastic potential is *convex*.

The no-passing rule can be used to prove many useful properties, such as the asymptotic uniqueness of the sliding state for CDW's [69] and the intriguing memory effects [89]. In fact, just after its introduction by Middleton, the no-passing rule was used in the non-equilibrium zero-temperature random-field Ising model (RFIM) by Sethna *et al.* to prove the return point memory effect [89]. In this case, the natural partial ordering of two configurations can be defined similarly as in the CDW case. A difference is that $s_i = \pm 1$ while φ_i is real. The no-passing rule states: Let a system $C^{\mathrm{G}}(t)$ be evolved under the fields $H^{\mathrm{G}}(t)$ and similarly $C^{\mathrm{L}}(t)$ evolved under $H^{\mathrm{L}}(t)$. Suppose the fields $H^{\mathrm{G}}(t) \geq H^{\mathrm{L}}(t)$ and the initial configurations satisfy $C^{\mathrm{G}}(0) \geq C^{\mathrm{L}}(0)$, then $C^{\mathrm{G}}(t) \geq C^{\mathrm{L}}(t)$ at all times later $t > 0$, i.e. the partial ordering will be preserved by the dynamics. With a local metastable single-spin-flip dynamics, i.e.

a spin flips when its effective local field

$$h_i^{\text{eff}} = J \sum_j s_j + h_i + H \tag{3.16}$$

changes sign, the proof of the no-passing rule is straightforward [89]. Even with a two-spin-flip dynamics, it has been shown by Vives *et al.* that the no-passing rule is still true at zero-temperature [101]. Note that for the magnetization process, the no-passing rule is equivalent to the fact that the flipped spins can never flip back as H is swept monotonically. Again, this rule is not unconditionally true. It relies crucially on the nearest-neighbor interaction being *ferromagnetic* ($J > 0$). Just like the convex elastic potential, the ferromagnetic interaction also tends to decrease the separation of nearest-neighbor degrees of freedom, i.e. it tends to align the spins.

Recently, in the study of the equilibrium zero-temperature RFIM, Vives *et al.* conjectured that when the external field H is swept from $-\infty$ to ∞, flipped spins cannot flip back in the equilibrium $M(H)$ curve [27]. In other words, the no-passing rule is valid even for the zero-temperature equilibrium dynamics, i.e. the evolution of the ground state (GS). Vives *et al.* further conjectured that this rule can be used to speed up the calculation of the equilibrium $M(H)$ curve since flipped spins at a lower field can be removed from the GS calculation for all higher fields. Unfortunately, this simple but powerful rule has not been proven so far for the equilibrium RFIM. This is the main motivation of our work.

3.2.2 Equilibrium $M(H)$ curve

To calculate the equilibrium $M(H)$ curve of the zero-temperature RFIM, we first need to calculate the exact GS in the RFIM at an arbitrary applied external field H. This is the basic step of calculating the equilibrium $M(H)$ curve, i.e. the GS evolution for varying H. Fortunately, there is a well-known mapping of the RFIM GS problem to a min-cut/max-flow problem in combinatorial optimization. The mapping and the so-called push-relabel algorithm for the min-cut/max-flow problem has been well described in the literatures [39, 13]. For RFIM, the run time of the push-relabel algorithm scales as $\mathcal{O}(N^{4/3})$ with N the system size [36, 70].

The equilibrium $M(H)$ curve can be simulated with the method reported in Refs. [36, 26]. It is essentially based on the fact that the GS energy $E(\{s_i\}, H)$ is convex up in H, which allows for estimates of the fields H where the magnetization jumps (called "avalanches" occur). This algorithm finds steps by narrowing down ranges where the magnetization jumps with an efficient linear interpolation scheme. An illustration of the algorithm is shown in Fig. 3.2. The details have been explained extensively in Ref. [26]. An example of the calculated equilibrium $M(H)$ curve is shown in Fig 3.3.

In the E-H diagram, for each state $\{s_i\}$, the total energy E is represented

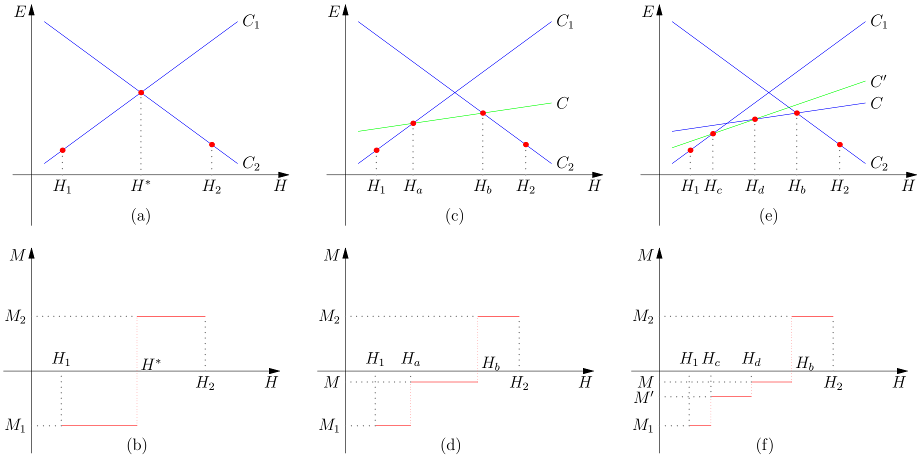

Figure 3.2: (Color online) An illustration of the algorithm to calculate the equilibrium M-H curve. Calculate the energies E_1 and E_2 of the two simplest states $C_1 = \{s_i = -1\}$ and $C_2 = \{s_i = +1\}$, respectively, as a function of H. According to Proposition. 1, C_1 (or C_2) would be the ground state for $H < -h_{\max}$ (or $H > -h_{\min}$). Calculate the crossing field $H^*(C_1, C_2)$ where $E_1 = E_2$. Check whether there is a GS at H^* which is different from C_1 and C_2. According to Proposition. 3, if no such a GS exists, the algorithm ends; if yes, denote the GS as C, calculate the crossing field $H^*(C, C_1)$ and $H^*(C, C_2)$. At the new crossing fields, check whether there is a GS which is different from the two intersected states. The algorithm will not end until all the crossing fields have been checked. An example of the calculated equilibrium M-H curve is shown in Fig. 3.3.

by a straight line with slope $-M \equiv -\sum_i s_i$ since

$$E(\{s_i\}, H) = E_0(\{s_i\}) - HM \tag{3.17}$$

with

$$E_0(\{s_i\}) = -\sum_{<i,j>} J\, s_i s_j - \sum_i h_i\, s_i \tag{3.18}$$

the energy axis intercept. E_0 is also called the *internal energy*, i.e. the total energy of the configuration when $H = 0$. And the total energy E is also referred to as the *magnetic enthalpy*. Consider a D-dimensional hypercubic lattice of size $N = L^D$. Let $h_{\max}$ ($h_{\min}$) be the maximum (minimum) values of h_i for a certain realization of the random fields. (Usually, random fields are chosen from a Gaussian distribution with mean 0 and standard deviation R. R is often called the disorder parameter.)

Four simple propositions follow here, which are very useful in understanding the algorithm to calculate the equilibrium M-H curve. Note that Proposition. 1, 2 and 3 and their proofs are just reproduced from Ref. [26]. Proposition. 4 is new and the proof is given here.

Proposition 1 *For $H < -h_{\max}$ ($H > -h_{\min}$), the ground state is $\{s_i = -1\}$ ($\{s_i = +1\}$).*

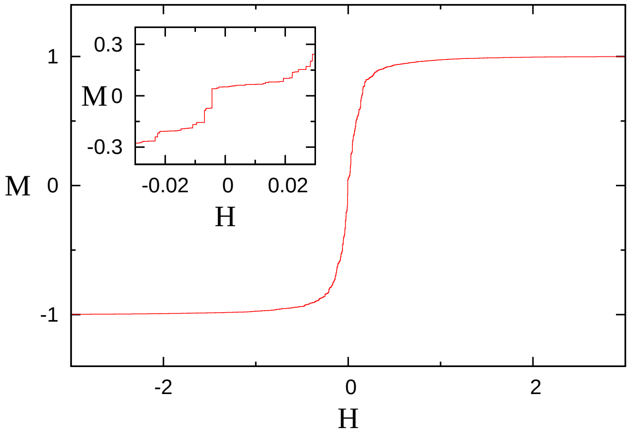

Figure 3.3: The equilibrium M-H curve (the ground state evolution) for the Gaussian RFIM with $D = 3$, $L = 32$ and $R = 2.837$. Here R is the standard deviation of the Gaussian random field distribution. The inset shows a detail of the $M(H)$ curve near $H = 0$, where magnetization jumps are clearly seen.

Proof. The proof is straightforward, since under such circumstances $\{s_i = -1\}$ ($\{s_i = +1\}$) minimizes not only the first term of the Hamiltonian but also the last two terms. Q.E.D

Proposition 2 *Let the spin configuration C_1 (C_2) be the ground state for $H = H_1$ ($H = H_2$). They have magnetization M_1 and M_2, respectively. If $C_1 \neq C_2$ and $H_2 > H_1$, then $M_2 > M_1$.*

Proof. Because C_1 and C_2 are the ground states at H_1 and H_2, respectively, we have

$$\begin{aligned} E\{C_1, H_1\} = E_0\{C_1\} - H_1 M_1 &< E\{C_2, H_1\} = E_0\{C_2\} - H_1 M_2 \\ E\{C_2, H_2\} = E_0\{C_2\} - H_2 M_2 &< E\{C_1, H_2\} = E_0\{C_1\} - H_2 M_1 \end{aligned} \quad (3.19)$$

Here, $E_0 = -\sum_{<i,j>} J\, s_i s_j - \sum_i h_i s_i$. Adding the above two equations, one gets

$$(H_1 - H_2)(M_1 - M_2) > 0 \quad (3.20)$$

Thus, when sweeping the external field from $H = -\infty$ to $H = \infty$, the magnetization M will increase monotonically. Q.E.D

Thus, when sweeping the external field from $H = -\infty$ to $H = \infty$, the magnetization M will increase monotonically. A corollary of this proposition is that in the E-H diagram if the slopes of the lines corresponding to the ground states C_1 and C_2 are different, i.e. $M_1 \neq M_2$, and without loss of generality we can assume $M_1 < M_2$, then the lines intersect at a field H^* such that $H_1 < H^* < H_2$. This field $H^*(C_1, C_2)$ is defined as the *crossing field* between C_1 and C_2. According to the definition, one has $E_0(C_1) - H^* M_1 = E_0(C_2) - H^* M_2$, so

$$H^*(C_1, C_2) = \frac{E_0(C_2) - E_0(C_1)}{M_2 - M_1} \tag{3.21}$$

For example, we can calculate the crossing field between the two simplest ground states: $C_1 = \{s_i = -1\}$ with $M_1 = -N$ and $C_2 = \{s_i = +1\}$ with $M_2 = N$. We have $H^* = -1/N \sum_i h_i = -\bar{h}_i$. [2]

Proposition 3 *Let the spin configuration C_1 (C_2) be the ground state for $H = H_1$ ($H = H_2$). $C_1 \neq C_2$, $H_2 > H_1$ and the crossing field between C_1 and C_2 is H^*. If there is no configuration C such that $E(C, H^*) < E(C_1, H^*) = E(C_2, H^*)$ then: (i) C_1 is the ground state at least for the field range $[H_1, H^*)$ and (ii) C_2 is the ground state at least for the field range $(H^*, H_2]$.*

Proof. Suppose that there is a configuration $\tilde{C}$ such that for $H = \tilde{H} \in (H_1, H^*)$ the relation $E\{C, \tilde{H}\} < E\{C_1, \tilde{H}\}$ holds, i.e. $\tilde{C}$ is the ground state for $H = \tilde{H}$. Due to Proposition. 2, we have $\tilde{M} > M_1$. The energy of the configuration $\tilde{C}$ at H^* would be

$$\begin{aligned} E\{\tilde{C}, H^*\} &= E\{\tilde{C}, \tilde{H}\} - (H^* - \tilde{H})\tilde{M} \\ &< E\{C_1, \tilde{H}\} - (H^* - \tilde{H})\tilde{M} \\ &< E\{C_1, \tilde{H}\} - (H^* - \tilde{H})M_1 \\ &= E\{C_1, H^*\} \end{aligned} \tag{3.22}$$

in contradiction with the hypothesis of the proposition. Proof of (ii) is very similar. Q.E.D

This is the most important proposition. Its power comes from the fact that it can be applied iteratively. And finally we get the $M(H)$ curve with all the ground states (see Fig. 3.2).

Proposition 4 *If the ground state is non-degenerate, then there cannot be more than one avalanche connecting two nearest ground states in the E-H diagram.*

Proof. Suppose when the field is increased from H_1 to H_2, the GS C_1 evolves to the nearest GS C_2 with two avalanches (A_1 and A_2 with size $S_1 \geq 1$ and $S_2 \geq 1$, respectively).

The crossing field is given by

$$H^*(C_1, C_2) = \frac{E_0(C_2) - E_0(C_1)}{M_2 - M_1} = \frac{f_{A_1}(0) + f_{A_2}(0)}{2(S_1 + S_2)} \tag{3.23}$$

The last line is due to Eq.3.37. We can choose a trial state C which is evolved from C_1 with only avalanche A_1 occurring. We want the following relation to hold

$$E(C, H^*) < E(C_1, H^*) = E(C_2, H^*) \tag{3.24}$$

---

[2] Random fields are usually generated according to a zero-mean distribution. But in practical simulation we are always dealing with a finite size system. So it is impossible to get exactly $\bar{h}_i = 1/N \sum_i h_i = 0$.

which is equivalent to

$$E(C, H^*) - E(C_1, H^*) = f_{A_1}(H^*) = f_{A_1}(0) - 2S_1 H^* < 0 \tag{3.25}$$

Plugging Eq. 3.23 in it, we just need to prove

$$S_2 f_{A_1}(0) < S_1 f_{A_2}(0). \tag{3.26}$$

If we do have $S_2 f_{A_1}(0) < S_1 f_{A_2}(0)$, then we choose the trial state C, which has lower energy than C_1 and C_2 at the field H^*; if $S_2 f_{A_1}(0) > S_1 f_{A_2}(0)$, then we can choose another trial state C', which is evolved from C_1 through only avalanche A_2 and has lower energy than both C_1 and C_2 at H^*. In both cases, we have shown that C_2 can not be the nearest GS at H_2 for the GS C_1 at H_1, if C_1 evolves to C_2 with two avalanches. If $S_2 f_{A_1}(0) = S_1 f_{A_2}(0)$, it is easy to show that $E(C_1, H^*) = E(C, H^*) = E(C', H^*) = E(C_2, H^*)$, then there will be degenerate ground states at H^*, which is in contradiction to the hypothesis of Proposition. 4. Q.E.D

3.2.3 Preparations of the Proof

In this section, we will work out the total energy change of the spin configuration due to multiple spin flips and external field varying. The spin configuration is not necessarily the ground state.

First, let us consider the simplest case of a single spin flip. Suppose only one spin (s_i) flips during the evolution of configuration C at H to configuration C' at H', with $\Delta H = H' - H$ and $\Delta M = M' - M$. Define n_i (or n_i') to be the number of the i-th spin's nearest neighbors that point in the same direction as the spin in configuration C (or C'). We call these spins the same-direction nearest neighbors (SDNN) of the i-th spin. Note that $n_i = 0, 1, 2, ...Z$ with $Z = 2D$ the coordination number of the D-dimensional hypercubic lattice.

It is easy to get the bond energy change $4J(n_i - D)$. And the total energy change due to the single spin-flip and the varying external field is given by

$$f_i(H, \Delta H) = f_i(H) - \Delta H M' \tag{3.27}$$

Here we have defined

$$f_i(H) \equiv f_i(H, 0) = 4J(n_i - D) - (h_i + H)\Delta s_i \tag{3.28}$$

which is the energy change due to spin i flipping for the configuration C just at the field H, i.e. $\Delta s_i = \pm 2$ with $\Delta H = 0$. It is easy to check that

$$f_{i,\pm}(H) = f_{i,\pm}(0) \pm 2H = \pm 2h_i^{\text{eff}} \tag{3.29}$$

where '±' represents $s_i = \pm 1$ and $\Delta s_i = \mp 2$ accordingly.

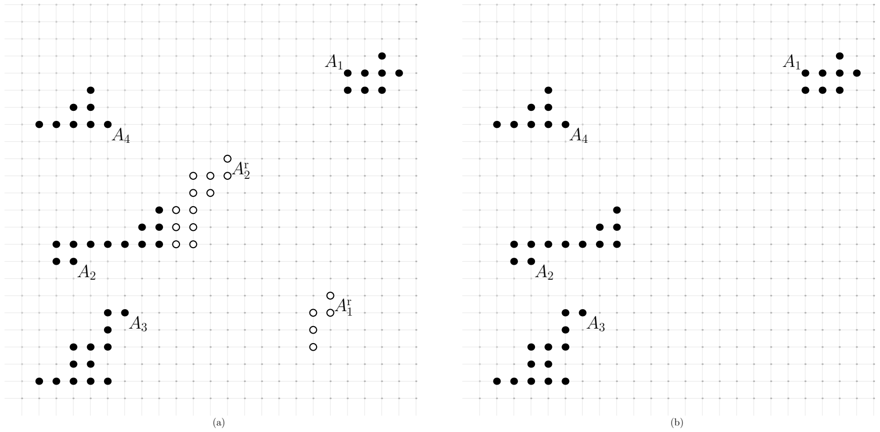

Figure 3.4: States evolved from C_1, with only the change of the spin configuration, i.e. avalanches and reverse avalanches are explicitly shown. (a) State C_2: evolved from state C_1 with both avalanches and reverse avalanches. (Black dot) spins flip up, forming avalanches (A_1, A_2, A_3 and A_4). (White dot) spins flip down (reverse flip), forming reverse avalanches (A_1^{r}, A_2^{r}). Note that there are three interacting bonds between avalanche A_2 and reverse avalanche A_2^{r}. (b) State $\tilde{C}$ evolved from state C_1 without reverse avalanches.

Second, we consider two spin flips. Suppose two different spins (s_i and s_j) flip during the evolution of configuration C at H to configuration C' at H'. There are two subcases.

(1) s_i and s_j are not next to each other. The energy change is

$$f_{i,j}(H,\Delta H) = f_i(H) + f_j(H) - \Delta H M' \tag{3.30}$$

(2) s_i and s_j are next to each other. The energy change is

$$f_{\langle i,j\rangle}(H,\Delta H) = f_i(H) + f_j(H) - 4J(s_i \cdot s_j) - \Delta H M' \tag{3.31}$$

Note that the term $-4J(s_i \cdot s_j)$ is just due to the fact that the energy of the $i-j$ bond will not change during the flip.

Finally, let us consider the general case (see Fig. 3.4(a)). There are many spin flips during the evolution of configuration C at field H to C' at field H'. It is easy to check that the total energy change is given by

$$\Delta E(H,\Delta H) = \big[f_i(H)+f_j(H)+\cdots\big]-4J\,(s_i\cdot s_j+\cdots)-\Delta H(M+\Delta s_i+\Delta s_j+\cdots) \tag{3.32}$$

On the RHS, the first term includes all the flipping spins. The second term includes all the nearest-neighbor interactions among those flipping spins. The last term is due to the varying external field. In particular, if all the flipping spins flip at the same H and they are connected to each other and have the same spin value -1 (or $+1$) before the flip, then this collective spin flip is called *an avalanche* (or *a reverse avalanche*).

Denote the energy change due to an avalanche A_α as $f_{A_\alpha}(H, \Delta H)$, we have

$$\begin{aligned} f_{A_\alpha}(H,\Delta H) &= \big[f_i(H) + f_j(H) + \cdots\big] - 4JN_{\mathrm{b}}(A_\alpha) - \Delta H(M + 2S_\alpha) \\ &\equiv f_{A_\alpha}(H) - \Delta H(M + 2S_\alpha) \end{aligned} \qquad (3.33)$$

with $N_{\mathrm{b}}(A_\alpha)$ defined as the number of interacting bonds in A_α, S_α the size of the avalanche and $f_{A_\alpha}(H)$ the energy change due to the avalanche when $\Delta H = 0$. Similarly, for the reverse avalanche, we have

$$\begin{aligned} f_{A^{\mathrm{r}}_\beta}(H,\Delta H) &= \big[f_i(H) + f_j(H) + \cdots\big] - 4JN_{\mathrm{b}}(A^{\mathrm{r}}_\beta) - \Delta H(M - 2S^{\mathrm{r}}_\beta) \\ &\equiv f_{A^{\mathrm{r}}_\beta}(H) - \Delta H(M - 2S^{\mathrm{r}}_\beta) \end{aligned} \qquad (3.34)$$

Due to Eq. 3.29, we have

$$f_{A_\alpha}(H) = f_{A_\alpha}(0) - 2S_\alpha H \qquad (3.35)$$

$$f_{A^{\mathrm{r}}_\beta}(H) = f_{A^{\mathrm{r}}_\beta}(0) + 2S^{\mathrm{r}}_\beta H \qquad (3.36)$$

Now we can rewrite Eq. 3.32 in terms of f_{A_α} and $f_{A^{\mathrm{r}}_\beta}$. The total energy change due to avalanches and reverse avalanches is given by

$$\Delta E(H,\Delta H) = F_A(H) + F_{A^{\mathrm{r}}}(H) + 4JN_{\mathrm{b}}(A, A^{\mathrm{r}}) - \Delta H(M + 2S_A - 2S_{A^{\mathrm{r}}}) \qquad (3.37)$$

with notations $F_A(H) \equiv \sum_\alpha f_{A_\alpha}(H)$, $F_{A^{\mathrm{r}}}(H) \equiv \sum_\beta f_{A^{\mathrm{r}}_\beta}(H)$, $S_A \equiv \sum_\alpha S_\alpha$, $S_{A^{\mathrm{r}}} \equiv \sum_\beta S^{\mathrm{r}}_\beta$. Here $N_{\mathrm{b}}(A, A^{\mathrm{r}})$ denotes the number of interacting bonds between avalanches and reverse avalanches. For example, in Fig. 3.4(a), $N_{\mathrm{b}}(A, A^{\mathrm{r}}) = 3$.

3.2.4 Proof of the No-passing rule

Now we are ready for the proof of the no-passing rule. Let the spin configuration C_1 (C_2) be the ground state for $H = H_1$ ($H = H_2$). $H_2 > H_1$. Suppose C_1 and C_2 are connected with multiple avalanches: $A_1, A_2 \cdots A_n$ with sizes $S_1, S_2 \cdots S_n$ and reverse avalanches $A^{\mathrm{r}}_1, A^{\mathrm{r}}_2 \cdots A^{\mathrm{r}}_m$, with sizes $S^{\mathrm{r}}_1, S^{\mathrm{r}}_2, \cdots, S^{\mathrm{r}}_m$ respectively. To compensate these reverse avalanches (so as to make sure M is monotonically increasing, see Proposition. 2), we must have $S_A = \sum_{\alpha=1}^{n} S_\alpha > S_{A^{\mathrm{r}}} = \sum_{\beta=1}^{m} S^{\mathrm{r}}_\beta$. See Fig. 3.4(a).

The idea is that if C_2 is the GS at field H_2, then it should have lower energy than any other spin configuration at H_2. But we will prove this is not true. Just consider another spin configuration $\tilde{C}$. The only difference between C_2 and $\tilde{C}$ is that $\tilde{C}$ is evolved from C_1 without any reverse avalanches (see Fig. 3.4(b)). We now try to prove that $E(\tilde{C}, H_2) < E(C_2, H_2)$, so C_2 can not be the GS at

H_2. But this is equivalent to proving that $\Delta\tilde{E} < \Delta E$. Here,

$$\begin{aligned} \Delta E &\equiv E(C_2, H_2) - E(C_1, H_1) \\ &= F_{A^{\mathrm{r}}}(H_1) + F_A(H_1) + \ 4J\ N_{\mathrm{b}}(A, A^{\mathrm{r}}) - \ \Delta H(M - 2S_{A^{\mathrm{r}}} + 2S_A). \end{aligned} \tag{3.38}$$

On the other hand,

$$\Delta\tilde{E} \equiv E(\tilde{C}, H_2) - E(C_1, H_1) = F_A(H_1) - \Delta H(M + 2S_A) \tag{3.39}$$

Therefore,

$$\Delta E - \Delta\tilde{E} = F_{A^{\mathrm{r}}}(H_1) + 4JN_{\mathrm{b}}(A, A^{\mathrm{r}}) + 2S_{A^{\mathrm{r}}}\Delta H > 0 \tag{3.40}$$

Here we have used the fact that C_1 is the ground state for $H = H_1$ such that any kinds of spin flip will increase the energy: $f_{A^{\mathrm{r}}_\beta}(H_1) > 0 \Rightarrow F_{A^{\mathrm{r}}}(H_1) > 0$. Also, for the ferromagnetic RFIM, $J > 0$. Since each term is positive, so the sum is positive, i.e. $\Delta E > \Delta\tilde{E}$ or $E > \tilde{E}$. Actually, for any state C_2 which evolved from C_1 with reverse avalanches, we can find a corresponding state $\tilde{C}$ which evolved from C_1 without any reverse avalanches that has lower energy than C_2 at field H_2. So reverse spin flips are impossible for ground state evolution when increasing external field. Generally, flipped spins can never flip back when we sweep the external field monotonically.

3.2.5 Application

The straightforward application of the no-passing rule is very useful to accelerate the calculation of the ground states when varying the external field. Suppose the GS C_1 at field H_1 has already been obtained, and we want to calculate the GS C_2 at field H_2 with $H_2 > H_1$. According to the no-passing rule, the up spins in C_1 will stay up in C_2, i.e. those spins are frozen, so we need not consider them in the ground state analysis. We just need to consider the down spins in C_1. The only cost is that we have to deal with the frozen up spins as complicated fixed boundary conditions for the down spins. (For details, see Sec. A.3.3.) At first sight, one may think that only when the density of the frozen spins is big enough can we make the GS calculation faster. But how big is enough? To optimize our calculation, we consider the running time difference (Δt) between the two methods: (I) without using the earlier solution C_1, and (II) using the earlier solution C_1. For both methods, ground states are found by using the push-relabel algorithm. The numerical experiments are conducted on a desktop with 2.80 GHz CPU and 2GB memory. And we tune the up-spin density n_{up} (down-spin density n_{down}) by varying H_1. The result is shown in Fig. 3.5. It is found that for $H_2 > H_1$, as long as $n_{\mathrm{up}} \gtrsim 0.07$ in GS C_1, method II will be faster than method I. Symmetrically, for $H_2 < H_1$, as long as $n_{\mathrm{down}} \gtrsim 0.07$ in

GS C_1, method II will be faster than I. This suggests it is not necessary to have an extremely large portion of frozen spins to use the earlier solution. Freezing a tiny part of spins will accelerate the GS calculation already. Furthermore, for larger and larger density of the frozen spins, using the earlier solution will save more and more running time. (Keep in mind that for RFIM, the running time of the push-relabel algorithm scales as $\mathcal{O}(N^{4/3})$.) Consequently, the calculation of the whole $M(H)$ curve will be sped up dramatically.

3.2.6 Discussions

Throughout our proof of the no-passing rule, we do not assume that the ground state is unique. In other words, the no-passing rule is correct even when the ground state is degenerate. For example, this happens for the RFIM when the random fields are chosen from a bimodal distribution [38].

In the proof we explicitly use the fact that the nearest neighbor interaction should be *ferromagnetic* ($J > 0$). We think any antiferromagnetic interactions will destroy the no-passing rule. Thus, for other random magnet models, if J_{ij} could be negative, such as the random-bond Ising model (RBIM) with negative J_{ij} or the spin glasses, the rule will be violated.

Finally, we conjecture that for elastic manifolds in random media, there could be a similar equilibrium no-passing rule at zero temperature, provided that the elastic potential is convex and partial ordering of the configurations can be clearly defined.

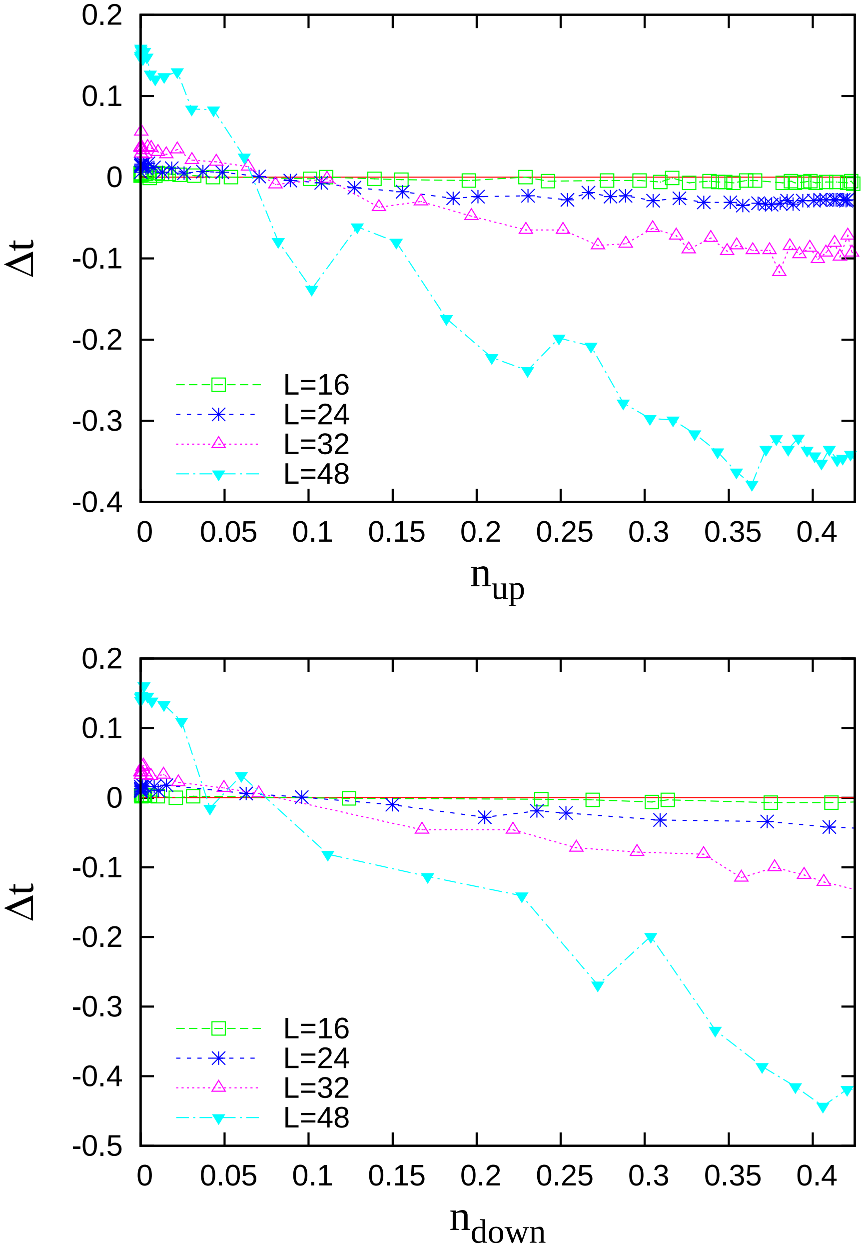

Figure 3.5: Running time difference (Δt) between methods with and without using the earlier solution, i.e the GS C_1 at field H_1, to calculate the GS C_2 at field H_2. The time difference Δt (given in seconds) is plotted against the up-spin (or down-spin) density of the GS C_1. $\Delta t < 0$ means using the earlier solution will save the running time. Calculations are done for 3D Gaussian RFIM (with disorder parameter $R = 2.27$) for different system sizes. (Left) $H_2 > H_1$. up spins in C_1 at field H_1 will stay up at field H_2. (Right) $H_2 < H_1$. down spins in C_1 at field H_1 will stay down at field H_2.

Chapter 4

Numerical results on Gaussian random-fields

We compare the avalanche exponents and scaling functions associated with the avalanche size distribution and avalanche correlation function. The number of spins participating in an avalanche is called its size S. The avalanche correlation function measures the probability that a distance x between any two flipping spins occurs in the same avalanche. For avalanches in equilibrium, no much theoretical work has been done. All the previous studies are not very accurate for the following reasons: the system size is pretty small; exponents are obtained via fitting rather than scaling collapse [26, 27]. In non-equilibrium the avalanche exponents and the associated scaling function have been well studied. Therefore, comparing them with the corresponding equilibrium ones constitutes a particularly strong test for universality.

We compare the spatial structure of avalanches and clusters near the critical disorder. Here, clusters are connected regions of flipped spins, formed by the aggregation of avalanches. In non-equilibrium, it is known that near the critical disorder the spatial structure of avalanches is visually interesting(Fig. 1.3): fractal and anisotropic [90]. In equilibrium it also has been found that near the critical disorder clusters have fractal surfaces [71]. Up to now, the comparison of spatial structures of avalanches (or clusters) in equilibrium and non-equilibrium has never been done. This would be another independent test of the universality. Moreover, though the avalanches show such interesting spatial structure, there has not much theoretical work been done on it up to now. One can say that, the spacial structure of avalanches (or clusters) is worthy to be studied in its own right. Recently, interesting experiments imaging avalanches in magnetic films have been reported. Experimental approaches include using the magneto-optic Kerr effect [53, 49], the magnetic force microscopy [87] and the x-ray speckle metrology [81].

4.1 Avalanche size distribution

Now, we report new 3D simulation results which present evidence of universality for the two DIPTs.

We compare the critical exponents and scaling functions associated with the avalanche size distribution first. At disorder R and within a small range of fields around a particular value H, with (R, H) near the critical point (R_c, H_c), the scaling form of the "binned" avalanche size distribution can be written as

$$D(S, R, H) \sim S^{-\tau} \bar{\mathcal{D}}_{\pm}(S^{\sigma}|r|, h/|r|^{\beta\delta}) \tag{4.1}$$

where S is the size, i.e the number of spins participating in an avalanche, ± refers to the sign of the reduced disorder $r = (R_c - R)/R$, and $h = H - H_c$ is the reduced field. The critical exponent σ gives the scaling of the largest avalanche size $S_{\max} \sim |r|^{-1/\sigma}$, which diverges as we approach the critical disorder. The critical exponents β and δ come from the scaling form of the magnetization near the critical point (H_c, R_c): $M(H, R) - M_c(H_c, R_c) \sim |r|^{\beta}\mathcal{M}_{\pm}(h/|r|^{\beta\delta})$. Note that in equilibrium both H_c and M_c are zero due to symmetry. This is generally not the case far from equilibrium. The critical values of M_c, H_c and R_c in equilibrium and non-equilibrium are generally different [80, 40].

For simplicity, instead of measuring $D(S, R, H)$, we measure the integrated avalanche size distribution $D_{\text{int}}(S, R)$, which is obtained by integrating $D(S, R, H)$ over H:

$$D_{\text{int}}(S, R) \sim S^{-(\tau+\sigma\beta\delta)}\ \bar{\mathcal{D}}^{\text{int}}_{\pm}(S^{\sigma}|r|) \tag{4.2}$$

In non-equilibrium, the quantity $D_{\text{int}}(S, R)$ for Gaussian $\rho(h)$ has been studied extensively, where $(\tau + \sigma\beta\delta)^{\text{neq}} = 2.03 \pm 0.03$ and $\sigma^{\text{neq}} = 0.24 \pm 0.02$ were obtained from scaling collapses and linear extrapolation to R_c [89, 80]. This is done by collapsing three curves at a time, plotting the values of the exponents against $|r|_{\text{avg}}$ (the average of the reduced disorder $|r|$ for the three curves), and then linear extrapolating to $|r|_{\text{avg}} = 0$.

In equilibrium, using the same method, we have $(\tau + \sigma\beta\delta)^{\text{eq}} = 2.00 \pm 0.01$ and $\sigma^{\text{eq}} = 0.23 \pm 0.01$. Both σ^{eq} and $(\tau + \sigma\beta\delta)^{\text{eq}}$ match their non-equilibrium values. Plotting the non-equilibrium universal scaling function [80]:

$$\bar{\mathcal{D}}^{\text{int}}_{-}(X) = e^{-0.789X^{1/\sigma}}(0.021 + 0.002X + 0.531X^2 - 0.266X^3 + 0.261X^4) \tag{4.3}$$

on top of the equilibrium collapse, we find an excellent match, up to the overall horizontal and vertical scaling factors, see inset of Fig. 4.1. According to this scaling function, we plot the distribution curves on top of the original data, we find excellent fits for all disorders. The match in both critical exponents and scaling functions strongly indicate that the two DIPTs belong to the same universality class. We notice that in a previous work, $(\tau + \sigma\beta\delta)^{\text{eq}} = 1.70 \pm 0.07$ was obtained via power-law fitting [27]. However, due to the "bump" in the scaling function, the power law exponent can not be extracted from a linear fit to the raw data since it will underestimate the exponent $\tau + \sigma\beta\delta$. See inset of Fig. 4.1.

The extrapolation is shown in Fig. 4.2. Here, we do the scaling collapse by using two kinds of scaling variables: $r = (R_c - R)/R_c$ and $r = (R_c - R)/R$.

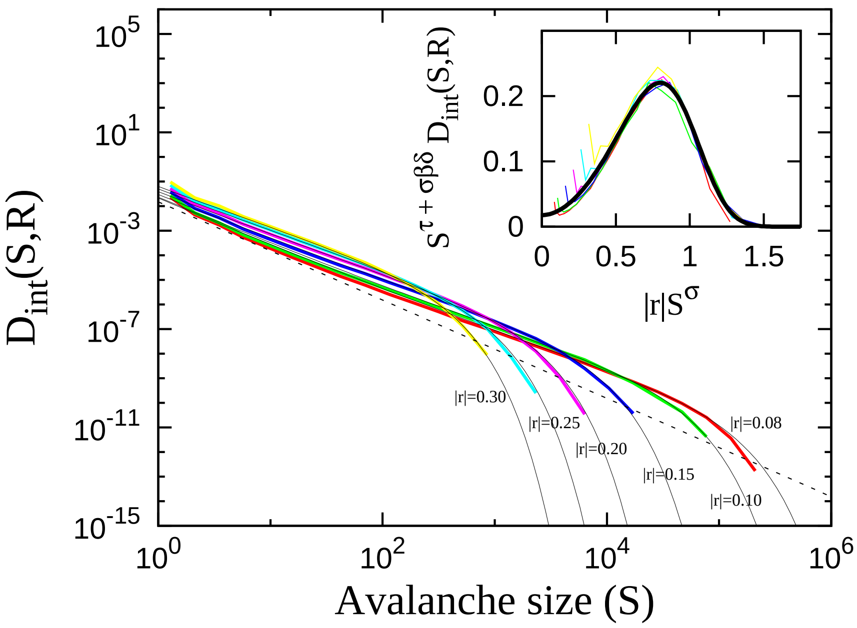

Figure 4.1: Integrated equilibrium avalanche size distribution curves in 3D for 64^3 spins and different disorders. Those curves are averaged up to 500 initial random-field configurations. The inset shows the scaling collapse of the integrated avalanche size distribution, using $(\tau + \sigma\beta\delta)^{\mathrm{eq}} = 2.00$ and $\sigma^{\mathrm{eq}} = 0.23$. (Even with $(\tau + \sigma\beta\delta)^{\mathrm{neq}} = 2.03$ and $\sigma^{\mathrm{neq}} = 0.24$, the collapse still looks good.) The thick black curve through the collapse is the non-equilibrium universal scaling function $\bar{\mathcal{D}}_{-}^{\mathrm{int}}(X)$ (see text). In the main panel, the equilibrium distribution curves obtained from the non-equilibrium scaling function are plotted (thin solid lines) alongside the raw data (thick solid lines). The straight dashed line is the expected asymptotic power-law behavior: $S^{-2.00}$, which does not agree with the measured slope of the raw data quoted in Ref. [27] due to the "bump" in the scaling function.

The extrapolation results are consistent. To minimize the finite size effect, we require that $rL^{1/\nu} \gg 1$, i.e. $r \gg L^{-1/\nu}$. This implies that to get data points even closer to $|r_{\mathrm{avg}}| = 0$, one has to go to larger system size.

4.2 Avalanche correlation function

The avalanche correlation function $G(x, R, H)$ measures the probability that a distance x between any two flipping spins occurs in the same avalanche [80]. Historically, there is a slightly different avalanche correlation function defined for dynamic avalanches [80]. This "triggered" avalanche correlation function $G_{\mathrm{trig}}(x, R, H)$ measures the probability that the initial spin of an avalanche will trigger, in that avalanche, another spin a distance x away. This definition doesn't make sense for a static avalanche simply because there is no initial spin there. In fact, all spins in a static avalanche are equivalent to each other and

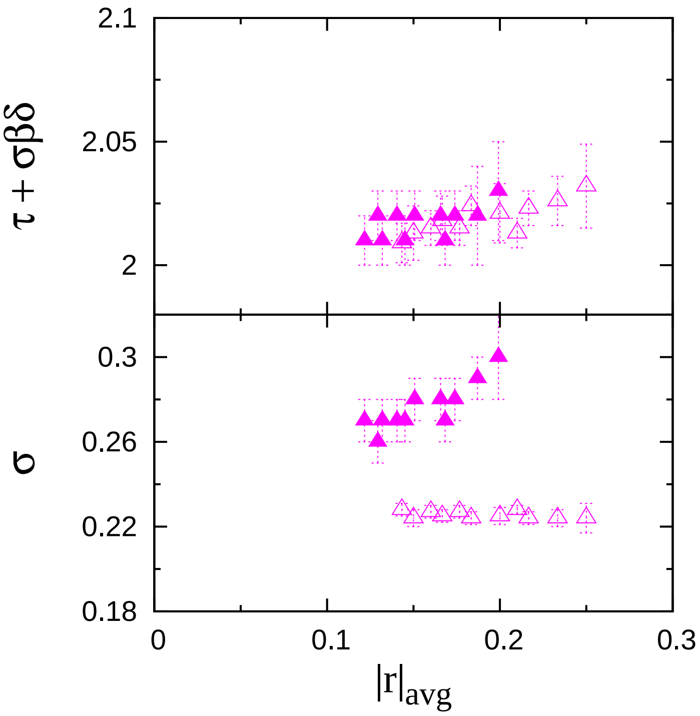

Figure 4.2: (Top) $\tau + \sigma\beta\delta$ and (bottom) σ respectively, from collapse of the ground state integrated avalanche size distribution curves for 64^3 system sizes. Solid symbols denote using scaling variable $r = (R_c - R)/R_c$ and hollow symbols for $r = (R_c - R)/R$. The extrapolation to $|r_{\text{avg}}| = 0$ gives: $\tau + \sigma\beta\delta = 2.00 \pm 0.01$ and $\sigma = 0.23 \pm 0.01$.

will flip as a whole to shift the system to another ground state. [1] Interestingly, non-equilibrium studies have checked that in three dimensions, $G(x, R, H)$ and $G_{\text{trig}}(x, R, H)$ agree with each other very well [80]. This makes the general definition of $G(x, R, H)$ more meaningful.

The RG description suggests that close to the critical point (R_c, H_c) and for large distance x, the avalanche correlation function can be written as [17]

$$G(x, R, H) \sim x^{-(d-2+\eta)} \mathcal{G}_{\pm}(x/\xi(r, h)) \tag{4.4}$$

where ± indicates the sign of r, d is the dimension, and η is called the "anomalous dimension". ξ is the correlation length, which roughly gives the length scale of the mean linear extent of avalanches in our system. Near the critical point, we expect ξ to diverge and scale as: $\xi \sim |r|^{-\nu} \mathcal{Y}_{\pm}(h/|r|^{\beta\delta})$ where $\mathcal{Y}_{\pm}$ is

---

[1] We thank Andrei A. Fedorenko who pointed out the dynamical exponent z cannot be the same in equilibrium and non-equilibrium, since near equilibrium there are exponentially large energy barriers leading to very slow (glass-like) relaxation to equilibrium, while in the non-equilibrium model the exponent z is associated with the duration of avalanches. In our simulation, we just flip the static avalanche as a whole, so there is no well-defined duration. The dynamical exponent z instead describes slow relaxation in this case.

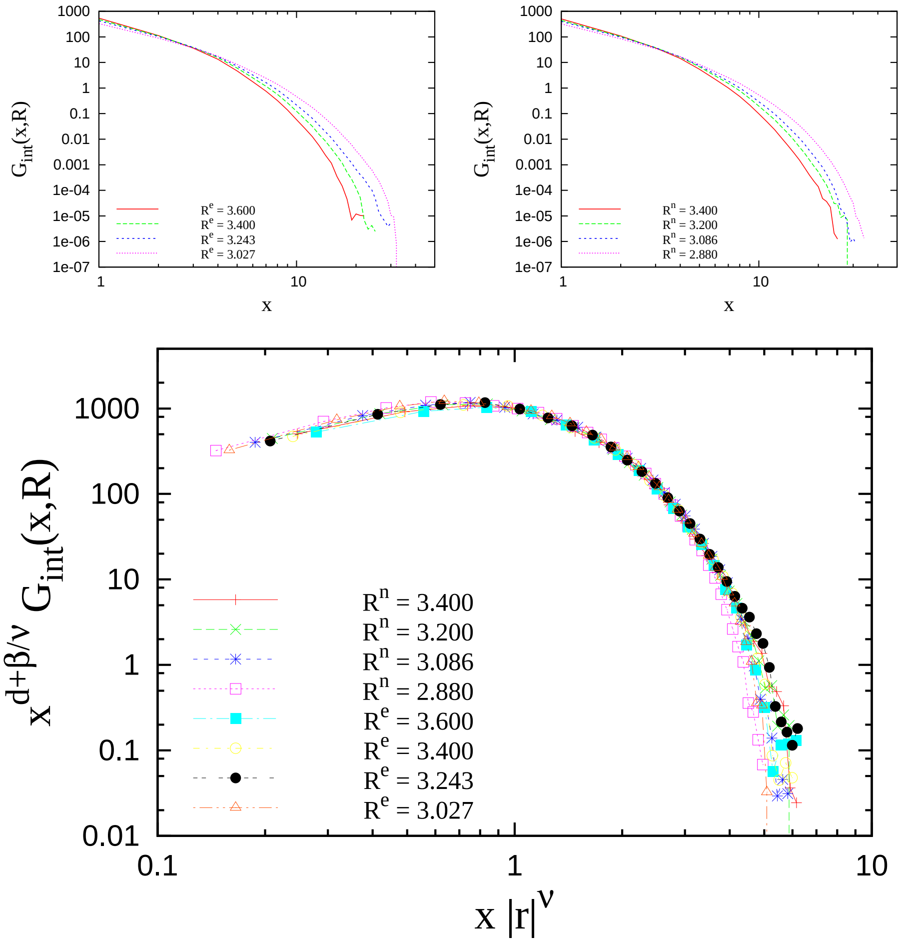

Figure 4.3: Integrated avalanche correlation function at different disorders. In the legend, the subscripts stand for equilibrium (e) or non-equilibrium (n). Those curves collapse to each other, with $d + \beta/\nu = 3.07$ and $\nu = 1.37$, which are consistent with previous results of non-equilibrium Gaussian RFIM [80].

a universal scaling function. Similarly as in the calculation of avalanche size distribution, it is much easier to measure the integrated avalanche correlation function, which is obtained by integrating $G(x, R, H)$ over H:

$$G_{\text{int}}(x, R) \sim \frac{1}{x^{d+\beta/\nu}} \bar{\mathcal{G}}_{\pm}(x|r|^{\nu}) \tag{4.5}$$

where we have used the scaling relation $(2 - \eta)\nu = \beta\delta - \beta$ in the derivation [17].

Fig. 4.3 shows that for the integrated avalanche correlation function, both critical exponents and scaling functions match for static and dynamic avalanches. This again strongly indicate that the two DIPTs belong to the same universality class.

4.3 Fractal dimensions of avalanches and clusters

Spin avalanches and clusters have fractal spatial structure (rugged on all scales). This is not very surprising at all, because fractal spatial structure and the power law scaling of various related quantities indicate a certain degree of criticality — the absence of characteristic spatial and temporal scales at the critical point [90].

The goal of this section is to compute the fractal dimensions of the volume, surface and size(or mass) of avalanches and clusters in equilibrium and non-equilibrium zero-temperature RFIM. First of all, let's give the exact definitions of those quantities. The size S just means the number of spins participating in the avalanche. By surface we mean the outermost surface of the avalanche (regardless of the possible holes inside). The surface area a is defined as the number of nearest-neighbor bonds that separate the avalanche from its surrounding region. The volume v is defined as the number of spins that are enclosed by the outermost surface of the avalanche (treating the possible holes inside as if they were filled). Obviously, if there are no fully enclosed holes inside the avalanche, then the volume v is the just the same as the size S. Otherwise, v will be greater than S. The similar definitions are applied to the clusters.

In the thermodynamic limit, the fractal behavior for all those quantities can be written as

$$f(l;R) = l^{d_\mathrm{f}}\, f^*((R-R_\mathrm{c})\, l^{1/\nu}) \tag{4.6}$$

Here, f could be S, v or a. d_f is the fractal dimension at the critical point. ν is the critical exponent of the correlation length. The pre-factor is related to the lacunarity of the fractal [60]. l is the characteristic length scale of the avalanche (or cluster). l can be defined as either the geometric mean (l_gm) or the maximum (l_max) of the lengths of the sides of the minimal rectilinear box that encloses the avalanche and has sides paralleled to system sides.

Eq.4.6 may naively indicate that one can get the fractal dimension d_f by fitting the data with a power law. However, "Widom scaling" has proven to be better than power law fitting in analyzing both numerical and experimental data near a critical point for two reasons. First, finite-size effects can be explicitly studied through finite-size scaling analysis. Second, scaling collapses are more accurate because they automatically extrapolate to the correct scaling exponent at the critical point even if the data is taken away from the critical point [79].

a. Using scaling variable l/L: For finite systems, the natural finite-size scaling hypothesis reads

$$f(l;R,L) = L^{d_\mathrm{f}} \hat{f}(rL^{1/\nu}, l/L) \tag{4.7}$$

where $r \equiv (R-R_\mathrm{c})/R$ and $\hat{f}$ is a universal scaling function. At $R = R_\mathrm{c}$, the above equation is just

$$f(l; R_{\mathrm{c}}, L) = L^{d_{\mathrm{f}}} \hat{f}(0, l/L) \tag{4.8}$$

Therefore, we can do the data collapse by plotting $L^{-d_{\mathrm{f}}} f(l; R_{\mathrm{c}}, L)$ against l/L to determine the fractal dimension d_{f} and even the universal scaling function $\hat{f}(0, l/L)$. We tune d_{f} until all the curves lie on top of each other. The collapsed function is the universal function $\hat{f}(0, l/L)$. For S, v and a, we can get the respective fractal dimension: d_{S}, d_{v} and d_{a}. One may worry about the fact that the scaling forms we use for the collapses do not include the corrections that are present when the data is not taken in the limit $L \to \infty$. Therefore, it is necessary to extrapolate to $L \to \infty$ (or $L^{-1} \to 0$) to obtain the the correct exponents. Considering this, we have collapsed the curves for three different system sizes and plotted the values of the exponents extracted from such collapses against the average of the three system sizes (or the inverse of the system sizes), which we call $\langle L \rangle$ (or $\langle L^{-1} \rangle$). Then the extrapolation to $\langle L \rangle \to \infty$ (or $\langle L^{-1} \rangle \to 0$) yields the quoted exponents with error bars, For example, the scaling collapse of the size of avalanches in non-equilibrium $S(l; R_{\mathrm{c}}, L)$ is shown in Fig. 4.4. The extrapolation to the limit $L \to \infty$ yields $d_{\mathrm{S}} = 2.78 \pm 0.05$, see the inset of Fig. 4.4. Note that the error bar at each $\langle L^{-1} \rangle$ represent the estimated range of values for which the collapses are satisfactory. We can do the similar collapse for the volume and surface for avalanches and clusters in equilibrium and non-equilibrium. All the results are shown in Table 4.1.

b. Using scaling variable v/V: Note that if we start from

$$f(v; R, V) = V^{\tilde{d_{\mathrm{f}}}} \hat{f}(r V^{1/3\nu}, v/V) \tag{4.9}$$

with $V = L^3$, we have, at $R = R_{\mathrm{c}}$,

$$f(v; R_{\mathrm{c}}, V) = V^{\tilde{d_{\mathrm{f}}}} \hat{f}(0, v/V) \tag{4.10}$$

Here, f could be S or a. This enables us to get the relative fractal dimensions: $\tilde{d_{\mathrm{a}}} \equiv d_{\mathrm{a}}/d_{\mathrm{v}}$ and $\tilde{d_{\mathrm{S}}} \equiv d_{\mathrm{S}}/d_{\mathrm{v}}$. Then we can check the result obtained directly from the data collapse using l/L. For example, the scaling collapse of the surface area a of avalanche in non-equilibrium $a(v; R_{\mathrm{c}}, V)$ yields $\tilde{d_{\mathrm{a}}} = 0.84 \pm 0.01$, see Fig. 4.5. We can do the similar collapse for avalanches in equilibrium and clusters in equilibrium and non-equilibrium. All the results are shown in Table 4.1.

c. Taking discrete logarithmic derivative Besides Widom scaling collapses, there is another useful method to analyze the data obeying power-law relations such as Eq.4.6, the so-called discrete logarithmic derivative (DLD) [71]. To take the DLD is nothing but to calculate the local slope from a log-log plot. This is easily understood by deriving

$$d_{\mathrm{f}} = \mathrm{d} \log f(l, R_{\mathrm{c}}) / \mathrm{d} \log l \tag{4.11}$$

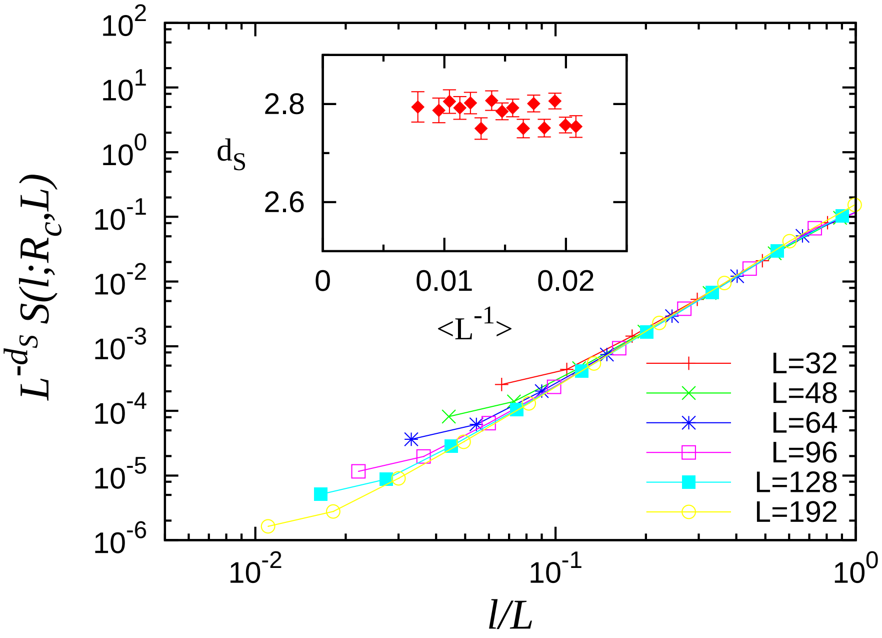

Figure 4.4: Finite-size scaling (using scaling variable l/L) for the size S of avalanches in non-equilibrium, using $d_{\mathrm{S}} = 2.78$. System sizes: $L^3 = 32^3, 48^3, 64^3, 96^3, 128^3$ and 192^3 (from the top curve to the bottom one). Insets show the extrapolation of the exponents to the thermodynamic limit, which yields $d_{\mathrm{S}} = 2.78 \pm 0.05$ for avalanches in non-equilibrium. Note that E.Vives et al. get the size fractal dimension for the so-called critical non-spanning avalanches [78]: $d_{\mathrm{nsc}} = 2.78 \pm 0.05$. This is consistent with our result, though here we didn't separate the non-spanning avalanches into two categories: critical and noncritical ones. According to Vives, these two kinds of non-spanning avalanches have very different averaged numbers and size distributions. However, up to our knowledge, the direct separation of those two kinds non-spanning avalanches has not been done yet.

from Eq.4.6. Note that this method is only useful for the pure power-law functions while Widom scaling collapse is a general method to obtain the unknown exponents even from data that is taken too far away from a critical point to be strictly power law distributed.

We bin the avalanches (and clusters) by volume v, logarithmically spaced by powers of 2. Averaging over bins and samples gives the mean surface area $\bar{a}$. Estimates of the relative dimension, i.e. $\tilde{d}_{\mathrm{a}}(R, L, v) = d_{\mathrm{a}}/d_{\mathrm{v}}$, can then be obtained by taking the DLD:

$$\tilde{d}_{\mathrm{a}}(R, L, v) = \frac{\ln\left[\bar{a}(R, L, \sqrt{2}v)/\bar{a}(R, L, v/\sqrt{2})\right]}{\ln(2)} \tag{4.12}$$

Plots of this estimate with statistical errors for avalanches in non-equilibrium is shown in Fig.4.6. At the critical disorder, the surface area appears to scale as $v^{0.83\pm0.02}$, i.e. $\tilde{d}_{\mathrm{a}} = 0.83 \pm 0.02$ for intermediate-size avalanches with $1 \ll v \ll$

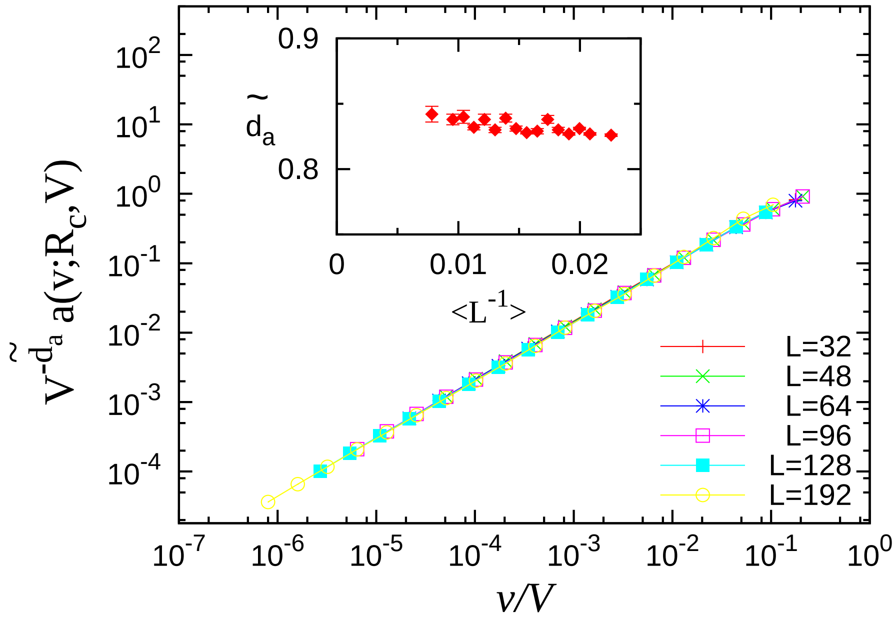

Figure 4.5: Finite-size scaling (using scaling variable v/V) for the surface area a of avalanches in non-equilibrium, using $\tilde{d}_a = 0.84$. System sizes: $L^3 = 32^3, 48^3, 64^3, 96^3, 128^3$ and 192^3. All the curves lie on top of each other. Insets show the extrapolation of the exponents to the thermodynamic limit, which yields $\tilde{d}_a = 0.84 \pm 0.01$.

L^3. We can do the similar collapse for avalanches in equilibrium and clusters in equilibrium and non-equilibrium. All the results are shown in Table 4.1.

4.4 Anisotropy measures of avalanches and clusters

Spin avalanche/cluster in non-equilibrium RFIM has been found to be anisotropic [22] and topologically interesting [18]. It is longer than it is wide. It has tunnels and sometimes during the avalanche it forms a tunnel and later winds itself through it, forming a knot. In equilibrium, anisotropy studies of spin clusters are still absent. However, universal features of the shapes of percolation clusters and polymer chains have been studied for more than twenty years [22, 6, 7, 46]. By computing proper quantities which characterize the shape of the clusters, both numerical simulations and renormalization group calculations show that clusters in those systems are quite anisotropic in the large cluster limit. At first sight, the structural anisotropy of clusters in systems with isotropic coupling seems to be very surprising. Nevertheless, as argued by Aronovitz *et al.*, the isotropy of coupling just implies that a given cluster conformation will appear with equal probability in arbitrary orientations. It doesn't guarantee that the cluster it-

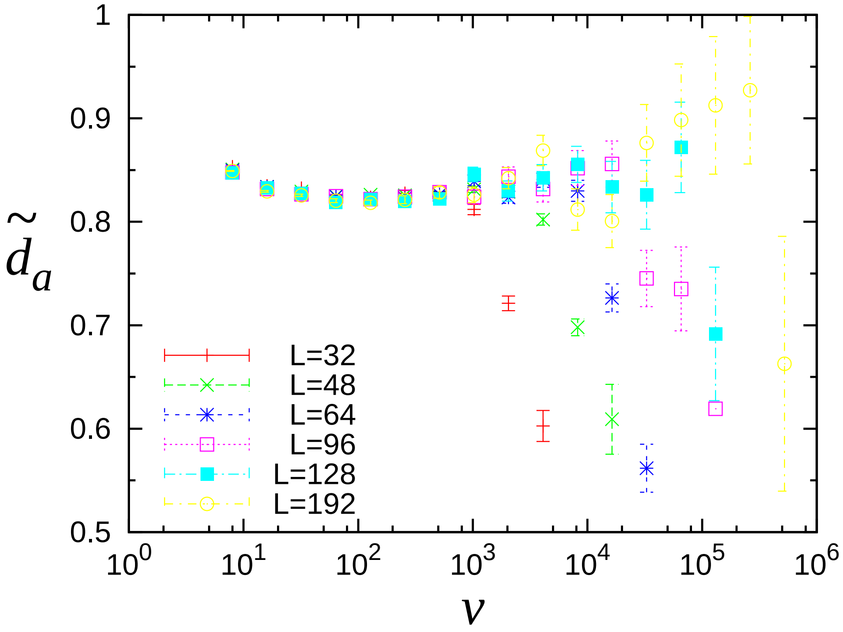

Figure 4.6: Dependence of the surface area of avalanches in non-equilibrium on the enclosed volume v is expressed as an effective exponent, i.e. the relative fractal dimension, $\tilde{d_a}(R, L, v)$ at $R = R_c$, for $L = 32, 48, 64, 96, 128, 192$. The avalanche surface area scales as $v^{\tilde{d_a}(R,L,v)}$ with $\tilde{d_a} = 0.83 \pm 0.02$ for the largest avalanches that are not affected by finite-size effects.

self is isotropic [7]. Considering this, we conjecture that both avalanches and clusters in RFIM could be anisotropic in the large avalanche and cluster limit.

To characterize the shape of a given conformation, we introduce the radius of gyration tensor Q as follows [46]. For a given specified conformation of S points in D-dimensional space, (representing either the monomer positions in a polymer chain or the occupied sites in a percolation cluster, or RFIM avalanche/cluster), the position vectors read: $R_j = (X_{j,1}, X_{j,2}, ..., X_{j,D})$ with $j = 1, ..., S$. Here, each point represents a spin in an avalanche (or a cluster) in the non-equilibrium RFIM. Then the radius of gyration tensor Q (with D eigenvalues λ_α) is defined as

$$Q_{\alpha\beta} = \frac{1}{2S^2} \sum_{i,j=1}^{S} [X_{i,\alpha} - X_{j,\alpha}][X_{i,\beta} - X_{j,\beta}]. \tag{4.13}$$

Note that the usual square radius of gyration R_G^2 is given by the trace of Q, i.e. $R_G^2 = \sum_{\alpha=1}^{D} \lambda_\alpha \equiv D\bar{\lambda}$, which characterizes the linear overall extension or size of the conformation. To characterize the shape of the conformation one has to consider ratios of those eigenvalues of Q. There are three kinds of measures with exact definitions given in the following sections.

a. Anisotropy: A_1 and A_2 In $D = 3$, assuming eigenvalues $\lambda_1 \geq \lambda_2 \geq \lambda_3$, two

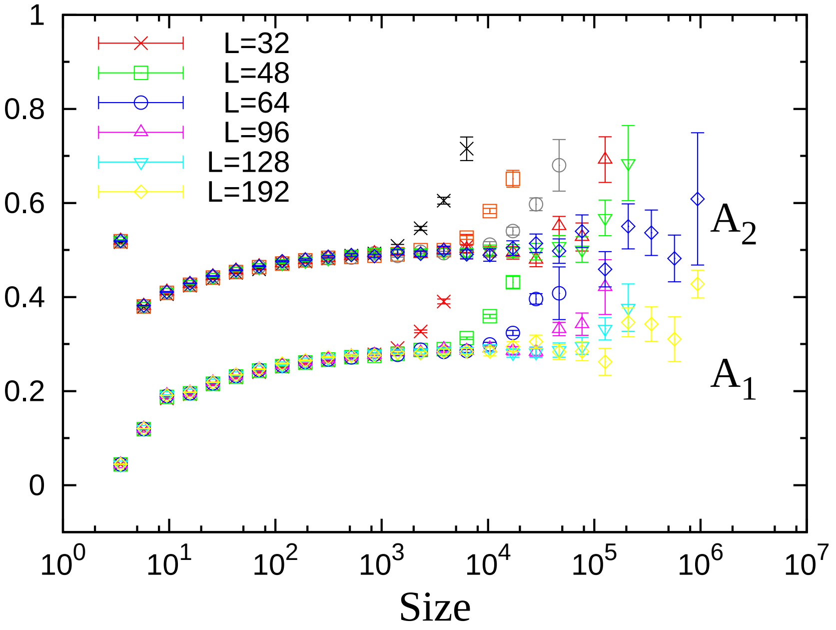

Figure 4.7: Size dependent A_1 and A_2 for avalanches in non-equilibrium. System sizes: $L^3 = 32^3, 48^3, 64^3, 96^3, 128^3$ and 192^3. $R = R_c$. The asymptotic value of A_1 as $S \to \infty$ for avalanches is obtained by looking at the largest avalanches that are not affected by the finite-size effects. We get $A_1(S \to \infty) = 0.29 \pm 0.01$ and $A_2(S \to \infty) = 0.50 \pm 0.02$.

simple quantities, the so-called anisotropies A_1 and A_2 can be defined as [22]:

$$A_1 = \lambda_{\mathrm{D}}/\lambda_1 \text{ and } A_2 = \lambda_{\mathrm{D}-1}/\lambda_1 \tag{4.14}$$

The numerical results are shown in Fig.4.7. We notice that for both the clusters and the avalanches, there is a regime of one to two decades in S over which finite-size effects are almost negligible. Below this regime, A_1 drops (A_2 increases) significantly due to the discrete-size effects. Above this regime, finite-size effects lead to big statistical errors. We can get the asymptotic value of A_1 and A_2 as $S \to \infty$ for both avalanches and clusters, by looking at the largest avalanches (or clusters) that are not affected by the finite-size effects. For example, as $S \to \infty$, for avalanches in non-equilibrium, we have $A_1 = 0.29 \pm 0.01$ and $A_2 = 0.50 \pm 0.02$, see Fig. 4.7.

b. Asphericity: Δ_D The above two measures are very hard to generalize to higher dimensions. Another quantity which is easy to generalize to higher dimensions is the so called asphericity [6], which is defined as

$$\Delta_D = \frac{1}{D(D-1)} \sum_{\alpha=1}^{D} \frac{(\lambda_\alpha - \bar{\lambda})^2}{\bar{\lambda}^2}. \tag{4.15}$$

Note that Δ_D vanishes for conformations with all eigenvalues $\lambda_\alpha = \bar{\lambda}$ equal and

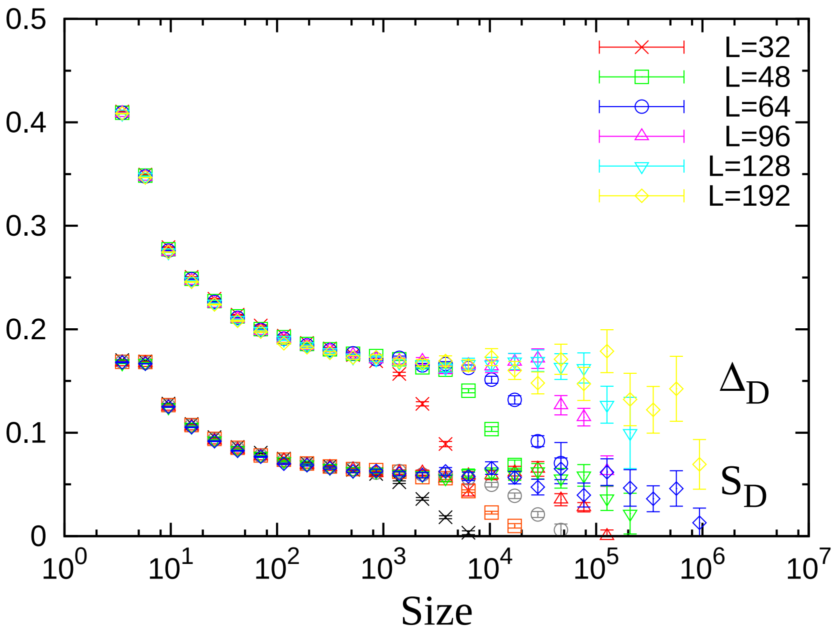

Figure 4.8: Size dependent Δ_D and S_D for avalanches in non-equilibrium. System sizes: $L^3 = 32^3, 48^3, 64^3, 96^3, 128^3$ and 192^3. $R = R_c$. The asymptotic values of Δ_D and S_D for avalanches in non-equilibrium as $S \to \infty$ are $\Delta_D(S \to \infty) = 0.16 \pm 0.01$ and $S_D(S \to \infty) = 0.06 \pm 0.01$, respectively.

takes a maximum value of 1 for a completely collinear conformation where all eigenvalues vanish except one. Δ_D characterizes the shape's overall deviation from spherical symmetry. See Fig.4.8. We notice that, except for the decay trend, these two plots have similar features as plots of A_1 and A_2. We can do the same estimation to get the asymptotic value of Δ_D as $S \to \infty$. For avalanches in non-equilibrium, we have $\Delta_D = 0.16 \pm 0.01$.

c. Prolateness: S_D The prolateness S_D is defined as

$$S_D = \frac{(\lambda_1 - \bar{\lambda})(\lambda_2 - \bar{\lambda})(\lambda_3 - \bar{\lambda})}{2\bar{\lambda}^3}, \tag{4.16}$$

which can distinguish prolate from oblate shapes in $D = 3$. S_D is bounded to the interval $[-0.125, 1]$. The maximum (minimum) is taken when two eigenvalues vanish (one vanishes and the other two are equal) [6, 7]. Positive (negative) values belong to prolate (oblate) shapes, with one eigenvalues greater (smaller) than and the other two smaller (greater) than $\bar{\lambda}$. Our result is shown in Fig.4.8. Similar estimation yields the asymptotic value of S_D as $S \to \infty$, for avalanches in non-equilibrium: $S_D = 0.06 \pm 0.01$. The result suggests that avalanches in non-equilibrium are *prolate*.

4.5 Avalanche surface area distribution

In this section, we discuss the field integrated avalanche surface area distribution for given sizes at R_c in both equilibrium and non-equilibrium. We know that the surface area a of avalanches (or clusters) scales with the size S as

$$a \sim S^{\hat{d_\mathrm{a}}} \tag{4.17}$$

with $\hat{d_a} \equiv d_\mathrm{a}/d_\mathrm{S}$. Then the distribution of surface areas $D_\mathrm{a}(S, R, H, a)$ for an avalanche of size S close to the critical field H_c and critical disorder R_c is given by

$$D_\mathrm{a}(S, R, H, a) \sim S^{-q} \mathcal{D}_\pm (S^\sigma |r|, h/|r|^{\beta\delta}, a/S^{\hat{d_a}}) \tag{4.18}$$

with $q = \tau + \hat{d_a}$, and is defined such that

$$\int_{-\infty}^{+\infty} \int_{Z}^{+\infty} D_\mathrm{a}(S, R, H, a)\ \mathrm{d}H\mathrm{d}a = S^{-(\tau+\sigma\beta\delta)} \mathcal{D}_\pm^{\mathrm{int}}(S^\sigma |r|) \tag{4.19}$$

where $\mathcal{D}_\pm^{\mathrm{int}}$ was defined in the integrated avalanche size distribution section. The avalanche surface area distribution integrated over the field H, at the critical disorder $r = 0$ is then easily derived:

$$D_\mathrm{a}^{(\mathrm{int})}(S, a) \sim a^{-(\tau+\sigma\beta\delta+\hat{d_\mathrm{a}})/\hat{d_\mathrm{a}}}\ \mathcal{D}_\mathrm{a}^{(\mathrm{int})}(a/S^{\hat{d_\mathrm{a}}}). \tag{4.20}$$

(This is very similar to the derivation of the avalanche time distribution [80].)

Fig. 4.9 shows the surface area distributions for different avalanche sizes and collapses of those curves using Eq. 4.20. Here, we use $\hat{d_\mathrm{a}} = 0.81$ and $\tau + \sigma\beta\delta = 2.01$ for both equilibrium and non-equilibrium collapses. The values are also consistent with what we obtained from the study of the field integrated avalanche size distribution and the fractal dimensions of avalanches. We find that with the same set of exponents, the scaling function $\mathcal{D}_\mathrm{a}^{(\mathrm{int})}(X)$ in equilibrium and non-equilibrium match very well.

4.6 Summary

All the quantities we calculated are shown in Table 4.1.

First, the integrated size distribution of the avalanches. We find an excellent match in both the critical exponents (σ and $\tau+\sigma\beta\delta$) and scaling functions. *Second, fractal dimensions.* We find that $d_\mathrm{S} = d_\mathrm{v}$ for all the cases, which indicates the "holes" would be ignorable in the thermodynamic limit. The relative fractal dimensions obtained from different methods are consistent. Moreover, considering the systematic errors could be even larger than the ones listed here, we conclude that the fractal dimensions (d_S, d_v or d_a) of avalanches (or clusters) in equilibrium and non-equilibrium are very close. *Third, anisotropy measures.* It is interesting to mention that avalanches (or clusters) are prolate in both equi-

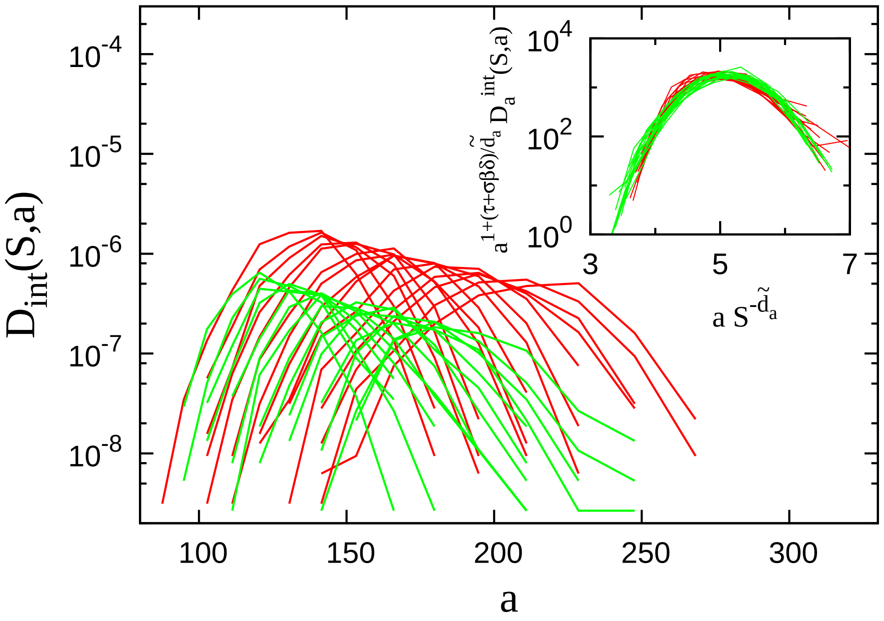

Figure 4.9: (Color online) Avalanche surface area distribution curves in 3D at R_c, for avalanche size bins from 50 to 88 (from upper left to lower right corner). The system size is 192^3 for non-equilibrium (solid lines, averaged over 45 initial random-field configurations) and 64^3 in equilibrium (dashed lines, averaged over 1431 initial random-field configurations). The inset shows the scaling collapse of curves in the main panel, using the same set of exponents for both equilibrium and non-equilibrium: $\hat{d}_a = 0.81$, $\tau + \sigma\beta\delta = 2.01$.

librium and non-equilibrium. More importantly, we find that the asymptotic values of all the anisotropy measures of avalanches (or clusters) in equilibrium and non-equilibrium are very close. *Forth, the integrated surface area distribution of the avalanches.* We find that with the same set of exponents, the scaling function in equilibrium and non-equilibrium match very well.

All in all, we have shown that the equilibrium and non-equilibrium DIPTs of the zero-temperature Gaussian RFIM behave surprisingly similarly in critical exponents, scaling functions and spatial structures of avalanches and clusters. Also, they both obey the no-passing rule. All of these results indicate that the two DIPTs are very likely in the same universality class. Larger system sizes could be a direct way to test it further, especially for the fractal dimensions and anisotropy measures. Different disorder distributions and lattice types would also be useful methods to test the universality. We will investigate the former in the next chapter.

Also, we want to emphasize the connection between all the known DIPTs associated with different dynamics (history dependence). As we know, the demagnetization curve displays a very similar DIPT as that of the saturation loop and the ground state [12, 16]. Together with our new result, we suggests

Table 4.1: Critical exponents and anisotropy measures obtained from numerical simulations in 3D for both equilibrium and non-equilibrium zt-GRFIM. Here, values in parenthesis are quoted from Ref. [80]. Note that for clusters in equilibrium, in Ref. [71], $\tilde{d_{\mathrm{a}}} = 0.755 \pm 0.007$ is obtained by taking DLD. Then, the authors assume compact volumes: $d_{\mathrm{v}} = 3$ and thus they obtain $d_{\mathrm{a}} = 2.27 \pm 0.02$.

	non-equilibrium		equilibrium	
Quantities	Avalanches	Clusters	Avalanches	Clusters
σ	(0.24 ± 0.02)		0.23 ± 0.01	
$\tau + \sigma\beta\delta$	(2.03 ± 0.03)		2.00 ± 0.01	
d_{S}	2.78 ± 0.05	2.76 ± 0.04	2.77 ± 0.09	2.78 ± 0.05
d_{v}	2.78 ± 0.05	2.76 ± 0.04	2.77 ± 0.09	2.78 ± 0.05
d_{a}	2.33 ± 0.04	2.18 ± 0.04	2.16 ± 0.05	2.11 ± 0.03
$\tilde{d_{\mathrm{a}}}$ $(d_{\mathrm{a}}/d_{\mathrm{v}})$	0.84 ± 0.02	0.79 ± 0.02	0.78 ± 0.03	0.76 ± 0.02
$\tilde{d_{\mathrm{a}}}$ (collapse)	0.84 ± 0.01	0.80 ± 0.01	0.79 ± 0.01	0.76 ± 0.01
$\tilde{d_{\mathrm{a}}}$ (DLD)	0.83 ± 0.02	0.80 ± 0.01	0.78 ± 0.01	0.76 ± 0.01
A_1	0.29 ± 0.01	0.25 ± 0.01	0.30 ± 0.02	0.28 ± 0.01
A_2	0.50 ± 0.02	0.45 ± 0.02	0.50 ± 0.02	0.48 ± 0.02
Δ_d	0.16 ± 0.01	0.21 ± 0.02	0.16 ± 0.02	0.18 ± 0.02
S_d	0.06 ± 0.01	0.09 ± 0.01	0.06 ± 0.01	0.07 ± 0.01

that all the three DIPTs, associated with the saturation loop, the demagnetization curve and the equilibrium magnetization curve respectively, are indeed in the same universality class. This would be very exciting. So far there is no RG treatment for the demagnetization curve, while there is for the saturation loop [17]. Motivated by these results, we find that analytic studies comparing the RG descriptions of the DIPTs with different dynamics are indeed an exciting prospect.

Chapter 5

Numerical results on different random-field distributions

Recently, the universality concept with respect to the shape of random-field distribution $\rho(h)$ has been questioned in both 3D simulations and mean-field theory [5, 21]. It would be then interesting to understand whether the unexpected universality reported in the last section is affected by varying the shape of $\rho(h)$.

Generally, to model quenched disorders, the local fields h_i are randomly chosen from a distribution $\rho(h)$ which is symmetric around zero with a peak of width R. Here, the width R is often called disorder parameter or just disorder. We consider four different distributions: (1) Gaussian with zero mean and disorder R defined to be the standard deviation: $\rho(h) = \frac{1}{\sqrt{2\pi}R}\exp(-\frac{h^2}{2R^2})$; (2) Lorentzian $\rho(h)$ with peak location at zero and R defined to be the distribution width at the half-maximum: $\rho(h) = \frac{1}{2\pi}\frac{R}{h^2+(R/2)^2}$; (3) parabolic distribution between $-R$ and R, i.e. $\rho(h) = \frac{R^2-h^2}{4R^3/3}$ for $-R < h < R$ and 0 for rest; (4) uniform distribution between $-R$ and R: $\rho(h) = \frac{1}{2R}$ for $-R < h < R$ and 0 for rest. [1]

5.1 Avalanche size distribution

We compare the critical exponents and scaling functions associated with the integrated avalanche size distribution first:

$$D_{\text{int}}(S,R) \sim S^{-(\tau+\sigma\beta\delta)}\ \bar{\mathcal{D}}^{\text{int}}_{\pm}(S^{\sigma}|r|) \tag{5.1}$$

In non-equilibrium, the quantity $D_{\text{int}}(S,R)$ for Gaussian $\rho(h)$ has been studied extensively, where $(\tau+\sigma\beta\delta) = 2.03 \pm 0.03$ and $\sigma = 0.24 \pm 0.02$ were obtained from scaling collapse of the $D_{\text{int}}(S,R)$ curves at different disorders [89]. Here, in Fig. 5.2(a), we show that for Gaussian, Lorentzian and parabolic $\rho(h)$'s in both equilibrium and non-equilibrium, 24 data sets of $D_{\text{int}}(S,R)$ curves for different disorders, collapse onto a single curve, with the same pair of critical exponents: $(\tau+\sigma\beta\delta) = 2.03$ and $\sigma = 0.24$. Note that in doing the scaling collapse, there are only two types of tuning parameters: (1) critical disorder R_{c}; (2) overall horizontal and vertical scale factors A and B. Both are non-universal constants and depend on the details of $\rho(h)$ and whether the system is in equilibrium or

---

[1] Note that here we don't consider the bimodal distribution, $\rho(h_i) = \frac{1}{2}[\delta(h_i-R)+\delta(h_i+R)]$ simply because it will cause degeneracy problems and avalanches cannot be clearly identified.

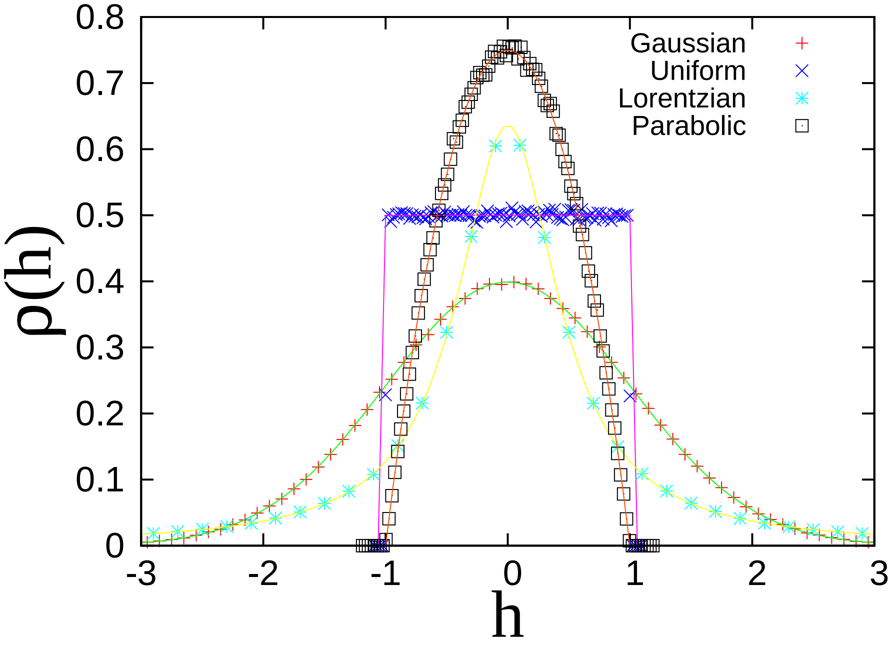

Figure 5.1: Different random-field distributions. Lines are exact functions. Points are random fields generated by random-number generators using transformation method [83].

not.

Note that the match in critical exponents and scaling functions for the three different $\rho(h)$'s is not a surprise at all. A RG analysis has shown that, at least in non-equilibrium, what matters is just $\rho''(0)$, i.e. the second derivative of $\rho(h)$ at $h = 0$ [17]. Other details about the shape of $\rho(h)$ don't enter the RG analysis. According to the definitions of Gaussian, Lorentzian and parabolic $\rho(h)$'s, one has $\rho''(0) \sim -R^3$ for all of them. Therefore, their universal behaviors agree, as expected. However, the match in critical exponents and scaling functions for static and dynamics avalanches is surprising. It indicates strongly that the equilibrium and non-equilibrium RFIM behave the same near their corresponding critical points.

In Fig. 5.2(b) we show that for uniform $\rho(h)$ in both equilibrium and non-equilibrium, 8 data sets of $D_{\text{int}}(S, R)$ for different disorders, collapse onto a single curve, with critical exponent set: $(\tau + \sigma\beta\delta) = 2.08 \pm 0.02$ and $\sigma = 0.52 \pm 0.03$. Here, we want to emphasize that: (1) The critical exponents, especially σ, are significantly different from those of the above three kinds of $\rho(h)$'s. (2) The scaling function shows significantly different shape from that observed in Fig. 5.2(a). These two findings are still consistent with the RG analysis mentioned above. We notice that for a uniform $\rho(h)$, $\rho''(0) = 0$ is independent of R and is qualitatively different from the other three distributions. (3) For a uniform $\rho(h)$, both the critical exponents and scaling functions for static and dynamic avalanches do match. This is an interesting result. On the one hand, the conventional concept of universality holds: All the scaling behaviors are the same for different $\rho(h)$'s with a bump ($\rho''(0) < 0$). On the other hand, scaling behavior in equilibrium and non-equilibrium are the same.

5.2 Avalanche correlation function

To convince ourselves that the above result is not just a coincidence, we make another independent test. We compare the critical exponents and scaling functions associated with the avalanche correlation function in equilibrium and non-equilibrium for all four different $\rho(h)$'s.

The integrated avalanche correlation function is given by

$$G_{\text{int}}(x,R) \sim \frac{1}{x^{d+\beta/\nu}}\bar{\mathcal{G}}_{\pm}(x|r|^{\nu}) \tag{5.2}$$

In non-equilibrium, the quantity $G_{\text{int}}(x,R)$ for the Gaussian $\rho(h)$ has been studied extensively, where $d+\beta/\nu = 3.07 \pm 0.30$ and $\nu = 1.37 \pm 0.18$ were obtained from scaling collapses of the $G_{\text{int}}(x,R)$ curves at different disorders [80]. In Fig. 5.3(a) we show that for Gaussian, Lorentzian and parabolic $\rho(h)$'s in both equilibrium and non-equilibrium, with the same critical exponent set: $d+\beta/\nu = 3.07$ and $\nu = 1.37$, 24 data sets for $G_{\text{int}}(x,R)$ at different disorders collapse onto a single curve (apart from the non-universal critical disorders and overall scale factors). In Fig. 5.3(b) we show that for uniform $\rho(h)$ in both equilibrium and non-equilibrium, 8 data sets of $G_{\text{int}}(x,R)$ for different disorders, collapse onto a single curve, with critical exponents: $d+\beta/\nu = 3.0 \pm 0.3$ and $\nu = 0.8 \pm 0.2$. Note that the R_{c} values used here in the scaling collapse are exactly the same as that used in Fig. 5.2. Therefore, these results on avalanche correlation functions are completely consistent with what we found in integrated avalanche size distributions.

5.3 Discussion

To discuss the effect of a general dynamics on the critical behavior of avalanches, we need a more general definition of a stable state. The k-spin-flip stable state with $1 <= k < \infty$ is a good one, which is first introduced in the study of spin glasses [73]. It is defined to be the infinite-volume spin configuration whose energy cannot be lowered by the flip of any subset of $1, 2, \cdots, k$ spins. For example, $k = 1$ is just the single-spin-flip stable state while $k = \infty$ corresponds to the exact ground state. Then it is natural to introduce the k-spin-flip dynamics, which means that all the metastable states connected by avalanches are k-spin-flip metastable states [78]. In the case of $k = 1$, it is just the single-spin-flip dynamics used in our non-equilibrium calculations. While for $k = \infty$, it is just the dynamics obeyed by the ground state evolution used in our equilibrium calculations. It has been found that the change of dynamics from $k = 1$ to $k = 2$

will not alter the critical behavior of the dynamic avalanches [101]. Together with our finding, i.e $k = 1$ and $k = \infty$ give the same avalanche behavior, we suggest that avalanches associated with the whole series of k-spin-flip dynamics (with $k = 1, 2, \cdots \infty$) would have the same critical behavior.

The concept of k-spin-flip dynamics is quite general but it definitely cannot encompass all kinds of dynamics. For instance, it is not expected to capture the demagnetization dynamics associated with the demagnetization curve. Here, the demagnetization curve is obtained by applying an oscillating external field with very slowly decreasing amplitude. The system will then be taken through a series of subloops. The line connecting the tips of those subloops is known as the demagnetization curve and the final state is called the demagnetized state. Obviously, the demagnetization dynamics is out of equilibrium but it does not belong to any k-spin-flip dynamics. The demagnetized state is often used as an "approximation" of the exact ground state but it differs from the exact ground state. However, at least for Gaussian $\rho(h)$, there are two very interesting results. First, the avalanches associated with the demagnetization curve are found (within numerical error bars) to display the same scaling behavior as the avalanches associated with the saturation hysteresis loop [12]. Second, the demagnetized state and ground state show similarity near their corresponding critical points: the critical exponents and scaling function associated with the magnetization curve coincide [16].

Considering all the findings, we suggest that all the different dynamics yield the same scaling behavior of avalanches — a unexpected universality, see Fig. 5.4 and Fig. 5.5.

So far, there is no RG analysis taking into account the dynamics as a tuning parameter. The k-spin-flip dynamics may be a good candidate to start with since k (or $1/k$) is a natural parameter [78]. But for demagnetization dynamics, it is still unclear how to conduct an RG analysis. On the other hand, it would be very interesting to numerically test this universality in other disordered systems, especially for those systems with frustrations where the no-passing rule is broken. We suspect that a necessary condition for equilibrium and non-equilibrium critical behavior to scale in the same way is that the scaling behavior is dominated in both cases by a zero-temperature fixed point. For example, for the random-bond Ising model, which has a non-trivial finite-temperature fixed point [44], the equilibrium and non-equilibrium critical behavior are different [17].

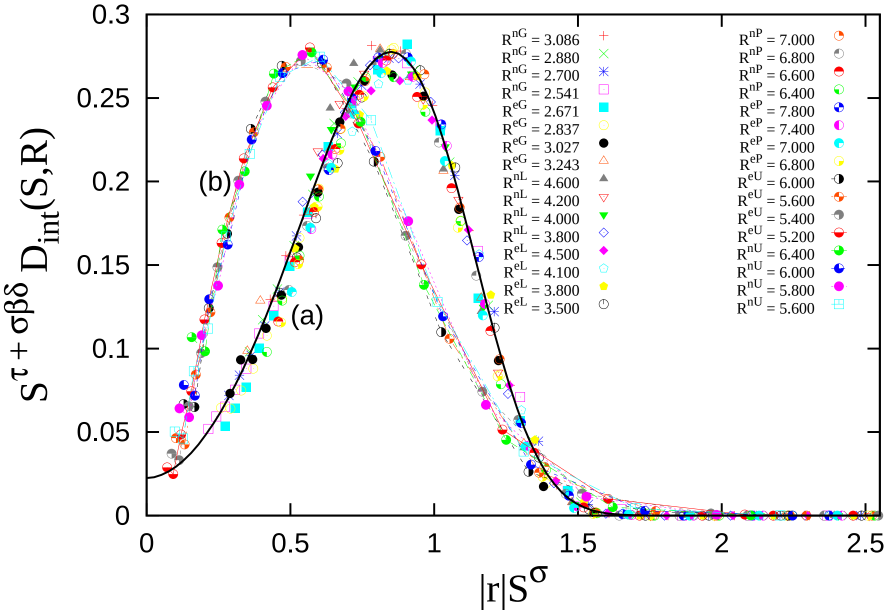

Figure 5.2: Scaling functions of integrated avalanche size distribution. The scaling collapses of the equilibrium and non-equilibrium integrated avalanche size distributions with different disorders and different random-field distributions in 3D for 64^3 spins are plotted. Those curves are averaged up to 100 initial random-field configurations. In the legend, the subscripts stand for equilibrium (e) or non-equilibrium (n) and the type of $\rho(h)$: Gaussian (G), Lorentzian (L), parabolic (P), and uniform (U). For Gaussian, Lorentzian and parabolic $\rho(h)$'s, those curves collapse to each other up to non-universal critical disorders and overall horizontal and vertical scale factors. Here, we use $R_c^{nG} = 2.16$, $R_c^{eG} = 2.29$; $R_c^{nL} = 1.92$, $R_c^{eL} = 2.08$; $R_c^{nP} = 4.84$, $R_c^{eP} = 5.0$. For the critical exponents, we use $(\tau + \sigma\beta\delta) = 2.03$ and $\sigma = 0.24$ for all the curves. And the thick black curve through the collapse is the universal scaling function $\bar{\mathcal{D}}_{-}^{\text{int}}(X) = e^{-0.789X^{1/\sigma}}(0.021 + 0.002X + 0.531X^2 - 0.266X^3 + 0.261X^4)$. Both the critical exponent set $(\tau + \sigma\beta\delta, \sigma)$ and the scaling function $\bar{\mathcal{D}}_{-}^{\text{int}}(X)$ are consistent with previous results of non-equilibrium Gaussian RFIM [80]. For uniform $\rho(h)$, the equilibrium and non-equilibrium curves collapse to each other, with $R_c^{nU} = 4.64$ and $R_c^{eU} = 4.46$. The collapse yields critical exponents $(\tau+\sigma\beta\delta) = 2.08\pm0.02$ and $\sigma = 0.52\pm0.03$, which are significantly different from the exponents of the Gaussian RFIM. Moreover, the scaling function does not match that of the Gaussian RFIM, no matter how we tune the overall horizontal and vertical scale factors.

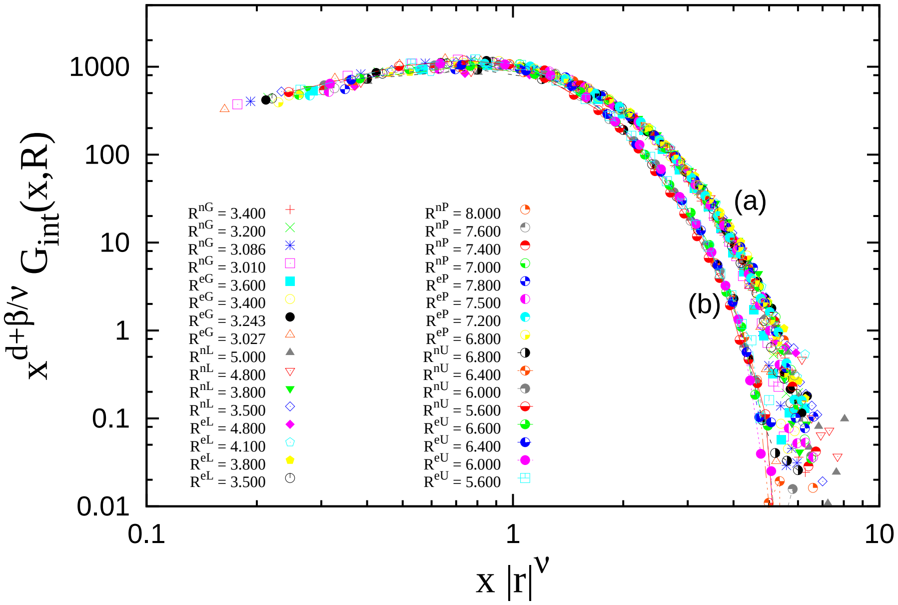

Figure 5.3: Scaling functions of integrated avalanche correlation function. The scaling collapse of the equilibrium and non-equilibrium integrated avalanche correlation functions with different disorders and different random-field distributions in 3D for 64^3 spins are plotted. Here, the same critical disorder values are used as in the collapse of $D_{\text{int}}(S, R)$ shown in Fig. 5.2. For Gaussian, Lorentzian and parabolic $\rho(h)$'s, up to non-universal critical disorders and overall horizontal and vertical scale factors, those curves collapse to each other, with $d + \beta/\nu = 3.07$ and $\nu = 1.37$, which are consistent with previous results of non-equilibrium Gaussian RFIM [80]. For uniform $\rho(h)$, the equilibrium and non-equilibrium curves collapse to each other with $d + \beta/\nu = 3.0 \pm 0.3$ and $\nu = 0.8 \pm 0.2$. Both the critical exponents and the scaling function are different from those of the Gaussian RFIM.

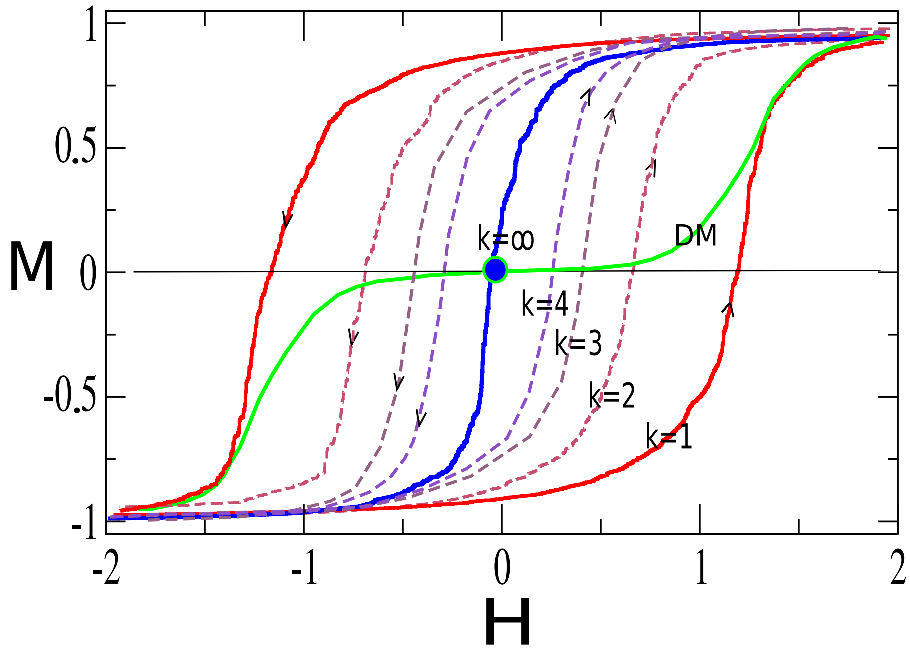

Figure 5.4: DIPTs in RFIM associated with different dynamics belong to the same universality class. Here $k = 1$ refers to the single-spin-flip dynamics, $k = 2$ refers to the two-spin-flip dynamics, $\cdots$, $k = \infty$ refers to the ground state evolution. DM refers to the demagnetization dynamics.

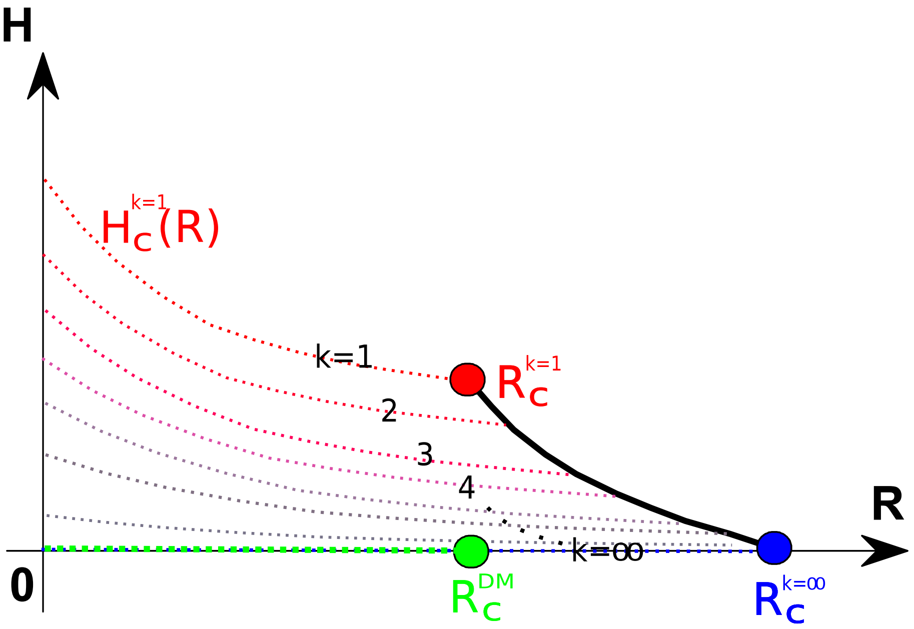

Figure 5.5: Phase diagram of zero-temperature RFIM with k-spin-flip dynamics and demagnetization dynamics. Dashed lines indicate the first-order phase transitions occurring at the critical field H_c. Note that for demagnetization dynamics and ground state evolution ($k = \infty$), $H_c = 0$ due to symmetry.

Part II

Applied Perspective: Modeling Perpendicular Recording Media

Chapter 6

Introduction

6.1 Perpendicular magnetic recording

Perpendicular magnetic recording (PMR) is a technology for data recording on hard disk drives (HDDs). All HDDs store the data as tiny areas ("bits") of either positive or negative magnetization on the surfaces of the disks, which represents a "bit" of information ("1" or "0"). The bits are written closely-spaced to form circular concentric "tracks" on the rotating disk surface. Typically, there are 10^6 bits on each track and $10^4 \sim 10^5$ tracks on each disk surface. The total storage capacity of a HDD with a given size depends directly on how small we can make the bits: the smaller the bits, the greater the capacity. Usually, the areal density is defined to be the product of bits per inch along the track times tracks per inch radially on the disk with units bits/inch^2.

Note that in LMR, the magnetization in the bits is directed circumferentially along the track direction. While in PMR, the magnetic bits point up or down perpendicular to the disk surface. Fig. 6.1 contrasts how the recording media, the write head, and the read head are configured for a longitudinal and a perpendicular recording system [104]. Historically, it was first proven advantageous than the conventional longitudinal magnetic recording (LMR) in 1976 by Shun-ichi Iwasaki. And it was first commercially implemented in 2005 by Hitachi Global Storage Technologies.

In recent years the growth-rate of area density has slowed due to a fundamental limit in magnetic recording — the so called *superparamagnetic limit*. This limit comes from the fact that the magnetic material on the disk is composed of small grains. If the thermal fluctuation is too big, there may be enough thermal energy to reverse the magnetization in a region of the medium, destroying the data stored there. The energy required to reverse the magnetization of a magnetic region is proportional to the size of that region and the magnetic coercivity of the material.

$$\Delta E \sim M\, V\, H_{\mathrm{C}} \tag{6.1}$$

Obviously, the larger the magnetic region is and the higher the magnetic coercivity of the material, the more stable the medium is. [1] At a given temperature

---

[1] Because of the randomness of the grain shapes and sizes, each bit written on the disk must cover about 100 grains to ensure that the information is reliably stored.

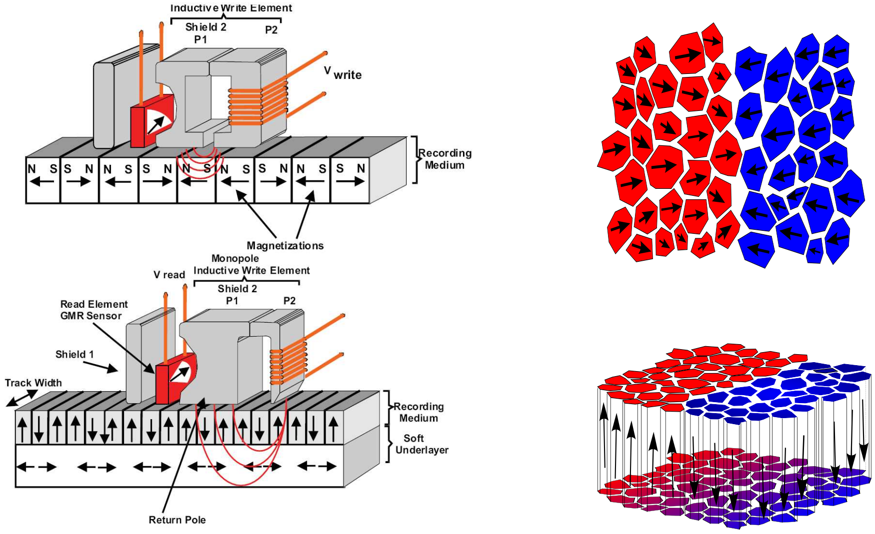

Figure 6.1: (Top) Longitudinal recording diagram and (bottom) perpendicular recording diagram [104]. Corresponding grain alignments are also shown.

and coercivity, there is an unfortunate lower limit to the size of a grain. Below this limit, there is a risk that the magnetization may spontaneously reverse just due to the thermal fluctuation, which is ubiquitously present in the environment of HDDs.

Fortunately, perpendicular recording addresses this limit and allows continued advances in areal density. First of all, aligning the bits perpendicularly to the surface of the disk takes less space than what would have been required had they been placed longitudinally. Therefore, bits can be placed closer together on the disk to increase the areal density. This partially explains why perpendicular recording can achieve higher storage densities. However, it is not quite accurate. There is another reason, which relates to the use of a higher coercivity material as the recording medium. As seen in the perpendicular recording diagram, there is a unique feature, i.e. the soft magnetic underlayer incorporated into the disk. This underlayer conducts magnetic flux very readily. Consequently, when the write head is energized, magnetic flux concentrates under the small pole-tip and generates an intense magnetic field in the short gap between the pole-tip and soft underlayer. The recording layer that stores the data is directly in this gap where the field is most intense. Intenser magnetic fields allow higher coercivity media to be used. [2] And with higher coercivity, grain sizes can be much smaller. This fully explains the advantage of perpendicular recording.

Current hard disk technology with longitudinal recording has an estimated limit of 100 to 200 Gbit/inch^2 due to the superparamagnetic effect, though this

---

[2] Such media require higher fields to set the magnetization, but once set, the magnetization is inherently more stable.

estimate is constantly changing. [3] Perpendicular recording is predicted to allow information densities of up to around 1000 Gbit/inch^2.

6.2 Intrinsic switching-field distribution

One of the key challenges in advancing the nanotechnology of magnetic recording is the optimization of recording media and its physical properties [82]. This challenge is particularly demanding because magnetic recording is by its nature a local process. Thus, it is not so much the average physical properties that are crucial, but the distributions of such properties that determine continued technological advancement and success [82]. In general, it is important to devise recording media structures that have very homogeneous properties on recording relevant length scales, so that a position independent physical description of all properties and magnetization processes is appropriate. However, this can only be achieved to a limited degree and it is therefore essential to have exact knowledge of the corresponding parameter distributions. One of the most crucial properties is the intrinsic switching-field distribution $D(H_\mathrm{S})$ of the media grains because it defines the recording quality of a media layer in both magnetic stability and the achievable recording density [94]. Hereby, one has to realize that it is not the macroscopic switching field distribution $D_\mathrm{m}(H_\mathrm{S})$ in a uniformly applied field that is relevant, but the local distribution $D(H_\mathrm{S})$ of switching fields in a recording process, which takes place in a narrowly defined field geometry. The difference between $D_\mathrm{m}(H_\mathrm{S})$ and $D(H_\mathrm{S})$ is caused by the inter-granular interactions between the media grains. In particular, for perpendicular media the dipolar interaction is large and dominates the behavior of hysteresis loops $M(H)$. Thus, the knowledge of $D_\mathrm{m}(H_\mathrm{S})$, which can be derived from the slope of $M(H)$, is insufficient for recording performance predictions. [4]

Over the years, several methodologies have been developed to determine $D(H_\mathrm{S})$ with varying success [96, 14, 97, 98, 2, 9, 103]. Most of these methods apply a measurement scheme, in which magnetization reversal of media grains is probed starting from different magnetization states to allow for a variation of the grain-to-grain interaction under measurement conditions. Such procedures should then in principle and under certain limiting conditions allow for a separation of the intrinsic switching field distribution from inter-granular interactions.

---

[3] Gigabit is a unit of digital information storage, with the symbol G bit (or Gb). 1gigabit = 10^9 bits. Note that there is no standard but a byte most often consists of eight bits.

[4] In the case of no inter-grain interactions,

$$M = 1 - 2 \int_{-\infty}^{-H(M)} D_\mathrm{m}(H_\mathrm{S})\, \mathrm{d}H_\mathrm{S}.$$

Take the derivative with respect to H,

$$\frac{\mathrm{d}M}{\mathrm{d}H} = 2\; D_\mathrm{m}(H_\mathrm{S}).$$

Therefore, the macroscopic switching field distribution $D_\mathrm{m}(H_\mathrm{S})$ can be easily read off from the hysteresis loop.

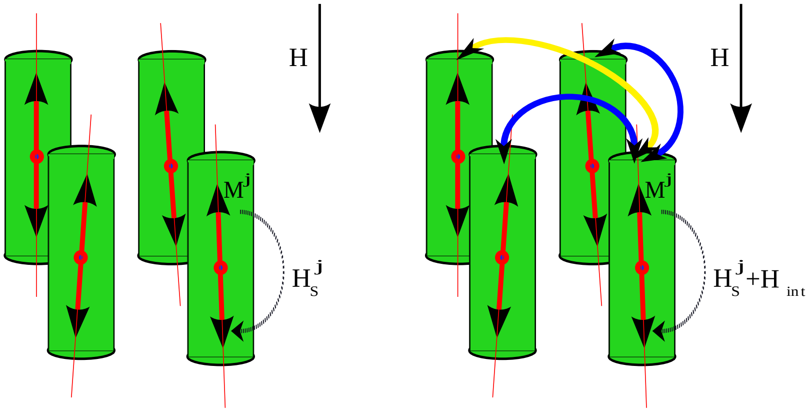

Figure 6.2: Schematic representation of the problem addressed by the $\Delta H(M, \Delta M)$ method. Each grain is characterized by an intrinsic switching field H_S as a local material property. (Left) Only in the case of no inter-granular interactions, $D_\mathrm{m}(H_\mathrm{S}) = D(H_\mathrm{S})$. (Right) In realistic, $D_\mathrm{m}(H_\mathrm{S}) \neq D(H_\mathrm{S})$. The distribution of these local fields $D(H_\mathrm{S})$ is not easily accessible in macroscopic measurements due to the intergranular exchange and dipolar interactions.

In the following chapters, we study the reliability of the recently developed $\Delta H(M, \Delta M)$ method, which has been used successfully in analyzing progress in recording media fabrication [2,9]. The method itself is a generalization of an earlier measurement technique, the ΔH_C method [96], but has the advantage that it allows the determination of the entire $D(H_\mathrm{S})$ distribution and not just a single characteristic parameter. Furthermore, it enables oversampling, which makes consistency checks feasible and gives one the opportunity to quantify the confidence level of measurement results. In contrast to the also quite robust method developed by van de Veerdonk *et al.* [97,98], it does not rely on a specific distribution form or the rather limiting assumption that interactions can be removed from the problem by a simple de-shearing of the major hysteresis loop. Recent data indicate that this very assumption appears to be an overly simplistic view of inter-granular interactions [9]. Another method that has recently gained certain popularity is the FORC-method [14, 103], which is very similar to the measurement of Preisach distributions [62]. However, this technique cannot really be compared to the previously mentioned methods, because it represents for the most part a data transformation tool and does not appear to allow a self-consistent way of extracting microscopic information such as $D(H_\mathrm{s})$, because all interactions are removed from the model in an ad hoc fashion simply by definition [14, 103].

Chapter 7

$\Delta H(M, \Delta M)$ methodology

7.1 Measurement scheme

The $\Delta H(M, \Delta M)$ method measures the field difference ΔH at constant magnetization M between the major hysteresis loop and a number of recoil curves, which each start at a certain distance ΔM away from saturation M_S.

This method assumes that the effective field at each grain can be written as $H_\mathrm{eff} = H + H_\mathrm{int}(M)$ with H being the external field and $H_\mathrm{int}(M)$ the volume-averaged interaction field at magnetization M. Assuming that M is normalized to its saturation value M_S, the upper branch of the major hysteresis loop driven by the major loop external field H, and the recoil curve starting at $M_\mathrm{rev} = 1 - \Delta M$ driven by the recoil curve external field H_r are given as

$$M = 1 - 2\int_{-\infty}^{-[H(M)+H_\mathrm{int}(M)]} D(H_\mathrm{S})\,\mathrm{d}H_\mathrm{S} \tag{7.1a}$$

$$M = 1 - \Delta M - 2\int_{-\infty}^{-[H_\mathrm{r}(M)+H_\mathrm{int}(M)]} D(H_\mathrm{S})\,\mathrm{d}H_\mathrm{S} \tag{7.1b}$$

respectively, i.e. field integrals over the intrinsic switching field distribution $D(H_\mathrm{S})$. Defining an integral function $I(x) = \int_{-\infty}^{x} D(H_\mathrm{S})\,\mathrm{d}H_\mathrm{S}$, one finds

$$H(M) = -I^{-1}\Big(\frac{1-M}{2}\Big) - H_\mathrm{int}(M) \tag{7.2a}$$

$$H_\mathrm{r}(M) = -I^{-1}\Big(\frac{1-M-\Delta M}{2}\Big) - H_\mathrm{int}(M) \tag{7.2b}$$

with I^{-1} being the inverse of the integral function. Therefore, one can derive

$$\Delta H(M, \Delta M) \equiv H_\mathrm{r}(M) - H(M) = I^{-1}\Big(\frac{1-M}{2}\Big) - I^{-1}\Big(\frac{1-M-\Delta M}{2}\Big) \tag{7.3}$$

as a closed functional form for the field axis distance ΔH between major and recoil curves, a quantity that is illustrated in Fig. 7.2. Important is hereby that within the framework of this approach ΔH is independent from the grain interaction, which allows for a direct experimental access to $D(H_\mathrm{S})$. For certain parameterized distribution functions, one can derive analytic expressions for ΔH. For example, for the Gaussian, Lorentzian, Lognormal, and truncated-

Lorentzian $D(H_\mathrm{S})$ distributions, [1]

$$D_\mathrm{G}(H_\mathrm{S}) = \frac{1}{\sqrt{2\pi}\sigma}\exp\left[-\frac{(H_\mathrm{S}-h_0)^2}{2\sigma^2}\right] \tag{7.4a}$$

$$D_\mathrm{L}(H_\mathrm{S}) = \frac{2w}{\pi}\frac{1}{w^2+4(H_\mathrm{S}-h_0)^2} \tag{7.4b}$$

$$D_\mathrm{LN}(H_\mathrm{S}) = \frac{1}{\sqrt{2\pi}\tilde{\sigma}H_\mathrm{S}}\exp\left[-\frac{(\log H_\mathrm{S}-\tilde{\mu})^2}{2\tilde{\sigma}^2}\right] \tag{7.4c}$$

$$D_{\mathrm{L}_\mathrm{t}}(H_\mathrm{S}) = \frac{2w}{\pi}\frac{C}{w^2+4(H_\mathrm{S}-h_0)^2} \qquad \text{for } H_\mathrm{S}\geq 0 \text{ only.} \tag{7.4d}$$

we find

$$\Delta H_\mathrm{G}(M,\Delta M) = \sqrt{2}\sigma\left(\mathrm{erf}^{-1}(M+\Delta M)-\mathrm{erf}^{-1}(M)\right) \tag{7.5a}$$

$$\Delta H_\mathrm{L}(M,\Delta M) = \frac{w}{2}\left\{\tan[\frac{\pi}{2}(M+\Delta M)]-\tan[\frac{\pi}{2}M]\right\} \tag{7.5b}$$

$$\Delta H_\mathrm{LN}(M,\Delta M) = \exp\left[\tilde{\mu}-\sqrt{2}\tilde{\sigma}\mathrm{erf}^{-1}(M)\right]-\exp\left[\tilde{\mu}-\sqrt{2}\tilde{\sigma}\mathrm{erf}^{-1}(M+\Delta M)\right] \tag{7.5c}$$

$$\begin{aligned}\Delta H_{\mathrm{L}_\mathrm{t}}(M,\Delta M) = \frac{w}{2}\Bigg\{&\tan\left[(\frac{\pi}{2}+\theta)\left(\frac{1-M}{2}\right)-\theta\right]\\ &-\tan\left[(\frac{\pi}{2}+\theta)\left(\frac{1-M-\Delta M}{2}\right)-\theta\right]\Bigg\}\end{aligned} \tag{7.5d}$$

Results for the Gaussian and Lorentzian distributions were reported previously [2,9]. Here, we introduce the disorder parameter σ for a general $D(H_\mathrm{S})$ distribution. σ is defined to be the standard deviation of a given distribution, such as Gaussian and Lognormal. However, for the Lorentzian distribution neither variance nor higher moments are defined, so that we need to quantify the disorder level in another form. For the Lorentzian, we define the disorder parameter to be the distribution width at the half-maximum and the mean to be the center of the distribution. For the distributions given by Eq. 7.4a, 7.4b and 7.4c, we then have the disorder parameter: $\sigma^\mathrm{G}=\sigma$, $\sigma^\mathrm{L}=w$, $\sigma^\mathrm{LN}=e^{\tilde{\mu}+\tilde{\sigma}^2/2}(e^{\tilde{\sigma}^2}-1)^{1/2}$ and the mean value $h_0^\mathrm{G}=h_0$, $h_0^\mathrm{L}=h_0$, $h_0^\mathrm{LN}=e^{\tilde{\mu}+\tilde{\sigma}^2/2}$. For the truncated Lorentzian distribution, we define the disorder parameter $\sigma^{\mathrm{L}_\mathrm{t}}=w$ to make it comparable with the Lorentzian distribution.

By making a least-squares fit of the $\Delta H(M,\Delta M)$ curves to the above formulas, one can extract the key features of $D(H_\mathrm{S})$. Note that both $\Delta H_\mathrm{G}(M,\Delta M)$ and $\Delta H_\mathrm{L}(M,\Delta M)$ have no h_0 dependence. But for the Lognormal distribution,

---

[1] In numerical simulation, the random switching fields with any distributions are generated by a random number generator. To avoid any negative tails in the Lorentzian distribution, we can artificially suppress any negative random numbers and instead create another random number for the switching field until we get a positive one. The corresponding switching field distribution is then represented by the truncated Lorentzian distribution $D_{\mathrm{L}_\mathrm{t}}(H_\mathrm{S})$ as shown in Eq. 7.4d. Note that C is given by the condition that $\int_{-\infty}^{+\infty}D_{\mathrm{L}_\mathrm{t}}(H_\mathrm{S})\,\mathrm{d}H_\mathrm{S}=1$. Specifically, one finds that $C=\left(\frac{1}{2}+\frac{\theta}{\pi}\right)^{-1}$ with $\theta=\tan^{-1}(\frac{2h_0}{w})$. We notice that due to the truncation induced asymmetry in the distribution itself, the derived $\Delta H_{\mathrm{L}_\mathrm{t}}(M,\Delta M)$ depends on both w and h_0 (see Eq. 7.5d).

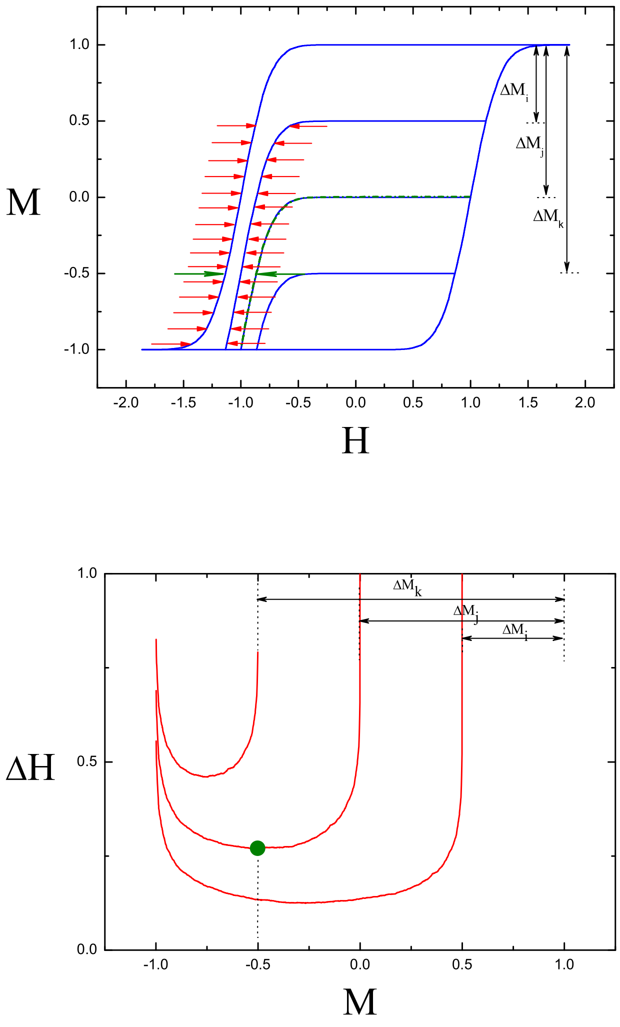

Figure 7.1: Schematic of the $\Delta H(M, \Delta M)$ method. Note that in the original ΔH_{C} method, ΔH is given by the field difference, measured at $M = -0.5$, between the major loop and the recoil curve that originates at $H = H_{\mathrm{C}}$. The ΔH_{C} point is shown as a single green dot on top of the experimentally accessible $\Delta H(M, \Delta M)$ data sets.

$\Delta H_{\mathrm{LN}}(M, \Delta M)$ depends on both $\tilde{\mu}$ and $\tilde{\sigma}$, and therefore it has both σ and h_0 dependencies.

It is easy to prove that simply shifting a general distribution will not alter the ΔH data. For this, we consider the case of a general distribution $D(H_{\mathrm{S}})$: If we shift it towards right by an amount H_0, then the integral function $\tilde{I}(x)$ of the new distribution $\tilde{D}(H_{\mathrm{S}}) = D(H_{\mathrm{S}} - H_0)$ is given by $\tilde{I}(x) = I(x - H_0)$ and its inverse $\tilde{I}^{-1}(y) = H_0 + I^{-1}(y)$. It is then clear that this shift will not change the $\Delta H(M, \Delta M)$ formula at all, since the H_0 terms will cancel according to

Eq. 7.3.

Also, we find that both $\Delta H_{\mathrm{G}}(M, \Delta M)$ and $\Delta H_{\mathrm{L}}(M, \Delta M)$ are symmetric with respect to $M = -\Delta M/2$ while $\Delta H_{\mathrm{LN}}(M, \Delta M)$ is not symmetric. This is consistent with the original distribution: Both $D_{\mathrm{G}}(H_{\mathrm{S}})$ and $D_{\mathrm{L}}(H_{\mathrm{S}})$ are symmetric around h_0 while $D_{\mathrm{LN}}(H_{\mathrm{S}})$ is not. Actually, for any $D(H_{\mathrm{S}})$ distribution being symmetric about h_0, one finds that $I(h_0 + x) = 1 - I(h_0 - x)$ and $I^{-1}(1/2+y) = -I^{-1}(1/2-y)$, from which it is easy to prove that $\Delta H(M, \Delta M)$ is symmetric about $M = -\Delta M/2$, i.e.

$$\Delta H(-\frac{\Delta M}{2} + M', \Delta M) = \Delta H(-\frac{\Delta M}{2} - M', \Delta M) \tag{7.6}$$

7.2 Reliability measures

In this section, we discuss the reliability measures of the $\Delta H(M, \Delta M)$ method for an arbitrary type of $D(H_{\mathrm{S}})$. The reliability is characterized by two types of measures: (1) conventional quality measures for numerical fits such as the *percentage difference* between the fitting and the actual parameter (P_{d}) and the *square of the multiple correlation coefficient* (R^2); (2) the average deviation from redundancy measure (r), which represents a consistency test of the data set alone.

7.2.1 Fit Quality

In simulations, one knows the input parameters exactly, such as the input distribution $D(H_{\mathrm{S}})$ in our case. Furthermore, we have also derived $\Delta H(M, \Delta M)$ formulas for certain specific $D(H_{\mathrm{S}})$ distributions as shown in Sec. 7.1. Thus, by fitting these analytical formulas to the $\Delta H(M, \Delta M)$ curves obtained from our 2D-RSFHM hysteresis loop simulations, we can get an estimate of the input $D(H_{\mathrm{S}})$ distribution. Obviously, if the input $D(H_{\mathrm{S}})$ is recovered by the fitting procedure with high accuracy, then the $\Delta H(M, \Delta M)$ method works. To quantify the reliability of the $\Delta H(M, \Delta M)$ method, we introduce the following fit quality measures. The most important fit quality measure, denoted as P_{d}, is the percentage difference between the parameters obtained from a least-square fit and the actual input parameters into our simulation. It describes how well the $\Delta H(M, \Delta M)$ method can indeed retrieve the information sought. Focusing on the disorder parameter of $D(H_{\mathrm{S}})$ as the most crucial fit parameter, we define

$$P_{\mathrm{d}} = \frac{\sigma_{\mathrm{f}} - \sigma}{\sigma} \tag{7.7}$$

Here σ_{f} is the fit value of the $D(H_{\mathrm{S}})$ distribution disorder parameter as defined in Sec. 7, while σ is the input value of the same parameter.

Another fit quality measure that can be utilized here is the square of the multiple correlation coefficient R^2, which measures how successful a fit and fit function is in explaining the data [19]. It is defined as

$$R^2 = 1 - \frac{\sum_i (Y_i - \hat{Y}_i)^2}{\sum_i (Y_i - \bar{Y})^2} \tag{7.8}$$

Y_i and $\hat{Y}_i$ are hereby the simulation result and the fit function value for $\Delta H(M, \Delta M)$ at a given data point $(M_i, \Delta M_i)$, respectively. $\bar{Y}$ is the average value of Y_i. According to the definition of R^2, we know that as R^2 approaches 1, the fit is a better and better representation of the data set. Hereby, it is important to emphasize two points in calculating P_d and R^2. First, we are comparing a mean-field theory to numerical simulations that contain the complexity of magnetization reversal in its complete detail. Second, we are using a finite size grid in our simulation while the analytic theory is derived for infinite systems. Naturally, the finite size will affect the R^2 and P_d calculation. Particularly, for data points near the beginning or end of the reversal curve, where only a few grains (hysterons) are reversed, the analytical theory for infinite hysteron numbers might not be accurate at all for the description of a finite system, independent from the validity of the mean-field approximation.

7.2.2 Deviation From Redundancy

Fit quality measures such as R^2 are not necessarily foolproof because physical models and corresponding fit functions may be used in a regime, for which the underlying theory does not apply anymore. In such cases, data fits and extracted materials parameters might appear very accurate, while they are not. Thus, it would be a tremendous help, if an independent data set evaluation would be available that allows a separate measure of the suitability of the underlying theory. Specifically here, this evaluation should tell us how good an approximation the mean-field theory is for any given data set, so that we know to which confidence level we can rely on the $\Delta H(M, \Delta M)$ method.

We find that it is indeed possible to define such a quantity. To do so one has to recognize that within the mean-field approximation $\Delta H(M, \Delta M)$ data sets contain redundancy. The data set redundancy can be seen from Fig. 7.2. For illustration purposes, we pick six points: (A and P), (B and U), (Q and V) located on the major loop, the i-th recoil curve and the j-th recoil curve, respectively. The i-th and j-th recoil curve start at $M_\mathrm{rev} = 1 - \Delta M_i$ and $1 - \Delta M_j$, respectively. Without limiting the generality of this consideration, we furthermore assume that $\Delta M_i < \Delta M_j$ and require that the six points satisfy: $M_\mathrm{A} = M_\mathrm{B} = M$, $M_\mathrm{P} = M_\mathrm{Q} = M - \Delta M_j + \Delta M_i$ and $M_\mathrm{U} = M_\mathrm{V} = M - \Delta M_j$ where M is an arbitrary value within $[-1, 1 - \Delta M_i]$. We then define

$$\Delta H_i(M) = H_\mathrm{B} - H_\mathrm{A} \tag{7.9a}$$

$$\Delta H_j(M - \Delta M_j + \Delta M_i) = H_\mathrm{Q} - H_\mathrm{P} \tag{7.9b}$$

$$\Delta H_j(M - \Delta M_j) - \Delta H_i(M - \Delta M_j) = H_\mathrm{V} - H_\mathrm{U} \tag{7.9c}$$

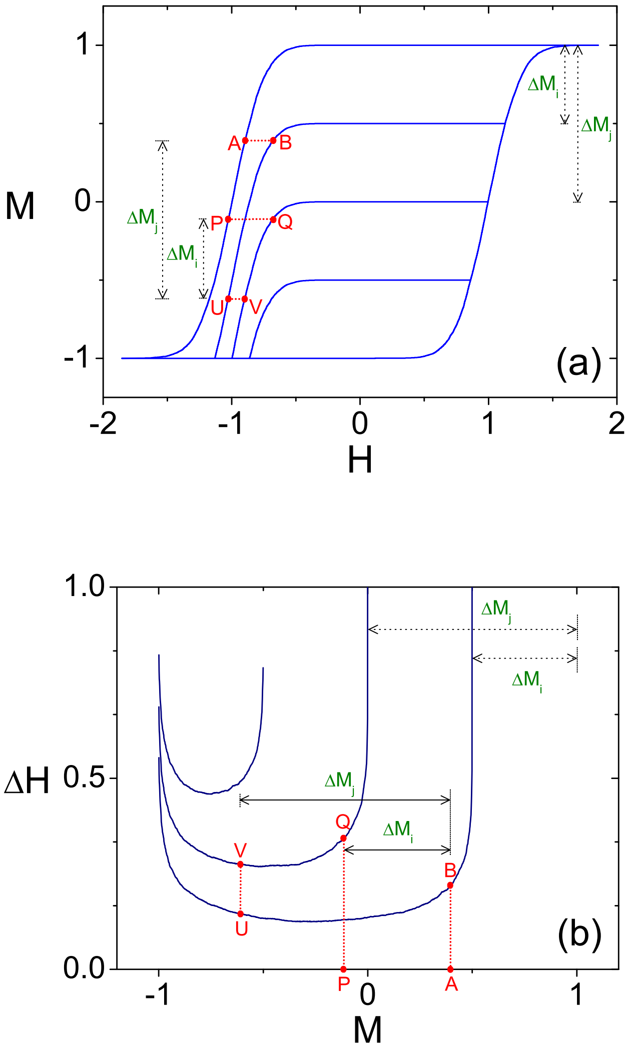

Figure 7.2: (Color online) (a) The major hysteresis loop and three recoil curves. Throughout the paper, M is normalized to its saturation value M_{S} and H is normalized to the coercive field H_{C}. The first two recoil curves start at $M_{\mathrm{rev}} = 1 - \Delta M_i$ and $1 - \Delta M_j$, respectively, with $\Delta M_i < \Delta M_j$. For the six points (A and P), (B and U), (Q and V) shown in the figure with $M_{\mathrm{A}} = M_{\mathrm{B}} = M$, $M_{\mathrm{P}} = M_{\mathrm{Q}} = M - \Delta M_j + \Delta M_i$ and $M_{\mathrm{U}} = M_{\mathrm{V}} = M - \Delta M_j$ where M is an arbitrary value within $[-1, 1 - \Delta M_i]$, one can prove the existence of data redundancy, i.e. the equality $(H_{\mathrm{B}} - H_{\mathrm{A}}) + (H_{\mathrm{V}} - H_{\mathrm{U}}) = (H_{\mathrm{Q}} - H_{\mathrm{P}})$ within the mean-field approximation. (b) The corresponding $\Delta H(M, \Delta M)$ data for the three recoil curves.

Within the mean-field approximation, it is easy to prove that

$$(H_{\mathrm{B}} - H_{\mathrm{A}}) + (H_{\mathrm{V}} - H_{\mathrm{U}}) - (H_{\mathrm{Q}} - H_{\mathrm{P}}) = 0 \tag{7.10}$$

as shown below.

Proof. As shown in Fig. 7.2, we choose six states (A, B, P, Q, U and V) from the major loop and recoil curves with

$$M_{\mathrm{A}} = M_{\mathrm{B}} = M \tag{7.11a}$$

$$M_{\mathrm{P}} = M_{\mathrm{Q}} = M - \Delta M_j + \Delta M_i \tag{7.11b}$$

$$M_{\mathrm{U}} = M_{\mathrm{V}} = M - \Delta M_j \tag{7.11c}$$

and M is an arbitrary value within $[-1, 1 - \Delta M_i]$. The hysteron distributions for the six states are shown in Fig. 7.3. Shadowed areas denote down-hysterons ($S_i = -1$), while open areas indicate up-hysterons ($S_i = +1$). In the following, we use the symbol $n_\downarrow$ and $n_\uparrow$ for the density of down-hysteron and up-hysteron, respectively. For the states chosen from the upper branch of the major loop with magnetization M_0, it is easy to get $n_\downarrow = (1 - M_0)/2$. For example,

$$n_\downarrow(A) = (1 - M)/2 \tag{7.12a}$$

$$n_\downarrow(P) = (1 - M - \Delta M_i + \Delta M_j)/2 \tag{7.12b}$$

For states chosen from the recoil curves with magnetization M_0, there are two shadowed areas, which can be denoted as $n_{\downarrow 1}$ and $n_{\downarrow 2}$. Note that the left one $n_{\downarrow 1}$ is just due to the distance from saturation at the starting point of the recoil curve, i.e. ΔM, so that $n_{\downarrow 1} = \Delta M/2$. For example, B and U are picked from the i-th recoil curve with distance from saturation ΔM_i, so that

$$n_{\downarrow 1}(B) = n_{\downarrow 1}(U) = \Delta M_i/2 \tag{7.13}$$

Similarly, for Q and V, we have

$$n_{\downarrow 1}(Q) = n_{\downarrow 1}(V) = \Delta M_j/2 \tag{7.14}$$

Combining this with the number conservation equation $n_\downarrow = n_{\downarrow 1} + n_{\downarrow 2} = (1 - M_0)/2$, we find

$$n_{\downarrow 2}(B) = (1 - M - \Delta M_i)/2 \tag{7.15a}$$

$$n_{\downarrow 2}(Q) = (1 - M - \Delta M_i)/2 \tag{7.15b}$$

$$n_{\downarrow 2}(U) = (1 - M - \Delta M_i + \Delta M_j)/2 \tag{7.15c}$$

$$n_{\downarrow 2}(V) = (1 - M)/2 \tag{7.15d}$$

It follows that

$$n_\downarrow(A) = n_{\downarrow 2}(V) \tag{7.16a}$$

$$n_\downarrow(P) = n_{\downarrow 2}(U) \tag{7.16b}$$

$$n_{\downarrow 2}(B) = n_{\downarrow 2}(Q) \tag{7.16c}$$

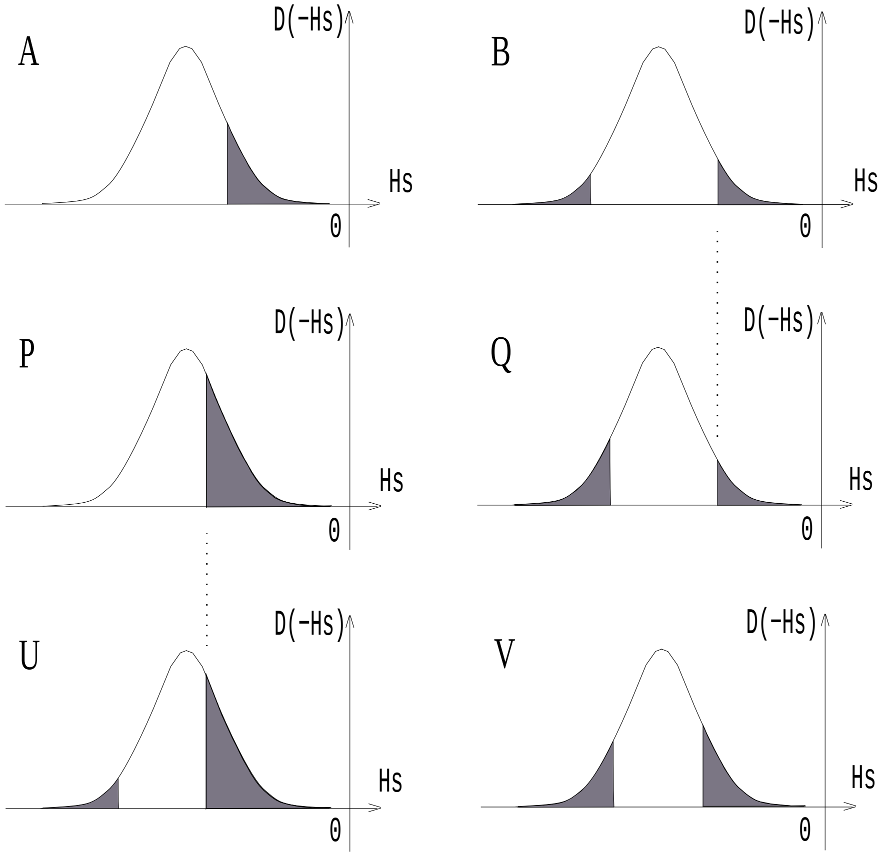

Figure 7.3: Hysteron distributions for the various states (A, B, P, Q, U and V) shown in Fig. 7.2. The shadowed areas symbolize down-hysterons ($S_i = -1$), the open areas correspondingly up-hysterons ($S_i = +1$).

and

$$H_{\mathrm{A}} + H_{\mathrm{int}}(M) = H_{\mathrm{V}} + H_{\mathrm{int}}(M - \Delta M_j) \tag{7.17a}$$

$$H_{\mathrm{P}} + H_{\mathrm{int}}(M - \Delta M_j + \Delta M_i) = H_{\mathrm{U}} + H_{\mathrm{int}}(M - \Delta M_j) \tag{7.17b}$$

$$H_{\mathrm{B}} + H_{\mathrm{int}}(M) = H_{\mathrm{Q}} + H_{\mathrm{int}}(M - \Delta M_j + \Delta M_i) \tag{7.17c}$$

So, overall we find

$$(H_{\mathrm{B}} - H_{\mathrm{A}}) + (H_{\mathrm{V}} - H_{\mathrm{U}}) - (H_{\mathrm{Q}} - H_{\mathrm{P}}) = 0 \tag{7.18}$$

Q.E.D

More generally, one finds that

$$\Delta H_i(M) + \Delta H_j(M - \Delta M_j) - \Delta H_i(M - \Delta M_j) - \Delta H_j(M - \Delta M_j + \Delta M_i) = 0 \tag{7.19}$$

This data set redundancy is due to the fact that successive recoil curves are not fully independent and contain repeated information. However, Eq. 7.19 is derived under the assumption of the mean-field approximation and is only true if the mean-field approximation is indeed fulfilled by the data set. For general data sets this property is not conserved. Therefore, we can define an M-dependent measure as

$$r_{ij}(M) \equiv \frac{\Delta H_i(M) + \Delta H_j(M - \Delta M_j) - \Delta H_i(M - \Delta M_j) - \Delta H_j(M - \Delta M_j + \Delta M_i)}{\Delta H_i(M) + \Delta H_j(M - \Delta M_j) + \Delta H_i(M - \Delta M_j) + \Delta H_j(M - \Delta M_j + \Delta M_i)} \tag{7.20}$$

that monitors deviations from the mean-field approximation based upon the above redundancy criterion (Eq. 7.19). Eq. 7.20 has an M definition range of $[\Delta M_j - 1, 1 - \Delta M_i]$. For a general set of multiple recoil curves, the average deviation from redundancy measure can be defined as

$$r \equiv \frac{1}{n} \sum_{i,j} \left\langle r_{ij}^2(M) \right\rangle^{\frac{1}{2}} \tag{7.21}$$

with n being the total number of all the possible (i, j) pairs. [2] Thus, r is a quantitative measure that allows an accurate and independent check of how close or far any $\Delta H(M, \Delta M)$ data set is from fulfilling the mean-field approximation.

Note that in calculating r, we are comparing the data set with itself. Thus, the validity of the underlying mean-field approximation used for all the $\Delta H(M, \Delta M)$ data fits, can be assessed independently and from the data set alone.

An additional benefit in the calculation of r is that the finite size inaccuracies at the definition range boundaries for the recoil curves will cancel out, at least to some degree. See Eq. 7.20. For $M = 1 - \Delta M_i$, the finite size inaccuracies in $\Delta H_i(M)$ and $\Delta H_j(M - \Delta M_j + \Delta M_i)$ will cancel out. Similarly, for $M = \Delta M_j - 1$, the finite size inaccuracies in $\Delta H_j(M - \Delta M_j)$ and $\Delta H_i(M - \Delta M_j)$ will cancel out. In this sense, the deviation from redundancy measure is more robust than the fit quality measures.

---

[2] Since the definition range of M in $r_{ij}(M)$ is $[\Delta M_j - 1, 1 - \Delta M_i]$, we must have $1 - \Delta M_i > \Delta M_j - 1$, i.e. $\Delta M_i + \Delta M_j < 2$.

Chapter 8

Modeling

8.1 Basic assumptions

For our numerical studies, we model each grain as a hysteron, which is the simplest mathematical construction for the description of a hysteretic system. Each hysteron will generate a rectangular hysteresis loop in an applied field H as shown in Fig. 8.1. We assume the transition of each hysteron is infinitely sharp and it has no additional field dependence, such as finite susceptibility, for instance. The half-width of the rectangular hysteresis loop is referred to as the intrinsic switching field of the hysteron, which is a well defined property of each individual hysteron.

We also assume that the hysteron switching fields are symmetric around zero field, i.e. there is no bias. A hysteron with zero bias is called a symmetric hysteron and is consistent with the time reversal symmetry that ferromagnets exhibit [29]. These hysteron properties can be regarded as fairly good representation of perpendicular media grains, because they have relatively high magnetic anisotropy and the applied field in typical characterization measurements is applied along the easy axis [96, 14, 97, 98, 2, 9, 103].

We further assume that there is no time structure to the hysteron switch itself. This should be an appropriate picture as long as one considers field change rates that are much slower than single grain reversal times. Given that such reversal times are typically of the order of several hundred pico seconds [28], this condition is generally fulfilled in typical measurement setups [93].

Finally, the thermal effects are completely ignored here. While thermal activations play a large role in conventional hysteresis loop measurements, they are not a fundamental limit of the $\Delta H(M, \Delta M)$ method, because one can resort to low temperature measurements to suppress thermal effects, at least in principle. Considering this, thermal effects are beyond the scope of the present study and would be the topic of future work.

8.2 Simplest hysteron model

Considering all these assumptions, the PRM is represented by a two-dimensional hysteron system with periodic boundary conditions. Depending on details of

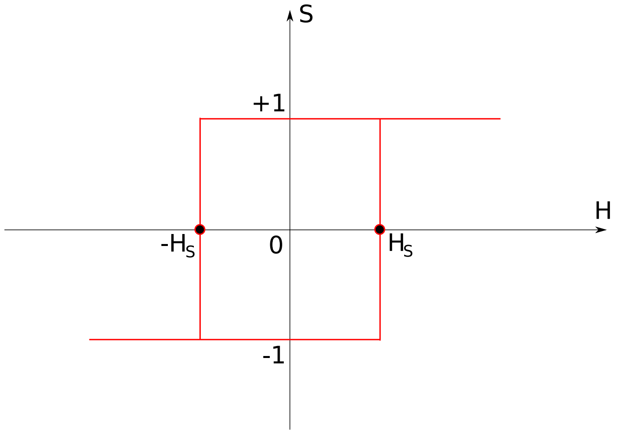

Figure 8.1: A symmetric hysteron S with intrinsic switching field H_{S}.

the inter-granular interactions, we come up with models with different levels of complications. Those models will be explained in details in following chapters. But here, we give the simplest example, which turns out to be very useful in studying the effect of inter-granular exchange interactions on the reliability of $\Delta H(M, \Delta M)$ method.

In this model, the PRM is modeled as a simple square or triangular lattice of symmetric hysterons with periodic boundary conditions. Under the assumptions that hysterons ($S_i = \pm 1$) have an intrinsic switching field distribution $D(H_{\mathrm{S}i})$ with $H_{\mathrm{S}i} > 0$, interact ferromagnetically with their nearest neighbors with strength J and experience a uniform external field H, the Hamiltonian of the system can be written as [1]

$$\mathcal{H} = -\sum_{<i,j>} J\, S_i S_j - \sum_i \Big(H + \mathrm{sgn}(S_i) H_{\mathrm{S}i} \Big)\, S_i \tag{8.1}$$

This model is referred to as the *interacting random hysteron model* (IRHM).

Note that the IRHM is very similar to the random field Ising model (RFIM):

$$\mathcal{H} = -\sum_{<i,j>} J\, s_i s_j - \sum_i (H + h_i)\, s_i \tag{8.2}$$

where the spins $s_i = \pm 1$ interact ferromagnetically with their nearest neighbors with strength J and experience a uniform external field H and a local quenched field h_i. For the RFIM, a local metastable dynamics has been introduced by Sethna *et al.* [89] to study the disorder-induced phase transition in the hysteretic

---

[1] The exchange coupling constant J has dimensions of energy. J measures the strength of one spin interacting with one of its nearest neighbors. The magnetic field H and the switching fields $H_{\mathrm{S}i}$ are also in units of J. Consequently, the disorder parameter σ is also in unit of J. Note that J is not normalized to the anisotropy field H_{k}. Actually, there is no independent H_{k} in our model, even though our switching field distribution mimics the H_{k} distribution of real recording media structures.

behavior at $T = 0$: Initially, all spins point down, as H is slowly increased from $-\infty$ to ∞ and decreased back to $-\infty$, each spin flips deterministically when its effective local field

$$h_i^{\text{eff}} = J \sum_j s_j + H + h_i \tag{8.3}$$

changes sign. For the IRHM, we introduce a similar local metastable dynamics at $T = 0$: Initially, all hysterons point down, as H is slowly increased from $-\infty$ to ∞ and decreased back to $-\infty$, each hysteron flips deterministically when its effective local field

$$H_i^{\text{eff}} = J \sum_j S_j + H + \text{sgn}(S_i)\ H_{\text{S}i} \tag{8.4}$$

changes sign. Considering the only slight difference between the RFIM and the IRHM, it is possible to introduce a simple mapping:

$$h_i \leftrightarrow \text{sgn}(S_i)\ H_{\text{S}i} \tag{8.5}$$

with $H_{\text{S}i} > 0$. This enables us to calculate the $M(H)$ curve of the interacting symmetric hysterons with the developed algorithms used for previous RFIM computational work at zero-temperature [89, 51]. The big advantage is that the system size we can study is much larger than that of the micromagnetic calculations at a room temperature [9]. Consequently, the noise level of data is lower and the statistics is better. The obvious disadvantage is that the thermal effects are completely ignored here. They are beyond the scope of the present study and should be the topic of future work.

Chapter 9

Effect of exchange interactions

In this chapter, we present numerical results calculated from the simple hysteron model (Eq. 8.1). We performed studies on both square lattice and triangular lattice of hysterons (grains) with periodic boundary conditions.

Note that we are ignoring dipolar interactions here, even though we know that they are substantial in real structures. But a previous micromagnetic study demonstrated that the dipolar interactions can very well be treated within the mean-field $\Delta H(M, \Delta M)$ method and do not cause any significant precision problems, while exchange interactions did [2, 9, 41]. Thus, we focus here on the effect of inter-granular exchange interactions only, because they represent the much more serious problem for the reliability of the $\Delta H(M, \Delta M)$ method. Effects of dipolar interactions will be presented later. Also, we are acutely aware of the fact that the assumption of a uniform exchange coupling constant J in Eq. 8.1 is a substantial simplification of the problem, if one compares our model to real materials structures. Again, including a distribution of J would be an extension of the present model and will be the topic of a later chapter.

9.1 Square lattice

Note that a square lattice is not necessarily a very good approximation of actual media structures [9], in which grains typically have coordination numbers of 5 or 6. However, in the section, we neglect this detail of actual media structures for reasons of simplicity.

With this model, we evaluate different types of $D(H_S)$ to study the reliability of the $\Delta H(M, \Delta M)$ method. In our simulation, we set the ferromagnetic nearest-neighbor coupling strength $J = 1$ and tune the disorder parameter σ. In our model, only the ratio σ/J is relevant. Setting $J = 1$ is just a standard and convenient way for simulations. Since $J = 1$, tuning σ is equivalent to tuning σ/J. In this sense, a small (big) σ corresponds to strong (weak) nearest-neighbor interactions of hysterons. We calculate the $M(H)$ curves, both major hysteresis loop and recoil curves, for system sizes up to 1000^2 and σ values from 1.6 to 1000.

To show that the $\Delta H(M, \Delta M)$ method fails reproducibly in a well-defined manner, we calculate $\Delta H(M, \Delta M)$ data sets for four different distributions:

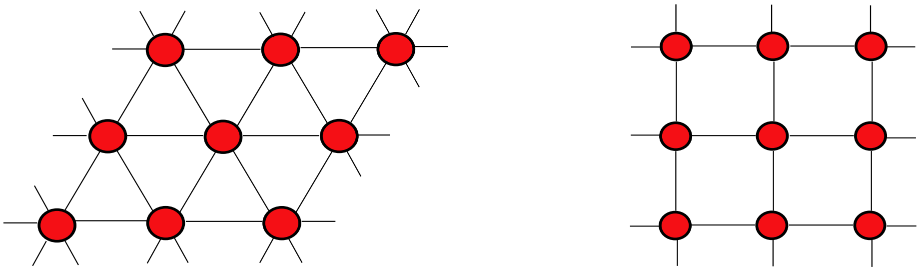

Figure 9.1: Triangular and square lattice in 2D.

Gaussian, Lorentzian, Lognormal, and truncated-Lorentzian. For all these distributions, we tune the disorder parameter σ from 1.6 to 1000, but keep the ratio h_0/σ to be a positive constant. This is done to avoid any negative switching fields, which would otherwise describe non-physical behavior in violation of the second law of thermodynamics. For a Gaussian, $h_0/\sigma = 5$ is generally big enough to avoid any negative H_S for system sizes of up to 1000^2. For a Lorentzian, we choose $h_0/\sigma = 5\times10^3$ for systems of size 100^2 and $h_0/\sigma \sim 2\times10^5$ for systems of size 1000^2. To avoid the long negative tails of the Lorentzian, we can truncate the distribution instead of choosing a huge h_0/σ ratio, creating a new type of distribution, which we refer to as truncated Lorentzian distribution $D_{\mathrm{L_t}}(H_\mathrm{S})$ in the following. For this $D_{\mathrm{L_t}}(H_\mathrm{S})$ distribution, we also choose $h_0/\sigma = 5$ in our calculations. For the Lognormal distribution, there is by definition no distribution density for negative fields. But we still choose $h_0/\sigma = 5$ to make it comparable with the Gaussian and the truncated Lorentzian distribution. [1]

We will show that even though the $\Delta H(M, \Delta M)$ method approximates the inter-granular interactions on the mean-field level, it can predict its own reliability correctly.

9.1.1 Comparison with the mean-field approximation

Key results of our numerical hysteresis loop calculations for all these different switching field distributions are shown in Figs. 9.7- 9.5. In each case, we show plots for $\sigma = 1.6, 5$ and 50 only to illustrate the general trends. All the calculations shown here are done in $2D$ with linear system size $L = 1000$, i.e. $L^2 = 10^6$ hysterons.

At first, we discuss the results for the Gaussian $D(H_\mathrm{S})$ distribution in detail. Fig. 9.7 displays the results for different σ's in different rows: (Top) $\sigma = 1.6$. (Middle) $\sigma = 5$. (Bottom) $\sigma = 50$. For each σ, we calculate a complete set of $M(H)$ curves, both the saturation hysteresis loop and recoil curves, as shown in the left column of Fig. 9.7. Note that here and throughout the paper, M (or

---

[1] The value of the constant h_0/σ is not relevant for checking the reliability range of the $\Delta H(M, \Delta M)$ method, as long as we have positive switching fields for all the hysterons.

ΔM) is normalized to the saturation value M_S and H (or ΔH) is normalized to the coercive field H_C. In particular, we choose 5 equally-spaced recoil curves, for which the distance to saturation is given by $\Delta M_i = i/3$. From the left column of Fig. 9.7, one can see that the hysteresis curves get broader for higher σ. Note that it is not the larger σ itself that causes this effect, because this type of broadening is taken out due to the normalization of H with H_C, and the constant h_0/σ ratio. [2] The difference in shape here actually reflects the fact that for lower σ, one gets correlated magnetization reversal which sharpens the macroscopic switching field distribution substantially.

In the middle column of Fig. 9.7, we show the corresponding $\Delta H(M, \Delta M)$ curves (solid lines) derived from the simulated $M(H)$ curves, as well as the mean-field approximation of the $\Delta H(M, \Delta M)$ curves (dotted lines) calculated from Eq. 7.5a. The mean-field curves are calculated by using the exact input parameter and are not least-squares fits. This allows for a clear illustration of the deviations from mean-field behavior. From Fig. 9.7(d), we see that for small σ (corresponding to strong hysteron interactions) the difference between the numerical result and the mean-field approximation is large. For intermediate σ (corresponding to intermediate hysteron interactions), the difference diminishes but is still visible, especially near the negative saturation $M = -1$, as shown in Fig. 9.7(e). For high σ (corresponding to weak hysteron interactions), the difference is so small that it is not visible in Fig. 9.7(f). It should be mentioned that due to the constant h_0/σ ratio and the normalization of ΔH, the mean-field $\Delta H(M, \Delta M)$ curves look almost identical for different σ's. Furthermore, it is apparent that the $\Delta H(M, \Delta M)$ curves obtained from numerical simulations are asymmetric, in particular for small σ. They show much larger deviations from the mean-field approximation on the left hand side, i.e. near negative saturation $M = -1$. This can also be seen in the hysteresis loops themselves, where the curves seem to bundle up near negative saturation for small σ values.

In the right column of Fig. 9.7, we show numerical values for the deviation from redundancy measures $r_{ij}(M)$ which are calculated from the simulated recoil curves shown in the left column. Due to the definition range of $r_{ij}(M)$, only the recoil curve pairs $(i, j) = (1, 2)$, $(1, 3)$, $(1, 4)$ and $(2, 3)$ produce data. From Fig. 9.7(g), we see that for small σ the deviation from data redundancy is quite substantial for the whole M definition range and for all the recoil curve pairs. For intermediate σ, the deviation becomes smaller but is still visible, as shown in Fig. 9.7(h). For high σ, the deviation is almost negligible in the whole M definition range and for all recoil curve pairs, as one can see from Fig. 9.7(i).

For the other $D(H_\mathrm{S})$ distributions, we observe very similar results as shown in Figs. 9.3–9.5. Thus, one has to realize that for small σ, i.e. strong hysteron

---

[2] This statement only makes sense if H_C and h_0 are very similar, which should be fulfilled as long as the hysteron coupling is not too strong and the main cause of hysteresis is the single hysteron hysteresis. In fact, in our simulations, we find that h_0 and H_C are almost identical (or very similar) for high σ. Moreover, one could make this an exact statement by normalizing H and ΔH to h_0.

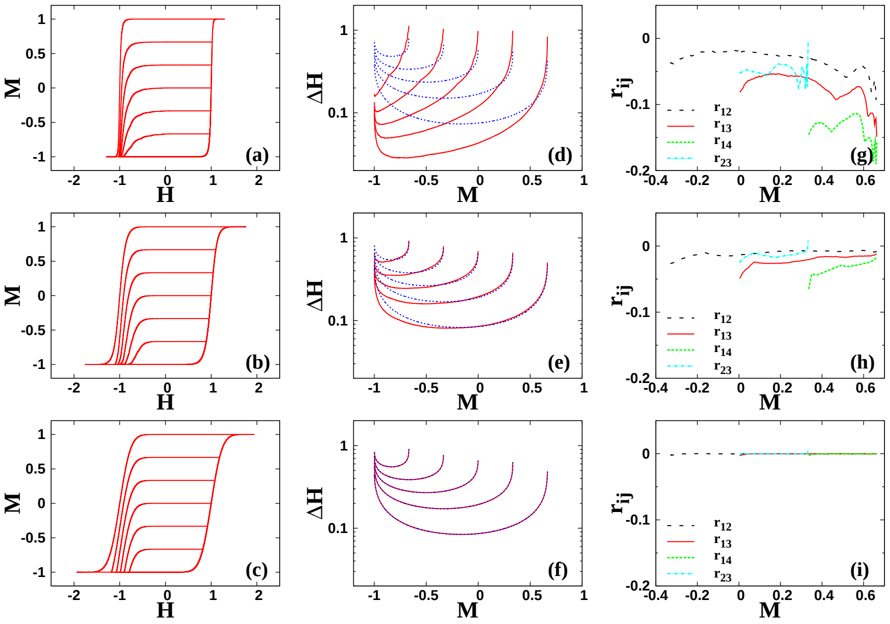

Figure 9.2: Numerical results using a Gaussian intrinsic SFD. Rows: (Top, fig.a,d,g): $\sigma = 1.6$. (Middle, fig.b.e.h): $\sigma = 5$. (Bottom, fig.c,f,i): $\sigma = 50$. Columns: (Left, fig.a,b,c): $M(H)$ curves, main loop and 5 recoil curves. (Middle, fig.d,e,f): $\Delta H(M, \Delta M)$ curves for the 5 recoil curves: (solid lines) numerical result; (dotted lines) mean-field approximation. (Right, fig.g,h,i): M-dependent deviation from redundancy ($r_{ij}(M)$) for all the possible recoil curve pairs.

interactions, the $\Delta H(M, \Delta M)$ method is not accurate. The mean-field approximation does not match the numerical result and deviations from redundancy are large. This is the expected result because once coupling dominates the magnetization reversal the mean-field approximation will not be valid any more. On the other hand, for large σ, i.e. weak hysteron interactions, the $\Delta H(M, \Delta M)$ method works very well, which is indicated by both the small deviation from redundancy and the match of the mean-field approximation to the numerical results.

9.1.2 Emergent feature of the $\Delta H(M, \Delta M)$ method

The similarities in the failure of the $\Delta H(M, \Delta M)$ method for different $D(H_S)$ distributions indicates that this method may be not very sensitive to the particular type of distribution in general. To study this further, we plot the reliability measures against the tuning parameter σ for all $D(H_S)$ distributions in Fig. 9.8.

The fit quality measures P_d and R^2 are shown in Fig. 9.8(a) and (b), respectively. We see that P_d approaches 0 with increasing σ, which means that for high σ, the input value of σ can be recovered with very high accuracy by fitting the $\Delta H(M, \Delta M)$ data to the mean-field fit function. In other words, the $\Delta H(M, \Delta M)$ method works well for high σ. Furthermore, we see that with in-

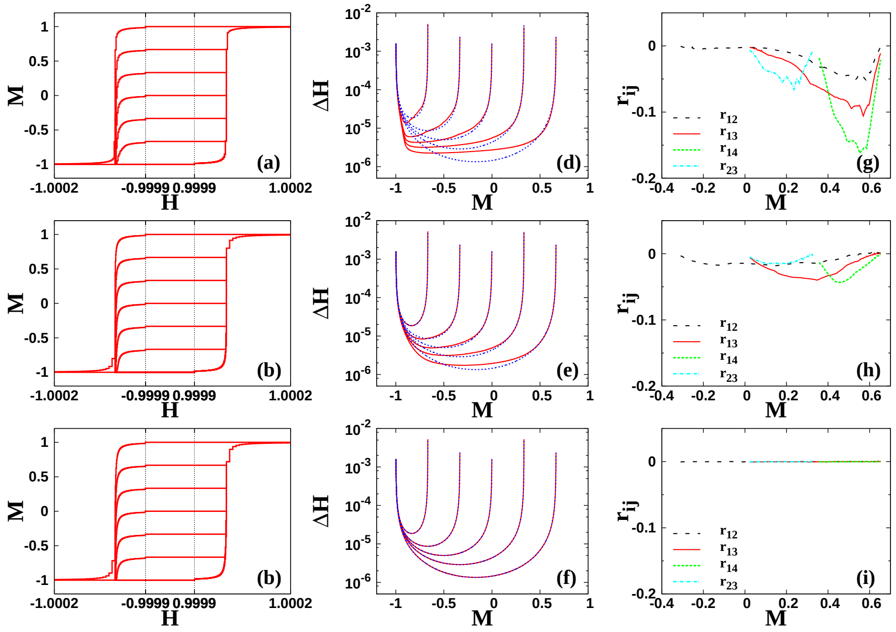

Figure 9.3: Numerical results using a Lorentzian intrinsic SFD. Rows: (Top, fig.a,d,g): $\sigma = 1.6$. (Middle, fig.b.e.h): $\sigma = 5$. (Bottom, fig.c,f,i): $\sigma = 50$. Columns: (Left, fig.a,b,c): $M(H)$ curves, main loop and 5 recoil curves. Note that due to the very large h_0/σ ratio ($\sim 2 \times 10^5$ for this system size 1000^2, chosen to avoid negative H_S), the differences between the major loop and all the recoil curves are extremely hard to see from the $M(H)$ plot itself. The small differences will be more clear with log scale as shown in the middle column. (Middle, fig.d,e,f): $\Delta H(M, \Delta M)$ curves for the 5 recoil curves: (solid lines) numerical result; (dotted lines) mean-field approximation. Here, we see that normalized ΔH values are very small compared to the Gaussian $D(H_\mathrm{S})$ case due to the large h_0/σ ratio. (Right, fig.g,h,i): M-dependent deviation from redundancy ($r_{ij}(M)$) for all the possible recoil curve pairs.

creasing σ, R^2 approaches 1 corroborating a successful fit of the $\Delta H(M, \Delta M)$ data in this regime. The average deviation from redundancy (r) is shown in Fig. 9.8(c). It is clearly seen that with increasing σ, r approaches 0, i.e. data redundancy is obtained, which is the key feature of the mean-field approximation.

The reliability range of the $\Delta H(M, \Delta M)$ method can be obtained from the reliability measures shown in Fig. 9.8. We find that for all the four $D(H_\mathrm{S})$ distributions, with the definitions of σ given in Sec. 7, the $\Delta H(M, \Delta M)$ method works virtually perfect for $\sigma \geq \sigma_0$ with σ_0 being approximately equal to 20. Here, σ_0 is just a rough criterion, above which the reliability measures have merged into their mean-field approximation values.

Note that in the original micromagnetic test [9], it is found that the $\Delta H(M, \Delta M)$ method is still valid for $\sigma/J \simeq 7.4$ in our notations. [3] However, due to the noise

---

[3] In Ref. [9], it is found that the $\Delta H(M, \Delta M)$ method is still valid for $H_\mathrm{ex} = 0.21 H_\mathrm{k}$ with $\sigma(H_\mathrm{k}) = 0.23$ (resulting in $\sigma(H_\mathrm{S}) \simeq 0.26$). Here H_ex is the exchange field and H_k is the

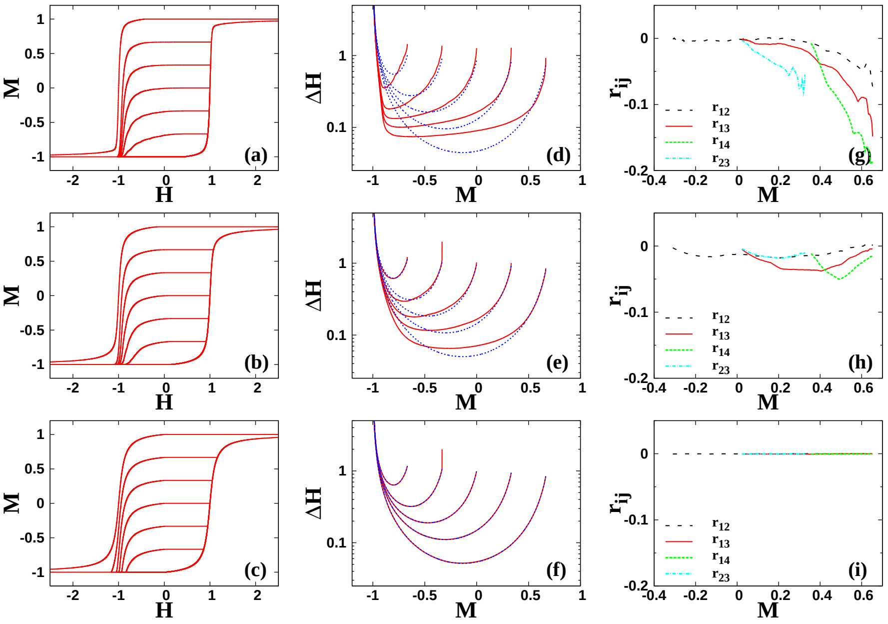

Figure 9.4: Numerical results using a truncated Lorentzian intrinsic SFD. Numerical results using a truncated Lorentzian intrinsic SFD. Rows: (Top, fig.a,d,g): $\sigma = 1.6$. (Middle, fig.b.e.h): $\sigma = 5$. (Bottom, fig.c,f,i): $\sigma = 50$. Columns: (Left, fig.a,b,c): $M(H)$ curves, main loop and 5 recoil curves. (Middle, fig.d,e,f): $\Delta H(M, \Delta M)$ curves for the 5 recoil curves: (solid lines) numerical result; (dotted lines) mean-field approximation. (Right, fig.g,h,i): M-dependent deviation from redundancy ($r_{ij}(M)$) for all the possible recoil curve pairs.

level of the micromagnetic calculations, R^2 is limited to 0.98 or smaller even in the best of circumstances there. If we check where R^2 becomes smaller than 0.98 in our calculations, then it is exactly in the same range of $\sigma/J = 7 \sim 8$. Thus, it is perfectly consistent with the previous work. Our calculations are much more sensitive and the statistic is much better, because we have much more particles in our calculation (10^6 hysterons) than the original micromagnetic work (1330 gains), demonstrating the clear advantage of our approach using the RSFHM.

It should be emphasized that the σ_0 values obtained from all three reliability measures are fairly consistent. If there are differences at all, r appears to show the highest sensitivity to deviations from the mean-field approximation, while R^2 seems to be slightly less sensitive. This is important, because r can be evaluated without any fit from a data set alone. So, the independent reliability test is the most sensitive measure and gives one confidence that not only the $\Delta H(M, \Delta M)$ method fails in a well-defined way, but also that one can very reliably check for this failure mode.

Finally, we note that the different r vs. σ curves in Fig. 9.8(c) for the different distribution types track each other almost exactly. However, this particular

---

anisotropy field. This result corresponds to $\sigma/J \simeq 7.43$ in our notations, assuming the grains have coordination numbers of 6.

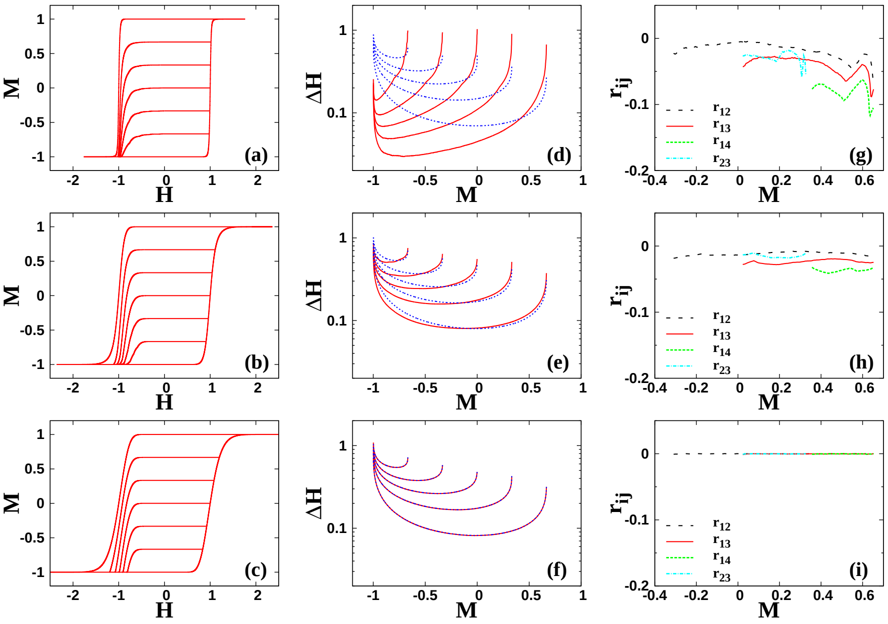

Figure 9.5: Numerical results using a Lognormal intrinsic SFD. Rows: (Top, fig.a,d,g): $\sigma = 1.6$. (Middle, fig.b.e.h): $\sigma = 5$. (Bottom, fig.c,f,i): $\sigma = 50$. Columns: (Left, fig.a,b,c): $M(H)$ curves, main loop and 5 recoil curves. (Middle, fig.d,e,f): $\Delta H(M, \Delta M)$ curves for the 5 recoil curves: (solid lines) numerical result; (dotted lines) mean-field approximation. (Right, fig.g,h,i): M-dependent deviation from redundancy ($r_{ij}(M)$) for all the possible recoil curve pairs.

observation dependents somewhat on how exactly we define σ in the various $D(H_\mathrm{S})$ distributions, because only for the Gaussian and Lognormal distribution are we using the natural definition given by the standard deviation. Thus, the curve collapse seen in Fig. 9.8(c) might be partially artificial. P_d and R^2 on the other hand do not exhibit such a collapse, not even for the Gaussian and Lognormal distributions as is apparent from Fig. 9.8(a) and (b). The fact that the two kinds of reliability measures show different behavior can be understood in the following way. As mentioned in the end of Sec. 7.2.1 and Sec. 7.2.2, finite size inaccuracies at the definition range boundaries of the recoil curves will not affect the calculation of r very much due to the cancellation effect. But it will affect the calculation of the fit quality measures, both P_d and R^2. Generally speaking, the shape of the hysteresis loops and recoil curves depends on the particular type of the chosen $D(H_\mathrm{S})$. Consequently, the finite size inaccuracies will also depend on $D(H_\mathrm{S})$. As a result, we see different (similar) behaviors of the fit quality measures (deviation from redundancy measure) for different $D(H_\mathrm{S})$ distributions at small σ. In this sense, it is natural to choose the deviation from redundancy measure r as the best measure to determine the reliability range of the $\Delta H(M, \Delta M)$ method.

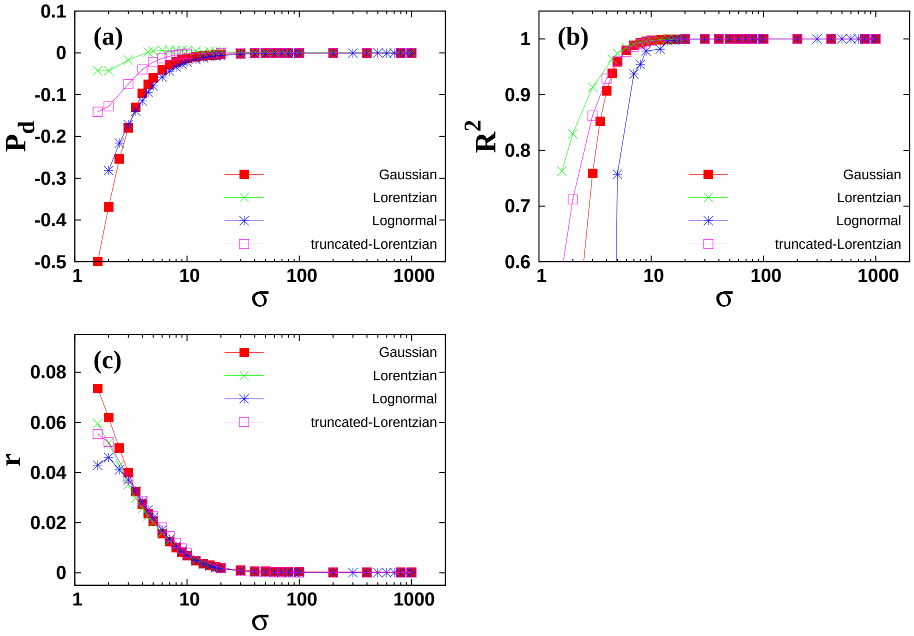

Figure 9.6: Reliability measures for the different $D(H_{\mathrm{S}})$ as a function of the distribution width σ: (a) P_{d}. (b) R^2. (c) r.

9.2 Triangular lattice

To furthermore show that deviations from a more realistic grain structure are not fundamentally altering the overall significance of our previous result, i.e. the $\Delta H(M, \Delta M)$ method fails reproducibly in a well-defined manner, we also analyze the $\Delta H(M, \Delta M)$ data for Gaussian intrinsic SFD on a $2D$ triangular lattice with 10^6 hysterons.

Key results of our numerical simulations are shown in Fig. 9.7. We show plots for $\sigma/J = 5$ and 50 only to illustrate the general trends. Fig. 9.7 displays the results for different σ/J's in different rows: (Top) $\sigma/J = 5$. (Bottom) $\sigma/J = 50$. For each σ/J, we calculate a complete set of $M(H)$ curves, both the saturation hysteresis loop and recoil curves, as shown in the left column of Fig. 9.7. Note that M (or ΔM) is normalized to the saturation value M_{S} and H (or ΔH) is normalized to the coercive field H_{C}. In particular, we choose 5 equally-spaced recoil curves, for which the distance to saturation is given by $\Delta M_i = i/3$ with i being an integer between 1 and 5. In the middle column of Fig. 9.7, we show the corresponding $\Delta H(M, \Delta M)$ curves (solid lines) derived from the simulated $M(H)$ curves, as well as the mean-field approximation of the $\Delta H(M, \Delta M)$ curves (dotted lines) calculated from Eq. 7.5a. The mean-field curves are calculated by using the exact input parameter, which allows for a clear illustration of the deviations from mean-field behavior. From Fig. 9.7(b,e), we see that as σ/J increases and the role of exchange interaction decreases, the difference between the numerical result and the mean-field approximation

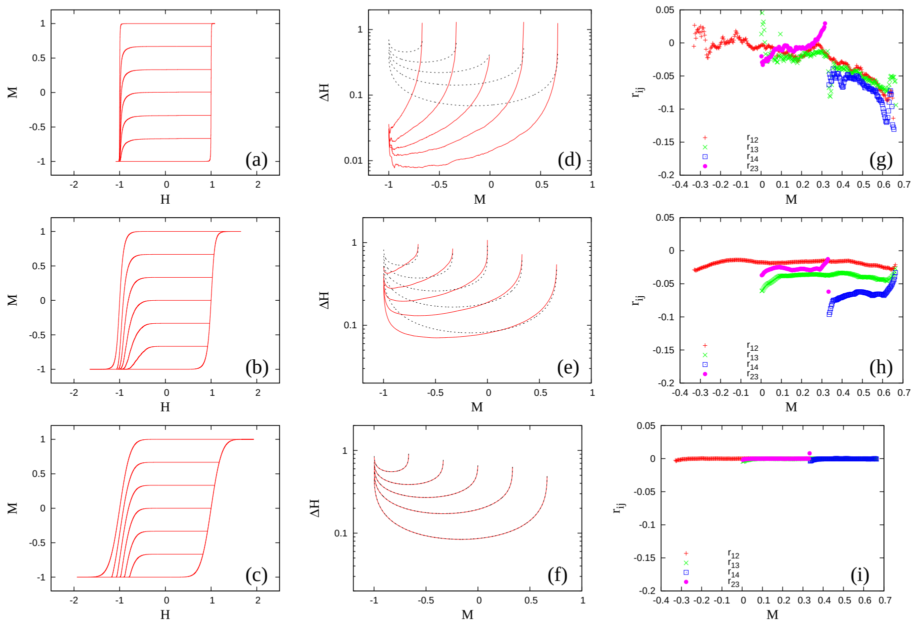

Figure 9.7: Numerical results for Gaussian intrinsic SFD on a 2D triangular lattice. (Top, fig.a,d,g): $\sigma = 1.6$. (Middle, fig.b.e.h): $\sigma = 5$. (Bottom, fig.c,f,i): $\sigma = 50$. Columns: (Left, fig.a,b,c): $M(H)$ curves, main loop and 5 recoil curves. (Middle, fig.d,e,f): $\Delta H(M, \Delta M)$ curves for the 5 recoil curves: (solid lines) numerical result; (dotted lines) mean-field approximation. (Right, fig.g,h,i): M-dependent deviation from redundancy ($r_{ij}(M)$) for all the possible recoil curve pairs.

becomes smaller. In the right column of Fig. 9.7, we show numerical values for the deviation from redundancy measures $r_{ij}(M)$ which are calculated from the simulated recoil curves shown in the left column. From Fig. 9.7(c), we see that for small σ/J the deviation from data redundancy is quite substantial in the entire M definition range and for all the recoil curve pairs. While for high σ/J, the deviation is almost negligible for all M values and all recoil curve pairs, as one can see from Fig. 9.7(f).

The results here are very similar to the results obtained from a $2D$ square lattice with Gaussian ISFD [58]. To study the reliability range of the $\Delta H(M, \Delta M)$ method quantitatively, we plot the three previously mentioned reliability measures against the tuning parameter σ/J for both square and triangular lattice in Fig. 9.8.

Firstly, we find that those measures show very similar features for the two different lattices. All three quantities approach their mean-field approximation values with increasing σ/J (decreasing exchange interaction), i.e. $P_\mathrm{d} \to 0$, $R^2 \to 1$ and $r \to 0$ as $\sigma/J \to \infty$. As expected, the $\Delta H(M, \Delta M)$ method works very well for high σ/J in the sense that the fit quality is excellent and data redundancy is obtained.

Secondly, a clear shift of the failure towards higher σ/J values is seen in the

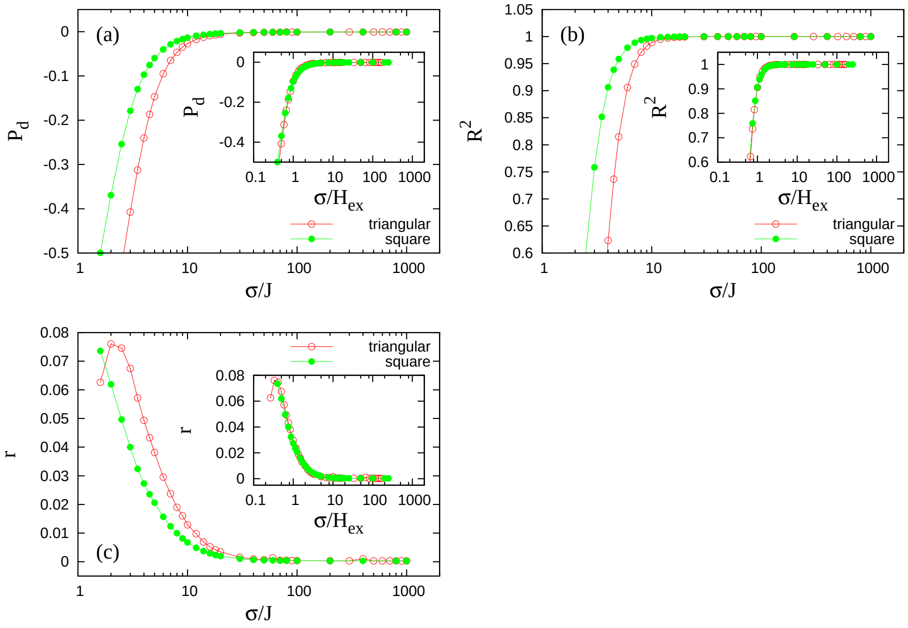

Figure 9.8: Reliability measures as functions of σ/J. (a) P_{d}. (b) R^2. (c) r. Insets show the reliability measures as functions of σ/H_{ex}. All the calculations are done for Gaussian ISFD on 2D lattices with 10^6 hysterons.

reliability measures of the triangular lattice. To understand this shift, one has to keep in mind that the total exchange field H_{ex} to which every grain is exposed in triangular lattice is on average 50% higher than in square lattice, simply because the number of nearest neighbors n in triangular lattice is 6 instead of 4 (see Fig. B.3). If we normalize for this effect, (defining $H_{\mathrm{ex}} = n\ J$), by the saturated magnetization state, we find that the curves of the reliability measures against σ/H_{ex} for the two different lattices collapse onto each other very well, as can be seen from the insets in Fig. 9.8. This collapse strongly indicates that the deviation of the reliability measures as functions of σ/J is only due to the difference in the total aggregate exchange effect upon each lattice site.

The reliability range of the $\Delta H(M, \Delta M)$ method can be quantified by determining at which point one of the reliability measures becomes smaller (or greater) than a certain value. For example, we find that $R^2 \geq 0.98$ when $\sigma/H_{\mathrm{ex}} \geq (\sigma/H_{\mathrm{ex}})_{\mathrm{c}}$. Here, we choose the measure R^2 and the certain value 0.98 specifically to compare it quantitatively with the earlier micromagnetic results [9]. In our calculations, we find $(\sigma/H_{\mathrm{ex}})_{\mathrm{c}} \simeq 1.5$ for both square and triangular lattice. In the original micromagnetic test [9], it is found that the $\Delta H(M, \Delta M)$ method is still valid (in the sense that $R^2 = 0.98$) for $H_{\mathrm{ex}} = 0.21$ with $\sigma(H_{\mathrm{k}}) = 0.23$ (resulting in $\sigma(H_{\mathrm{S}}) \simeq 0.26$) with all quantities given in units of the mean anisotropy field $\langle H_{\mathrm{k}} \rangle$. This yields $(\sigma/H_{\mathrm{ex}})_{\mathrm{c}} \simeq 1.24$, which is in rough agreement with our result here. The difference could be related to the fact that the micromagnetic calculations included dipolar effects, which by themselves do not impact the reliability of the $\Delta H(M, \Delta M)$ method, but cause a general broadening of magnetization curves. This could shift the onset of the exchange coupling caused failure towards lower σ values or higher levels of intergranular exchange coupling. However, this observed numerical difference could also be simply due to the noise level of the previously reported micromagnetic calculations. In these calculations, R^2 is limited to values near 0.98 even in the best of circumstances. In general, our calculations here exhibit much better statistics, simply because we have much more particles in our calculations (10^6 hysterons) than were used in the original micromagnetic work (1330 gains).

9.3 Summary

We study the $\Delta H(M, \Delta M)$ method and its reliability by means of numerical simulations of the zero-temperature interacting random hysteron model. We present strong evidence that the $\Delta H(M, \Delta M)$ method, which is based on the mean-field approximation, has a well-defined reliability range. This reliability range can be checked with two types of independent measures: deviation from redundancy and fit quality. The former is the superior tool because it is calculated from the data set alone and is independent from any inaccuracies that might be induced by data fitting procedures itself.

We also check that the failure mode of the $\Delta H(M, \Delta M)$ method is a universal property of this method and independent from the detailed lattice structure.

Chapter 10

Effect of dipolar interactions

The $\Delta H(M, \Delta M)$ method was demonstrated to have several advantages over comparable methods. For example, it allows for the determination of the entire $D(H_\mathrm{S})$ distribution and its functional form and not just a single characteristic parameter [2, 9]. In Chapter. 9, we have shown that: (1) it has a well-defined reliability range and it allows for oversampling, which makes self-consistency checks feasible [58]. (2) its failure mode was found to show universal behavior, independent from the detailed lattice structure in numerical simulations [57].

Despite these advantages, it is still unknown whether the reliability range of the $\Delta H(M, \Delta M)$ method with respect to exchange interactions might be affected by the simultaneous presence of dipolar interactions. Given the fact that this simultaneous presence of both interactions is the realistic case for actual recording media, it is an important issue, which we have studied in this chapter.

10.1 Hysteron model: consider dipolar interactions

Adding dipolar interactions into the RHS of Eq. 8.1, the model Hamiltonian turns to be

$$\mathcal{H} = -J_\mathrm{ex} \sum_{<i,j>} S_i S_j + J_\mathrm{dp} \sum_{i \neq j} \frac{S_i S_j}{r_{ij}^3} - \sum_i (H + \mathrm{sgn}(S_i) H_{\mathrm{S}i}) S_i \tag{10.1}$$

. Here, the first term represents that hysterons interact ferromagnetically with their nearest neighbors by means of exchange interactions of strength J_ex. The second term represents that hysterons exhibit a distance-dependent and anti-ferromagnetic dipolar interaction of strength J_dp with all other hysterons. Here, r_{ij} denotes the distance between hysteron i and j in lattice units. [1] Note that due to our restricted geometry with perfectly aligned perpendicular magnetization (representing high-anisotropy materials), dipolar effects cause an effective interaction that is anti-ferromagnetic in its nature. The third term accounts for

---

[1] The lattice constant by itself is not relevant in our model, because it is effectively included in J_dp. A quantitative comparison with real granular geometries can easily be done, if the corresponding Hamiltonian is written into a functional form similar to ours.

the effect of the external field and the intrinsic switching field.

The algorithm for the simulation of the major hysteresis loops and the corresponding recoil curves of this model has been described in the above section and Ref. [58]. For the numerical calculations of long-range dipolar interactions in a system with periodic boundary conditions, we utilized the efficient formalism described by Lekner [54]. For details, see App. B.

10.2 Results

10.2.1 Sheared $M(H)$ curves

For our numerical study of the $\Delta H(M, \Delta M)$ method's reliability, we assume a Gaussian distribution $D(H_{\mathrm{S}})$ of width σ for a two-dimensional square lattice comprising of total N hysterons. Different system sizes ranging from 50^2 to 400^2 have been studied to estimate finite-size inaccuracies. Results presented here were calculated for 100^2, which we found to be sufficiently precise in all cases. In our model Hamiltonian, J_{ex}, J_{dp}, H, H_{S} and σ all have dimensions of energy. And we set $\sigma = 1$ to be the unit of energy. We vary both J_{ex} and J_{dp}. For each parameter set (J_{ex}, J_{dp}), we calculate the complete set of $M(H)$-curves (both the saturation hysteresis loop and recoil curves), from which $\Delta H(M, \Delta M)$ data sets are then extracted.

The results displayed in Fig. 10.1 show several specific examples for parameter sets $(J_{\mathrm{ex}}, J_{\mathrm{dp}}) = (0.4,0)$, $(0.4,0.4)$ and $(0.4,0.8)$. The simulated $M(H)$ curves are shown in the left column. It is clearly seen that increasing the strength of dipolar interactions shears the hysteresis loops substantially as expected. The right column displays the corresponding $\Delta H(M, \Delta M)$ curves. The solid lines are the numerically extracted results from the simulated $M(H)$ curves while the dotted lines denote the mean-field behavior according to the expression of $\Delta H_{\mathrm{G}}(M, \Delta M)$. Comparing Fig. 10.1(d), (e) and (f), we find that dipolar interactions of intermediate strength make the system most mean-field like.

10.2.2 Contour plots of reliability measures

To study the effect of dipolar interactions on the $\Delta H(M, \Delta M)$ method's reliability in a more systematic and quantitative way, we need to introduce quantitative reliability measures. Obviously, the reliability range of the mean-field approximation, upon which the $\Delta H(M, \Delta M)$ method is based, can be checked by means of a least-squares fit of $\Delta H_{\mathrm{G}}(M, \Delta M)$ to the numerical data and a subsequent analysis of the conventional fit-quality measures, such as: (1) the square of the multiple correlation coefficient R^2 and (2) the percentage difference P_{d} between the fitting result and the input parameter σ. By definition, $R^2 = 1$ and $P_{\mathrm{d}} = 0$ would correspond to perfect data fitting, i.e. the exactness of the mean-field limit. We therefore calculated a least-squares fit to $\Delta H_{\mathrm{G}}(M, \Delta M)$ for the numerically extracted $\Delta H(M, \Delta M)$ data for each parameter set of $(J_{\mathrm{ex}}, J_{\mathrm{dp}})$.

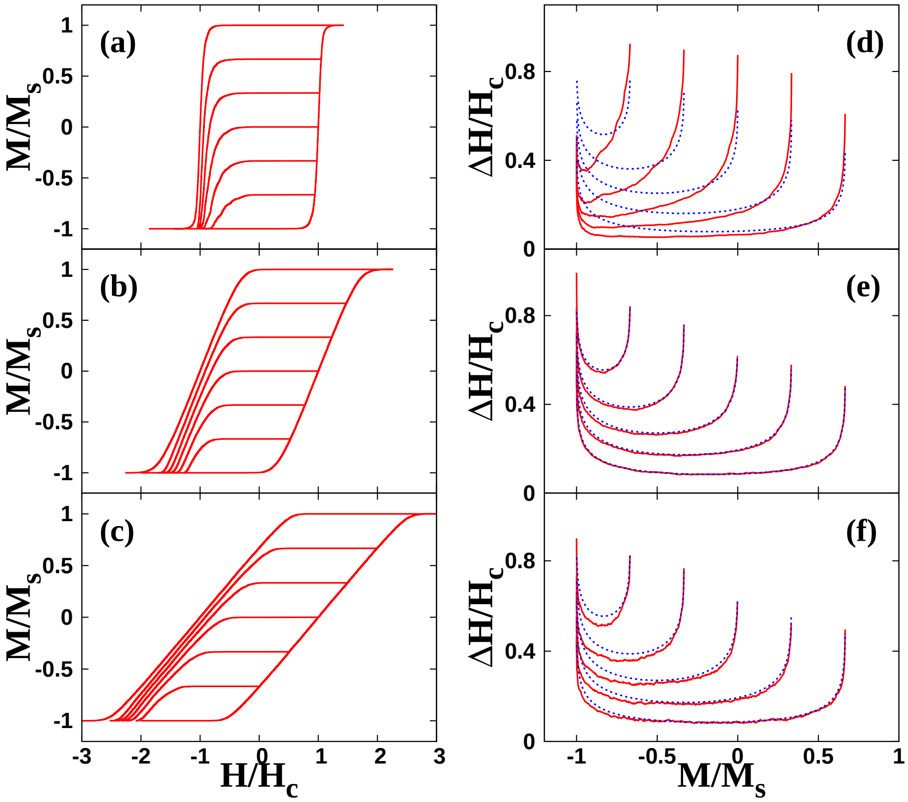

Figure 10.1: Using Gaussian $D(H_S)$ with width $\sigma = 1.0$ to calculate the $M(H)$ curves and $\Delta H(M, \Delta M)$ curves on a 2D square lattice with $N = 100^2$ hysterons and $J_{ex} = 0.4$. (a,d) $J_{dp} = 0$. (b,e) $J_{dp} = 0.4$. (c,f) $J_{dp} = 0.8$. (Left) $M(H)$ curves: main loop and 5 recoil curves. (Right) $\Delta H(M, \Delta M)$ curves for the 5 recoil curves: (solid lines) numerical result; (dotted lines) mean-field approximation. Here M (or ΔM) is normalized to the saturation value $M_S = N$ and H (or ΔH) is normalized to the coercive field H_C.

From these fits, we then computed both P_d and R^2. The results are shown in contour plots (see Fig. 10.2).

The shape of the contour plots is rather interesting. First, it is nearly symmetric along the diagonal direction, i.e. $J_{dp}/J_{ex} = 1$. This clearly demonstrates that the roles of exchange and dipolar interactions in determining $D(H_S)$ are almost equally important. Individually increasing either one will make the $\Delta H(M, \Delta M)$ method less reliable, while increasing both of them with proper strength ratio of order 1 will substantially extend the reliability range. Second, the shape is not really symmetric. It is tilted upwards and smoother on the high J_{dp} side than the high J_{ex} side. This suggests that the $\Delta H(M, \Delta M)$ method can clearly cope with higher dipolar interactions than exchange interactions, in agreement with previous micromagnetic tests [9].

The overall shape of the contours can be qualitatively explained by the *interaction compensation effect*. From the model Hamiltonian, we know that

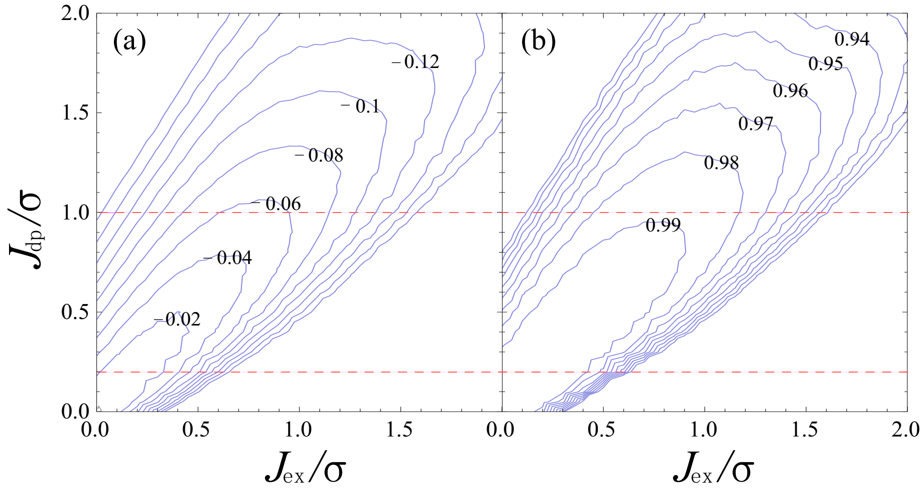

Figure 10.2: Contour plots of the fit quality measures as functions of J_{ex} and J_{dp}, both in units of σ. (a) P_{d}. (b) R^2. Dotted lines indicate the range of J_{dp}/σ for realistic materials.

the intergranular exchange interactions are ferromagnetic (FM) and short-range while the dipolar interactions are anti-ferromagnetic (AFM) and long-range. The competition between the two "opposite" interaction tendencies will yield a variety of system behaviors. Generally speaking, as we steadily increase J_{ex} from 0 to higher values while keeping J_{dp} constant, we shift the system from the AFM-interaction-dominated regime to the mean-field regime and to the FM-interaction-dominated regime. Only within the interaction compensation region, the FM and AFM interaction tendencies nearly cancel each other. Consequently, the system is most mean-field like and the $\Delta H(M, \Delta M)$ method becomes most reliable there. From the model Hamiltonian, we also notice that if $J_{\mathrm{ex}}/J_{\mathrm{dp}} = 1$, the exchange and dipolar interactions will cancel exactly for the nearest-neighboring hysterons which have $r_{ij} = 1$ in the lattice units. However, due to the long-range and distance-dependent features of dipolar interactions, this cancellation will not be exact for hysterons with longer distances. This explains why the interaction compensation region is only roughly symmetric along the diagonal direction.

10.2.3 Correlations between reliability measures

To quantify the interaction compensation region or equivalently the reliability range of the $\Delta H(M, \Delta M)$ method, one can define a critical value for each reliability measure, above which this method is sufficiently accurate. For example, we might define $R^2_{\mathrm{c}} = 0.98$ to be the critical value for R^2 in accordance with the best available experimental data [9]. Then the reliability range for the parameter set $(J_{\mathrm{ex}}, J_{\mathrm{dp}})$ can be clearly seen from the region enclosed by the second highest contour in the R^2 plot. This particular contour will be referred to as

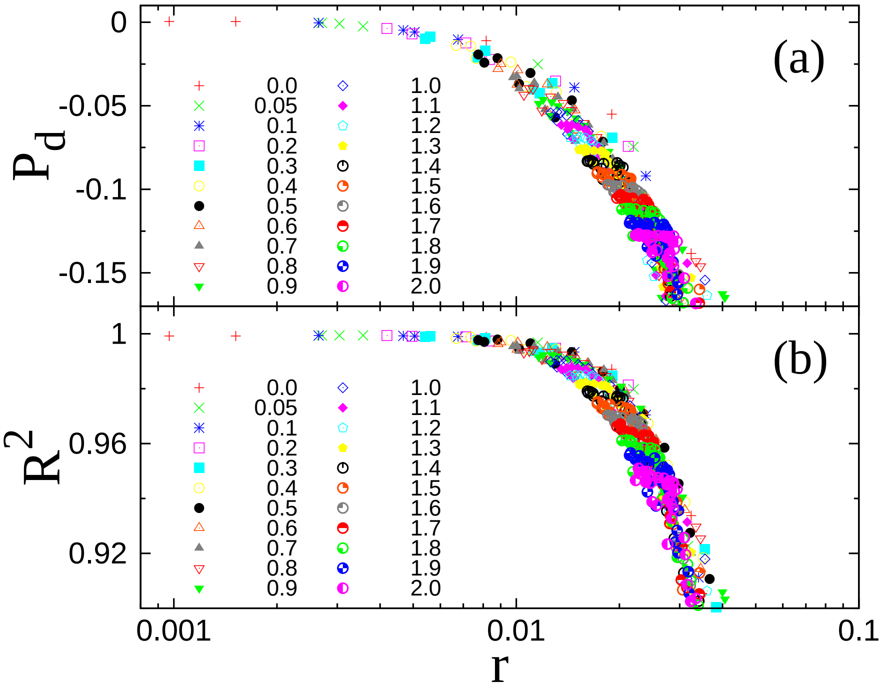

Figure 10.3: Correlations between the reliability measures: (a) $P_{\rm d}$ and r; (b) R^2 and r. Each data point represents a different parameter set ($J_{\rm ex}$, $J_{\rm dp}$). Data points with the same $J_{\rm dp}$ values are grouped and shown with the same point symbol, as indicated by the legend.

the critical contour, inside which the system is virtually mean-field like and the $\Delta H(M,\Delta M)$ method is reliable. Note that for practical recording media, the ratio of $J_{\rm dp}/\sigma$ will probably be limited within the range of $0.2 \sim 1$, which happens to have an overlap with the critical contour (see Fig. 10.2). [2] One can then easily see that within the realistic $J_{\rm dp}/\sigma$ range, the dipolar interactions improve the reliability range of the $\Delta H(M,\Delta M)$ method up to higher $J_{\rm ex}$ values. We also notice that for $J_{\rm ex}/\sigma \leq 0.2$ (read off from the intercept of the R^2 critical contour on the $J_{\rm ex}$-axis), higher dipolar interaction will only make the $\Delta H(M,\Delta M)$ method worse. But this part is very small compared to the part where dipolar interactions make the $\Delta H(M,\Delta M)$ method robust.

Besides the fit-quality measures R^2 and $P_{\rm d}$, there is a self-consistency-check measure, which is based upon data redundancy in between multiple recoil curves. One can test data for deviations from this redundancy by means of a quantity $r = \frac{1}{n}\sum_{i,j}\left\langle r_{ij}^2(M)\right\rangle^{\frac{1}{2}}$ where $r_{ij}(M)$ is by definition identical to zero within the mean-field approximation, so is r. The specific advantage of this quantity r is that it can be directly calculated from data sets alone without the need for any data fitting. Therefore, it is important to analyze the possible correlation between the fit-quality measure (either R^2 or $P_{\rm d}$) and the deviation-

---

[2] For the realistic range of $J_{\rm ex}/\sigma$, that's what nobody knows (or is supposed to know - Hitachi patent application), and is actually very tunable in reality.

from-redundancy measure r. Knowledge of this correlation will enable us to estimate the suitability of the $\Delta H(M, \Delta M)$ method without any data fitting. Considering this, we calculated r from the numerical $\Delta H(M, \Delta M)$ data for each parameter set of (J_{ex}, J_{dp}). Overall, the contour plot of r shows very similar features as of the ones being displayed in Fig. 10.2 for R^2 and P_{d}. To visualize and quantify the correlation between R^2 (P_{d}) and r, we plot R^2 (P_{d}) vs. r for the complete set of different (J_{ex}, J_{dp}) parameter (see Fig. 10.3). We find that the data collapse fairly well onto a single line in the high R^2 or low $|P_{\mathrm{d}}|$ range, in which the utilization of the $\Delta H(M, \Delta M)$ method is sensible and accurate. This indicates that R^2 and P_{d} are highly correlated with r in the regime where these quantities matter. Due to the knowledge of these correlations, one now has a criterion that enables a judgment on the usefulness and reliability of any $\Delta H(M, \Delta M)$-data set evaluation. For that, one simply determines the r value from experimental or modeling data sets, looks up the expected precision with the help of Fig. 10.3 and then decides if a further data analysis is warranted or not.

10.3 summary

In summary, we find that the presence of dipolar interactions similar in size to those of real PRM makes the $\Delta H(M, \Delta M)$ method substantially more precise and robust. The deviation-from-redundancy measure r, which is a self-consistency-check, is found to be a good predictor of the $\Delta H(M, \Delta M)$ method's reliability and can be utilized as a criterion to decide if a full scale data-analysis is warranted.

Chapter 11

Effect of nonuniform exchange and magnetostatic couplings

Recently, it has been shown that the microstructural disorder and the resulting randomness in exchange and magnetostatic inter-granular interaction have a detrimental effect on the performance of PRM. [94, 30, 72]

In real granular materials, the randomness in exchange couplings arises from irregularities at the grain boundaries, while the randomness in magnetostatic couplings results from the distribution of locations and volumes of the grains. Therefore, it is important to find a self-consistent approach to generating a realistic distribution of grains and the corresponding inter-granular interactions. The purpose of the present chapter is twofold. First, the aim is to develop a realistic model of the PRM that self-consistently accounts for locally varying random interactions while still allowing for the macroscopic hysteresis loop description of PRM. Secondly, the so developed model is subsequently used to address the question: to what extent can the presence of random interactions influence the proper determination of microscopic materials information, such as the intrinsic switching field distribution (SFD) $D(H_{\mathrm{S}})$?

11.1 Hysteron model: consider randomness in couplings

The model Hamiltonian introduced in the last chapter, i.e. Eq. 10.1, has been demonstrated to be very useful for understanding the applicability of the $\Delta H(M, \Delta M)$ method to PRM. [59] However, it has substantial deficiencies. First, mapping grains to structureless hysterons is of course the simplest mathematical construction, in which any effect due to the grain volume distributions is completely ignored. Second, the assumption of uniform exchange and dipolar couplings (J_{ex} and J_{dp}) is a substantial simplification of the real material structures. Due to microstructural disorder, such as irregularities at the grain boundaries, (or random locations and volumes of grains), there is a distribution of exchange (or magnetostatic) couplings between grains. Third, the dipole approximation is satisfactory for grains which are far away from each other. For grains which are close to each other, the dipole approximation will significantly overestimate the magnetostatic interactions, as reported in the literature. [52,85]

Considering all these deficiencies, and to systematically study the effect of non-uniform exchange and magnetostatic interactions on the reliability of the $\Delta H(M, \Delta M)$ method, we have generalized the above simple model, Eq. 10.1, in the following three aspects.

11.1.1 Non-uniform exchange couplings

For realistic PRM materials, the randomness in the inter-granular exchange couplings is determined mostly by the quality of the grain boundaries (or by an additional layer introducing a well defined amount of inter-granular interactions), while the randomness in magnetostatic interactions is determined by the grain volume distribution. Thus for all practical purposes, it is reasonable to view the probability distributions of inter-granular exchange and magnetostatic couplings as mutually uncorrelated. Therefore, for the modeling purposes, the two distributions can be generated using independent processes.

Correspondingly, we introduce randomness in the exchange couplings by simply choosing random bonds J_{ex}^{ij} from a Gaussian distribution with mean $\langle J_{\text{ex}}^{ij} \rangle \equiv J_{\text{ex}}$ and standard deviation $\sigma(J_{\text{ex}}^{ij}) \equiv R_{\text{ex}} J_{\text{ex}}$. The relative width of the random bond distribution R_{ex} will be called the randomness in the exchange couplings. The bond index $b = (ij)$ runs from 1 to $NZ/2$ with Z the coordination number of the embedded lattice. To make a good approximation of actual media structures in which grains typically have coordination numbers of $5 \sim 6$, we choose a triangular lattice of grains with constant coordination number $Z = 6$.

11.1.2 Non-uniform magnetostatic couplings

Due to the non-local nature of magnetostatic interactions, a self-consistent generation of random coupling constants J_{ms}^{ij} is a non-trivial task. In a first step, we represent the volume of a grain by a hexagonal prism with a side length $a/\sqrt{3}$ and height d (Fig. 11.1(a) and Fig. 11.5(b)). Thus the grains form a two dimensional assembly of thickness d with grains arranged on a triangular lattice of spacing a (Fig. 11.1(d) and Fig. 11.5(a)). Then we randomize volumes of grains by a random hexagonal tiling process (see below), in which the plane of the triangular lattice is randomly tiled with irregular hexagons on each lattice site (Fig. 11.1(e)). The height d remains the same for all grains. Note that this process guarantees that every grain has exactly six neighbors, which complies with the definition of non-uniform exchange interactions above.

The random hexagonal tiling (RHT) process is illustrated in Fig. 11.1(a-c). First we assume regular tiling case and draw a circle of radius $r = Pa/(2\sqrt{3})$ around every vertex of all regular hexagons. Then we randomly generate a point inside every such circle. These are the points that define locations of vertices of randomized hexagons. The randomized volumes, v_i, are calculated by multiplying the area of hexagons A_i by the height d. The extent of randomness can be controlled by the tuning parameter P, where $P = 0$ corresponds to regular hexagonal tiling case. As shown in Figs. 11.1(a-c), with increasing P, the grain becomes more and more irregular. Figs. 11.1(d-f) illustrate the corresponding deformation of the entire lattice.

It is interesting to study the correlation between the tuning parameter P and the grain volume distribution $D(v_i)$ generated by the described RHT. First of all, we plot the $D(v_i)$ obtained from RHT at different P values (see Fig. 11.2). Note that here we have normalized the grain volume v_i to the value of the regular tiling case which is just $v_0 = \sqrt{3}a^2d/2$. For $P = 0$, $D(v_i)$ corresponds to a δ-function. As P increases, we see that $D(v_i)$ becomes broader and more asymmetrical. Secondly, the tuning parameter P is correlated with the characteristics (moments) of the grain volume distribution $D(v_i)$, e.g. the mean, variance and skewness. To see this, we plot the moments of $D(v_i)$ as functions of P in Fig. 11.3. The first moment, i.e. the mean value, is always equal to unity (in units of v_0) no matter how randomly the hexagons are drawn (see Fig. 11.3(a)). This is because that the total area of grain assembly is conserved due to the periodic boundary conditions. The second moment (variance) of the distribution follows parabolic behavior (Fig. 11.3(b)). To confirm this, we also plot the standard deviation $\sigma(v_i)$ as a function of P. A straight line $\sigma(v_i) = 0.17P$ (in units of v_0) can fit the data very well (see Fig. 11.3(d)). For the third moment, i.e. the skewness, a positive value increases roughly linearly with P, which indicates that the $D(v_i)$ becomes more asymmetric with increasing P as seen in Fig. 11.3(c).

A self-consistent distribution of the magnetostatic couplings $D(J_{\mathrm{ms}}^{ij})$ is then naturally obtained by setting $J_{\mathrm{ms}}^{ij} = J_{\mathrm{ms}} v_i v_j / v_0^2$ with J_{ms} the magnetostatic coupling strength in the $P = 0$ limit, i.e. no randomness in grain volume distribution: $v_i = v_j = v_0$. Due to the long-range feature of the magnetostatic interaction, the index (ij) (with $i \neq j$) denotes here all grain pairs in the system.

11.1.3 Magnetostatic vs. Dipolar picture

To calculate the inter-granular magnetostatic interactions, we conduct the following procedures. Suppose we have a grain assembly with volume distribution $D(v_i)$ obtained by RHT, as shown in Fig. 11.5(a).

Generally, the magnetic scalar potential Φ_M of a given body, e.g. a media grain, with known magnetization $\boldsymbol{M}$ is given by

$$\Phi_M(\boldsymbol{r}) = -\int_{\mathrm{V}} \frac{\nabla \cdot \boldsymbol{M}(\boldsymbol{r'})}{|\boldsymbol{r} - \boldsymbol{r'}|}\, \mathrm{d}V' + \oint_{\mathrm{A}} \frac{\hat{\boldsymbol{n}} \cdot \boldsymbol{M}(\boldsymbol{r'})}{|\boldsymbol{r} - \boldsymbol{r'}|}\, \mathrm{d}A' \tag{11.1}$$

in the Gaussian c.g.s. system of units. Since in our model, we assume uniform magnetization inside each grain, the volume integral of the first term vanishes. Furthermore, since we consider the high anisotropy limit where magnetization of each grain can be aligned only along the z-axis, only the top and bottom surfaces will contribute to the surface integral of the second term. We define

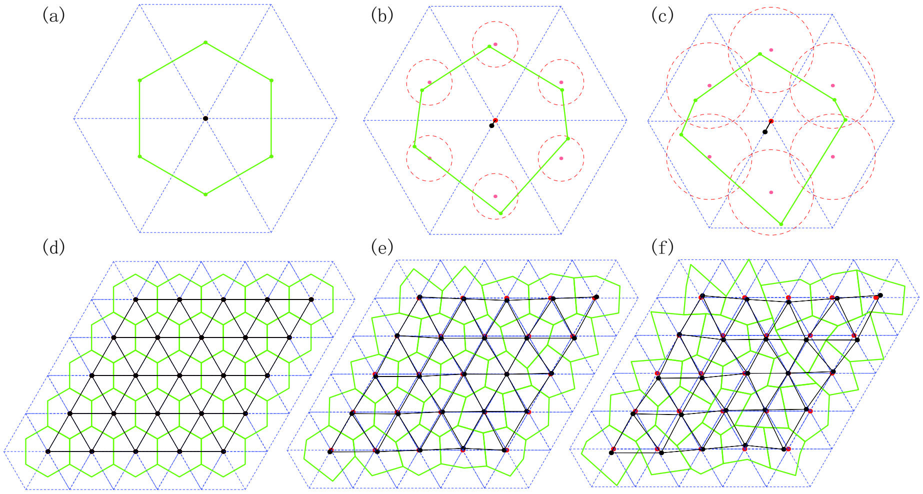

Figure 11.1: Random hexagonal tiling. Tuning parameter P varies the shape of a single grain and causes a non-uniform grain volume distribution for the grain assembly. (a,d) $P = 0$; (b,e) $P = 0.6$; (c,f) $P = 1.2$. In (b) and (c), the red dashed circle shows the permitted region of the grain vertices with radius $r = Pa/(2\sqrt{3})$. Here $a = 1$ is the lattice spacing. The grains are shown in green hexagons. The embedded triangular lattice of grains with periodic boundary conditions is shown in blue dashed lines. The bonds between lattice sites (or grain centroids) and their nearest neighbors are shown in blue (or black) solid lines. For $P > 0$, the grain centroids (black dots) become deviating the lattice sites (red dots). Only in the regular hexagonal tiling case ($P = 0$), as shown in (a) and (d), the grain centroids match the lattice sites.

the magnetostatic field produced by grain j as $\boldsymbol{H}_{M_j}(\boldsymbol{r}) = -\nabla\Phi_{M_j}(\boldsymbol{r})$. The magnetostatic energy between grain i and grain j can then be written as

$$\begin{aligned} U_{\mathrm{ms}}^{ij} &= -\frac{1}{2}\int_{V_i} \boldsymbol{M}_i \cdot \boldsymbol{H}_{M_j}\ \mathrm{d}V \\ &= \frac{1}{2}\boldsymbol{M}_i \cdot \int_{V_i} \nabla\Phi_{M_j}\ \mathrm{d}V \\ &= \frac{1}{2}\boldsymbol{M}_i \cdot \oint_{A_i} \Phi_{M_j}\hat{\boldsymbol{n}}_i\ \mathrm{d}A \\ &= \frac{1}{2}\oint_{A_i}\oint_{A_j} \frac{(\hat{\boldsymbol{n}}_i \cdot \boldsymbol{M}_i)(\hat{\boldsymbol{n}}_j \cdot \boldsymbol{M}_j)}{|\boldsymbol{r} - \boldsymbol{r}'|}\ \mathrm{d}A'\mathrm{d}A \end{aligned} \tag{11.2}$$

The coordinates of points in the top/bottom surface of grain i and grain j are (x,y,$\pm d/2$) and (x',y',$\pm d/2$), respectively. Then it is easy to check that

$$U_{\mathrm{ms}}^{ij} = \frac{1}{2}S_iS_jM_0^2\ \mathcal{I}(\boldsymbol{r}_i, \boldsymbol{r}_j; d). \tag{11.3}$$

Here, $\boldsymbol{M}_i = S_iM_0\hat{\boldsymbol{z}}$, $\boldsymbol{M}_j = S_jM_0\hat{\boldsymbol{z}}$ with $S_i, S_j = \pm 1$ and M_0 a material param-

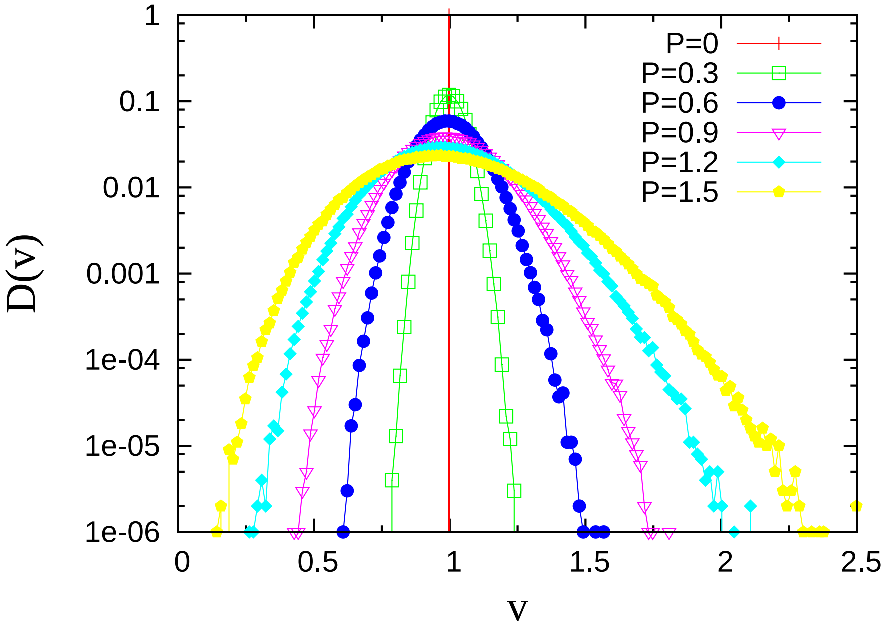

Figure 11.2: The normalized grain volume distribution $D(v)$ at different RHT parameter P on a triangular lattice with $L = 1000$ and $N = 10^6$ grains. Here v is in units of the mean grain volume v_0.

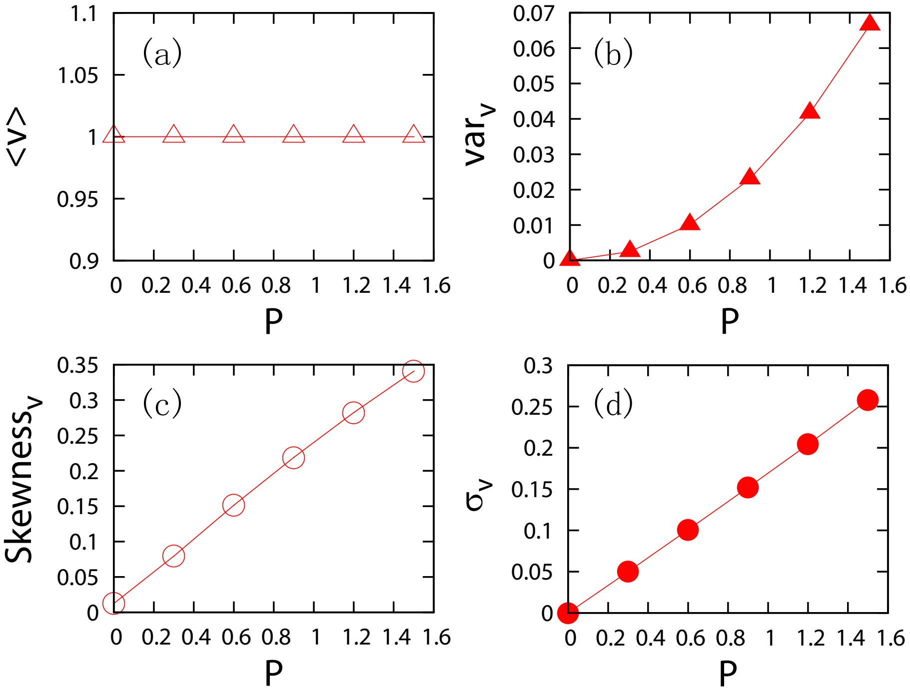

Figure 11.3: The mean, variance, skewness and standard deviation of the grain volume distribution $D(v)$ as functions of the RHT parameter P on a triangular lattice with $L = 1000$ and $N = 10^6$ grains. Here v is in units of the mean grain volume v_0.

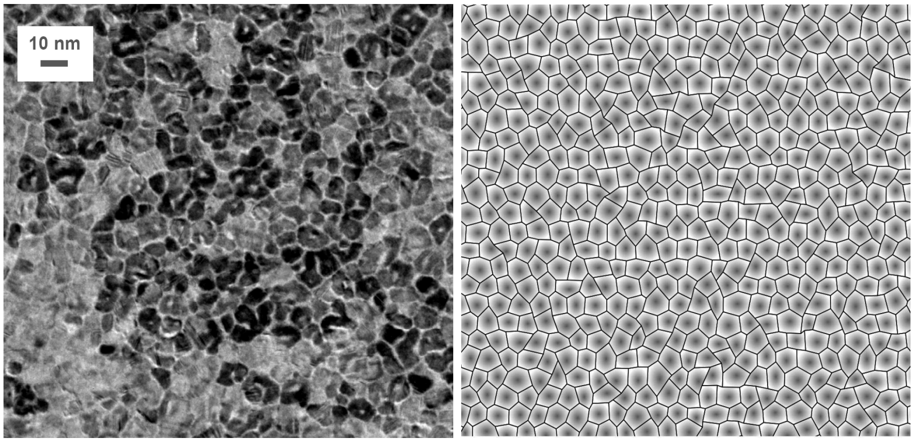

Figure 11.4: (left) Electron micrograph of media. (right) Grain assembly obtained by RHT with $P = 1.0$.

eter. The integral

$$\begin{aligned}\mathcal{I}(\boldsymbol{r}_i, \boldsymbol{r}_j; d) &= \iint\limits_{A_i} \mathrm{d}x\mathrm{d}y \iint\limits_{A_j} \mathrm{d}x'\mathrm{d}y' \; 2 \\ &\quad \cdot \left[\frac{1}{\sqrt{(x-x')^2+(y-y')^2}} - \frac{1}{\sqrt{(x-x')^2+(y-y')^2+d^2}} \right] \end{aligned} \tag{11.4}$$

is evaluated along the top surfaces (A_i and A_j) of the two grains with centroid coordinates $\boldsymbol{r}_i = (x_i, y_i, d/2)$ and $\boldsymbol{r}_j = (x_j, y_j, d/2)$, respectively.

In the limit that the two grains are far away from each other

$$\sqrt{(x_i - x_j)^2 + (y_i - y_j)^2} \equiv r_{ij} \gg d$$

the above integral can be calculated as:

$$\mathcal{I}(\boldsymbol{r}_i, \boldsymbol{r}_j; d) \approx A_i A_j \; 2(\frac{1}{r_{ij}} - \frac{1}{\sqrt{r_{ij}^2 + d^2}}) \approx \frac{A_i A_j d^2}{r_{ij}^3}$$

so that

$$U_{\mathrm{ms}}^{ij} \approx \frac{M_0^2 d^2 A_i A_j}{2a^3} \frac{S_i S_j}{\tilde{r}_{ij}^3} \equiv J_{\mathrm{ms}}^{ij} \frac{S_i S_j}{\tilde{r}_{ij}^3} \tag{11.5}$$

which is the dipole approximation. Here, $\tilde{r}_{ij} = r_{ij}/a$ is the reduced distance and J_{ms}^{ij} is naturally defined to be the magnetostatic coupling strength between grain i and j in the long distance limit:

$$J_{\mathrm{ms}}^{ij} = \frac{M_0^2 d^2 A_i A_j}{2a^3} = J_{\mathrm{ms}} \frac{A_i A_j}{A_0^2} = J_{\mathrm{ms}} \frac{v_i v_j}{v_0^2} \tag{11.6}$$

with $J_{\mathrm{ms}} = 3M_0^2 d^2 a/8$ being the magnetostatic coupling strength in the regular

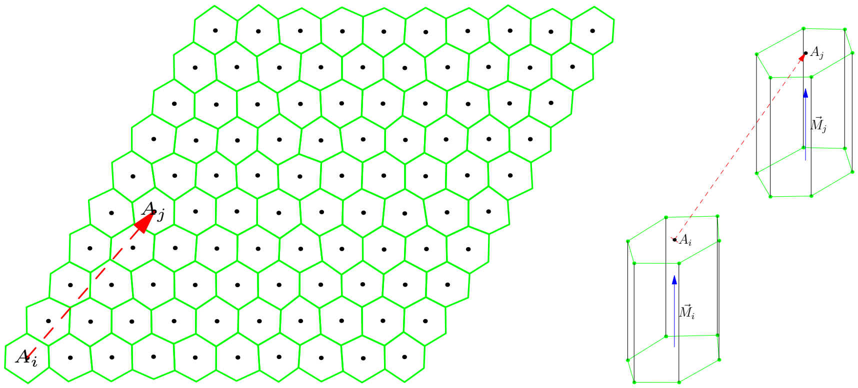

Figure 11.5: (left) A two-dimensional grain assembly (with $L = 10$ and $N = 100$) obtained by RHT with tuning parameter $P = 0.2$, which results in grain volume distribution $D(v)$ with $\sigma(v) \approx 0.035$. A particular grain pair is labeled with their surface area A_i and A_j. (right) Schematic 3D view of the chosen grain pair.

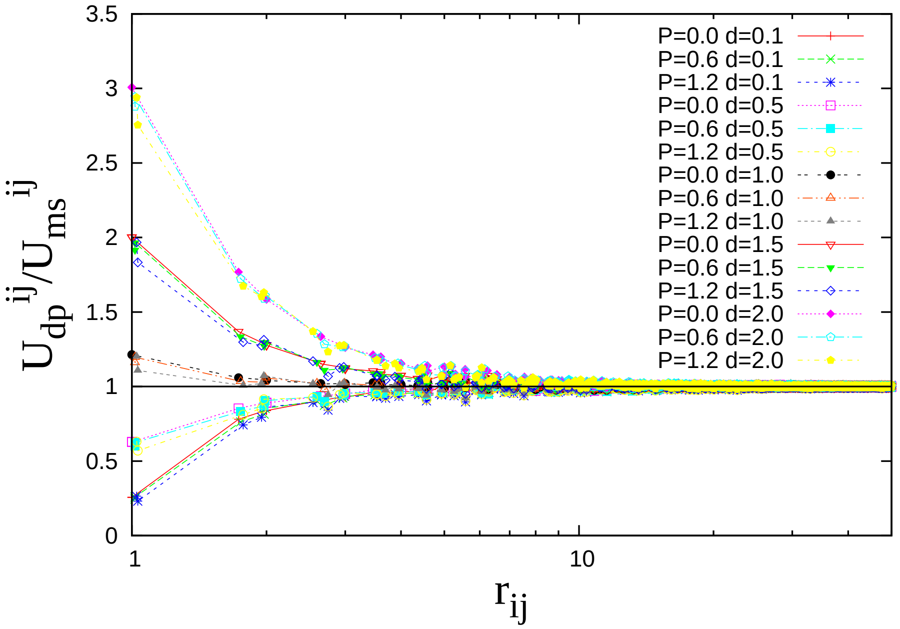

Figure 11.6: The ratio of the magnetostatic interactions between two grains calculated from Eq. 11.5 and Eq. 11.3, respectively, as a function of centroid distance r_{ij}, at various d and P. (Both r and d are in units of a.) Grains are chosen from a triangular lattice with $L = 100$ and $N = 10^4$.

hexagonal tiling case ($A_i = A_j = A_0 = \sqrt{3}a^2/2$). It is easy to recognize that J_{ms} is just the dipolar coupling constant J_{dp} used in our previous study. [59]

Having the complete magnetostatic solution, it is now possible to calculate how good the dipole approximation is. In Fig. 11.6, we show the ratio between the integration result calculated from Eq. 11.3 and the dipole-approximation result calculated from Eq. 11.5 as a function of r_{ij} (the distance between the two grains' centroids), for various d and P.

One sees that for $d = 2$, at $r = 1$, the dipole approximation overestimates the magnetostatic interaction by almost 200%. While for $d = 1$, at $r = 1$, the dipole approximation overestimates the magnetostatic interaction by only 20%. Note that in a previous work [85], the magnetostatic interaction energy of a three-dimensional array of ferromagnetic cubes was calculated and the authors showed that the dipole approximation for nearest neighboring cubes overestimates the magnetostatic energy by more than 17%, which is comparable to our result given the fact that we are using different grain shapes.

We define r_{c} to be the cutoff distance beyond which the magnetostatic interaction can be calculated with the dipole approximation, i.e $U_{\mathrm{dp}}/U_{\mathrm{ms}} \approx 1$ with less than 1% error. It is seen that r_{c} depends on d crucially. For example, for $d = 1$, $r_{\mathrm{c}} \approx 4$; for $d = 2$, $r_{\mathrm{c}} \approx 15$. (In our calculations, we set $d = 2$ and $r_{\mathrm{c}} = 20$.) We also find that varying the RHT parameter P will not change r_{c} too much. This is demonstrated by the collapse of the curves with same d but different P values. To save computing time, we explicitly calculate the exact magnetostatic interactions only for grains with distance $r < r_{\mathrm{c}}$, while for $r > r_{\mathrm{c}}$ grains are still treated as in the dipole approximations.

Considering all the above changes, the model Hamiltonian of the interacting random hysteron model can now be written as

$$\mathcal{H} = -\sum_{\langle i,j\rangle} J_{\mathrm{ex}}^{ij}\ S_i S_j + \sum_{i\neq j} \frac{1}{2} M_0^2\ \mathcal{I}(\boldsymbol{r}_i, \boldsymbol{r}_j; d)\ S_i S_j - \sum_i \left[H + \mathrm{sgn}(S_i) H_{\mathrm{S}i}\right] \tilde{v}_i S_i. \tag{11.7}$$

with $\tilde{v}_i = v_i/\langle v\rangle$ being the scaled grain volume. Note that in the absence of randomness in exchange and magnetostatic couplings and within the dipole approximation, the original Hamiltonian Eq. 10.1 is easily recovered from Eq. 11.7. The algorithm for the simulation of the major hysteresis loops and the corresponding recoil curves of this model is described in Ref. [58]. For the numerical calculations of long-range magnetostatic interactions in a system with periodic boundary conditions, we utilized the efficient Lekner formalism [54].

Calculate long-range magnetostatic interactions

In our previous study, the Lekner formalism was used to deal with the long-range dipolar interactions within a periodic system. [59] All grains were considered as dipoles there. In calculating the long-range dipolar interaction between grain i and j, we have to take into account the dipolar interaction between grain i

and j in the central simulation cell and the dipolar interactions between grain i in the central simulation cell and all the images of grain j in the image cells. Therefore, the dipolar interaction energy must be calculated as

$$U_{\mathrm{dp}} = J_{\mathrm{dp}} \sum_{\substack{i\neq j \\ \text{all cells}}} \frac{S_i S_j}{\tilde{r}_{ij}^3} = J_{\mathrm{dp}} \sum_{i,j} S_i S_j {\sum_{\boldsymbol{C}}}' \frac{1}{|\tilde{\boldsymbol{r}}_{ij} + \tilde{\boldsymbol{C}}|^3} \equiv J_{\mathrm{dp}} \sum_{i,j} S_i S_j \, \tilde{\mathcal{F}}_{ij}. \tag{11.8}$$

Here the $\boldsymbol{C}$-sum is over all the simulation cells. The prime on the $\boldsymbol{C}$-sum indicates that it is over all images of grain j except $\boldsymbol{C} = 0$ if $j = i$ because we assume that grain i interacts with all its periodic images, but not, of course, with itself. In the case that the central simulation cell is a two-dimensional lattice with rhombus shape of angle ψ and side length $L = \tilde{L}a$, one has $\boldsymbol{C} = (l + \beta m, \gamma m)\tilde{L}a = \tilde{\boldsymbol{C}}a$ with l, m integers, $\beta = \cos\psi$ and $\gamma = \sin\psi$. The $\boldsymbol{C}$-sum can then be written as

$$\tilde{\mathcal{F}}_{ij} = \tilde{L}^{-3} {\sum_{l,m=-\infty}^{\infty}}' \frac{1}{[(\xi_{ij} + l + \beta m)^2 + (\eta_{ij} + \gamma m)^2]^{\frac{3}{2}}} \tag{11.9}$$

with $\xi_{ij} = (x_i - x_j)/L$ and $\eta_{ij} = (y_i - y_j)/L$. Here the prism indicates that we omit the $l = m = 0$ term if $\xi_{ij} = \eta_{ij} = 0$. $\tilde{\mathcal{F}}_{ij}\tilde{L}^3$ can be efficiently calculated with the Lekner formalism, which converts the slowly convergent summation to a rapidly convergent one:

$$F_{\perp}(\xi,\eta) = \frac{2\pi^2}{\gamma^2 \sin^2(\pi\eta/\gamma)} + 8\pi \sum_{l>0} \sum_{m} \cos(2\pi l(\xi + \beta m)) \frac{l}{|\eta + \gamma m|} K_1(2\pi l|\eta + \gamma m|) \tag{11.10}$$

or

$$F_{\perp}(\xi,\eta) = \frac{2\pi^2}{\gamma^2 \sin^2(\pi\xi'/\gamma)} + 8\pi \sum_{m>0} \sum_{l} \cos(2\pi m(\eta' + \beta l)) \frac{m}{|\xi' + \gamma l|} K_1(2\pi m|\xi' + \gamma l|) \tag{11.11}$$

with $\eta' = \gamma\xi - \beta\eta$, $\eta' = \beta\xi + \gamma\eta$ and $K_\nu(z)$ is the modified Bessel function of the second kind [54, 32].

Similarly, in the magnetostatic-picture, the magnetostatic energy of the periodic system has to be calculated as

$$\begin{aligned} U_{\mathrm{ms}} &= \sum_{\substack{i\neq j \\ \text{all cells}}} \frac{1}{2} S_i S_j M_0^2 \, \mathcal{I}(\boldsymbol{r}_i, \boldsymbol{r}_j; d) \\ &= \sum_{\substack{i\neq j \\ \text{all cells}}} \frac{1}{2} S_i S_j M_0^2 a^3 \, \mathcal{I}(\tilde{\boldsymbol{r}}_i, \tilde{\boldsymbol{r}}_j; \tilde{d}) \\ &= \sum_{i,j} \frac{1}{2} S_i S_j M_0^2 a^3 {\sum_{\boldsymbol{C}}}' \mathcal{I}(\tilde{\boldsymbol{r}}_i, \tilde{\boldsymbol{r}}_j + \tilde{\boldsymbol{C}}; \tilde{d}) \end{aligned} \tag{11.12}$$

with $\tilde{d} = d/a$. At first glance, the $\boldsymbol{C}$-sum here is extremely complicated due to the four-dimensional integrals $\mathcal{I}(\tilde{\boldsymbol{r}}_i, \tilde{\boldsymbol{r}}_j + \tilde{\boldsymbol{C}}; \tilde{d})$. However, as discussed in Sec. 11.1.3, if $r_{ij} \geq r_{\mathrm{c}}$, these integrals can be calculated with the dipole approximation very well. Only when $r_{ij} < r_{\mathrm{c}}$, shall we deal with the integrals explicitly. Fortunately, this does not happen too often. As long as $r_{\mathrm{c}} \leq L/2$, it is easy to show that for grain i and grain j (and all grain j's images), if there is one pair which fulfills $r < r_{\mathrm{c}}$, then this is the only pair. Because grain j and all its images are separated by at least distance L. (This proof is very similar to that of the "minimum image criterion" used in the molecular dynamics simulation.) Therefore, we can easily correct the dipole approximation:

$$\sum_{\boldsymbol{C}}{}' \mathcal{I}(\tilde{\boldsymbol{r}}_i, \tilde{\boldsymbol{r}}_j + \tilde{\boldsymbol{C}}; \tilde{d}) = \sum_{\boldsymbol{C}}{}' \frac{\tilde{A}_i \tilde{A}_j \tilde{d}^2}{|\tilde{\boldsymbol{r}}_{ij} + \tilde{\boldsymbol{C}}|^3} - \frac{\tilde{A}_i \tilde{A}_j \tilde{d}^2}{\tilde{r}^3_{ij_{\min}}} + \mathcal{I}(\tilde{\boldsymbol{r}}_i, \tilde{\boldsymbol{r}}_{j_{\min}}; \tilde{d}) \tag{11.13}$$

with $\tilde{A}_i = A_i/a^2$, $\tilde{A}_j = A_j/a^2$. The first term, i.e. the dipole approximation, can be calculated within the Lekner formalism. The rest is the correction and can be easily calculated. Note that $j_{\min}$ denotes the minimal image of grain j which satisfies $r_{ij_{\min}} < r_{\mathrm{c}}$. For some pairs of grains, there are no such minimal images at all, which means we can safely use the dipole approximation without corrections. Otherwise, we just use Eq. 11.13 to calculate the magnetostatic interaction. In all cases, this can be done in advance and saved into a file for future use in the calculation of $M(H)$ curves.

It is useful to combine Eq. 11.12 and Eq.11.13 to derive

$$U_{\mathrm{ms}} = \sum_{i,j} J^{ij}_{\mathrm{ms}} S_i S_j \tilde{\mathcal{F}}'_{ij} \tag{11.14}$$

with

$$\tilde{\mathcal{F}}'_{ij} \equiv \tilde{\mathcal{F}}_{ij} - \frac{1}{\tilde{r}^3_{ij_{\min}}} + \frac{1}{\tilde{A}_i \tilde{A}_j \tilde{d}^2} \mathcal{I}(\tilde{\boldsymbol{r}}_i, \tilde{\boldsymbol{r}}_{j_{\min}}; \tilde{d}) \tag{11.15}$$

Comparing Eq. 11.14 with Eq. 11.8, one can easily see the modification we have done so far. In the limit that there is no microstructural disorder, one has $J^{ij}_{\mathrm{ex}} = J_{\mathrm{ex}}$, $\tilde{v}_i = 1$, and $J^{ij}_{\mathrm{ms}} = J_{\mathrm{ms}}$. Furthermore, if dipole approximation is used then $J_{\mathrm{ms}} = J_{\mathrm{dp}}$ and we have $\tilde{\mathcal{F}}'_{ij} = \tilde{\mathcal{F}}_{ij}$, i.e. the original Hamiltonian Eq. 10.1 is recovered from Eq. 11.7.

11.2 Results

For our numerical study of the $\Delta H(M, \Delta M)$ method's reliability, we assume a Gaussian distribution $D(H_{\mathrm{S}})$ of width σ for a two-dimensional triangular lattice comprising of total N grains. Different systems sizes ranging from $N = 50^2$ to 100^2 have been studied to estimate finite-size inaccuracies. In our model Hamiltonian, J^{ij}_{ex}, J^{ij}_{ms}, H, H_{S} and σ all have dimensions of energy. And we set $\sigma = 1$ to be the unit of energy.

The randomness in J^{ij}_{ex} is explicitly varied by tuning R_{ex}, the relative width of $D(J_{\mathrm{ex}}^{ij})$. In our simulation, we tune R_{ex} from 0 up to 0.2. Note that for a Gaussian $D(J_{\mathrm{ex}}^{ij})$ with positive mean, the ratio $R_{\mathrm{ex}} = \sigma(J_{\mathrm{ex}}^{ij})/\langle J_{\mathrm{ex}}^{ij}\rangle \leq 0.2$ is generally small enough for probability of finding negative J_{ex}^{ij} to be negligible and, therefore, the exchange coupling is always ferromagnetic in our simulations. The randomness in J_{ms}^{ij} is implicitly varied by tuning the RHT parameter P from 0 up to 1.2. Correspondingly, the relative width of the grain volume distribution $D(v)$, i.e. $R_{\mathrm{v}} \equiv \sigma(v_i)/\langle v_i\rangle \sim 0.17P$, is tuned from 0 to 0.2. Note that $0 \leq R_{\mathrm{ex}} \leq 0.2$ and $0 \leq R_{\mathrm{v}} \leq 0.2$ are the parameter ranges that are relevant for typical recording media. We set the grain height $d = 2a$. In calculating magnetostatic interactions, Eq. 11.3 is used for grains with distance $r < r_{\mathrm{c}} = 20a$ and Eq. 11.5 is used otherwise. We set the lattice spacing $a = 1$ to be the unit of length.

For every pre-defined randomness parameter set (P, R_{ex}), we tune both J_{ms} and J_{ex}. Note that J_{ms} denotes the magnetostatic coupling strength between two grains in the long distance and $P = 0$ limit. J_{ex} is mean value of the introduced $D(J_{\mathrm{ex}}^{ij})$. We calculate the complete set of $M(H)$-curves (both the saturation hysteresis loop and recoil curves), from which $\Delta H(M, \Delta M)$ data sets are then extracted.

11.2.1 $M(H)$ curves

The results displayed in Fig. 3.3 show several specific examples. The simulated $M(H)$ curves are shown in the left column. It is clearly seen that increasing the strength of magnetostatic interaction J_{ms} shears the hysteresis loops substantially as expected. The right column display the corresponding $\Delta H(M, \Delta M)$ curves. The solid lines are the numerically extracted results from the simulated $M(H)$ curves while the dotted lines denote the mean-field behavior according to the expression of $\Delta H_{\mathrm{G}}(M, \Delta M)$. Comparing Fig. 3.3(d1), (e1) and (f1), we find that magnetostatic interactions of intermediate strength make the system most mean-field like and consequently the $\Delta H(M, \Delta M)$ method is most reliable there, corroborating our earlier result. [59] On the other hand, comparing Fig. 3.3(e1) with Fig. 3.3(e2), we find that the presence of randomness in J_{ms} and J_{ex} slightly change the system behavior from mean-field like and consequently decreases the reliability of the $\Delta H(M, \Delta M)$ method somewhat.

11.2.2 Reliability Measures

We calculated a least-squares fit to $\Delta H_{\mathrm{G}}(M, \Delta M)$ for the numerically extracted $\Delta H(M, \Delta M)$ data for each parameter set of $(P, R_{\mathrm{ex}}; J_{\mathrm{ms}}, J_{\mathrm{ex}})$. From these fits, we then computed both P_{d} and R^2. The results are shown in contour plots in Fig. 11.8 and 11.9.

From the numerically extracted $\Delta H(M, \Delta M)$ data, the deviation from redundancy measure is directly calculated without the need for any data fitting. The results are shown in contour plots in Fig. 11.10.

Contour plots

The overall shape of the contour plots in the absence of interaction randomness has been qualitatively explained by the *interaction compensation effect*. [59] From the model Hamiltonian Eq. 11.7, we know that the inter-granular exchange interactions are ferromagnetic (FM) and short-range while the magnetostatic interactions are anti-ferromagnetic (AFM) and long-range. The competition between the two "opposite" interaction tendencies will yield a variety of system behaviors. The key point is that only when J_{ms} is comparable with J_{ex} can the magnetostatic and exchange interactions cancel most. Consequently, the system is most mean-field like and the $\Delta H(M, \Delta M)$ method is most reliable there. This parameter range is called the interaction compensation region or equivalently the reliability range of the $\Delta H(M, \Delta M)$ method. Individually increasing either one will make the $\Delta H(M, \Delta M)$ method less reliable, while increasing both of them with proper strength ratio will substantially extend the reliability range. This explains why the overall contour shape is nearly symmetric along the direction with $J_{\mathrm{ms}}/J_{\mathrm{ex}} \sim$ constant. The slight tilt of the ellipse upwards results from the fact that only the nearest neighbor interactions are compensated, but not the total interaction fields. Due to its long-range nature the total magnetostatic field actually dominates the exchange. However, due to the almost perfect suppression of the nearest neighbor interactions in this case, the correlation processes that produce deviations from mean-field behavior are effectively suppressed. This suggests that the $\Delta H(M, \Delta M)$ method can clearly cope with higher magnetostatic interactions than exchange interactions, in agreement with previous micromagnetic tests. [9]

Upon looking at the resulting structures in Figs. 11.8, 11.9, 11.10, we notice that the overall contour shape is nearly symmetric along the $J_{\mathrm{ms}}/J_{\mathrm{ex}} = 3$ direction. Note that in our previous study where the dipole approximation was used, we found the contour plot to be nearly symmetric along the $J_{\mathrm{dp}}/J_{\mathrm{ex}} = 1$ direction. From the Eq. 10.1 we notice that if $J_{\mathrm{dp}}/J_{\mathrm{ex}} = 1$, the exchange and dipolar interactions will cancel exactly for the nearest-neighboring grains, which have $\tilde{r}_{ij} = 1$. This partially explains why the contour plot is nearly symmetric along the $J_{\mathrm{dp}}/J_{\mathrm{ex}} = 1$ direction. In contrast to these earlier studies, we consider here the exact magnetostatic interaction (U_{ms}) instead of dipole interaction approximation (U_{dp}) for grains that are close to each other. In the case of $d/a = 2$, our calculation demonstrates that the dipole approximation is rather unreliable with $U_{\mathrm{dp}}/U_{\mathrm{ms}} \approx 3$ for the nearest neighbor grains ($\tilde{r}_{ij} = 1$). Correspondingly, J_{ms} needs to be about three times the size of J_{ex} to compensate the nearest neighbor grain interactions in the proper magnetostatic calculations. This explains why the contour is nearly symmetric along the $J_{\mathrm{ms}}/J_{\mathrm{ex}} = 3$ direction.

Secondly, we find that with increasing randomness in the couplings, the reliability range shrinks slightly but in a well-defined fashion. To quantify the shrink, one can define a critical value for each reliability measure, above which this method is sufficiently accurate. For example, we might define $P_{\rm d}^{\rm c} = -0.04$, $R_{\rm c}^2 = 0.99$, $r_{\rm c} = 0.012$ to be the critical value for $P_{\rm d}$, R^2 and r, respectively. These particular contours will be referred to as the critical contours, and marked with thick solid lines in our plots. We find that the areas of these critical contours keep decreasing upon increasing randomness in exchange and magnetostatic couplings. Moreover, in the limit that $P = 0$, i.e. uniform grain volumes and uniform magnetostatic couplings, the shrink of the critical contours upon increasing $R_{\rm ex}$ is faster than the $P > 0$ cases. Similarly, in the limit that $R_{\rm ex} = 0$, i.e. no randomness in the exchange couplings, the shrink of the critical contours upon increasing P is faster than the $R_{\rm ex} > 0$ cases. This behavior can be understood as above using the *interaction compensation effect* argument. In the case of one interaction type being uniform, the probability of canceling the contributions from the nearest neighbor interactions is smaller than the case of both interaction types being random. Because even though the first moment contributions from exchange and magnetostatic interactions might be equal, the second and higher moments of the coupling constant distributions will not be. In other words exact cancellation for nearest neighbors is very unlikely in this case. However, in case of random exchange and magnetostatic coupling constants, there exists a possibility for cancellation of even higher order moment contributions. Therefore, it is expected that the presence of randomness in both interaction types can actually improve performance of the $\Delta H(M, \Delta M)$ method compared to cases with either one interaction type being uniform.

Correlations

Overall, the contour plots of the three reliability measures show very similar features, which indicates that there could be correlations with each other. Moreover, as mentioned above, the deviation-from-redundancy measure r can be directly calculated from data sets alone without the need for any data fitting. Knowledge of a possible correlation between the fit-quality measure (either R^2 or $P_{\rm d}$) and the deviation-from-redundancy measure r will enable the estimation of the suitability of the $\Delta H(M, \Delta M)$ method even without any data fitting. Considering this, we plot R^2 vs. r, $P_{\rm d}$ vs. r and R^2 vs. $-P_{\rm d}$ for the complete data set of different $(P, R_{\rm ex}; J_{\rm ms}, J_{\rm ex})$, see Fig. 11.11. In order to show the trend more clearly, only three sets of $(P, R_{\rm ex})$ are shown here.

From Fig. 11.11(a) (or (b)), we find that in the absence of random couplings, i.e $(P, R_{\rm ex}) = (0, 0)$, the data points fall onto a fairly well-defined curve, in the high R^2 or low $|P_{\rm d}|$ range, where the utilization of the $\Delta H(M, \Delta M)$ method is sensible and accurate. This indicates that R^2 and $P_{\rm d}$ are highly correlated with r in the regime where these quantities matter, corroborating our earlier result. [59] One now has a criterion that enables a judgment on the usefulness and reliability of any $\Delta H(M, \Delta M)$-data set evaluation. In practice, one simply determines the r value from experimental or modeling data sets, looks up the expected precision with the help of the correlation plots Fig. 11.11 and then decides if a further data analysis is warranted or not. This procedure can be termed as the r-parameter quality control.

Upon adding randomness into J_{ex} and J_{ms} through increasing R_{ex} and P, the P_{d} vs. r (or R^2 vs. r) correlation is approximately preserved but the curve is slightly shifted to right. Also, the data spread has increased slightly illustrated by the increasing error bars. This right shift in the r-dependence of the fit qualities simply reflects the fact that increasing R_{ex} and P causes an elevated level of redundancy suppression, even though the $\Delta H(M, \Delta M)$ method still works well and gives precise fit parameters. This right shift also means that the r-parameter quality control still works and produces an even more stringent quality control test in the presence of non-uniform couplings.

From Fig. 11.11(c), we find that the data points fall onto fairly well-defined curves in spite of the presence of non-uniform couplings. This indicates that R^2 and P_{d} are highly correlated with each other and this correlation is not affected by the randomness of couplings.

11.3 Summary

In summary, we developed an interacting random hysteron model, which self-consistently accounts for the local variations of exchange and magnetostatic interactions and their correlations with the geometrical distribution of grains in magnetic recording media. We used the so developed model to generate hysteresis loop data for different interaction magnitudes and different amounts of the randomness and performed an identification analysis aimed at extracting intrinsic switching field distribution from the hysteresis loops. The conventional $\Delta H(M, \Delta M)$ -methodology has been used as an extraction tool. We find that, even in the presence of locally varying exchange and magnetostatic couplings, the switching field distribution can be determined by means of the $\Delta H(M, \Delta M)$ method, however, with a somewhat reduced accuracy. The strong and robust correlations among the reliability measures gives a natural r-parameter quality control procedure, which can be utilized as a criterion to decide if a full scale data-analysis is warranted, even in the case of non-uniform couplings.

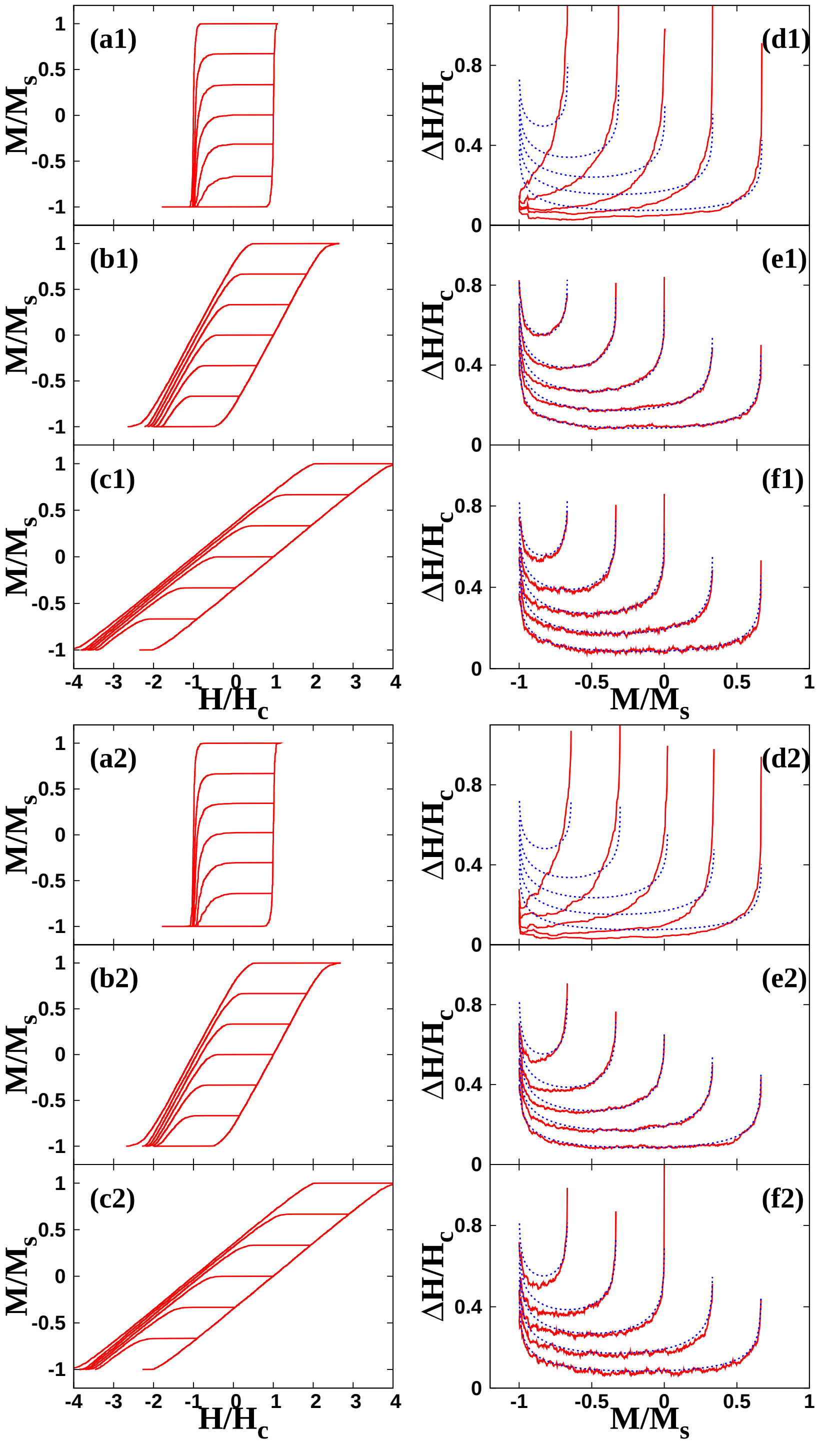

Figure 11.7: Using Gaussian $D(H_{\mathrm{S}})$ with width $\sigma = 1.0$ to calculate the $M(H)$ and $\Delta H(M, \Delta M)$ curves on a 2D triangular lattice with $N = 50^2$ grains and $J_{\mathrm{ex}} = 0.4$. (a1,$\cdots$,f1) $P = 0$, $R_{\mathrm{ex}} = 0$. (a2,$\cdots$,f2) $P = 1.2$, $R_{\mathrm{ex}} = 0.2$. (a1,d1;a2,d2) $J_{\mathrm{ms}} = 0.01$. (b1,e1;b2,e2) $J_{\mathrm{ms}} = 1.2$. (c1,f1;c2,f2) $J_{\mathrm{ms}} = 2.5$. (a1-b1-c1;a2-b2-c2) $M(H)$ curves: main loop and 5 recoil curves. (d1-e1-f1;d2-e2-f2) $\Delta H(M, \Delta M)$ curves for the five recoil curves: (solid lines) numerical result; (dotted lines) mean-field approximation. Here M (or ΔM) is normalized to the saturation value $M_{\mathrm{S}} = N$ and H (or ΔH) is normalized to the coercive field H_{C}.

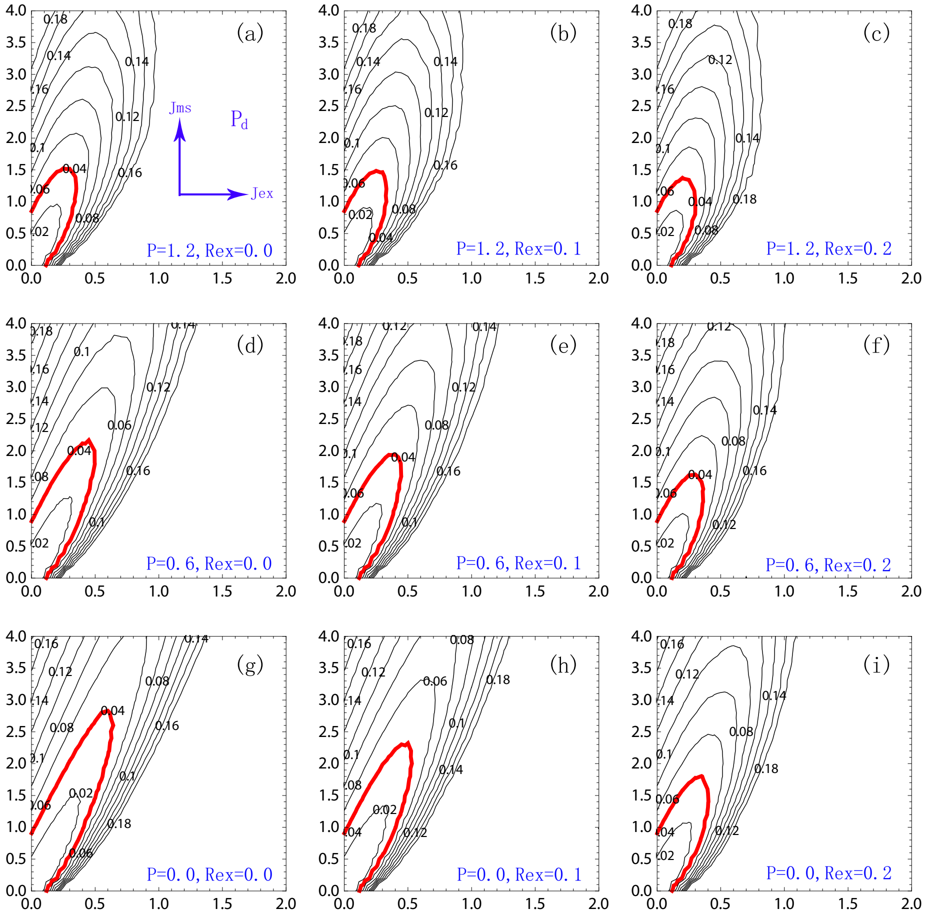

Figure 11.8: P and $R_{\rm ex}$ dependent contour plots of the reliability measure P_d. The critical contour with $P_{\rm d}^{\rm c} = -0.04$ is marked with thick solid lines.

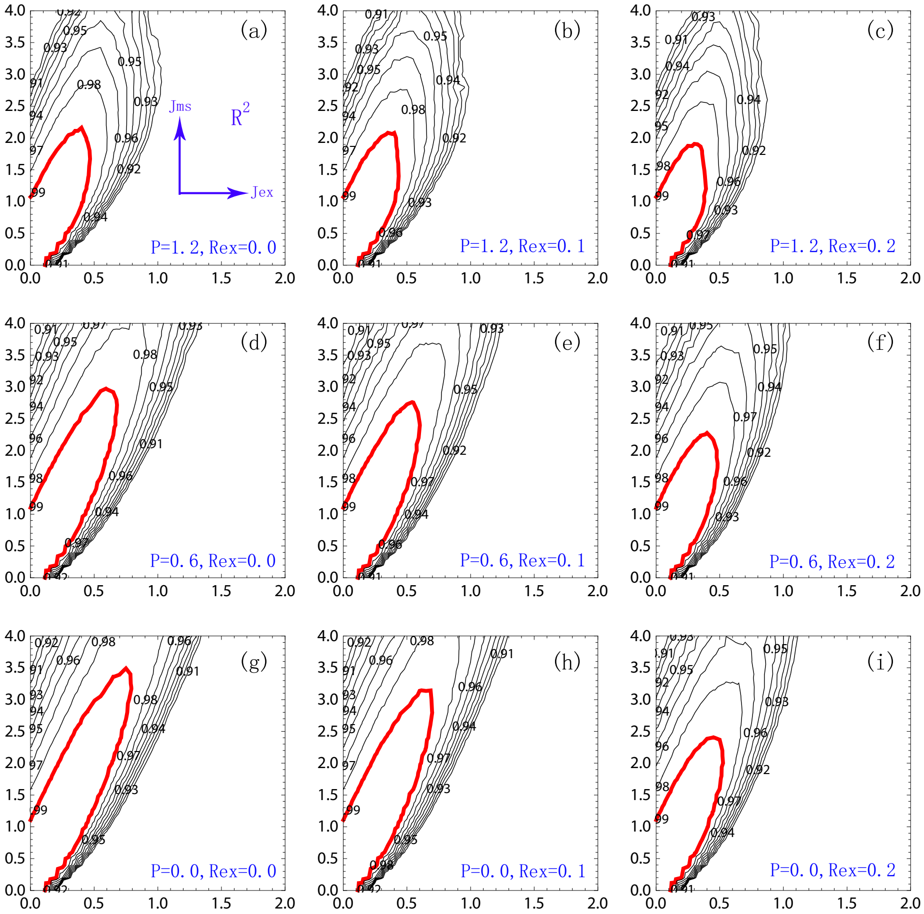

Figure 11.9: P and R_{ex} dependent contour plots of the reliability measure R^2. The critical contour with $R_{\mathrm{c}}^2 = 0.99$ is marked with thick solid lines.

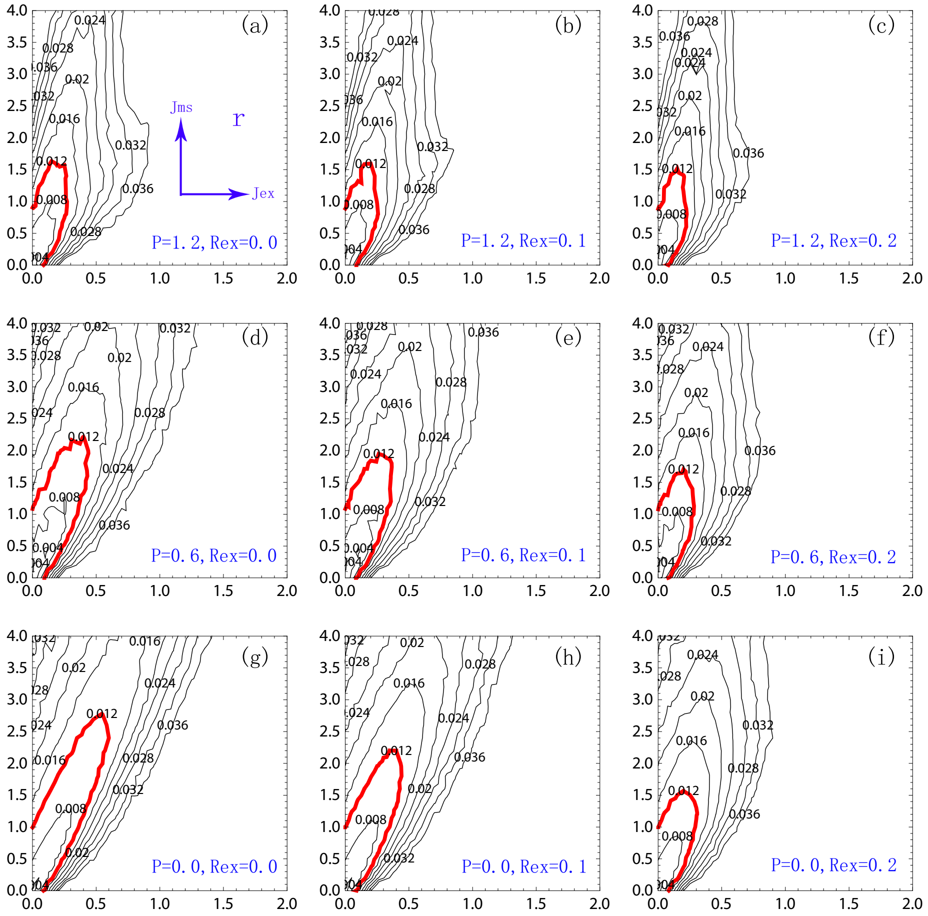

Figure 11.10: P and R_{ex} dependent contour plots of the reliability measure r. The critical contour with $r_{\mathrm{c}} = 0.012$ is marked with thick solid lines.

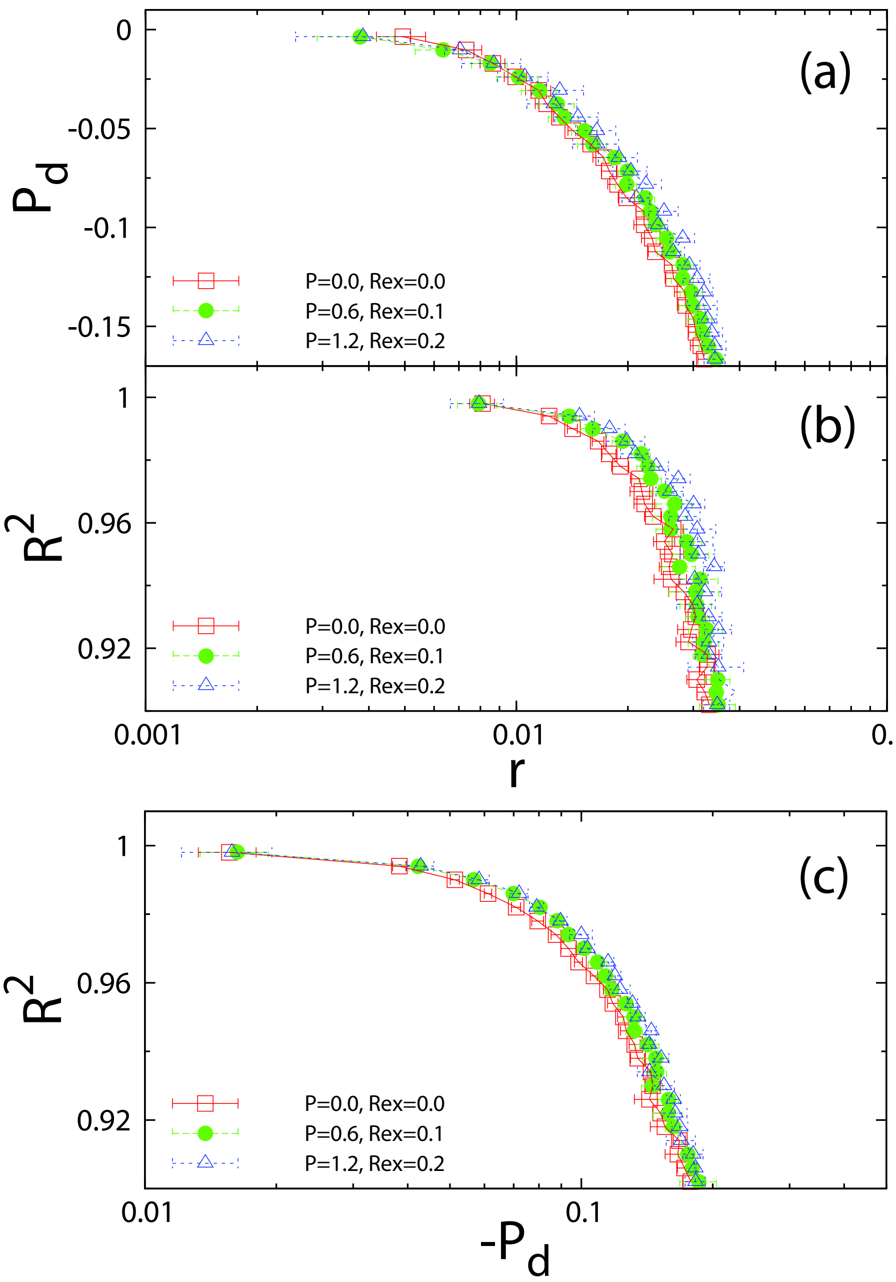

Figure 11.11: Correlations between the reliability measures: (a) $P_{\rm d}$ and r; (b) R^2 and r; (c) R^2 and $-P_{\rm d}$. Data points with the same $(P, R_{\rm ex})$ value are grouped and shown with the same symbol, as indicated by the legend. In these $Y(X)$-correlation plots, we calculate the average X values within linear Y-bins. The error bars present the 95% confidence interval, i.e. $\pm 2\sigma$.

Appendix A

Algorithms

A.1 Droplet Analysis

The Droplet Analysis code was originally developed by A. A. Middleton for the full 3D RFIM solution code. It takes ASCII description of spin configurations and outputs their "cluster" and "domain" descriptions and the depth of the configuration. Here, "clusters" are simply connected regions while "domains" are the volumes enclosed by the domain walls. Domains incorporate subdomains in their structure. The number of levels of nesting of the spin clusters is defined to be the "depth" of the full spin configuration. Here is a 2D example:

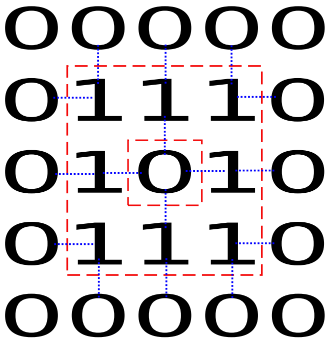

```
00000
01110
01010
01110
00000
```

Figure A.1: ASCII description of spin configuration of a 2D lattice. The symbol '1' ('0') indicates an up (down) spin. Domain walls are indicated by dotted lines.

The result of the Droplet Analysis code follows:

```
cluster_count: (up/down) volume/surface/boxvol/maxdim
0:  (0)  16/12/25/5
1:  (1)  8/16/9/3
2:  (0)  1/4/1/1
Domain_count: (up/down) volume/surface/boxvol/maxdim
1:  (1)  9/12/9/3
2:  (0)  1/4/1/1
Depth=2
```

This spin configuration has 3 clusters, of volume(size) 16, 8, and 1, with surface areas of 12, 16, and 4 (4 nearest neighbors in 2D) respectively, and maxdim (maximal lengths) of 5, 3, and 1, and "box volumes" (volume of smallest box enclosing the cluster) of 25, 9, and 1.

The domains would be the "infinite" outer domain (chosen to be the largest cluster), which is NOT reported. What is reported is the first domain wall (volume and box volume of 9, surface area 12, and linear dimension 3), the second domain wall (surrounding the central spin) of area 4, and value 1 for the volume, box volume and dimension. The nesting of spin clusters can also be seen here. And the depth is 2.

For each simply connected cluster, its volume v is just the size of the cluster, i.e. the number of spins in this cluster, which *excludes* the volume of the possible "holes" of opposite spin. The surface area a of the cluster is defined to be the number of unsatisfied nearest neighbor bonds that separate the cluster from its *surrounding* region of opposite spin, which *includes* the surface of the possible "holes" of opposite spin.

For each domain, its volume is defined as the number of spins that are enclosed by the outermost surface of the domain (treating the possible holes inside as if they were filled). And the surface area is just the area of the outermost surface, i.e. it does not include the surface of subdomains.

It is trivial to get the connected cluster information for a given spin configuration. However, it is not easy to get the domain wall information due to the possible subdomains, i.e. "holes". In the Droplet Analysis code, the domain walls are determined by working recursively inwards from the majority (down) spin cluster. This is done by labeling all connected spin clusters. The algorithm follows:

1. Determine and label all connected spin clusters (trace out droplet surfaces).
2. Start from the largest cluster with index Q and volume Q_{vol}. Relabel it with index -1.
3. While Q_{vol}(number of spins with index -1) is less than the system volume V,
    (a) Find all the clusters whose indices are NOT -1. These clusters form domains and they could have holes (different spin values) inside themselves.
    (b) Determine their volume and surface area. Report these (in this way, we get the domain volume and domain surface in this depth).
    (c) In this depth, find all the connected clusters (same spin value) which are touching with the cluster of index -1. Add their volume to Q_{vol} (though not same spin value with the cluster of index -1) and relabel those connected clusters with index -1.
    (d) depth++.

(e) Do (a) until $Q_{\text{vol}} = V$, i.e. until we get the deepest level.

Note that here we have assumed that the spin value of the majority cluster is down and the majority cluster is the outermost cluster. For spin configurations that this condition is not valid, special attention should be given to get the correct domain wall information.

A.2 Hysteresis Loop

A.2.1 Hysteresis Loop without long-range interactions

Kuntz et al. developed three different algorithms to study the ztne-RFIM based on the single-spin-flip dynamic rule — spin flips when its local field changes sign. Due to the inherent sequential nature of the dynamics and the absence of thermal fluctuations, all these algorithms have a basic algorithmic loop: scanning the lattice for nucleation sites and then propagating an avalanche.

The three algorithms in order of increasing complexity are: **brute-force**, **sorted-list** and **bits**.

- The brute-force searches through the entire lattice with N sites to find each nucleation site (A nucleation site is the next unstable spin in the external driving field is raised adiabatically slowly). Since there are $\mathcal{O}(N)$ avalanches in a saturation hysteresis loop, the runtime scaling for the brute-force algorithm is $\mathcal{O}(N^2)$.

- The sorted-list algorithm uses a clever pointer construct to find nucleation events that diminishes the number of operations each spin is involved in from $\mathcal{O}(N)$ to $\mathcal{O}(1)$ during the simulation. As a result, the asymptotic run-time scaling of the sorted-list algorithm is due to the sorting of the list (i.e., $\mathcal{O}(N \log N)$).

- The bits algorithm was developed to minimize the amount of memory required in the simulation. It achieves this by taking advantage of the fact that, in the saturation loop, it is not necessary to store the random fields of the spins. Instead they can be generated, when needed, at the interface of propagating fronts. The asymptotic runtime scaling for the bits algorithm is fixed by the search for nucleation events and is bounded below by $\mathcal{O}(N \log N)$. Despite being comparable in asymptotic scaling to the sorted-list algorithm the bits algorithm is, in practice, significantly slower than the sorted list algorithm but allows for roughly $8X$ larger system sizes.

Efficiency in the simulation of the ztne-RFIM is borne out of the nearest neighbor only interaction and the correspondingly local relaxations to metastable states. Moreover, for monotonic field histories a spin, once flipped, need never be flipped again. This property has been taken advantage of by Kuntz et al. in these algorithms.

Brute-Force

The brute-force algorithm is the easiest one to implement and is competitive for system sizes up to about 10,000 spins. In this method, we store a spin direction and a random field for each site of the lattice.

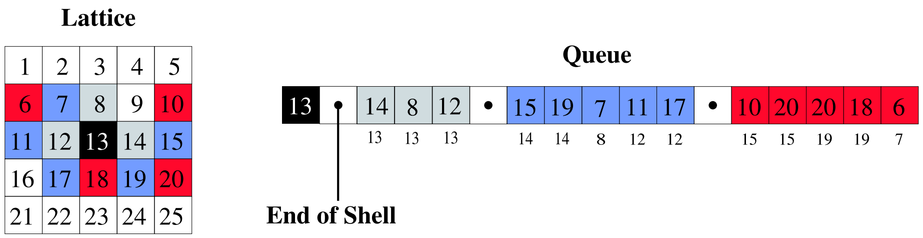

Figure A.2: Use a FIFO queue to propagate avalanche (related to cluster flips in Wolff algorithm).

This algorithm follows:

1. Find the triggering spin for the next avalanche by checking through the lattice for the unflipped site with the largest internal field $h_i^{\mathrm{int}} = h_i^{\mathrm{eff}} - H$.
2. Increment the external field so it is just large enough to flip the site, and push the spin onto a first-in first-out (FIFO) queue.
3. Pop the top spin off the queue.
4. If the spin has not been flipped, flip it and push all unflipped neighbors with positive local fields onto the queue.
5. While there are spins on the queue, repeat from step 3.
6. Repeat from step 1 until all spins are flipped.

The FIFO queue and a propagating avalanche are shown in Fig. A.2.

Sorted-List

The brute force method is very inefficient at locating the origin of the next avalanche, and we are immediately led to think of storing the several largest local fields in each sweep. If we take this thinking to its logical conclusion, we are led to store a list of all of the spins in the system, sorted according to their random fields. Unfortunately, life is complicated by the fact that spins experience not only their local random fields, but also fields from their neighbors.

Case 1: Zero sweeprate ($\Omega = 0$).

Beginning the simulation of the saturation loop with all spins pointing down, the sorted-list algorithm consists of the following:

1. Initialize an array of N double variables representing the local random field of the $N = L^d$ spins on the hypercubic lattice. Sort the array by increasing random field.
2. Define an array nextPossible[$n_\uparrow$], $n_\uparrow = 0, 1 \ldots z$, which points to the location in the sorted list of the next spin which would flip if it had $n_\uparrow$ neighbors. Initially, all the elements of nextPossible[$n_\uparrow$] point to the spin with the largest local random field, h_i.

3. Choose from the $z+1$ spins pointed to by nextPossible, the one with the largest total local field. The total local field will be negative because the external field has not been increased since step 2.
4. Move the pointer nextPossible[$n_\uparrow$] selected in step 3 to the next spin on the sorted list.
5. If that spin actually has $n_\uparrow$ up neighbors, increment the field to just flip that spin, push the spin onto a first in first out (FIFO) queue, and hence nucleate an avalanche. If not, to go back to step 3. It is important to note here that this step is the only step in which the external field H changes.
6. Pop spin off the FIFO queue.
7. If the spin has not been flipped, flip it and push all unflipped neighbors with positive local fields onto the queue.
8. As long as the size of the FIFO queue is greater than zero, loop back to step 6.
9. Repeat from step 2 until all spins in the lattice are flipped.

To ensure that the temporal flip order is maintained, an end of shell (EOS) marker is pushed onto the FIFO queue to keep track of the order in which the spins are flipped. For example, suppose that the nucleating spin occurs at t_n. The spins it causes to flip at t_{n+1} are pushed onto the queue followed by an EOS marker m_1. After the spins that flip at t_{n+1} are popped off the queue and potentially cause other spins to flip, m_1 is popped of the queue and m_2 is pushed on. The spins now in the queue represent the spins that flipped due to shell 2. Surprisingly the asymptotic scaling derives from the first step of the algorithm. Sorting the list of N random fields takes $\mathcal{O}(N \log N)$ time steps while all other aspects of the algorithm scale, at most, with the system size, $\mathcal{O}(N)$.

Case 2: Finite sweeprate ($\Omega > 0$).

When the external field is allowed to increase during the propagation of an avalanche the basic algorithmic loop has to be modified. The purely sequential and local dynamics forced by the nearest neighbor interaction and adiabatic increase in the external field are replaced by a hybrid dynamics in which the external field can nucleate other avalanches throughout the lattice as causally related avalanches propagate. Fortunately the sorted-list algorithm was easily augmented to allow for this change. The modified algorithm for the finite sweeprate, sorted-list algorithm is as follows:

1. Initialize an array of N double variables representing the local random field of the $N = L^d$ spins on the hypercubic lattice. Sort the array by increasing random field.

2. Define an array nextPossible[$n_\uparrow$], $n_\uparrow = 0, 1 \ldots z$, which points to the location in the sorted list of the next spin which would flip if it had $n_\uparrow$ neighbors. Initially, all the elements of nextPossible[$n_\uparrow$] point to the spin with the largest local random field, h_i.
3. Choose from the $z + 1$ spins pointed to by nextPossible, the one with the largest total local field.
4. Move the pointer nextPossible[$n_\uparrow$] selected in step 3 to the next spin on the sorted list.
5. If that spin actually has $n_\uparrow$ up neighbors and the spin flip queue is empty, increment the field to just flip that spin, push the spin onto a FIFO queue (nucleate a pulse), and push an EOS marker on the queue. If not, to go back to step 3. If that spin actually has $n_\uparrow$ up neighbors and the spin flip queue is not empty; if the field required to flip that spin is less than the current field, push the spin on the FIFO queue (nucleate an avalanche) and go back to step 3; If the field required to flip that spin is greater than the current field, do not push the spin on the FIFO queue but do push a EOS marker on the queue and continue.
6. Pop shell off the FIFO queue spin by spin. Increment the external field by $\Omega\delta t$, where the field sweeprate is again $\Omega = \mathrm{d}H/\mathrm{d}t$.
7. If the spins in the shell have not been flipped, flip them and push all unflipped neighbors with positive local fields onto the queue.
8. As long as the size of the FIFO queue is greater than zero, loop back to step 2.
9. Repeat from step 2 until all spins in the lattice are flipped.

Inside a pulse, the time proceeds in unit increments ($\delta t = 1$). The time between pulses, however, is obtained by taking the difference between the field at the conclusion of a pulse and the field at the nucleation of the next (determined in the same manner as the sorted list algorithm) and dividing by the sweeprate. The potential time shift in the “clock” of the simulation between avalanches has no effect on the pulse size and duration distributions. This augmentation maintains all of the benefits of the ztneRFIM KS co de in the adiabatic limit. The asymptotic scaling is unchanged and the difference between the actual runtimes of the adiabatic and the finite sweeprate code was negligible.

A.2.2 Hysteresis Loop with long-range interactions

We consider the dipolar random-field Ising model in 2D at zero temperature.

$$\mathcal{H} = -J_{\mathrm{ex}} \sum_{<i,j>} s_i s_j + J_{\mathrm{dp}} \sum_{i \neq j} \frac{s_i s_j}{r_{ij}^3} - \sum_i \Big(H + h_i - J_{\mathrm{dm}} M \Big)\, s_i \tag{A.1}$$

The terms on the RHS are, in sequence: the nearest-neighbor exchange interaction term (ferromagnetic), the long-range dipolar interaction term (antiferromagnetic), the external field interaction term, the random-field term, the infinite range demagnetization field term. Here, the long-range dipolar interactions can be calculated with the Lekner formalism. For details, see App. B.

The local effective field experienced by spin i is given by

$$h_i^{\mathrm{eff}} \equiv H + h_i + J_{\mathrm{ex}} \sum_{<j>_i} s_j - J_{\mathrm{dp}} \sum_{j \neq i} \frac{s_j}{r_{ij}^3} - J_{\mathrm{dm}} M \tag{A.2}$$

The system state is considered to be stable when each spin is directed according to the sign of the local effective field h_i^{eff}. So the stability condition can be written as

$$s_i \, h_i^{\mathrm{eff}} > 0 \tag{A.3}$$

This algorithm used to calculate the lower branch of the hysteresis loop at zero temperature follows (the upper branch can be similarly calculated):

1. Check the stability condition.
    (a) If the state is stable, find the triggering spin for the next avalanche by checking through the lattice for the unflipped site with the largest internal field $H_i^{\mathrm{int}} = h_i^{\mathrm{eff}} - H$. Increment the external field H so it is just large enough to flip the site.
    (b) If the state is unstable, search the lattice to find the most unstable spin, i.e. the unstable spin with the largest absolute value of the effective local field.

    And push the spin onto a first-in first-out (FIFO) queue.
2. Pop the top spin off the queue.
3. (a) If the spin has not been flipped and it is unstable now, flip it.
    (b) If we have flipped the spin, but now it is unstable now, flip it back.

    And update H^{int} for all spins. Loop over the spin's nearest neighbors and push them onto the queue if they are unstable.
4. While there are spins on the queue, repeat from step 3.
5. While the system state is unstable, repeat from step 1(b).
6. Repeat from step 1(a) until all spins are flipped.

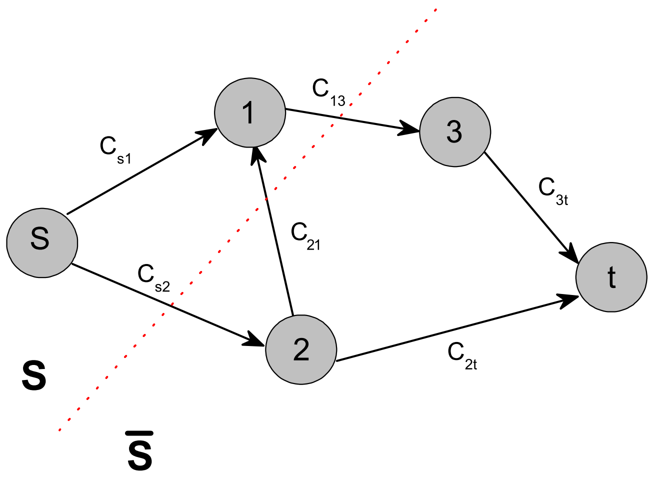

Figure A.3: A simple network with 5 vertices. The dotted line shows a (s,t)-cut, which separates the network into two parts: S and $\bar{S}$.

A.3 Ground State Calculation

The mapping of the RFIM GS problem to a min-cut/max-flow problem has been well established. The following derivation is based on Eq.6.12-6.15 of Ch.6 in Ref. [39].

A.3.1 Map RFIM onto a network

A network can be written as $N = (G, C, s, t)$. Here $G = (V, E)$ is a directed graph with $n+2$ vertices. $C : V \times V \to \mathcal{R}_0^+$ are the capacities of the edges $(i, j) \in E$ with $C(i, j) = 0$ if $(i, j) \notin E$. The vertices $s, t \in V$ are the source and sink of the network, respectively. For convenience, we use $V = 0, 1, 2, \cdots, n, n+1$ to mark the $n+2$ vertices, where $s \equiv 0$ and $t \equiv n+1$. Also, we define $C_{ij} = C(i, j)$. The vertices in $V \backslash \{s, t\}$ are called *inner vertices*. Edges connecting only inner vertices are called *inner edges*. See Fig. A.3.

A (s,t)-cut separates the network into two parts: S and $\bar{S}$. The capacity of this cut is defined as

$$C(S, \overline{S}) \equiv \sum_{i \in S, j \in \overline{S}} C_{ij} \tag{A.4}$$

For example, as shown in Fig. A.3, the capacity of that cut is just $C(S, \overline{S}) = C_{s2} + C_{13}$. A minimum cut means that it is a cut among all cuts which has minimum capacity. It is also the bottleneck of the flow. Each flow must pass the edges crossing an arbitrary cut, especially the minimum cut. Therefore, the minimum cut capacity is an upper bound for the flow. This is the max-flow/min-cut theorem. In Fig. A.3, suppose the cut is the minimum cut with capacity $C_{s2} + C_{13}$, then $f_{\max} = C_{s2} + C_{13}$ is the max flow of the network.

For a general (s,t)-cut, we can define a binary vector $\underline{X} = (x_0, x_1, \cdots, x_n, x_{n+1})$

with $x_i = 1$ (or 0) for $i \in S$ (or $\overline{S}$). Obviously, one has $x_0 = 1$ and $x_{n+1} = 0$. The binary variable x_i enables us to transform it to an Ising spin $s_i = \pm 1$. Then the capacity of this cut can be written as

$$
\begin{aligned}
C(\underline{X}) \quad &\equiv \quad C(S,\overline{S}) = \sum_{i \in S, j \in \overline{S}} C_{ij} = \sum_{i,j=0}^{n+1} x_i(1-x_j)\ C_{ij} \\
&= \quad -\sum_{i,j=0}^{n+1} C_{ij} x_i x_j + \sum_{i=0}^{n+1} \left(\sum_{j=0}^{n+1} C_{ij} \right) x_i \\
&= \quad -\Bigg[C_{00} x_0 x_0 + \sum_{j=1}^{n} C_{0j} x_0 x_j + C_{0,n+1} x_0 x_{n+1} \\
&\qquad + \sum_{i=1}^{n} C_{i0} x_i x_0 + \sum_{i,j=1}^{n} C_{ij} x_i x_j + \sum_{i=1}^{n} C_{i,n+1} x_i x_{n+1} \\
&\qquad + C_{n+1,0} x_{n+1} x_0 + \sum_{j=1}^{n} C_{n+1,j} x_{n+1} x_j + C_{n+1,n+1} x_{n+1} x_{n+1} \Bigg] \\
&\qquad + \Bigg[\left(C_{00} + \sum_{j=1}^{n} C_{0j} + C_{0,n+1} \right) x_0 + \sum_{i=1}^{n} \left(C_{i0} + \sum_{j=1}^{n} C_{ij} + C_{i,n+1} \right) x_i \\
&\qquad + \left(C_{n+1,0} + \sum_{j=1}^{n} C_{n+1,j} + C_{n+1,n+1} \right) x_{n+1} \Bigg] \\
&= \quad -\left[\sum_{j=1}^{n} C_{0j} x_j + \sum_{i=1}^{n} C_{i0} x_i + \sum_{i,j=1}^{n} C_{ij} x_i x_j \right] \\
&\qquad + \left[\sum_{j=1}^{n} C_{0j} + C_{0,n+1} + \sum_{i=1}^{n} \Big(C_{i0} + \sum_{j=1}^{n} C_{ij} + C_{i,n+1} \Big) x_i \right] \\
&= \quad -\sum_{i,j=1}^{n} C_{ij} x_i x_j + \sum_{i=1}^{n} \Big(-C_{0i} + C_{i,n+1} + \sum_{j=1}^{n} C_{ij} \Big) x_i + \sum_{i=1}^{n} C_{0i} + C_{0,n+1} \\
&= \quad -\sum_{i,j=1}^{n} C_{ij} \frac{s_i+1}{2} \frac{s_j+1}{2} + \sum_{i=1}^{n} \Big(-C_{0i} + C_{i,n+1} + \sum_{j=1}^{n} C_{ij} \Big) \frac{s_i+1}{2} + \sum_{i=1}^{n} C_{0i} + C_{0,n+1} \\
&= \quad -\frac{1}{4} \sum_{i,j=1}^{n} C_{ij} s_i s_j - \frac{1}{4} \sum_{i,j=1}^{n} C_{ij} s_i - \frac{1}{4} \sum_{i,j=1}^{n} C_{ij} s_j - \frac{1}{4} \sum_{i,j=1}^{n} C_{ij} \\
&\qquad + \sum_{i=1}^{n} \Big(-C_{0i} + C_{i,n+1} \Big) \frac{s_i}{2} + \frac{1}{2} \sum_{i,j=1}^{n} C_{ij} s_i + \frac{1}{2} \sum_{i=1}^{n} (-C_{0i} + C_{i,n+1}) \\
&\qquad + \frac{1}{2} \sum_{i,j=1}^{n} C_{ij} + \sum_{i=1}^{n} C_{0i} + C_{0,n+1} \\
&= \quad -\frac{1}{4} \sum_{i,j=1}^{n} C_{ij} s_i s_j + \frac{1}{4} \sum_{i,j=1}^{n} C_{ij} (s_i - s_j) + \frac{1}{4} \sum_{i,j=1}^{n} C_{ij} + \sum_{i=1}^{n} (-C_{0i} + C_{i,n+1}) \frac{s_i}{2} \\
&\qquad + \frac{1}{2} \sum_{i=1}^{n} (C_{0i} + C_{i,n+1}) + C_{0,n+1} \\
&= \quad -\frac{1}{4} \sum_{i<j} (C_{ij} + C_{ji}) s_i s_j + \sum_{i=1}^{n} \left[-\frac{1}{2} C_{0i} + \frac{1}{2} C_{i,n+1} + \frac{1}{4} \sum_{j=1}^{n} (C_{ij} - C_{ji}) \right] s_i \\
&\qquad + \frac{1}{4} \sum_{i<j} (C_{ij} + C_{ji}) + \frac{1}{2} \sum_{i=1}^{n} (C_{0i} + C_{i,n+1}) + C_{0,n+1}
\end{aligned}
\tag{A.5}
$$

where we have used the fact that $s_i = \pm 1$ and

$$\begin{aligned} x_i &= \frac{s_i + 1}{2} && \text{(A.6)} \\ \sum_{i,j=1}^{n} C_{ij} &= \sum_{i<j} (C_{ij} + C_{ji}) && \text{(A.7)} \\ \sum_{i,j=1}^{n} C_{ij}(s_i - s_j) &= \sum_{i,j=1}^{n} (C_{ij} - C_{ji}) s_i && \text{(A.8)} \end{aligned}$$

As mentioned above, the minimum of the (s,t)-cut capacity is actually the max flow which can flow through the network. Now we compare the last line of Eq. A.5 with the Hamiltonian of a general random ferromagnet:

$$\mathcal{H} = -\sum_{i<j} J_{ij} \epsilon_i \epsilon_j s_i s_j - \sum_i h_i \epsilon_i s_i \tag{A.9}$$

with $\epsilon_i = 0, 1$ and $J_{ij} \geq 0$. We have the mapping rule immediately:

$$\begin{aligned} -J_{ij}\epsilon_i\epsilon_j &= -\frac{1}{4}(C_{ij} + C_{ji}) && \text{(A.10)} \\ -h_i\epsilon_i &= -\frac{1}{2}C_{0i} + \frac{1}{2}C_{i,n+1} + \frac{1}{4}\sum_{j=1}^{n}(C_{ij} - C_{ji}) && \text{(A.11)} \\ 0 &= \frac{1}{4}\sum_{i<j}(C_{ij} + C_{ji}) + \frac{1}{2}\sum_{i=1}^{n}(C_{0i} + C_{i,n+1}) + C_{0,n+1} && \text{(A.12)} \end{aligned}$$

According to Eq. A.10, we can let

$$C_{ij} \equiv \begin{cases} 0 & i \geq j \\ 4J_{ij}\epsilon_i\epsilon_j & i < j \end{cases} \tag{A.13}$$

Since for a network only non-negative capacities are allowed, the bond values have to be non-negative as well. This is also the reason why this mapping fails for the spin glass but works for the random-bond ferromagnet.

According to Eq. A.11, we define an auxiliary field

$$w_i \equiv -2h_i\epsilon - \frac{1}{2}\sum_{j=1}^{n}(C_{ij} - C_{ji}) = -C_{0i} + C_{i,n+1} \tag{A.14}$$

then

$$\begin{aligned} C_{0i} = 0, \quad C_{i,n+1} = w_i \quad & \text{if } w_i > 0 \\ C_{0i} = -w_i, \quad C_{i,n+1} = 0 \quad & \text{if } w_i < 0 \end{aligned} \tag{A.15}$$

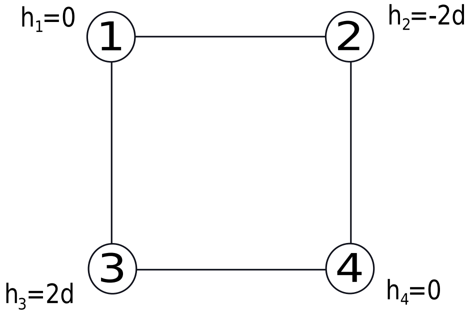

Figure A.4: A small random-field Ising magnet. There are 4 spins coupled via ferromagnetic interactions ($J_{12} = J_{13} = J_{24} = J_{34} = J = 1$). The local random fields are $h_1 = 0, h_2 = -2d, h_3 = 2d$ and $h_4 = 0$.

According to Eq. A.12, we define

$$C_{0,n+1} \equiv -\frac{1}{4}\sum_{i<j}(C_{ij} + C_{ji}) - \frac{1}{2}\sum_{i=1}^{n}(C_{0i} + C_{i,n+1}) \tag{A.16}$$

Now all the capacities ($C_{0i}, C_{i,n+1}, C_{ij}$ and $C_{0,n+1}$) are defined. The ground state energy of the random ferromagnet is mapped onto the max-flow of an equivalent network. Note that the capacity $C_{0,n+1}$ of the edge may be positive or negative. But actually it does not matter, since this edge crosses every (s,t)-cut of the network. Therefore, we can remove it from the network just at the beginning. Once the capacity of the minimum cut, i.e. the max flow of the network, has been obtained, we add the value of $C_{0,n+1}$ to get the ground state energy of the corresponding system. If we just need the ground state, then we needn't consider $C_{0,n+1}$ at all.

A.3.2 A Simple Example: without frozen spins

As an example, we look at a small random-field system, which is shown in Fig. A.4. There are four Ising spins arranged in a square, with ferromagnetic coupling of strength $J = 1$ and without periodic boundary conditions. The local random fields have the values $h_1 = 0, h_2 = -2d, h_3 = 2d$ and $h_4 = 0$.

Now we construct an equivalent network. It contains $n = 4$ inner nodes, one for each spin, and additionally one source 0 and one sink $n + 1 = 5$. According to the transformation rules Eq. A.13, we have the capacities of the inner edges.

$$\begin{aligned} C_{12} &= 4J_{12} = 4J \\ C_{13} &= 4J_{13} = 4J \\ C_{24} &= 4J_{24} = 4J \\ C_{34} &= 4J_{34} = 4J \\ C_{ij} &= 0 \text{ for all other cases } 1 \le i,j \le 4 \end{aligned} \tag{A.17}$$

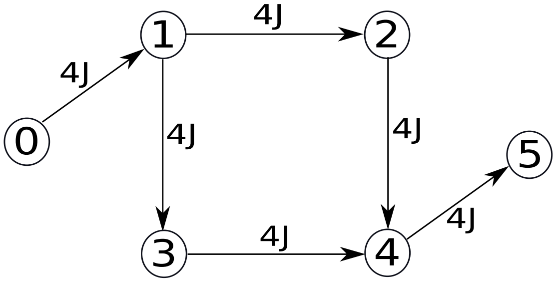

Figure A.5: The network obtained for the system from Fig. A.4 for the case $d = 0$. Vertex 0 is the source and vertex 5 is the sink. The capacities are denoted next to each edges. The edge connecting source and sink is not shown. For reasons, see the text.

According to Eq. A.14, the auxiliary fields w_i are given by

$$\begin{aligned}
w_1 &= -2h_1 - \tfrac{1}{2}\textstyle\sum_j (C_{1j} - C_{j1}) &&= -2h_1 - \frac{1}{2}(C_{12} + C_{13}) = -2h_1 - 4J = -4J \\
w_2 &= -2h_2 - \tfrac{1}{2}\textstyle\sum_j (C_{2j} - C_{j2}) &&= -2h_2 - \frac{1}{2}(C_{24} - C_{12}) = -2h_2 - 0 = 4d \\
w_3 &= -2h_3 - \tfrac{1}{2}\textstyle\sum_j (C_{3j} - C_{j3}) &&= -2h_3 - \frac{1}{2}(C_{34} - C_{13}) = -2h_3 - 0 = -4d \\
w_4 &= -2h_4 - \tfrac{1}{2}\textstyle\sum_j (C_{4j} - C_{j4}) &&= -2h_4 - \frac{1}{2}(-C_{24} - C_{34}) = -2h_4 + 4J = 4J
\end{aligned} \tag{A.18}$$

We then calculate the capacities of the edges connecting the inner nodes to the source and the sink. Suppose $d = 0$, so $w_2 = w_3 = 0$, according to Eq. A.15, we have

$$\begin{aligned}
C_{01} = 4J, &\quad C_{15} = 0 \\
C_{02} = 0, &\quad C_{25} = 0 \\
C_{03} = 0, &\quad C_{35} = 0 \\
C_{04} = 0, &\quad C_{45} = 4J
\end{aligned} \tag{A.19}$$

And due to Eq. A.16, we have $C_{05} = -8J$. The resulting network is shown in Fig. A.5.

A.3.3 A Simple Example: with frozen spins

If there are frozen spins, the problem might look somewhat complicated. However, by reorganizing the terms in the Hamiltonian, we find that the frozen spins just have two effects. First, they reduce the degrees of freedom of the system, i.e we obtain a smaller effective system. Second, for those spins which are nearest neighbors of the frozen spins, their local random fields are effectively shifted: $h'_i = h_i \pm J n^{\mathrm{f}}_i$. Here n^{f}_i is the number of spin i's frozen nearest neighbors and

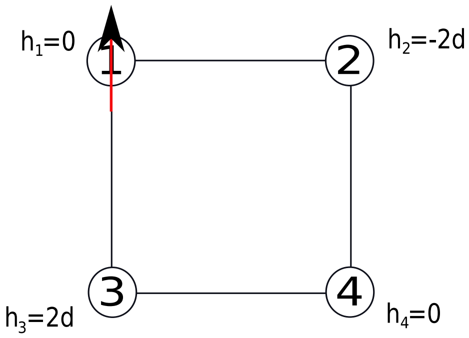

Figure A.6: A small random-field Ising magnet as shown in Fig. A.4. The only difference is that spin 1 to set to be up, i.e. $s_1 = +1$.

'+'('−') represents freezing up(down) spins. For the smaller effective system, we can do the mapping again and use the push-relabel algorithm to find the GS.

For example, now we freeze spin 1 to be up, i.e. let $s_1 = +1$. What is the equivalent network? For this tiny system, we can write down the Hamiltonian directly.

$$\begin{aligned}
\mathcal{H} &= -J\sum_{\langle i,j\rangle} s_i s_j - \sum_i h_i s_i \\
&= -J[s_1s_2 + s_1s_3 + s_2s_4 + s_3s_4] - [h_1s_1 + h_2s_2 + h_3s_3 + h_4s_4] \\
&= -J[s_2s_4 + s_3s_4] - [h_1s_1 + (h_2 + Js_1)s_2 + (h_3 + Js_1)s_3 + h_4s_4] \\
&= -J[s_2s_4 + s_3s_4] - [h'_2s_2 + h'_3s_3 + h'_4s_4] - h_1s_1 \\
&= -J[s_2s_4 + s_3s_4] - [h'_2s_2 + h'_3s_3 + h'_4s_4] + \text{const} \qquad \text{(A.20)}
\end{aligned}$$

with

$$\begin{aligned}
h'_2 &= h_2 + Js_1 \\
h'_3 &= h_3 + Js_1 \\
h'_4 &= h_4 \qquad \text{(A.21)}
\end{aligned}$$

By reorganizing the terms in the Hamiltonian, the effect of the frozen spin can be seen clearly. First, it reduces the degrees of freedom of the system, i.e we obtain a smaller effective system. Second, for those spins which are nearest neighbors of the frozen spin, their local random fields are effectively shifted:

$$h'_i = h_i + Jn_{i\uparrow} \qquad \text{(A.22)}$$

with $n_{i\uparrow}$ the number of spin i's up nearest neighbors. Similarly, with frozen down spins,

$$h'_i = h_i - Jn_{i\downarrow} \qquad \text{(A.23)}$$

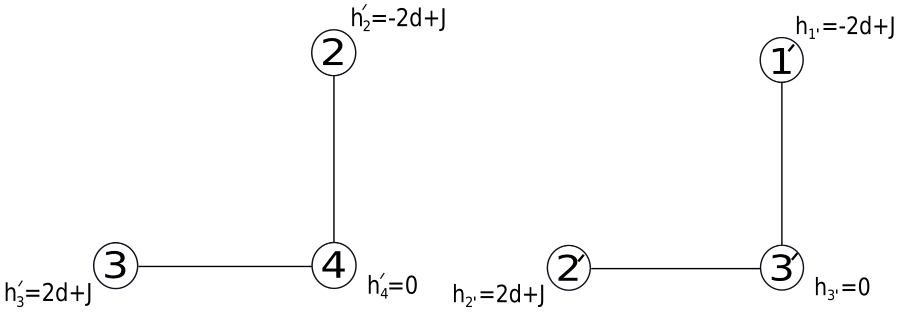

Figure A.7: The effective random-field Ising magnet as shown in Fig. A.6.

For convenience, we introduce a new set of index to mark the spins, i.e we set a 1-1 mapping between the old spin index (2,3,4) and the new index (1',2',3'):

$$\begin{gathered} 2 \leftrightarrow 1', \quad 3 \leftrightarrow 2', \quad 4 \leftrightarrow 3' \\ h'_2 \leftrightarrow h_{1'}, \quad h'_3 \leftrightarrow h_{2'}, \quad h'_4 \leftrightarrow h_{3'} \end{gathered} \tag{A.24}$$

See Fig. A.7. Then the Hamiltonian of the new system can be written as:

$$\mathcal{H} = -J \sum_{\langle i',j' \rangle} s_{i'} s_{j'} - \sum_{i'} h_{i'} s_{i'} \tag{A.25}$$

Now we construct the equivalent network. It contains $n = 3$ inner nodes, one for each spin, and additionally one source 0 and one sink $n + 1 = 4$. According to the transformation rules Eq. A.13, we have the capacities of the inner edges.

$$\begin{aligned} C_{1'3'} &= 4J_{1'3'} = 4J \\ C_{2'3'} &= 4J_{2'3'} = 4J \\ C_{i'j'} &= 0 \text{ for all other cases } 1 \leq i', j' \leq 3 \end{aligned} \tag{A.26}$$

According to Eq. A.14, the auxiliary fields $w_{i'}$ are given by

$$\begin{aligned} w_{1'} &= -2h_{1'} - \frac{1}{2}\sum_{j'}(C_{1j'} - C_{j'1}) = -2h_{1'} - \frac{1}{2}(C_{1'3'}) = 4d - 4J \\ w_{2'} &= -2h_{2'} - \frac{1}{2}\sum_{j'}(C_{2j'} - C_{j'2}) = -2h_{2'} - \frac{1}{2}(C_{2'3'}) = -4d - 4J \\ w_{3'} &= -2h_{3'} - \frac{1}{2}\sum_{j'}(C_{3j'} - C_{j'3}) = -2h_{3'} - \frac{1}{2}(-C_{1'3'} - C_{2'3'}) = 4J \end{aligned} \tag{A.27}$$

In the case $d = 0$, we have $w_{1'} = w_{2'} = -4J$ and $w_{3'} = 4J$. According to

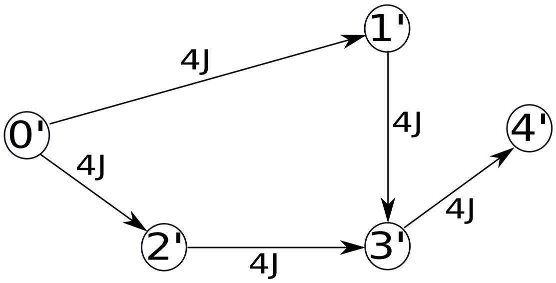

Figure A.8: The network obtained for the system from Fig. A.6 for the case $d = 0$. Vertex 0' is the source and vertex 4' is the sink. The capacities are denoted next to each edges. The edge connecting source and sink is not shown. For reasons, see the text.

Eq. A.15, we have

$$\begin{aligned} C_{0'1'} &= 4J, \quad C_{1'4'} = 0 \\ C_{0'2'} &= 4J, \quad C_{2'4'} = 0 \\ C_{0'3'} &= 0, \quad C_{3'4'} = 4J \end{aligned} \tag{A.28}$$

And due to Eq. A.16, we have $C_{0'4'} = -8J$. The resulting network is shown in Fig. A.8.

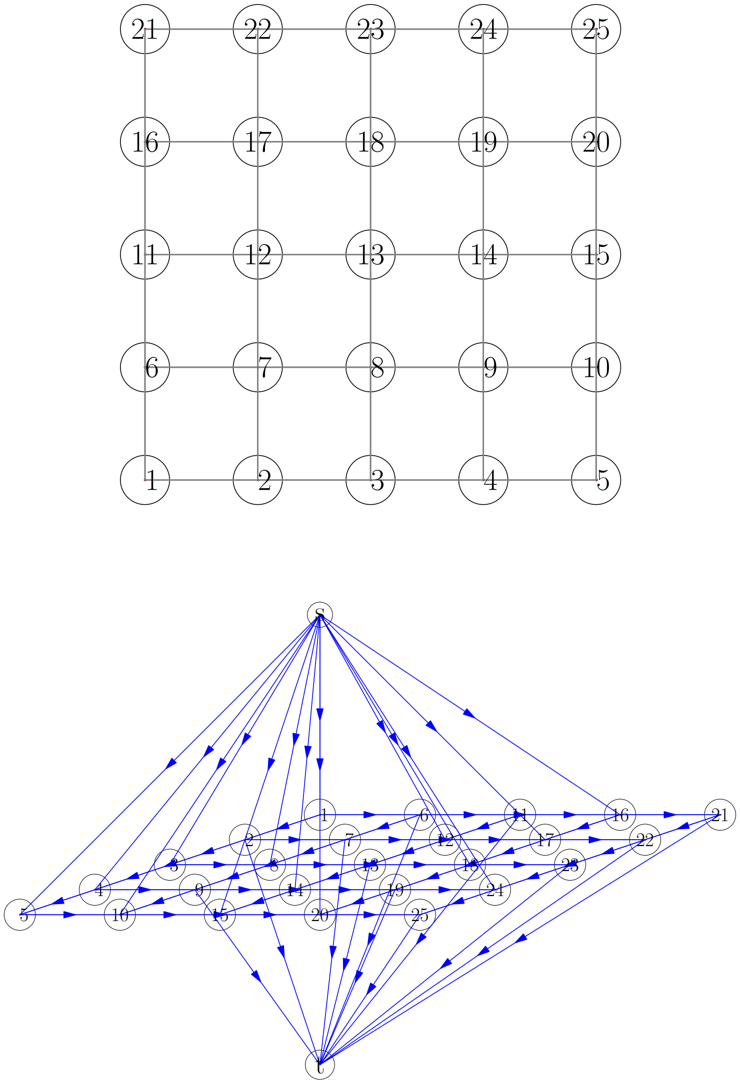

Figure A.9: A more complicated flow network (bottom) mapped from RFIM on a square lattice (top).

Appendix B

Lekner formalism

The long-range dipolar interaction in the random-field Ising model is calculated by a direct space summation method based on the Lekner formalism. The method is useful for the numerical study of the the perpendicular recording media and ferroelectrics.

B.1 Model

Consider a simple lattice of Ising spins with periodic boundary conditions. There is a quenched random field h_i at each lattice site. Spins interact with each other by means of exchange and dipolar interactions and experience a uniform external field H. The ferromagnetic exchange interactions have strength $J_{\rm ex}$ between each spin and its nearest neighbors. The long-range dipolar interactions between each spin pair have strength $J_{\rm dp}$. The Hamiltonian of the system can be written as:

$$\mathcal{H} = -J_{\rm ex} \sum_{<i,j>} \mathbf{S}_i \cdot \mathbf{S}_j - J_{\rm dp} \sum_{i \neq j} \frac{3(\mathbf{S}_i \cdot \hat{\mathbf{r}}_{ij})(\mathbf{S}_j \cdot \hat{\mathbf{r}}_{ij}) - \mathbf{S}_i \cdot \mathbf{S}_j}{r_{ij}^3} - \sum_i (\mathbf{H} + \mathbf{h}_i) \cdot \mathbf{S}_i \tag{B.1}$$

where $r_{ij} = |\mathbf{r}_{ij}| = |\mathbf{r}_i - \mathbf{r}_j|$ and $\hat{\mathbf{r}}_{ij} = \mathbf{r}_{ij}/r_{ij}$, with $\mathbf{r}_i$ and $\mathbf{r}_j$ the positions of spin i and spin j in the lattice, respectively. [1] Assume that the magnetization directions of all the Ising spins are always parallel or antiparallel with the applied external field and the quenched random fields, then the Hamiltonian can be simplified as

$$\mathcal{H} = -J_{\rm ex} \sum_{<i,j>} S_i S_j - J_{\rm dp} \sum_{i \neq j} \frac{3\cos^2\theta_{ij} - 1}{r_{ij}^3} S_i S_j - \sum_i (H + h_i) S_i \tag{B.2}$$

with θ_{ij} the angle between $\mathbf{S}_i$ and the vector $\mathbf{r}_{ij}$. We denote our model as the dipolar random-field Ising model (DRFIM).

In numerical simulation, we use periodic boundary condition to eliminate boundary effects. In other words, the central unit cell of the simulation is periodically repeated to infinity in all the dimensions. This will not cause any trou-

---

[1] Let θ_i (θ_j) be the angle between $\mathbf{S}_i$ ($\mathbf{S}_j$) and $\mathbf{r}_{ij}$. Two cases: (1) $\mathbf{S}_i$ is anti-parallel with $\mathbf{S}_j$, then $\theta_i = \pi - \theta_j = \theta_{ij}$; (2) $\mathbf{S}_i$ is parallel with $\mathbf{S}_j$, then $\theta_i = \theta_j = \theta_{ij}$. In both cases, we have $3(\mathbf{S}_i \cdot \hat{\mathbf{r}}_{ij})(\mathbf{S}_j \cdot \hat{\mathbf{r}}_{ij}) = 3 S_i S_j \cos^2\theta_{ij}$ where $S_i, S_j = \pm 1$.

ble for the short-range, i.e. nearest-neighboring, exchange interaction. However, we have to pay more attention to the long-range dipolar interaction. We need to take into account all the image cells, see Applied/Appendix/Lekner/Fig. B.1. Consider two particular Ising spins at $\mathbf{r}_i$ and $\mathbf{r}_j$ in the central cell. The dipolar interaction energy

$$U_{\mathrm{dp}} = -J_{\mathrm{dp}} \sum_{i \neq j} \frac{3\cos^2\theta_{ij} - 1}{r_{ij}^3} S_i S_j \tag{B.3}$$

has to be calculated as

$$U_{\mathrm{dp}} = -J_{\mathrm{dp}} \sum_{i,j} S_i S_j \sum_{\mathbf{C}}{}' \frac{3\cos^2\theta_{ij} - 1}{|\mathbf{r}_{ij} + \mathbf{C}|^3} \equiv -J_{\mathrm{dp}} \sum_{i,j} S_i S_j \, \mathcal{F}(\mathbf{r}_{ij}). \tag{B.4}$$

Here the sum over vector $\mathbf{C}$ indicates the sum over all the cells.

$$\mathbf{C} = \overleftrightarrow{V} \cdot \mathbf{n} = (\mathbf{a}, \mathbf{b}, \mathbf{c}) \cdot \mathbf{n} = \begin{pmatrix} a_x & b_x & c_x \\ a_y & b_y & c_y \\ a_z & b_z & c_z \end{pmatrix} \cdot \begin{pmatrix} n_x \\ n_y \\ n_z \end{pmatrix} \tag{B.5}$$

with n_x, n_y, n_z integers and vectors $\mathbf{a}, \mathbf{b}, \mathbf{c}$ the lattice vectors of the unit cell. In two-dimension, assuming the lattice vector $\mathbf{a}$ is along the $\hat{\mathbf{x}}$ direction, the cell vector $\mathbf{C}$ can be written as

$$\mathbf{C} = (\mathbf{a}, \mathbf{b}) \cdot \mathbf{n} = \begin{pmatrix} a_x & b_x \\ a_y & b_y \end{pmatrix} \cdot \begin{pmatrix} l \\ m \end{pmatrix} = \begin{pmatrix} L_x & L_y \cos\psi \\ 0 & L_y \sin\psi \end{pmatrix} \cdot \begin{pmatrix} l \\ m \end{pmatrix} \tag{B.6}$$

with L_x and L_y the dimensions of the unit cell and ψ the angle between the lattice vectors $\mathbf{a}$ and $\mathbf{b}$. (Note that hereafter we replace n_x, n_y,$\cdots$ by l,m,$\cdots$.) Particularly, for square unit cell ($\psi = \pi/2$) and rhombus unit cell with $\psi = \pi/3$ (see Fig. B.1 (left) and (right)), $L_x = L_y = L$, we have

$$\mathbf{C}^{\square} = \begin{pmatrix} l \\ m \end{pmatrix} L \tag{B.7}$$

and

$$\mathbf{C}^{\diamondsuit} = \begin{pmatrix} l + \frac{1}{2} m \\ \frac{\sqrt{3}}{2} m \end{pmatrix} L \tag{B.8}$$

respectively. (Thereafter, we will denote square unit cell with $\square$ and rhobus unit cell with $\diamondsuit$.)

The prime on the $\mathbf{C}$-summation in Eq. B.4 indicates that this sum is over all images of spins j except $\mathbf{C} = 0$ if $j = i$ because we assume that spin i interacts with all its periodic images, but not, of course, with itself.

The Hamiltonian Eq. B.2 is further simplified as

$$\mathcal{H} = -\sum_i \left[H + h_i + J_{\mathrm{ex}} \sum_{<j>_i} S_j - J_{\mathrm{dp}} \sum_j S_j \mathcal{F}(\mathbf{r}_{ij}) \right] S_i. \tag{B.9}$$

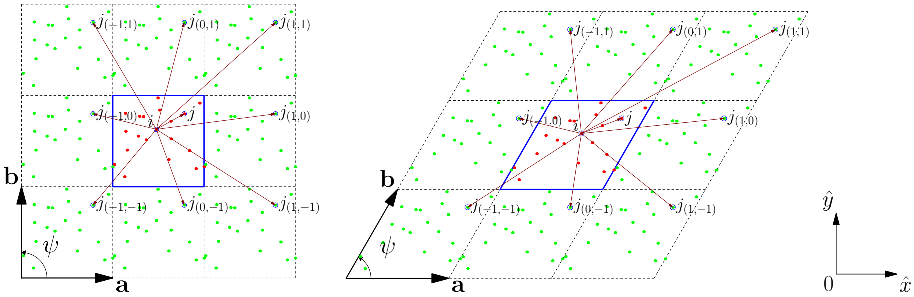

Figure B.1: Schematic top view of a two-dimensional system with periodic boundary conditions used in the simulations to calculate the contribution to the dipolar interaction between particle j (and all its images j') and particle i. Particles are not necessary to be set on regular lattice sites. Here only 8 image cells are drawn. But in real simulations, to calculate the long-range interactions, we need to consider all the image cells, i.e $\mathbf{n} = (n_x, n_y)$ with $n_x, n_y = 0, \pm 1, \pm 2, \cdots$. (Left) Square central cell $\psi = \pi/2$. (Right) Rhombus central cell $\psi = \pi/3$.

And the local effective field to which spin i is exposed can be written as

$$h_i^{\mathrm{eff}} = H + h_i + J_{\mathrm{ex}} \sum_{<j>_i} S_j - J_{\mathrm{dp}} \sum_j S_j \, \mathcal{F}(\mathbf{r}_{ij}) \tag{B.10}$$

which enables us to calculate the $M(H)$ curve with the brute-force algorithm. But we have to pay attention to the fact that the no-passing rule is broken here, due to the presence of the anti-ferromagnetic long-range dipolar interactions. We can see that from Eq. B.10. If spin j flip up ($S_j = -1 \to +1$), the effective field experienced by spin i will decrease by amount $2J_{\mathrm{dp}}\mathcal{F}(\mathbf{r}_{ij})$, which may cause spin i flip back.

Now we consider four different cases.

B.1.1 2D: square unit cell and $\mathbf{H} \perp \hat{\mathbf{x}}$, $\mathbf{H} \perp \hat{\mathbf{y}}$

This is used to model the perpendicular recording media. Obviously, we have $\cos\theta_{ij} = 0$ (because $\theta_{ij} = \pi/2$). We define dimensionless measures of the displacements between spin-i and spin-j: $x_i - x_j = \xi_{ij} L$ and $y_i - y_j = \eta_{ij} L$ with $0 < |\xi|, |\eta| < 1$. Plug Eq. B.7 into Eq. B.4, we have

$$U_{\mathrm{dp}} = J_{\mathrm{dp}} \sum_{i,j} S_i S_j \, \mathcal{F}(\mathbf{r}_{ij}) = J_{\mathrm{dp}} L^{-3} \sum_{i,j} \; S_i S_j \; F_{\perp}^{\square}(\xi_{ij}, \eta_{ij}) \tag{B.11}$$

with

$$F_{\perp}^{\square}(\xi, \eta) \equiv \sum_{l,m=-\infty}^{\infty}{}' \frac{1}{[(\xi + l)^2 + (\eta + m)^2]^{\frac{3}{2}}}. \tag{B.12}$$

Here the prism indicates that we omit the $l = m = 0$ term if $\xi = \eta = 0$.

It is easy to prove the following symmetries of $F_{\perp}^{\square}(\xi,\eta)$:

$$F_{\perp}^{\square}(\xi,\eta) = F_{\perp}^{\square}(\eta,\xi) \tag{B.13}$$
$$F_{\perp}^{\square}(\xi,\eta) = F_{\perp}^{\square}(-\xi,-\eta) \tag{B.14}$$
$$F_{\perp}^{\square}(\xi,\eta) = F_{\perp}^{\square}(-\xi,\eta) = F_{\perp}^{\square}(\xi,-\eta) \tag{B.15}$$
$$F_{\perp}^{\square}(\xi,\eta) = F_{\perp}^{\square}(\xi,n-\eta) = F_{\perp}^{\square}(n-\xi,\eta) = F_{\perp}^{\square}(n-\xi,n-\eta) \text{ with } n \in \mathbb{Z} \tag{B.16}$$

Those symmetries will be extensively used in our calculations. See Sec. B.3.1 for details.

B.1.2 2D: rhombus unit cell and $\mathbf{H} \perp \hat{\mathbf{x}}$, $\mathbf{H} \perp \hat{\mathbf{y}}$

For a general rhombus unit cell with $L_x = L_y = L$, plug Eq. B.6 into Eq. B.4, we have

$$U_{\mathrm{dp}} = J_{\mathrm{dp}} \sum_{i,j} S_i S_j \, \mathcal{F}(\mathbf{r}_{ij}) = J_{\mathrm{dp}} L^{-3} \sum_{i,j} \; S_i S_j \; F_{\perp}(\xi_{ij},\eta_{ij}) \tag{B.17}$$

with

$$F_{\perp}(\xi,\eta) \equiv \sum_{l,m=-\infty}^{\infty}{}' \frac{1}{[(\xi+l+\beta m)^2+(\eta+\gamma m)^2]^{\frac{3}{2}}}. \tag{B.18}$$

Here $\beta \equiv \cos\psi$, $\gamma \equiv \sin\psi$, and the prism again indicates that we omit the $l = m = 0$ term if $\xi = \eta = 0$.

Note that for general ψ $(\neq \pi/2)$, Eq. B.13 is not true. But we can show that

$$F_{\perp}(\xi,\eta) = F_{\perp}(-\xi,-\eta) \tag{B.19}$$
$$F_{\perp}(\xi,\eta) = F_{\perp}(n+\xi,\eta) \text{ with } n \in \mathbb{Z} \tag{B.20}$$
$$F_{\perp}(-\xi,\eta) = F_{\perp}(\xi,-\eta) \tag{B.21}$$

Interestingly, for $\psi = \pi/3$ (or $2\pi/3$), we can show that

$$F_{\perp}^{\diamond}(\xi,\eta) = F_{\perp}^{\diamond}(-\xi,\eta) \tag{B.22}$$
$$F_{\perp}^{\diamond}(\xi,\eta) = F_{\perp}^{\diamond}(\xi,-\eta) \tag{B.23}$$

See Sec.B.2.2 for proof. Those exchange symmetries will be extensively used in our calculation. See Sec. B.3.1 for details.

B.1.3 2D: square unit cell and $\mathbf{H} \parallel \hat{\mathbf{y}}$

In this case, $\cos\theta_{ij} = \frac{y_j - y_i}{r_{ij}}$. With the same definitions of η and ξ, we have

$$U_{dp} = J_{\mathrm{dp}} \sum_{i,j} S_i S_j \, \mathcal{F}(\mathbf{r}_{ij}) = -\sum_{i,j} J_{\mathrm{dp}} S_i S_j L^{-3} \; F_{\parallel}^{\square}(\xi_{ij},\eta_{ij}) \tag{B.24}$$

with

$$F_{\parallel}^{\square}(\xi,\eta) \equiv \sum_{l,m=-\infty}^{\infty}{}' \frac{3(\eta+m)^2 - [(\xi+l)^2 + (\eta+m)^2]}{[(\xi+l)^2 + (\eta+m)^2]^{\frac{5}{2}}} \tag{B.25}$$

Note that $F_{\parallel}^{\square}(\xi,\eta)$ does not have the $\xi \leftrightarrow \eta$ exchange symmetry. But the other symmetries, i.e. Eq. B.15 and B.16 are still valid for $F_{\parallel}^{\square}(\xi,\eta)$.

B.1.4 3D: cubic unit cell and $\mathbf{H} \parallel \hat{\mathbf{z}}$

In this case, $\cos\theta_{ij} = \frac{z_j - z_i}{r_{ij}}$. As the definitions of η and ξ, we define dimensionless measure of the displacements between spin-i and spin-j in the $\hat{z}$-direction as $z_i - z_j = \zeta L$ with $|\zeta| < 1$. Then we have

$$U_{dp} = J_{\mathrm{dp}} \sum_{i,j} S_i S_j \, \mathcal{F}(\mathbf{r}_{ij}) = -\sum_{i,j} J_{\mathrm{dp}} S_i S_j L^{-3} \; F_z(\xi_{ij}, \eta_{ij}, \zeta_{ij}) \tag{B.26}$$

with

$$F_z(\xi,\eta,\zeta) \equiv \sum_{l,m,n=-\infty}^{\infty}{}' \frac{3(\zeta+n)^2 - [(\xi+l)^2 + (\eta+m)^2 + (\zeta+n)^2]}{[(\xi+l)^2 + (\eta+m)^2 + (\zeta+n)^2]^{\frac{5}{2}}} \tag{B.27}$$

It is easy to check that $F_z(\xi,\eta,\zeta)$ has the $\xi \leftrightarrow \eta$ exchange symmetry and $\xi \leftrightarrow n-\xi$, $\eta \leftrightarrow n-\eta$, $\zeta \leftrightarrow n-\zeta$ symmetries, which will be extensively used in our calculation.

B.2 Lekner formalism

The summation over the cells, i.e. Eq. B.12, B.18, B.25 and B.27 can be done with the Lekner formalism. The conversion of these sums to rapidly convergent ones proceeds via three transformations, which are the key steps of the Lekner formalism.

1. The Euler transformation

$$\frac{1}{x^\nu} = \frac{1}{\Gamma(\nu)} \int_0^\infty \mathrm{d}t \; t^{\nu-1} e^{-xt} \qquad (\nu > 0). \tag{B.28}$$

2. The Poisson-Jacobi identity and its extensions [2]

$$\begin{aligned}
\sum_{l=-\infty}^{+\infty} \exp[-(\xi+l)^2 t] &= \left(\frac{\pi}{t}\right)^{\frac{1}{2}} \sum_{l=-\infty}^{+\infty} \exp\left(-\frac{\pi^2 l^2}{t}\right) \cos(2\pi l\xi) \\
\sum_{l=-\infty}^{+\infty} (\xi+l) \exp[-(\xi+l)^2 t] &= \left(\frac{\pi}{t}\right)^{\frac{3}{2}} \sum_{l=-\infty}^{+\infty} \exp\left(-\frac{\pi^2 l^2}{t}\right) \sin(2\pi l\xi) l \\
\sum_{l=-\infty}^{+\infty} (\xi+l)^2 \exp[-(\xi+l)^2 t] &= \frac{1}{2}\left(\frac{\pi}{t^3}\right)^{\frac{1}{2}} \sum_{l=-\infty}^{+\infty} \exp\left(-\frac{\pi^2 l^2}{t}\right) \cos(2\pi l\xi) \\
&\quad - \left(\frac{\pi}{t}\right)^{\frac{5}{2}} \sum_{l=-\infty}^{+\infty} \exp\left(-\frac{\pi^2 l^2}{t}\right) \cos(2\pi l\xi) l^2 .
\end{aligned} \tag{B.29}$$

3. An integral representation of the Bessel function K_ν

$$\int_0^\infty \mathrm{d}t\ t^{\nu-1} \exp(-\pi^2 l^2/t - m^2 t) = 2\left(\pi \left|\frac{l}{m}\right|\right)^{\nu} K_\nu(2\pi|lm|). \tag{B.30}$$

B.2.1 2D: square unit cell and $\mathbf{H} \perp \hat{\mathbf{x}}$, $\mathbf{H} \perp \hat{\mathbf{y}}$

Now we apply the Lekner formalism to Eq. B.12. For $\xi \neq 0$, $\eta \neq 0$. We have

$$\begin{aligned}
F_{\perp}^{\square}(\xi,\eta) &= \sum_{l,m=-\infty}^{\infty} \frac{1}{[(\xi+l)^2+(\eta+m)^2]^{\frac{3}{2}}} \\
&= \sum_{l,m=-\infty}^{\infty} \frac{1}{\Gamma(\frac{3}{2})} \int_0^\infty \mathrm{d}t\ t^{\frac{1}{2}} \exp\{-[(\xi+l)^2+(\eta+m)^2]t\} \\
&= \sum_{l,m=-\infty}^{\infty} \frac{1}{\Gamma(\frac{3}{2})} \int_0^\infty \mathrm{d}t\ t^{\frac{1}{2}} \left(\frac{\pi}{t}\right)^{\frac{1}{2}} \exp(-\pi^2 l^2/t) \cos(2\pi l\xi) \exp[-(\eta+m)^2 t] \\
&= \sum_{l,m=-\infty}^{\infty} 2\cos(2\pi l\xi) \int_0^\infty \mathrm{d}t\ \ \exp[-\pi^2 l^2/t - (\eta+m)^2 t]
\end{aligned} \tag{B.31}$$

where we have used $\Gamma(\frac{3}{2}) = \frac{\sqrt{\pi}}{2}$.

Evaluate the $l=0$ part separately,

$$F_{\perp,l=0}^{\square}(\xi,\eta) = \sum_m 2\int_0^\infty \mathrm{d}t\ \ \exp[-(\eta+m)^2 t] = 2\sum_m \frac{1}{(\eta+m)^2} = \frac{2\pi^2}{\sin^2(\pi\eta)}. \tag{B.32}$$

The last summation of the above equation can be done in two methods. See Sec. B.3.2 for details.

---

[2] Note that in Eq. B.29, the index l in the RHS is simply the index of a (geometrical) series. Wile the index l in the LHS is related to the periodic images along x- or y-axis. They are completely independent of each other. In fact, **all** periodic images along a chosen axis contribute to **any** terms of the series in RHS. For details, see Ref. [63] Sec II.

For the $l \neq 0$ part,

$$\begin{aligned} F^{\square}_{\perp,l\neq 0}(\xi,\eta) &= \sum_{l\neq 0}\sum_{m} 2\cos(2\pi l\xi)\int_0^{\infty} \mathrm{d}t\, \exp[-\pi^2 l^2/t-(\eta+m)^2 t] \\ &= 2\sum_{l>0}\sum_{m} 2\cos(2\pi l\xi)\ 2\left(\pi\left|\frac{l}{\eta+m}\right|\right)^1\ K_1(2\pi|l(\eta+m)|) \\ &= 8\pi\sum_{l>0} l\cos(2\pi l\xi)\sum_m \frac{1}{|\eta+m|}\ K_1(2\pi l|\eta+m|). \end{aligned} \quad \text{(B.33)}$$

So we have

$$F^{\square}_{\perp}(\xi,\eta) = \frac{2\pi^2}{\sin^2(\pi\eta)} + 8\pi\sum_{l>0} l\cos(2\pi l\xi)\sum_m \frac{1}{|\eta+m|}\ K_1(2\pi l|\eta+m|) \quad \text{(B.34)}$$

Note that if we apply the Poisson-Jacobi identity to the m-sum in the derivation of Eq. B.31, we will have

$$F^{\square}_{\perp}(\xi,\eta) = \frac{2\pi^2}{\sin^2(\pi\xi)} + 8\pi\sum_{m>0} m\cos(2\pi m\eta)\sum_l \frac{1}{|\xi+l|}\ K_1(2\pi m|\xi+l|) \quad \text{(B.35)}$$

The $\xi \leftrightarrow \eta$ symmetry is clearly seen from the above two equations. Moreover, this symmetry is extremely important in the numerical implementation of the Lekner formalism. The Lekner formalism is elegant and powerful because the Bessel functions decay fast. For example: $K_0(x) \to \sqrt{\frac{\pi}{2x}}e^{-x}$ as $x \to \infty$. However, for small arguments of the Bessel functions, the convergences of the above summations are very slow. Several different procedures have been proposed to overcome this problem, see Sec. B.3.6 for details. The simplest one is the so-called "Lekner-cyclic" method, i.e. switching between the two representations of summations (Eq. B.34 and Eq. B.35) so that the argument in the Bessel functions would be as large as possible. This allows us to achieve fast convergence.

We should pay attention to the special case $\xi = \eta = 0$, where the Lekner-cyclic method fails. Actually, we have to re-derive the formula based on the Lekner formalism. The result is shown here.

$$F^{\square}_{\perp}(0,0) = 2\zeta(3) + 4\zeta(2) + 16\pi\sum_{l>0}\sum_{m>0}\frac{m}{l}\ K_1(2\pi ml) \simeq 9.0336. \quad \text{(B.36)}$$

For details of this derivation, see Sec. B.3.3.

B.2.2 2D: rhombus unit cell and $\mathbf{H} \perp \hat{\mathbf{x}}$, $\mathbf{H} \perp \hat{\mathbf{y}}$

When the unit cell is not a square ($L_{\mathrm{x}} \neq L_{\mathrm{y}}$) or does not have a rectangular shape ($\psi \neq \pi/2$), the Lekner summations have been proposed in [31,15,55,32].

For $\xi \neq 0$, $\eta \neq 0$. We have

$$\begin{aligned}
F_\perp(\xi,\eta) &= \sum_{l,m=-\infty}^{\infty} \frac{1}{[(\xi+l+\beta m)^2+(\eta+\gamma m)^2]^{\frac{3}{2}}} \\
&= \sum_{l,m=-\infty}^{\infty} \frac{1}{\Gamma(\frac{3}{2})} \int_0^\infty \mathrm{d}t\; t^{\frac{1}{2}} \exp\{-[(\xi+l+\beta m)^2+(\eta+\gamma m)^2]t\} \\
&= \sum_m \frac{1}{\Gamma(\frac{3}{2})} \int_0^\infty \mathrm{d}t\; t^{\frac{1}{2}} \left[\sum_l \exp\{-(\tilde{\xi}_m+l)^2 t\}\right] \exp\{-(\eta+\gamma m)^2 t\} \\
&= \frac{1}{\Gamma(\frac{3}{2})} \sum_m \int_0^\infty \mathrm{d}t\; t^{\frac{1}{2}} \left[\left(\frac{\pi}{t}\right)^{\frac{1}{2}} \sum_l \exp(-\pi^2 l^2/t)\cos(2\pi l\tilde{\xi}_m)\right] \\
&\quad \cdot \exp\{-(\eta+\gamma m)^2 t\} \\
&= 2\sum_l \sum_m \cos(2\pi l\tilde{\xi}_m) \int_0^\infty \mathrm{d}t\;\; \exp[-\pi^2 l^2/t-(\eta+\gamma m)^2 t] \qquad \text{(B.37)}
\end{aligned}$$

where $\tilde{\xi}_m \equiv \xi + m$.

Evaluate the $l=0$ part separately,

$$F_{\perp,l=0}(\xi,\eta) = \sum_m 2\int_0^\infty \mathrm{d}t\;\; \exp[-(\eta+\gamma m)^2 t] = 2\sum_m \frac{1}{(\eta+\gamma m)^2} = \frac{2\pi^2}{\gamma^2\sin^2(\pi\eta/\gamma)}. \qquad \text{(B.38)}$$

Here we have used the result of Eq. B.32.

For the $l \neq 0$ part,

$$\begin{aligned}
F_{\perp,l\neq 0}(\xi,\eta) &= 2\sum_{l\neq 0}\sum_m \cos(2\pi l\tilde{\xi}_m)\; 2\left(\pi\left|\frac{l}{\eta+\gamma m}\right|\right)^1 \; K_1(2\pi|l(\eta+\gamma m)|) \\
&= 8\pi\sum_{l>0}\sum_m \cos(2\pi l(\xi+\beta m))\frac{l}{|\eta+\gamma m|}\; K_1(2\pi l|\eta+\gamma m|) \qquad \text{(B.39)}
\end{aligned}$$

So we have

$$F_\perp(\xi,\eta) = \frac{2\pi^2}{\gamma^2\sin^2(\pi\eta/\gamma)} + 8\pi\sum_{l>0}\sum_m \cos(2\pi l(\xi+\beta m))\frac{l}{|\eta+\gamma m|}\; K_1(2\pi l|\eta+\gamma m|) \qquad \text{(B.40)}$$

Generally speaking, $F_\perp(\xi,\eta)$ will not be an even function of ξ (or η). Square unit is an exception. But we can prove that for $\psi = \pi/3$ (or $2\pi/3$), $F_\perp(\xi,\eta)$ is an even function of ξ. The proof is simple by observing that for $\psi = \pi/3$, $\beta = \cos\psi = 1/2$, so

$$\cos(2\pi l(\xi+\beta m)) = \cos(2\pi l\xi + ml\pi) = \pm\cos(2\pi l\xi) \qquad \text{(B.41)}$$

with $+/-$ for even/odd lm. Obviously, this is an even function of ξ, so we have

$$F_\perp^\diamondsuit(\xi,\eta) = F_\perp^\diamondsuit(-\xi,\eta) \qquad \text{(B.42)}$$

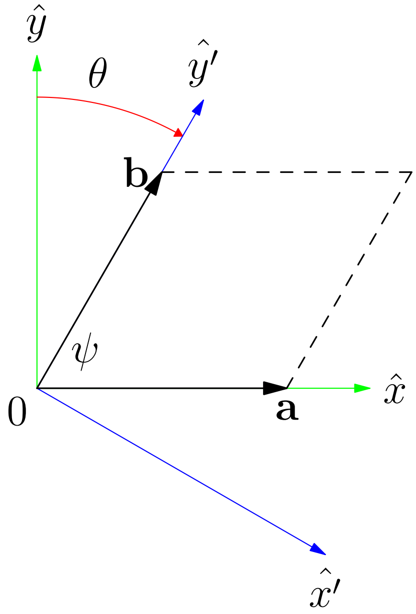

Figure B.2: Rotate the coordinate systems to use the Lekner-cyclic method.

Together with the general result Eq. B.21, we have

$$F_{\perp}^{\diamondsuit}(\xi,\eta) = F_{\perp}^{\diamondsuit}(\xi,-\eta) \tag{B.43}$$

as we claimed in Sec.B.1.2.

Note that Eq. B.40 does not apply to $\eta = 0$. Moreover, the convergence will be very slow for $\eta \to 0$. Unfortunately, we cannot apply the Poisson-Jacobi identity to the m-sum in the derivation, simply because m shows up in two places: $(\xi+l+\beta m)^2$ and $(\eta+\gamma m)^2$. The deep reason is that the $\xi \leftrightarrow \eta$ symmetry is generally broken. Therefore, the Lekner-cyclic method "fails". However, with a simple rotation trick [32, 25], the Lekner-cyclic method survives. The trick is using the new $x'y'$ coordinate system that is obtained by counterclockwise rotating the xy coordinate system about the z axis through an angle $\theta = \pi/2-\psi$, see Fig. B.2.

After the rotation, the coordinates (x, y) becomes

$$\begin{pmatrix} x' \\ y' \end{pmatrix} = \begin{pmatrix} \cos\theta & -\sin\theta \\ \sin\theta & \cos\theta \end{pmatrix} \begin{pmatrix} x \\ y \end{pmatrix} = \begin{pmatrix} \gamma & -\beta \\ \beta & \gamma \end{pmatrix} \begin{pmatrix} x \\ y \end{pmatrix}.$$

So we have

$$\begin{pmatrix} \xi' \\ \eta' \end{pmatrix} = \begin{pmatrix} \gamma & -\beta \\ \beta & \gamma \end{pmatrix} \begin{pmatrix} \xi \\ \eta \end{pmatrix}. \tag{B.44}$$

and the lattice vectors

$$\begin{aligned}
\mathbf{a} &= L\hat{\mathbf{x}} = L(\gamma\hat{\mathbf{x}}' + \beta\hat{\mathbf{y}}') \\
\mathbf{b} &= L(\beta\hat{\mathbf{x}} + \gamma\hat{\mathbf{y}}) = L\hat{\mathbf{y}}' \qquad \text{(B.45)}
\end{aligned}$$

So

$$\begin{aligned}
F_\perp(\xi,\eta) &\equiv \sum_{l,m=-\infty}^{\infty}{}' \frac{1}{[(\xi+l+\beta m)^2+(\eta+\gamma m)^2]^{\frac{3}{2}}} \qquad \text{(B.46)} \\
&= \sum_{l,m=-\infty}^{\infty}{}' \frac{1}{[(\xi'+\gamma l)^2+(\eta'+\beta l+m)^2]^{\frac{3}{2}}} \qquad \text{(B.47)} \\
&\equiv F'_\perp(\xi',\eta') \\
&= F_\perp(\eta',\xi'). \qquad \text{(B.48)}
\end{aligned}$$

The last equation is due to the $l \leftrightarrow m$ symmetry clearly seen from Eq. B.46 and B.47. Simply exchanging l and m and replacing ξ and η by η' and ξ' in Eq. B.40, we have

$$F_\perp(\xi,\eta) = \frac{2\pi^2}{\gamma^2\sin^2(\pi\xi'/\gamma)} + 8\pi\sum_{m>0}\sum_{l}\cos(2\pi m(\eta'+\beta l))\frac{m}{|\xi'+\gamma l|}K_1(2\pi m|\xi'+\gamma l|). \qquad \text{(B.49)}$$

Now switching between the two representations of summations (Eq. B.40 and Eq. B.49) allows us to achieve fast convergence. The naive switching criterion would be comparing η with ξ', if $\eta < \xi'$, we use Eq. B.49 and vice versa [3].

For the special case $\xi = \eta = 0$, we have

$$F_\perp(0,0) = 2\zeta(3) + \frac{4}{\gamma^2}\zeta(2) + 16\pi\sum_{m>0}\sum_{l>0}\frac{l}{\gamma m}K_1(2\pi l\gamma m)\cos(2\pi l\beta m). \qquad \text{(B.50)}$$

For details, see Sec. B.3.4.

B.2.3 2D: square unit cell and $\mathbf{H} \parallel \hat{\mathbf{y}}$

Now we apply the Lekner formalism to Eq. B.25.

$$F_\parallel^\square(\xi,\eta) \equiv \sum_l\sum_m \frac{3(\eta+m)^2-[(\xi+l)^2+(\eta+m)^2]}{[(\xi+l)^2+(\eta+m)^2]^{\frac{5}{2}}}$$

We use two methods.

Method I

$$F_\parallel^\square(\xi,\eta) = -\sum_m[1+\eta'\frac{\partial}{\partial\eta'}]f(\xi,\eta') \qquad \text{(B.51)}$$

---

[3] This criterion is naive because the oscillating cos() functions will complicate the calculations.

with $\eta' \equiv \eta + m$ and

$$f(\xi,\eta') \equiv \sum_l \frac{1}{[(\xi+l)^2+\eta'^2]^{\frac{3}{2}}} = \frac{2}{\eta'^2} + 8\pi \sum_{l>0} \cos(2\pi l\xi) \frac{l}{|\eta'|} K_1(2\pi l|\eta'|). \quad \text{(B.52)}$$

where we have used the result in deriving $F_\perp^\square(\xi,\eta)$. With the recurrence formulas for modified Bessel function, (see Sec. B.3.5), one can derive that

$$\begin{aligned} F_\parallel^\square(\xi,\eta) &= \sum_m \left(\frac{2}{\eta'^2} + 8\pi \sum_{l>0} \cos(2\pi l\xi) \left(\frac{l}{|\eta'|} K_1(2\pi l|\eta'|) + 2\pi l^2 K_0(2\pi l|\eta'|) \right) \right) \\ &= F_\perp^\square(\xi,\eta) + 16\pi^2 \sum_{l>0} \sum_m l^2 \cos(2\pi l\xi) K_0(2\pi l|\eta+m|) \qquad \text{(B.53)} \end{aligned}$$

Method II

$$F_\parallel^\square(\xi,\eta) = \sum_l \sum_m \left(\frac{3(\eta+m)^2}{[(\xi+l)^2+(\eta+m)^2]^{\frac{5}{2}}} - \frac{1}{[(\xi+l)^2+(\eta+m)^2]^{\frac{3}{2}}} \right) \quad \text{(B.54)}$$

Note that the 2nd term is just $F_\perp^\square(\xi,\eta)$. So we focus on the 1st term:

$$\begin{aligned} & \sum_l \sum_m \frac{3(\eta+m)^2}{[(\xi+l)^2+(\eta+m)^2]^{\frac{5}{2}}} \\ = \ & \sum_l \sum_m \frac{3(\eta+m)^2}{\Gamma(\frac{5}{2})} \int_0^\infty \mathrm{d}t\ t^{\frac{3}{2}} \exp\left\{-[(\xi+l)^2+(\eta+m)^2]t\right\} \\ = \ & \sum_l \frac{3}{\Gamma(\frac{5}{2})} \int_0^\infty \mathrm{d}t\ t^{\frac{3}{2}} \left\{ \sum_m (\eta+m)^2 \exp\left[-(\eta+m)^2 t\right] \right\} \exp\left[-(\xi+l)^2 t\right] \\ = \ & \sum_l \frac{3}{\Gamma(\frac{5}{2})} \int_0^\infty \mathrm{d}t\ t^{\frac{3}{2}}\ \exp\left[-(\xi+l)^2 t\right] \\ & \cdot \left\{ \frac{1}{2} \left(\frac{\pi}{t^3}\right)^{\frac{1}{2}} \sum_m e^{-\pi^2 m^2/t}\ \cos(2\pi m\eta) - \left(\frac{\pi}{t}\right)^{\frac{5}{2}} \sum_m m^2 e^{-\pi^2 m^2/t}\ \cos(2\pi m\eta) \right\} \end{aligned} \quad \text{(B.55)}$$

Note that the 1st term in Eq. B.55 is

$$\begin{aligned} & \frac{3}{\Gamma(\frac{5}{2})} \frac{\pi^{\frac{1}{2}}}{2} \sum_l \sum_m \cos(2\pi m\eta) \int_0^\infty \mathrm{d}t\ \exp\left[-\pi^2 m^2/t - (\xi+l)^2 t\right] \\ = \ & \sum_l \sum_m 2\cos(2\pi m\eta) \int_0^\infty \mathrm{d}t\ \exp\left[-\pi^2 m^2/t - (\xi+l)^2 t\right] \\ = \ & F_\perp^\square(\xi,\eta) \end{aligned} \quad \text{(B.56)}$$

which cancels the 2nd term in Eq. B.54 exactly. So we have

$$\begin{aligned} F_{\parallel}^{\square}(\xi,\eta) &= -4\pi^2 \sum_l \sum_{m\neq 0} m^2 \cos(2\pi m\eta) \int_0^\infty \mathrm{d}t\ t^{-1} \exp\left[-\pi^2 m^2/t - (\xi+l)^2 t\right] \\ &= -4\pi^2 \sum_l 2 \sum_{m>0} m^2 \cos(2\pi m\eta) 2 \left(\pi \left|\frac{m}{\xi+l}\right|\right)^0 K_0(2\pi|m(\xi+l)|) \\ &= -16\pi^2 \sum_l \sum_{m>0} m^2 \cos(2\pi m\eta) K_0(2\pi m|\xi+l|) \qquad \text{(B.57)} \end{aligned}$$

We have checked that Eq. B.57 is consistent with Eq. B.53.

B.2.4 3D: cubic unit cell and $\mathbf{H} \parallel \hat{\mathbf{z}}$

Now we apply the Lekner formalism to Eq. B.27.

$$F_z(\xi,\eta,\zeta) \equiv \sum_l \sum_m \sum_n \frac{3(\zeta+n)^2 - [(\xi+l)^2 + (\eta+m)^2 + (\zeta+n)^2]}{[(\xi+l)^2 + (\eta+m)^2 + (\zeta+n)^2]^{\frac{5}{2}}}$$

To apply the Lekner formalism, we use four methods.

Method I

$$F_z(\xi,\eta,\zeta) = -\sum_n [1 + \zeta' \frac{\partial}{\partial \zeta'}] f(\xi,\eta,\zeta') \qquad \text{(B.58)}$$

with $\zeta' \equiv \zeta + n$ and

$$\begin{aligned} f(\xi,\eta,\zeta') &\equiv \sum_l \sum_m \frac{1}{[(\xi+l)^2 + (\eta+m)^2 + \zeta'^2]^{\frac{3}{2}}} \\ &= \sum_l \sum_m \frac{1}{\Gamma(\frac{3}{2})} \int_0^\infty \mathrm{d}t\ t^{\frac{1}{2}} \exp\left\{-\left[(\xi+l)^2 + (\eta+m)^2 + \zeta'^2\right] t\right\} \\ &= 2 \sum_l \sum_m \cos(2\pi l\xi) \int_0^\infty \mathrm{d}t\ \ \exp\left\{-\pi^2 l^2/t - [(\eta+m)^2 + \zeta'^2] t\right\} \end{aligned} \qquad \text{(B.59)}$$

Evaluate the $l = 0$ part:

$$f_{l=0}(\xi,\eta,\zeta') = \sum_m \frac{2}{(\eta+m)^2 + \zeta'^2} = \frac{2\pi}{\zeta'} \frac{\sinh(2\pi\zeta')}{\cosh(2\pi\zeta') - \cos(2\pi\eta)}. \qquad \text{(B.60)}$$

The detail of the last line is shown in Sec. B.3.2 (Eq. B.78). For the $l \neq 0$ part:

$$\begin{aligned}
f_{l\neq 0}(\xi,\eta,\zeta') &= 2\sum_{l\neq 0}\sum_{m}\cos(2\pi l\xi)2\left(\pi\left|\frac{l}{[(\eta+m)^2+\zeta'^2]^{\frac{1}{2}}}\right|\right)^{1} \\
&\quad \cdot K_1(2\pi l[(\eta+m)^2+\zeta'^2]^{\frac{1}{2}}) \\
&= 8\pi\sum_{l>0}\sum_{m}\cos(2\pi l\xi)\frac{l}{[(\eta+m)^2+\zeta'^2]^{\frac{1}{2}}} \\
&\quad \cdot K_1(2\pi l[(\eta+m)^2+\zeta'^2]^{\frac{1}{2}}) \qquad \text{(B.61)}
\end{aligned}$$

Now plug Eq. B.60 and Eq. B.61 into Eq. B.58 and differentiate them w.r.t ζ', we have

$$\begin{aligned}
F_z(\xi,\eta,\zeta) &= 4\pi^2\sum_{n}\frac{\cos(2\pi\eta)\cosh(2\pi(\zeta+n))-1}{[\cos(2\pi\eta)-\cosh(2\pi(\zeta+n))]^2} \\
&\quad -8\pi\sum_{l>0}\sum_{m}\sum_{n}\cos(2\pi l\xi)\frac{l}{[(\eta+m)^2+(\zeta+n)^2]^{\frac{3}{2}}} \\
&\quad \cdot\left\{[(\eta+m)^2-(\zeta+n)^2]K_1(\lambda)-(\zeta+n)^2\lambda K_0(\lambda)\right\}
\end{aligned}$$

(B.62)

with $\lambda = 2\pi l[(\eta+m)^2+(\zeta+n)^2]^{\frac{1}{2}}$.

Method II

Note that in the calculation of $f(\xi,\eta,\zeta')$, if we apply the Poisson-Jacobi identity to both l and m summations, we have

$$\begin{aligned}
f(\xi,\eta,\zeta') &\equiv \sum_l \sum_m \frac{1}{[(\xi+l)^2+(\eta+m)^2+\zeta'^2]^{\frac{3}{2}}} \\
&= \sum_l \sum_m \frac{1}{\Gamma(\frac{3}{2})} \int_0^\infty \mathrm{d}t\; t^{\frac{1}{2}} \exp\left\{-\left[(\xi+l)^2+(\eta+m)^2+\zeta'^2\right] t\right\} \\
&= \frac{1}{\Gamma(\frac{3}{2})} \int_0^\infty \mathrm{d}t\; t^{\frac{1}{2}} \left[\left(\frac{\pi}{t}\right)^{\frac{1}{2}} \sum_l e^{-\pi^2 l^2/t} \cos(2\pi l\xi)\right] \\
&\quad \cdot \left[\left(\frac{\pi}{t}\right)^{\frac{1}{2}} \sum_m e^{-\pi^2 m^2/t} \cos(2\pi m\eta)\right] e^{-\zeta'^2 t} \\
&= \frac{\pi}{\Gamma(\frac{3}{2})} \int_0^\infty \mathrm{d}t\; t^{-\frac{1}{2}} \left[1+2\sum_{l>0} \cos(2\pi l\xi) e^{-\pi^2 l^2/t}\right] \\
&\quad \cdot \left[1+2\sum_{m>0} \cos(2\pi m\eta) e^{-\pi^2 m^2/t}\right] e^{-\zeta'^2 t} \\
&= \frac{\pi}{\Gamma(\frac{3}{2})} \Big\{ \int_0^\infty \mathrm{d}t\; t^{-\frac{1}{2}} e^{-\zeta'^2 t} + 2\sum_{l>0} \cos(2\pi l\xi) \int_0^\infty \mathrm{d}t\; t^{-\frac{1}{2}} e^{-\zeta'^2 t-\pi^2 l^2/t} \\
&\quad +2\sum_{m>0} \cos(2\pi m\eta) \int_0^\infty \mathrm{d}t\; t^{-\frac{1}{2}} e^{-\zeta'^2 t-\pi^2 m^2/t} \\
&\quad +4\sum_{l>0}\sum_{m>0} \cos(2\pi l\xi)\cos(2\pi m\eta) \int_0^\infty \mathrm{d}t\; t^{-\frac{1}{2}} e^{-\zeta'^2 t-\pi^2(l^2+m^2)/t} \Big\} \\
&= \frac{2\pi}{|\zeta'|} \Big\{ 1+2\sum_{l>0} \cos(2\pi l\xi) e^{-2\pi l|\zeta'|} + 2\sum_{m>0} \cos(2\pi m\eta) e^{-2\pi m|\zeta'|} \\
&\quad +4\sum_{l>0}\sum_{m>0} \cos(2\pi l\xi)\cos(2\pi m\eta) e^{-2\pi(l^2+m^2)^{\frac{1}{2}}|\zeta'|} \Big\} \qquad \text{(B.63)}
\end{aligned}$$

where we have used the fact that $\int_0^\infty \mathrm{d}t\, t^{-\frac{1}{2}} e^{-\zeta'^2 t} = \frac{\sqrt{\pi}}{|\zeta'|}$ and $K_{\frac{1}{2}}(z) = \left(\frac{\pi}{2z}\right)^{\frac{1}{2}} e^{-z}$.

The single sums are readily evaluated as the real part of a geometric series:

$$\sum_{l=1}^{\infty} \cos(2\pi l\xi) e^{-2\pi l|\zeta'|} = \mathrm{Re}\left\{\sum_{l=1}^{\infty} e^{-2\pi l(|\zeta'|+i\xi)}\right\} = \frac{Z\cos(2\pi\xi)-1}{Z^2-2Z\cos(2\pi\xi)+1} \qquad \text{(B.64)}$$

with $Z = e^{2\pi|\zeta'|}$. Then we have

$$\begin{aligned} F_z(\xi,\eta,\zeta) &= -\sum_n [1+\zeta'\frac{\partial}{\partial\zeta'}] f(\xi,\eta,\zeta') \\ &= 8\pi^2\Big\{\sum_n Z\Big[\frac{Z^2\cos(2\pi\xi)-2Z+\cos(2\pi\xi)}{(Z^2-2Z\cos(2\pi\xi)+1)^2} \\ &\quad +\frac{Z^2\cos(2\pi\eta)-2Z+\cos(2\pi\eta)}{(Z^2-2Z\cos(2\pi\eta)+1)^2}\Big] \\ &\quad +2\sum_n\sum_{l>0}\sum_{m>0}(l^2+m^2)^{\frac{1}{2}} Z^{-(l^2+m^2)^{\frac{1}{2}}}\cos(2\pi l\xi)\cos(2\pi m\eta)\Big\} \end{aligned} \tag{B.65}$$

I have checked that Eq. B.62 and Eq. B.65 give the same result.

Method III

$$\begin{aligned} F_z(\xi,\eta,\zeta) &= \sum_l\sum_m\sum_n\Bigg(\frac{3(\zeta+n)^2}{[(\xi+l)^2+(\eta+m)^2+(\zeta+n)^2]^{\frac{5}{2}}} \\ &\quad -\frac{1}{[(\xi+l)^2+(\eta+m)^2+(\zeta+n)^2]^{\frac{3}{2}}}\Bigg) \end{aligned} \tag{B.66}$$

For the 2nd term, if we apply the Poisson-Jacobi identity to the n sum, we will get

$$2\sum_l\sum_m\sum_n \cos(2\pi n\zeta)\int_0^\infty dt\ \exp\left\{-\pi^2n^2/t-[(\xi+l)^2+(\eta+m)^2]t\right\} \tag{B.67}$$

Now we consider the 1st term in Eq. B.66:

$$\begin{aligned}
& \sum_l \sum_m \sum_n \frac{3(\zeta+n)^2}{[(\xi+l)^2+(\eta+m)^2+(\zeta+n)^2]^{\frac{5}{2}}} \\
= & \sum_l \sum_m \sum_n \frac{3(\zeta+n)^2}{\Gamma(\frac{5}{2})} \int_0^\infty \mathrm{d}t\ t^{\frac{3}{2}} \exp\left\{-[(\xi+l)^2+(\eta+m)^2+(\zeta+n)^2]t\right\} \\
= & \sum_l \sum_m \frac{3}{\Gamma(\frac{5}{2})} \int_0^\infty \mathrm{d}t\ t^{\frac{3}{2}} \left\{\sum_n (\zeta+n)^2 \exp\left[-(\zeta+n)^2 t\right]\right\} \\
& \exp\left\{-[(\xi+l)^2+(\eta+m)^2]t\right\} \\
= & \sum_l \sum_m \frac{3}{\Gamma(\frac{5}{2})} \int_0^\infty \mathrm{d}t\ t^{\frac{3}{2}} \exp\left\{-[(\xi+l)^2+(\eta+m)^2]t\right\} \\
& \cdot \left\{\frac{1}{2}\left(\frac{\pi}{t^3}\right)^{\frac{1}{2}} \sum_n e^{-\pi^2 n^2/t}\ \cos(2\pi n\zeta) - \left(\frac{\pi}{t}\right)^{\frac{5}{2}} \sum_n n^2 e^{-\pi^2 n^2/t}\ \cos(2\pi n\zeta)\right\} \\
= & 2\sum_l \sum_m \sum_n \cos(2\pi n\zeta) \int_0^\infty \mathrm{d}t\ \exp[-\pi^2 n^2/t - [(\xi+l)^2+(\eta+m)^2]t] \\
& -4\pi^2 \sum_l \sum_m \sum_n n^2 \cos(2\pi n\zeta) \\
& \int_0^\infty \mathrm{d}t\ t^{-1} \exp[-\pi^2 n^2/t - [(\xi+l)^2+(\eta+m)^2]t] \qquad \text{(B.68)}
\end{aligned}$$

Note that the 1st term in Eq. B.68 will cancel exactly Eq. B.67, so we have

$$\begin{aligned}
F_z(\xi,\eta,\zeta) = & -4\pi^2 \sum_l \sum_m \sum_n n^2 \cos(2\pi n\zeta) \\
& \cdot \int_0^\infty \mathrm{d}t\ t^{-1} \exp\left\{-\pi^2 n^2/t - [(\xi+l)^2+(\eta+m)^2]t\right\} \\
= & -4\pi^2 \sum_l \sum_m \sum_{n\neq 0} n^2 \cos(2\pi n\zeta) \\
& \cdot \int_0^\infty \mathrm{d}t\ t^{-1} \exp\left\{-\pi^2 n^2/t - [(\xi+l)^2+(\eta+m)^2]t\right\} \\
= & -4\pi^2 \sum_l \sum_m 2 \sum_{n>0} n^2 \cos(2\pi n\zeta)\ 2K_0\left(2\pi\left|n[(\xi+l)^2+(\eta+m)^2]^{\frac{1}{2}}\right|\right) \\
= & -16\pi^2 \sum_l \sum_m \sum_{n>0} n^2 \cos(2\pi n\zeta)\ K_0\left(2\pi\left|n[(\xi+l)^2+(\eta+m)^2]^{\frac{1}{2}}\right|\right)
\end{aligned}$$

(B.69)

This is the simplest expression for $F_z(\xi,\eta,\zeta)$.

Method IV

$$
\begin{aligned}
F_z(\xi,\eta,\zeta) &= +\sum_l\sum_m\sum_n \frac{2(\zeta+n)^2}{[(\xi+l)^2+(\eta+m)^2+(\zeta+n)^2]^{\frac{5}{2}}} \\
&\quad -\sum_l\sum_m\sum_n \frac{(\xi+l)^2}{[(\xi+l)^2+(\eta+m)^2+(\zeta+n)^2]^{\frac{5}{2}}} \\
&\quad -\sum_l\sum_m\sum_n \frac{(\eta+m)^2}{[(\xi+l)^2+(\eta+m)^2+(\zeta+n)^2]^{\frac{5}{2}}} \\
&\equiv 2A_\zeta - B_\xi - C_\eta
\end{aligned}
\tag{B.70}
$$

Then we evaluate A_ζ,B_ξ, C_η separately. Actually, they have already been evaluated in method I and method II. We have

$$
\begin{aligned}
A_\zeta &= \frac{1}{3}\sum_m \frac{2\pi}{(\eta+m)}\frac{\sinh(2\pi(\eta+m))}{(\cosh(2\pi(\eta+m))-\cos(2\pi\xi))} \\
&\quad +\frac{8\pi}{3}\sum_l\sum_m\sum_{n>0} n\cos(2\pi n\zeta)[(\xi+l)^2+(\eta+m)^2]^{-\frac{1}{2}} \\
&\quad \cdot K_1(2\pi n[(\xi+l)^2+(\eta+m)^2]^{\frac{1}{2}}) \\
&\quad +\frac{16\pi^2}{3}\sum_l\sum_m\sum_{n>0} n^2\cos(2\pi n\zeta)K_0(2\pi n[(\xi+l)^2+(\eta+m)^2]^{\frac{1}{2}})
\end{aligned}
\tag{B.71}
$$

$$
\begin{aligned}
B_\xi &= \frac{1}{3}\sum_n \frac{2\pi}{(\zeta+n)}\frac{\sinh(2\pi(\zeta+n))}{(\cosh(2\pi(\zeta+n))-\cos(2\pi\eta))} \\
&\quad +\frac{8\pi}{3}\sum_n\sum_m\sum_{l>0} l\cos(2\pi l\xi)[(\zeta+n)^2+(\eta+m)^2]^{-\frac{1}{2}} \\
&\quad \cdot K_1(2\pi n[(\zeta+n)^2+(\eta+m)^2]^{\frac{1}{2}}) \\
&\quad +\frac{16\pi^2}{3}\sum_n\sum_m\sum_{l>0} l^2\cos(2\pi l\xi)K_0(2\pi l[(\zeta+n)^2+(\eta+m)^2]^{\frac{1}{2}})
\end{aligned}
\tag{B.72}
$$

$$
\begin{aligned}
C_\eta &= \frac{1}{3}\sum_l \frac{2\pi}{(\xi+l)}\frac{\sinh(2\pi(\xi+l))}{(\cosh(2\pi(\xi+l))-\cos(2\pi\zeta))} \\
&\quad +\frac{8\pi}{3}\sum_l\sum_n\sum_{m>0} m\cos(2\pi m\eta)[(\xi+l)^2+(\zeta+n)^2]^{-\frac{1}{2}} \\
&\quad \cdot K_1(2\pi m[(\xi+l)^2+(\zeta+n)^2]^{\frac{1}{2}}) \\
&\quad +\frac{16\pi^2}{3}\sum_l\sum_n\sum_{m>0} m^2\cos(2\pi m\eta)K_0(2\pi m[(\xi+l)^2+(\zeta+n)^2]^{\frac{1}{2}})
\end{aligned}
\tag{B.73}
$$

Summary of $F_z(\xi,\eta,\zeta)$. I have derived four different expressions, eq. Eq.B.62, B.65, B.69, B.70. Numerical tests show that only method I and method II are

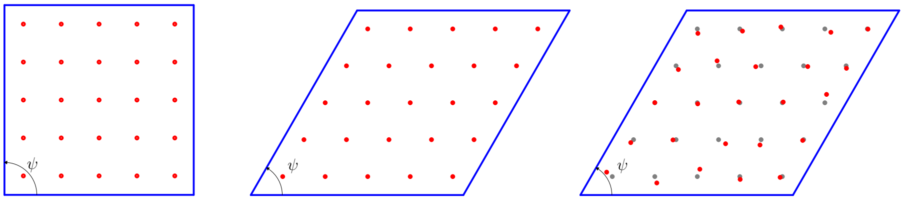

Figure B.3: Spins or particles (red points) within the unit cell (shown in blue lines). (Left) Spins are set on regular lattice sites. Square unit cell $\psi = \pi/2$. (Middle) Spins are set on regular lattice sites. Rhombus unit cell with $\psi = \pi/3$. (Right) Spin positions randomly deviate from the regular lattice sites (grey dots). Rhombus unit cell with $\psi = \pi/3$.

equivalent to each other. Method III and IV will give quite different results. Further investigations will be necessary to check the consistency of the Lekner formalism for dipolar interactions in 3D.

B.3 Some Details

B.3.1 Calculation of the F-matrix

Square lattice within square unit cell

Suppose that all spins sit on a $L \times L$ square lattice (within the square unit cell) with the grid spacing set to be 1, see Applied/Appendix/Lekner/Fig. B.3(left). Then the translation invariance plays a key role in saving the computing time of the pair-wise dipolar interactions.

The coordinates of those spins can be chosen from those values: $x_i, y_i, x_j, y_j = 0, 1, 2, \cdots, L-1$ and therefore $\xi_{ij}, \eta_{ij} = -\frac{L-1}{L}, -\frac{L-2}{L}, \cdots, \frac{L-2}{L}, \frac{L-1}{L}$. Since $F(\xi, \eta) = F(|\xi|, |\eta|)$, so what we really need is just the F-matrix with elements given by

$$\mathbf{F}_{mn} = F\left(\frac{m}{L}, \frac{n}{L}\right) \tag{B.74}$$

with $m, n = 0, 1, \cdots, L-1$.

Using the symmetry property of $F(\xi, \eta)$, i.e. Eq.B.13 and B.16, will further save the computing time. Due to Eq.B.13, we just need to calculate the upper or lower triangle of the symmetric $F-$matrix. Due to Eq.B.16, the number of rows (n_r) we need to calculate is $\frac{L}{2}+1$ for even L and $\frac{L+1}{2}$ for odd L. So the total number of elements we need to calculate is just $\frac{n_\mathrm{r}(1+n_\mathrm{r})}{2} = \frac{L^2+4L+3}{8}$ for even L and $\frac{L^2+6L+8}{8}$ for odd L, see the boxed elements shown in Eq. B.75 and B.76. The running time of the F-matrix calculation in the case of square unit cell thus scales as $\mathcal{O}(N)$ with $N = L^2$ the system size.

$$\begin{pmatrix} \boxed{F_{00}} & F_{01} & F_{02} & F_{03} \\ \boxed{F_{10}} & \boxed{F_{11}} & F_{12} & F_{13} \\ \boxed{F_{20}} & \boxed{F_{21}} & \boxed{F_{22}} & F_{23} \\ F_{30} & F_{31} & F_{32} & F_{33} \end{pmatrix} \tag{B.75}$$

$$\begin{pmatrix} \boxed{F_{00}} & F_{01} & F_{02} & F_{03} & F_{04} \\ \boxed{F_{10}} & \boxed{F_{11}} & F_{12} & F_{13} & F_{14} \\ \boxed{F_{20}} & \boxed{F_{21}} & \boxed{F_{22}} & F_{23} & F_{24} \\ F_{30} & F_{31} & F_{32} & F_{33} & F_{34} \\ F_{40} & F_{41} & F_{42} & F_{43} & F_{44} \end{pmatrix} \tag{B.76}$$

Triangular lattice within rhombus unit cell with $\psi = \pi/3$

For lattice within non-rectangular shape of unit cell, e.g. the triangular lattice within the rhombus with angle $\psi = \pi/3$, it is still possible to use the translation invariance of the lattice and symmetric properties of $F(\xi, \eta)$ to speed up the calculation of the F-matrix.

See Applied/Appendix/Lekner/Fig. B.3(middle), the coordinates of those spins can be written as $x_i = m + \beta n$, $y_i = \gamma n$ with $m, n \in [0, L)$ and $\beta = 1/2$, $\gamma = \sqrt{3}/2$. Considering Eq. B.22 and B.23, we define two new integer variables $X \equiv 2L|\xi| = 2|x_i - x_j|$ and $Y \equiv 2L|\eta|/\sqrt{3} = 2|y_i - y_j|/\sqrt{3}$, then we only need to calculate the F-matrix

$$\mathbf{F}_{XY} = F\left(\frac{X}{2L}, \frac{\sqrt{3}Y}{2L}\right) \tag{B.77}$$

with $X \in [0, 3(L-1)]$, $Y \in [0, (L-1)]$. $F(\xi, \eta) = F(\xi - 1, \eta)$ indicates $\mathbf{F}_{XY} = \mathbf{F}_{X-2L,Y}$, which will further save the computing time. The running time of the F-matrix calculation scales as $\mathcal{O}(N)$.

Note that for $Y = 0$ ($\eta = 0$), those elements with $X \geq 2L$ ($\xi \geq 1$) will cause divergence. [4] Fortunately, those elements will not show up in our calculation because if $Y = 0$ then the actual range of X is just $[0, 2(L-1)]$. In other words, if $\eta = 0$, then we must have $\xi < 1$.

Random spins within rhombus unit cell with $\psi = \pi/3$

If spins' positions randomly deviate from the regular lattice sites, then the translation invariance is broken, see Applied/Appendix/Lekner/Fig. B.3(right). We have to seriously consider all the $N(N-1)/2$ interaction pairs of spins. This computing scales as $\mathcal{O}(N^2)$ and is very expensive. Fortunately, spin positions are fixed in all our studies, which means we need to calculate the F-matrix

---

[4] From Eq. B.49, we see that the first term diverges if $\xi'/\gamma \in \mathbb{Z}$. This happens in case of $\eta = 0$ and $\xi = 1$.

only once. We can store the result into a binary file, which can be written/read faster than the ASCII (or text) one. Then in our program we just read the F-matrix into an array. The only problem is that this demands big memory space of computer. For $L = 100$, the array needs about $8 \times L^4$ bytes ~ 0.745GB memory.

B.3.2 Calculation of $F_{\perp,l=0}(\xi,\eta)$

Method I:

$$\begin{aligned} 2\sum_m \frac{1}{(\eta+m)^2} &= 2\lim_{\zeta\to 0}\sum_m \frac{1}{(\eta+m)^2+\zeta^2} \\ &= \lim_{\zeta\to 0}\frac{1}{i\zeta}\sum_m\left[\frac{1}{\eta+m-i\zeta}-\frac{1}{\eta+m+i\zeta}\right] \\ &= \lim_{\zeta\to 0}\frac{1}{i\zeta}\{\pi\cot[\pi(\eta-i\zeta)]-\pi\cot[\pi(\eta+i\zeta)]\} \\ &= \lim_{\zeta\to 0}\frac{(2\pi/\zeta)\sinh(2\pi\zeta)}{\cosh(2\pi\zeta)-\cos(2\pi\eta)} \\ &= \frac{2\pi^2}{\sin^2(\pi\eta)} \end{aligned} \tag{B.78}$$

where we have used the Mittag-Leffler expansion of a cotangent:

$$\sum_m \frac{1}{z+m} = \pi\cot(\pi z). \tag{B.79}$$

Method II:

$$\begin{aligned} \sum_m \frac{1}{(\eta+m)^2} &= \sum_{m<0}\frac{1}{(\eta+m)^2}+\sum_{m>0}\frac{1}{(\eta+m)^2}+\frac{1}{\eta^2} \\ &= \sum_{m>0}\frac{1}{(m-\eta)^2}+\sum_{m>0}\frac{1}{(m+\eta)^2}+\frac{1}{\eta^2} \\ &= \psi_1(1-\eta)+\psi_1(1+\eta)+\frac{1}{\eta^2} \\ &= \left[-\psi_1(\eta)+\frac{\pi^2}{\sin^2(\pi\eta)}\right]+\left[\psi_1(\eta)-\frac{1}{\eta^2}\right]+\frac{1}{\eta^2} \\ &= \frac{\pi^2}{\sin^2(\pi\eta)} \end{aligned} \tag{B.80}$$

where we have used the properties of the polygamma function $\psi_n(z)$:

$$\psi_n(z) = (-1)^{n+1}\; n! \sum_{k=0}^{+\infty} \frac{1}{(k+z)^{n+1}} \tag{B.81}$$

$$\psi_n(1+z) = (-1)^{n+1}\; n! \sum_{k=1}^{+\infty} \frac{1}{(k+z)^{n+1}} \tag{B.82}$$

$$\psi_n(1+z) = \psi_n(z) + (-1)^n\; n!\; z^{-n-1} \tag{B.83}$$

$$\psi_n(1-z) = (-1)^n \psi_n(z) + (-1)^n\; \pi \frac{\mathrm{d}^n}{\mathrm{d}z^n} \cot(\pi z). \tag{B.84}$$

B.3.3 Calculation of $F_\perp^\square(0,0)$

Note that this special case corresponds to the periodic repetition of particle i itself gives dipolar interactions on the particle i in the central cell, which is the so called self-energy. Since in the central cell the particle i does not interact with itself, so in calculating $F_\perp^\square(0,0)$, the $l = m = 0$ term must be explicitly excluded. The summation is then denoted as $\sum'_{l,m}(\cdots) = \sum_l \sum_m(\cdots) -$ ($l = m = 0$ term). So we have

$$\begin{aligned} F_\perp^\square(0,0) &= \sum_{l,m}{}' \frac{1}{(l^2+m^2)^{\frac{3}{2}}} \\ &= \sum_{m<0} \sum_{l} \frac{1}{(l^2+m^2)^{\frac{3}{2}}} + \sum_{l \neq 0} \frac{1}{|l|^3} + \sum_{m>0} \sum_{l} \frac{1}{(l^2+m^2)^{\frac{3}{2}}} \\ &= 2\sum_{l>0} \frac{1}{l^3} + 2\sum_{m>0}\sum_{l} \frac{1}{(l^2+m^2)^{\frac{3}{2}}} \\ &= 2\zeta(3) + 2S \end{aligned} \tag{B.85}$$

where $\zeta(n)$ is the Riemann zeta function:

$$\zeta(n) = \sum_{k=1}^{\infty} \frac{1}{k^n} \tag{B.86}$$

and

$$S \equiv \sum_{m>0} \sum_{l} \frac{1}{(l^2+m^2)^{\frac{3}{2}}} \tag{B.87}$$

which can be calculated with the Lekner formalism:

$$\begin{aligned} S &= \sum_{m>0} \sum_{l} \frac{1}{(l^2+m^2)^{\frac{3}{2}}} \\ &= \sum_{m>0} \sum_{l} \frac{1}{\Gamma(\frac{3}{2})} \int_0^\infty \mathrm{d}t\; t^{\frac{1}{2}} \exp[-(l^2+m^2)t] \\ &= \sum_{m>0} \frac{1}{\Gamma(\frac{3}{2})} \int_0^\infty \mathrm{d}t\; t^{\frac{1}{2}} \left[\left(\frac{\pi}{t}\right)^{\frac{1}{2}} \sum_{l} \exp(-\pi^2 l^2/t) \right] \exp(-m^2 t) \\ &= \sum_{m>0} \sum_{l} 2 \int_0^\infty \mathrm{d}t \exp\left[-\pi^2 l^2/t - m^2 t\right] \end{aligned} \tag{B.88}$$

Evaluate the $l = 0$ part separately

$$S_{l=0} = \sum_{m>0} 2 \int_0^\infty \mathrm{d}t \;\exp(-m^2 t) = 2 \sum_{m>0} \frac{1}{m^2} = 2\;\zeta(2) \tag{B.89}$$

For the $l \neq 0$ part,

$$\begin{aligned} S_{l\neq 0} &= \sum_{m>0} 2 \sum_{l>0} 2 \int_0^\infty \mathrm{d}t \;\exp\left[-\pi^2 l^2/t - m^2 t\right] \\ &= \sum_{m>0} 2 \sum_{l>0} 2 \cdot 2 \left(\pi \left|\frac{l}{m}\right|\right)^1 \; K_1(2\pi|lm|) \\ &= 8\pi \sum_{m>0} \sum_{l>0} \frac{l}{m} \; K_1(2\pi lm) \end{aligned} \tag{B.90}$$

So

$$S = 2\zeta(2) + 8\pi \sum_{m>0} \sum_{l>0} \frac{l}{m} \; K_1(2\pi lm) \tag{B.91}$$

and

$$F_\perp^\square(0,0) = 2\zeta(3) + 4\zeta(2) + 16\pi \sum_{m>0} \sum_{l>0} \frac{l}{m} \; K_1(2\pi lm). \tag{B.92}$$

Note that $\zeta(2) = \pi^2/6 = 1.64493$ and $\zeta(3) = 1.20206$. And $F_\perp^\square(0,0)$, which is just a constant, can be numerically calculated. The result is

$$F_\perp^\square(0,0) \simeq 9.0336 \tag{B.93}$$

B.3.4 The calculation of $F_\perp(0,0)$

$$\begin{aligned} F_\perp(0,0) &= \sum_{l,m}{}' \frac{1}{((l+\beta m)^2 + (\gamma m)^2)^{\frac{3}{2}}} \\ &= \sum_{l\neq 0} \frac{1}{|l|^3} + \sum_{m<0} \sum_{l} \frac{1}{((l+\beta m)^2 + (\gamma m)^2)^{\frac{3}{2}}} \\ &\quad + \sum_{m>0} \sum_{l} \frac{1}{((l+\beta m)^2 + (\gamma m)^2)^{\frac{3}{2}}} \\ &= 2 \sum_{l>0} \frac{1}{l^3} + \sum_{m>0} \sum_{l} \frac{1}{((l-\beta m)^2 + (-\gamma m)^2)^{\frac{3}{2}}} \\ &\quad + \sum_{m>0} \sum_{l} \frac{1}{((l+\beta m)^2 + (\gamma m)^2)^{\frac{3}{2}}} \\ &= 2\zeta(3) + 2S \end{aligned} \tag{B.94}$$

where

$$S \equiv \sum_{m>0} \sum_{l} \frac{1}{((l+\beta m)^2 + (\gamma m)^2)^{\frac{3}{2}}} \tag{B.95}$$

which can be calculated with the Lekner formalism:

$$\begin{aligned}
S &= \sum_{m>0}\sum_{l}\frac{1}{((l+\beta m)^2+(\gamma m)^2)^{\frac{3}{2}}} \\
&= \sum_{m>0}\sum_{l}\frac{1}{\Gamma(\frac{3}{2})}\int_0^\infty \mathrm{d}t\; t^{\frac{1}{2}}\exp\{-[(l+\beta m)^2+(\gamma m)^2)]t\} \\
&= \sum_{m>0}\frac{1}{\Gamma(\frac{3}{2})}\int_0^\infty \mathrm{d}t\; t^{\frac{1}{2}}\left[\left(\frac{\pi}{t}\right)^{\frac{1}{2}}\sum_{l}\exp(-\pi^2l^2t)\cos(2\pi l\beta m)\right]\exp[-(\gamma m)^2t] \\
&= \sum_{m>0}\sum_{l}2\int_0^\infty \mathrm{d}t\exp[-\pi^2l^2/t-(\gamma m)^2t]\cos(2\pi l\beta m) \qquad \text{(B.96)}
\end{aligned}$$

Evaluate the $l=0$ part separately

$$S_{l=0}=2\sum_{l>0}\int_0^\infty \mathrm{d}t\;\;\exp[-(\gamma m)^2t]=2\sum_{m>0}\frac{1}{(\gamma m)^2}=\frac{2}{\gamma^2}\;\zeta(2) \qquad \text{(B.97)}$$

For the $l\neq 0$ part,

$$\begin{aligned}
S_{l\neq 0} &= 4\sum_{m>0}\sum_{l>0}\int_0^\infty \mathrm{d}t\;\;\exp\left[-\pi^2l^2/t-(\gamma m)^2t\right]\cos(2\pi l\beta m) \\
&= 4\sum_{m>0}\sum_{l>0}2\left(\pi\left|\frac{l}{\gamma m}\right|\right)^1\;K_1(2\pi|l\gamma m|)\;\cos(2\pi l\beta m) \\
&= 8\pi\sum_{m>0}\sum_{l>0}\frac{l}{\gamma m}\;K_1(2\pi l\gamma m)\cos(2\pi l\beta m) \qquad \text{(B.98)}
\end{aligned}$$

So

$$S=\frac{2}{\gamma^2}\;\zeta(2)+8\pi\sum_{m>0}\sum_{l>0}\frac{l}{\gamma m}\;K_1(2\pi l\gamma m)\cos(2\pi l\beta m) \qquad \text{(B.99)}$$

and

$$F_\perp(0,0)=2\zeta(3)+\frac{4}{\gamma^2}\;\zeta(2)+16\pi\sum_{m>0}\sum_{l>0}\frac{l}{\gamma m}\;K_1(2\pi l\gamma m)\cos(2\pi l\beta m). \qquad \text{(B.100)}$$

For $\psi=\pi/3$ ($\beta=1/2$, $\gamma=\sqrt{3}/2$) we have

$$F_\perp^\diamondsuit(0,0)\simeq 11.0342 \qquad \text{(B.101)}$$

B.3.5 Modified Bessel function of the second kind $K_n(z)$

An integral formula for $K_\nu(z)$ is

$$K_n(z)=\frac{\sqrt{\pi}}{(n-\frac{1}{2})!}\left(\frac{z}{2}\right)^n\int_1^\infty \mathrm{d}t\;e^{-zt}(t^2-1)^{n-\frac{1}{2}} \qquad \text{(B.102)}$$

So we have

$$K_1(z)=z\int_1^\infty \mathrm{d}t\;e^{-zt}(t^2-1)^{\frac{1}{2}} \qquad \text{(B.103)}$$

which can be numerically calculated.

Some useful recurrence formulas for $K_\nu(z)$:

$$K'_\nu(z) = -\frac{1}{2}(K_{\nu-1}(z) + K_{\nu+1}(z)) \tag{B.104}$$

$$K_{\nu+1}(z) = K_{\nu-1}(z) + \frac{2\nu}{z}K_\nu(z) \tag{B.105}$$

$$K'_\nu(z) = -(K_{\nu-1}(z) + \frac{\nu}{z}K_\nu(z)) \tag{B.106}$$

B.3.6 Correct implementation of the Lekner summation

The Lekner summations have to be correctly implemented. Otherwise, a very complicated bias may plague computations. [64] The origin of this bias is the slow convergence rate of the modified Bessel functions as their argument tend to zero. Several different procedures have been proposed to overcome this problem.

Lekner-cyclic method

Lekner-cyclic method means switching between the two representations of summations (e.g. Eq. B.34 and Eq. B.35) so that the argument in the Bessel functions would be as large as possible. This allows us to achieve fast convergence. But from numerical point of view, the Lekner summation has been criticized due to a hidden parameter: the truncation cutoff parameter [63, 64]. Look at Eq. B.34 and Eq. B.35. When doing numerical calculations, one should truncate these infinite summations somewhere:

$$F_\perp^\square(\xi,\eta) = \frac{2\pi^2}{\sin^2(\pi\eta)} + 8\pi\sum_{l=1}^{n_\mathrm{c}} l\cos(2\pi l\xi)\sum_{m=-n_\mathrm{k}}^{m=+n_\mathrm{k}}\frac{1}{|\eta+m|}\,K_1(2\pi l|\eta+m|) \tag{B.107}$$

$$F_\perp^\square(\xi,\eta) = \frac{2\pi^2}{\sin^2(\pi\xi)} + 8\pi\sum_{m=1}^{n_\mathrm{c}} m\cos(2\pi m\eta)\sum_{l=-n_\mathrm{k}}^{l=+n_\mathrm{k}}\frac{1}{|\xi+l|}\,K_1(2\pi m|\xi+l|) \tag{B.108}$$

Mazars pointed out that for given n_c and n_k, the above two equations may have very different numerical values [64]. Therfore, the naive application of the Lekner-cyclic symmetry may introduce complicated bias [63].

To avoid this bias when using Lekner-cyclic method, we should use sophisticated truncation scheme based on the following considerations: (1) Bessel function cutoff: for $x > 35$, $K_1(x) < 1.35 \times 10^{-16} < 2.22 \times 10^{-16} =$ EPSILON. Where EPSILON is the machine epsilon (also called machine precision or unit roundoff) in floating point arithmetic, which gives an upper bound on the relative error due to rounding of floating point numbers. So we can safely set up the initial cutoffs (n_c and n_k) according to the condition that the argument of the Bessel function is less than 35. (2) Summation cutoff: we truncate the summation when the absolute value of the last term is within a certain fractional tolerance of the summation of all previous terms. We choose the fractional tolerance to be EPSILON, again. These two criterions will guarantee that we get the most accurate result.

One more thought. The tolerance criterion should be applied prior to multiplication by the trigonometric term, e.g. $\cos(2\pi l\xi)$, since it could be near zero for given l and ξ, regardless of the convergence of the summation of the Bessel functions. For rhombus unit cell, this is impossible due to the fact that both l and m show up in the argument of the cos() function. But for $\psi = \pi/3$, the property Eq. B.41 could be explicitly used to improve/accelerate the convergence.

Lekner-Sperb method

Using the Hurwitz zeta function, Sperb derived an alternative expression which converges faster then the original Lekner expression as the argument of the Bessel functions tends to zero [95]. For example,

$$F_{\perp}^{\square}(\xi,\eta) = \sum_m \sum_l \frac{1}{[(\xi+l)^2+(\eta+m)^2]^{\frac{3}{2}}} \equiv \sum_m g_1(r_m,\xi) \qquad \text{(B.109)}$$

with $r_m \equiv \eta + m$ and

$$\begin{aligned} g_p(r,\xi) &= \sum_l \frac{1}{[(\xi+l)^2+r^2]^{\frac{p+2}{2}}} \\ &= \frac{1}{(\xi^2+r^2)^{\frac{p+2}{2}}} + \sum_{l>0} \frac{1}{[(\xi+l)^2+r^2]^{\frac{p+2}{2}}} + \sum_{l>0} \frac{1}{[(\xi-l)^2+r^2]^{\frac{p+2}{2}}} \end{aligned} \qquad \text{(B.110)}$$

Furthermore, we have

$$\begin{aligned} \frac{1}{[(\xi+l)^2+r^2]^{\frac{p+2}{2}}} &= \frac{1}{(\xi+l)^{p+2}} \frac{1}{\left[1+(\frac{r}{\xi+l})^2\right]^{\frac{p+2}{2}}} \\ &= \frac{1}{(\xi+l)^{p+2}} \sum_{k=0}^{\infty} \binom{-\frac{p+2}{2}}{k} r^{2k} \frac{1}{(\xi+l)^{2k}} \\ &= \sum_{k=0}^{\infty} \binom{-\frac{p+2}{2}}{k} r^{2k} \frac{1}{(\xi+l)^{2k+p+2}} \end{aligned} \qquad \text{(B.111)}$$

and

$$\begin{aligned} \sum_{l>0} \frac{1}{[(\xi+l)^2+r^2]^{\frac{p+2}{2}}} &= \sum_{k=0}^{\infty} \binom{-\frac{p+2}{2}}{k} r^{2k} \sum_{l>0} \frac{1}{(\xi+l)^{2k+p+2}} \\ &= \sum_{k=0}^{\infty} \binom{-\frac{p+2}{2}}{k} r^{2k}\, \zeta(2k+p+2,\xi) \end{aligned} \qquad \text{(B.112)}$$

Here we are using the Hurwitz Zeta function $\zeta(n,x) \equiv \sum_{l=1}^{\infty} \frac{1}{(x+l)^n}$. Therefore,

$$g_p(r,\xi) = \frac{1}{(\xi^2+r^2)^{\frac{p+2}{2}}} + \sum_{k=0}^{\infty} \binom{-\frac{p+2}{2}}{k} r^{2k} \left[\zeta(2k+p+2,\xi) + \zeta(2k+p+2,-\xi)\right]. \tag{B.113}$$

The original Lekner expression Eq. B.34 can then be written as

$$\begin{aligned} F_{\perp}^{\square}(\xi,\eta) &= \frac{2\pi^2}{\sin^2(\pi\eta)} \\ &\quad + \sum_m \left\{ 8\pi \sum_{l>0} \cos(2\pi l\xi) \frac{l}{|\eta+m|}\ K_1(2\pi l|\eta+m|) \right\} \quad \text{(B.114)} \\ &= \frac{2\pi^2}{\sin^2(\pi\eta)} + \sum_m \left\{ -\frac{2}{(\eta+m)^2} + g_1(r_m,\xi) \right\} \quad \text{(B.115)} \\ &= \sum_m g_1(r_m,\xi) \quad \text{(B.116)} \end{aligned}$$

Note that here we have used the fact that $\sum_m \frac{2}{(\eta+m)^2} = \frac{2\pi^2}{\sin^2(\pi\eta)}$.

The Sperb method can then be described as the following procedure: When η is small, e.g. $2\pi\eta < 0.15$, we use the Superb formula, i.e. Eq. B.115. Otherwise, we use Eq. B.114.

B.4 Application

As an example, here we show the domain structure near the coercive field for 2D dipolar RFIM (square unit cell with $\mathbf{H} \perp \hat{\mathbf{x}}$, $\mathbf{H} \perp \hat{\mathbf{y}}$). We define $J_{\text{ex}} = 1$. All other coupling strengths as well as the fields are measured in unit of J_{ex}. With similar parameter ranges, we find similar domain structures (cluster, stripe, labyrinth and checkerboard) near coercive field as observed by Alessandro Magni (e.g. Fig.8 in PRB, 59, 985(1999)).

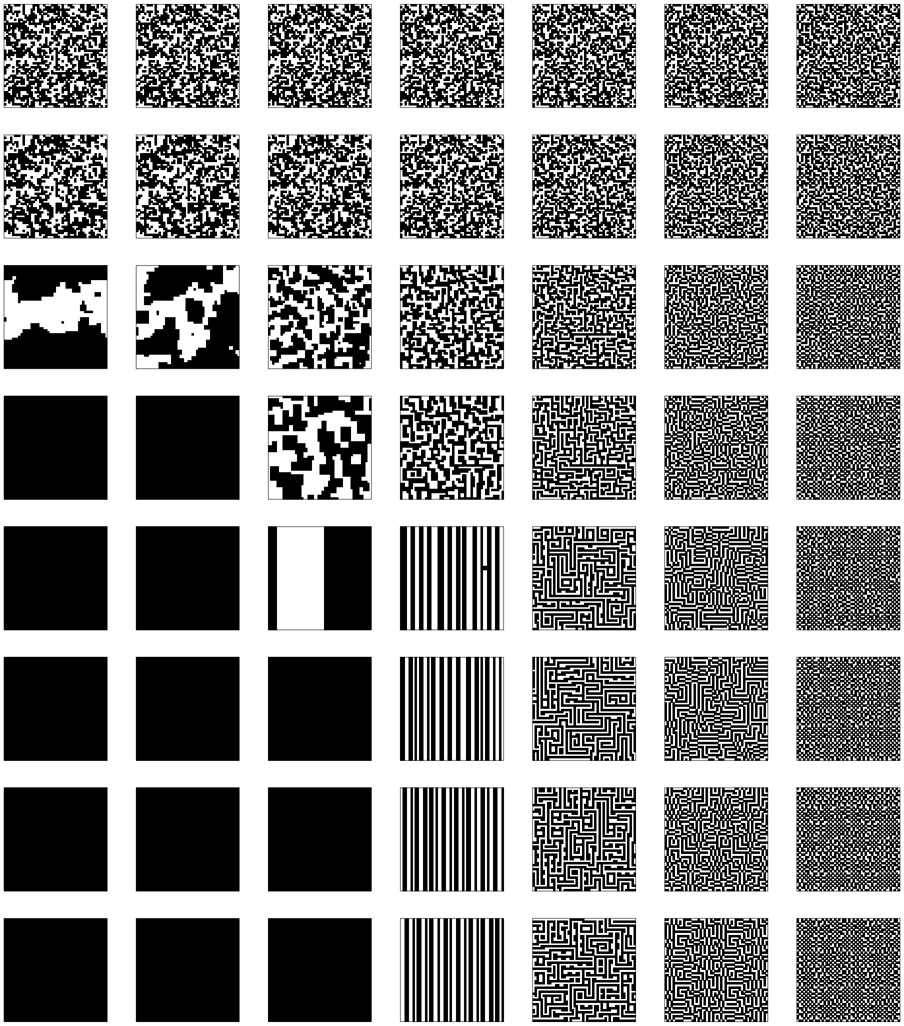

Figure B.4: Domain structure near the coercive field. Rows (from top to bottom): $R = 10, 5, 1, 0.5, 0.1, 10^{-3}, 10^{-6}, 0$. Columns (from left to right): $J_{\mathrm{dp}} = 0, 0.1, 0.3, 0.6, 1, 2, 3$. All the calculations are done for system size 50^2.

References

[1] The algorithm is available from Andrew Goldberg's Network Optimization Library, http://www.avglab.com/andrew/soft.html.

[2] $\Delta H(M, \Delta M)$ method for the determination of intrinsic switching field distributions in perpendicular media.

[3] Experimental Observation of Disorder-Driven Hysteresis-Loop Criticality.

[4] Random-field critical behavior of a $d = 3$ Ising system.

[5] Anglés d'Auriac, J., and Sourlas, N. The 3d random field Ising model at zero temperature. *Europhys. Lett. 39* (1997), 473.

[6] Aronovitz, J. A., and Nelson, D. R. Universal features of polymer shapes. *Journal De Physique 47* (Sep 1986), 1445–1456.

[7] Aronovitz, J. A., and Stephen, M. J. Universal features of the shapes of percolation clusters and lattice animals. *J. Phys. A: Math. Gen. 20* (1987), 2539–2556.

[8] Belanger, D. P., and Nattermann, T. In *Spin Glasses and Random Fields*, A. P. Young, Ed. World Scientific, Singapore, 1998.

[9] Berger, A., Lengsfield, B., and Ikeda, Y. Determination of intrinsic switching field distributions in perpendicular recording media (invited). *J. Appl. Phys. 99* (2006), 08E705.

[10] Bricmont, J., and Kupiainen, A. Lower critical dimension for the random-field Ising model. *Phys. Rev. Lett. 59*, 16 (Oct 1987), 1829–1832.

[11] Bricmont, J., and Kupiainen, A. Phase transition in the 3d random field Ising model. *Comm. Math. Phys. 116*, 4 (1988), 539–572.

[12] Carpenter, J. H., and Dahmen, K. A. Barkhausen noise and critical scaling in the demagnetization curve. *Phys. Rev. B 67*, 2 (2003), 020412.

[13] Cherkassky, B., and Goldberg, A. V. *Algorithmica 19* (1997), 390.

[14] Christopher R. Pike, A. P. R., and Verosub, K. L. Characterizing interactions in fine magnetic particle systems using first order reversal curves. *J. Appl. Phys. 85*, 9 (May 1999), 6660–6667.

[15] Clark, A., Madden, T., and Warren, P. Summation of electrostatic interactions in quasi-two-dimensional simulations. *Molec. Phys. 87*, 5 (Apr 1996), 1063.

[16] Colaiori, F., Alava, M. J., Durin, G., Magni, A., and Zapperi, S. Phase Transitions in a Disordered System in and out of Equilibrium. *Phys. Rev. Lett. 92*, 25 (Jun 2004), 257203.

[17] Dahmen, K. A., and Sethna, J. P. Hysteresis, avalanches, and disorder-induced critical scaling: A renormalization-group approach. *Phys. Rev. B 53*, 22 (Jun 1996), 14872–14905.

[18] Dotsenko, V. S., Windey, P., Harris, G., Marinari, E., Martinec, E., and Picco, M. Critical and topological properties of cluster boundaries in the 3D Ising model. *Phys. Rev. Lett. 71*, 6 (Aug 1993), 811–814.

[19] Draper, N. R., and Smith, H. *Applied regression analysis.* Wiley, New York, 1966.

[20] Durin, G., and Zapperi, S. In *The Science of Hysteresis*, G. Bertotti and I. Mayergoyz, Eds. Academic Press, 2005.

[21] Duxbury, P. M., and Meinke, J. H. Ground state nonuniversality in the random-field Ising model. *Phys. Rev. E 64*, 3 (Aug 2001), 036112.

[22] Family, F., Vicsek, T., and Meakin, P. Are Random Fractal Clusters Isotropic? *Phys. Rev. Lett. 55*, 7 (Aug 1985), 641–644.

[23] Field, S., Witt, J., Nori, F., and Ling, X. Superconducting Vortex Avalanches. *Phys. Rev. Lett. 74*, 7 (Feb 1995), 1206–1209.

[24] Fisher, D. S. Scaling and critical slowing down in random-field Ising systems. *Phys. Rev. Lett. 56*, 5 (Feb 1986), 416–419.

[25] Froltsov, V. A., Blaak, R., Likos, C. N., and Löwen, H. Crystal structures of two-dimensional magnetic colloids in tilted external magnetic fields. *Phys. Rev. E 68*, 6 (Dec 2003), 061406.

[26] Frontera, C., Goicoechea, J., Ortín, J., and Vives, E. Efficient Algorithm for Finding Ground-States in the Random Field Ising Model with an External Field. *J. Comp. Phys. 160* (2000), 117–125.

[27] Frontera, C., and Vives, E. "Avalanches" in the ground state of the 3D Gaussian random field Ising model driven by an external field. *Comp. Phys. Comm. 147* (Aug 2002), 455–458.

[28] Gao, K.-Z., and Bertram, H. N. Dynamic switching in tilted and conventional perpendicular recording media. *J. Appl. Phys. 96*, 12 (Dec. 2004), 7753–7755.

[29] Goldenfeld, N. *Lectures on Phase Transitions and the Renormalization Group.* Westview Press, 2005.

[30] Greaves, S. J., Goodman, A. M., Muraoka, H., and Nakamura, Y. Exchange coupling and grain-size distributions in perpendicular recording media. *J. Magn. Magn. Mater. 287* (2005), 66–71.

[31] Grønbech-Jensen, N. Lekner Summation of Long Range Interactions in Periodic Systems. *Int. J. mod. Phys. C 8*, 6 (Dec 2005), 1287.

[32] Grzybowski, A., and Bródka, A. Coulomb interactions in a computer simulation of a system periodic in two directions. *Molec. Phys. 100*, 7 (Apr 2002), 1017.

[33] Guagnelli, M., Marinari, E., and Parisi, G. Maximal mean-field solutions in the random field Ising model: the pattern of the symmetry breaking. *J. Phys. A: Math. Gen. 26* (Nov 1993), 5675–5685.

[34] Gutenberg, B., and Richter, C. F. *Seismicity of the Earth and Associated Phenomena.* Princeton Univ. Press, Princeton, 1954.

[35] Hagen, M., Cowley, R. A., Satija, S. K., Yoshizawa, H., Shirane, G., Birgeneau, R. J., and Guggenheim, H. J. Random fields and three-dimensional Ising models: $Co_xZn_{1-x}F_2$. *Phys. Rev. B 28*, 5 (Sep 1983), 2602–2613.

[36] Hartmann, A. K. Ground state structure of diluted antiferromagnets and random field systems. *Physica A 248* (1998), 1.

[37] Hartmann, A. K. Critical exponents of four-dimensional random-field Ising systems. *Phys. Rev. B 65*, 17 (May 2002), 174427.

[38] Hartmann, A. K., and Nowak, U. Universality in three dimensional random-field ground states. *Eur. Phys. J. B 7* (1999), 105.

[39] Hartmann, A. K., and Rieger, H. *Optimization algorithms in physics.* Wiley-VCH, 2002.

[40] Hartmann, A. K., and Young, A. P. Specific-heat exponent of random-field systems via ground-state calculations. *Phys. Rev. B 64*, 21 (Nov 2001), 214419.

[41] Hellwig, O., Berger, A., Thomson, T., Dobisz, E., Bandic, Z. Z., Yang, H., Kercher, D. S., and Fullerton, E. E. Separating dipolar broadening from the intrinsic switching field distribution in perpendicular patterned media. *Appl. Phys. Lett. 90* (2007), 162516.

[42] Houle, P. A., and Sethna, J. P. Acoustic emission from crumpling paper. *Phys. Rev. E 54*, 1 (Jul 1996), 278–283.

[43] Houston, H., Benz, H. M., and Vidale, J. E. Time functions of deep earthquakes from broadband and short-period stacks. *J. Geophys. Res. 103* (1998), 29895.

[44] Hukushima, K. Random Fixed Point of Three-Dimensional Random-Bond Ising Models. *J. Phys. Soc. Jpn. 69*, 3 (March 2000), 631–634.

[45] Imbrie, J. Z. Lower Critical Dimension of the Random-Field Ising Model. *Phys. Rev. Lett. 53*, 18 (Oct 1984), 1747–1750.

[46] Jagodzinski, O., Eisenriegler, E., and Kremer, K. Universal shape properties of open and closed polymer chains: renormalization group analysis and Monte Carlo experiments. *J. Phys. I France 2* (Dec 1992), 2243–2279.

[47] Ji, H., and Robbins, M. O. Percolative, self-affine, and faceted domain growth in random three-dimensional magnets. *Phys. Rev. B 46*, 22 (Dec 1992), 14519–14527.

[48] Jiles, D. *Introduction to magnetism and magnetic materials.* Chapman and Hall, London, 1996.

[49] Kim, D. H., Choe, S. B., and Shin, S. C. Direct Observation of Barkhausen Avalanche in Co Thin Films. *Phys. Rev. Lett. 90* (2003), 087203.

[50] Kolton, A. B., Rosso, A., Giamarchi, T., and Krauth, W. Dynamics below the Depinning Threshold in Disordered Elastic Systems. *Phys. Rev. Lett. 97*, 5 (2006), 057001.

[51] Kuntz, M. C., Perković, O., Dahmen, K. A., Roberts, B. W., and Sethna, J. P. Hysteresis, Avalanches and Noise. *Comp. Sci. Eng. 1*, 4 (1999), 73–81.

[52] LaBonte, A. E. Two-Dimensional Bloch-Type Domain Walls in Ferromagnetic Films. *J. Appl. Phys. 40* (1969), 2450.

[53] Lee, W. Y., Choi, B.-C., Xu, Y. B., and Bland, J. A. C. Magnetization reversal dynamics in epitaxial Fe/GaAs(001) thin films. *Phys. Rev. B 60*, 14 (Oct 1999), 10216–10221.

[54] Lekner, J. Summation of Coulomb fields in computer-simulated systems. *Physica A 176* (1991), 485.

[55] Liem, S., and Clarke, J. Calculation of Coulomb interactions in two-dimensionally periodic systems. *Molec. Phys. 92*, 1 (Sep 1997), 19.

[56] Lilly, M. P., Finley, P. T., and Hallock, R. B. Memory, congruence, and avalanche events in hysteretic capillary condensation. *Phys. Rev. Lett. 71*, 25 (Dec 1993), 4186–4189.

[57] Liu, Y., Dahmen, K. A., and Berger, A. Comparative Study of the $\Delta H(M, \Delta M)$ method reliability for square and triangular lattices. *J. Appl. Phys. 103* (2008), 07F504.

[58] Liu, Y., Dahmen, K. A., and Berger, A. Intrinsic switching field distribution in perpendicular recording media: numerical study of the $\Delta H(M, \Delta M)$ method. *Phys. Rev. B 77* (2008), 054422.

[59] Liu, Y., Dahmen, K. A., and Berger, A. The role of dipolar interactions for the determination of intrinsic switching field distributions. *Appl. Phys. Lett. 92* (2008), 222503.

[60] Mandelbrot, B. B. *The Fractal Geometry of Nature.* W. H. Freeman, New York, 1982.

[61] Maritan, A., Cieplak, M., Swift, M. R., and Banavar, J. R. Spin-flip avalanches and dynamics of first order phase transitions. *Phys. Rev. Lett. 72*, 6 (Feb 1994), 946.

[62] Mayergoyz, I. D. Mathematical Models of Hysteresis. *Phys. Rev. Lett. 56*, 15 (Apr 1986), 1518–1521.

[63] Mazars, M. Lekner summations. *J. Chem. Phys. 115*, 7 (Aug 2001), 2955.

[64] Mazars, M. Lekner summations and Ewald summations for quasi-two-dimensional systems. *Molec. Phys. 103*, 9 (May 2005), 1241.

[65] McClure, J. C. J., and Schröder, K. The Magnetic Barkhausen Effect. *CRC Crit. Rev. Solid State Sci. 6* (1976), 45.

[66] Mézard, M., and Monasson, R. Glassy transition in the three-dimensional random-field Ising model. *Phys. Rev. B 50*, 10 (Sep 1994), 7199–7202.

[67] Mézard, M., and Young, A. P. Replica symmetry breaking in the random field Ising model. *Europhys. Lett. 18*, 7 (Apr 1992), 653–659.

[68] Middleton, A. A. Scaling, domains, and states in the four-dimensional random field Ising magnet. arXiv:cond-mat/0208182.

[69] Middleton, A. A. Asymptotic uniqueness of the sliding state for charge-density waves. *Phys. Rev. Lett. 68*, 5 (Feb 1992), 670–673.

[70] Middleton, A. A. Critical Slowing Down in Polynomial Time Algorithms. *Phys. Rev. Lett. 88*, 1 (Dec 2001), 017202.

[71] Middleton, A. A., and Fisher, D. S. Three-dimensional random-field Ising magnet: Interfaces, scaling, and the nature of states. *Phys. Rev. B 65*, 13 (Mar 2002), 134411.

[72] Miles, J. Effect of Grain Size Distribution on the Performance of Perpendicular Recording Media. *IEEE Trans. Mag 43*, 3 (2007), 955.

[73] Newman, C. M., and Stein, D. L. Metastable states in spin glasses and disordered ferromagnets. *Phys. Rev. E 60*, 5 (Nov 1999), 5244–5260.

[74] Newman, M. E. J., and Barkema, G. T. Monte Carlo study of the random-field Ising model. *Phys. Rev. E 53*, 1 (Jan 1996), 393–404.

[75] Newman, M. E. J., Roberts, B. W., Barkema, G. T., and Sethna, J. P. Real-space renormalization group for the random-field Ising model. *Phys. Rev. B 48*, 22 (Dec 1993), 16533–16538.

[76] Ogielski, A. T. Integer Optimization and Zero-Temperature Fixed Point in Ising Random-Field Systems. *Phys. Rev. Lett. 57*, 10 (Sep 1986), 1251–1254.

[77] Ogielski, A. T., and Huse, D. A. Critical Behavior of the Three-Dimensional Dilute Ising Antiferromagnet in a Field. *Phys. Rev. Lett. 56*, 12 (Mar 1986), 1298–1301.

[78] Pérez-Reche, F. J., and Vives, E. Spanning avalanches in the three-dimensional Gaussian random-field Ising model with metastable dynamics: Field dependence and geometrical properties. *Phys. Rev. B 70* (Dec 2004), 214422.

[79] Perković, O., Dahmen, K. A., and Sethna, J. P. Avalanches, Barkhausen Noise, and Plain Old Criticality. *Phys. Rev. Lett. 75*, 24 (Dec 1995), 4528–4531.

[80] Perković, O., Dahmen, K. A., and Sethna, J. P. Disorder-induced critical phenomena in hysteresis: Numerical scaling in three and higher dimensions. *Phys. Rev. B 59*, 9 (Mar 1999), 6106–6119.

[81] Pierce, M. S., Moore, R. G., Sorensen, L. B., Kevan, S. D., Hellwig, O., Fullerton, E. E., and Kortright, J. B. Quasistatic X-Ray Speckle Metrology of Microscopic Magnetic Return-Point Memory. *Phys. Rev. Lett. 90*, 17 (May 2003), 175502.

[82] Plumer, M. L., van Ek, J., and Weller, D., Eds. *The Physics of Ultrahigh-Density Magnetic Recording (Springer Series in Surface Sciences).* Springer, 2001.

[83] Press, W. H., Teukolsky, S. A., Vetterling, W. T., and Flannery, B. P. *Numerical Recipes 3rd Edition: The Art of Scientific Computing.* Cambridge University Press, 2002.

[84] Rosso, A., and Krauth, W. Monte Carlo dynamics of driven elastic strings in disordered media. *Phys. Rev. B 65*, 1 (Nov 2001), 012202.

[85] Schabes, M., and Aharoni, A. Magnetostatic interaction fields for a three-dimensional array of ferromagnetic cubes. *IEEE Trans. Mag 23*, 6 (1987), 3882.

[86] Schneider, T., and Pytte, E. Random-field instability of the ferromagnetic state. *Phys. Rev. B 15*, 3 (Feb 1977), 1519–1522.

[87] Schwarz, A., Liebmann, M., Kaiser, U., Wiesendanger, R., Noh, T. W., and Kim, D. W. Visualization of the Barkhausen Effect by Magnetic Force Microscopy. *Phys. Rev. Lett. 92*, 7 (Feb 2004), 077206.

[88] Sethna, J. P., Dahmen, K., Kartha, S., Krumhansl, J. A., Perković, O., Roberts, B. W., and Shore, J. D. Sethna et al. reply. *Phys. Rev. Lett. 72*, 6 (Feb 1994), 947.

[89] Sethna, J. P., Dahmen, K. A., Kartha, S., Krumhansl, J. A., Roberts, B. W., and Shore, J. D. Hysteresis and hierarchies: Dynamics of disorder-driven first-order phase transformations. *Phys. Rev. Lett. 70*, 21 (May 1993), 3347–3350.

[90] Sethna, J. P., Dahmen, K. A., and Myers, C. R. Crackling noise. *Nature 410*, 6825 (March 2001), 242–250.

[91] Sethna, J. P., Dahmen, K. A., and Perkovic, O. Random-Field Ising Models of Hysteresis. arXiv:cond-mat/0406320, for inclusion in a book “The Science of Hysteresis, Vol. II”, edited by Giorgio Bertotti and Isaak Mayergoyz. Academic Press (2006).

[92] Sethna, J. P., Shore, J. D., and Huang, M. Scaling theory for the glass transition. *Phys. Rev. B 44*, 10 (Sep 1991), 4943–4959.

[93] Shimatsu, T., Kondo, T., Mitsuzuka, K., Watanabe, S., Aoi, H., Muraoka, H., and Nakamura, Y. Switching Field Distribution of CoPtCr-SiO_2Perpendicular Recording Media Obtained by Subtracting Thermal Agitation of Magnetization. *IEEE Trans. Mag 42*, 10 (Oct. 2006), 2384–2386.

[94] Shimizu, Y., and Bertram, H. N. Micromagnetic study of the transition parameter and position jitter in perpendicular recording. *IEEE Trans. Mag 39*, 3 (May 2003), 1846–1850.

[95] Sperb, R. Extension and simple proof of Lekner's summation formula for Coulomb forces. *Molec. Simul. 13* (1994), 189.

[96] Tagawa, I., and Nakamura, Y. Relationships between high density recording performance and particle coercivity distribution. *IEEE Trans. Mag 27*, 6 (Nov 1991), 4975–4977.

[97] van de Veerdonk, R., Wu, X., and Weller, D. Switching Field Distributions and ΔM Measurements for Perpendicular Media. *IEEE Trans. Mag 38*, 5 (Sep. 2002), 2450–2452.

[98] van de Veerdonk, R., Wu, X., and Weller, D. Determination of switching field distributions for perpendicular recording media. *IEEE Trans. Mag 39*, 1 (Jan. 2003), 590–593.

[99] Villain, J. Nonequilibrium "Critical" Exponents in the Random-Field Ising Model. *Phys. Rev. Lett. 52*, 17 (Apr 1984), 1543–1546.

[100] Vives, E., Ortín, J., Mañosa, L., Ràfols, I., Pérez-Magrané, R., and Planes, A. Distributions of avalanches in martensitic transformations. *Phys. Rev. Lett. 72*, 11 (Mar 1994), 1694–1697.

[101] Vives, E., Rosinberg, M. L., and Tarjus, G. Hysteresis and avalanches in the $T = 0$ random-field Ising model with two-spin-flip dynamics. *Phys. Rev. B 71*, 13 (2005), 134424.

[102] White, R. A., and Dahmen, K. A. Driving Rate Effects on Crackling Noise. *Phys. Rev. Lett. 91*, 8 (Aug 2003), 085702.

[103] Winklhofer, M., and Zimanyi, G. T. Extracting the intrinsic switching field distribution in perpendicular media: A comparative analysis. *J. Appl. Phys. 99* (Apr. 2006), 08E710.

[104] Wood, R., Hsu, Y., and Schultz, M. Perpendicular Magnetic Recording Technology. http://www.hitachigst.com/tech/techlib.nsf/techdocs/.

[105] Wu, Y., and Machta, J. Ground States and Thermal States of the Random Field Ising Model. *Phys. Rev. Lett. 95*, 13 (Sep 2005), 137208–137211.

[106] Young, A. P., and Nauenberg, M. Quasicritical Behavior and First-Order Transition in the $d = 3$ Random-Field Ising Model. *Phys. Rev. Lett. 54*, 22 (Jun 1985), 2429–2432.

Author's Biography

Yang Liu was born on February 19, 1980, in Suqian, Jiangsu Province, China. He graduated from Nanjing University with a B.S. in Physics (2000) and a M.S. in Physics (2003). In the Fall of 2003, he began study in Urbana, Illinois under the advisement of Prof. Karin Dahmen. He completed his doctorate in 2009.